

Novel characterisation methods for pore systems of seal rocks in reservoirs used for downhole gas production and storage

Eleanor Grace Pitcher
(ID: 4285248)

A thesis submitted to the University of Nottingham for the degree of Doctor of
Philosophy

University of Nottingham

Department of Environmental and Chemical Engineering

Preface

All the work in this thesis is believed to be original except where explicit reference to other people and authors is given.

The Marcellus and Utica shale samples in this thesis were supplied by Virginia Polytechnic Institute and State University (Department of Mining and Minerals Engineering), and the Bowland was supplied by the British Geological Survey. The pure kerogen sample used was supplied by Schlumberger and analysis was carried out by myself, the illite data was supplied by Imperial College London who were supplied by the Clay Mineral Society.

The computerised x-ray tomography (CXT) work throughout the thesis was carried out by Dr Martin Corfield (University of Nottingham). I carried out the mercury intrusion porosimetry experiments prior to CXT, and analysed the experimental data. RockEval Pyrolysis was carried out by Dr Christopher Vane (British Geological Survey). The overcondensation sorption experiments were carried out by Rob Fletcher (Johnson Matthey), who also carried out conventional sorption experiments for those sample samples, since it was not possible to perform the overcondensation experiments in Nottingham at the time.

At the onset of Covid-19 and the working practice of labs changing the following experimental work was carried out by others. The mercury intrusion porosimetry for Marcellus 7804'-7807' was carried out by Rob Fletcher (Johnson Matthey), and all the Bowland samples were carried out by Jason Greaves (University of Nottingham). The SEM MLA for the Bowland and the acid treated samples was carried out by Dr Elisabeth Steer (University of Nottingham). All other mercury intrusion porosimetry work and SEM MLA I carried out myself prior to Covid-19.

Prior to the onset of Covid-19 investigations began on the effect of acid (HCl of 0.12 weight%) on shale samples with contrasting mineralogy's (clay rich and carbonate rich) to assess the impact of fracking fluid on formation integrity and production. Acid treatment was carried out by Dr Veerle Vandeginste (University of Nottingham), in her geochemistry lab in the Department of Chemistry.

Acknowledgements

I would like to express my greatest thanks and appreciation to Prof. Sean Rigby for not only giving me the opportunity to take on the challenge of a PhD; but for the continued support, high level discussions and providing a brilliant platform to continually challenge my own understanding throughout the project. Not only this, but allowing the space to make the project my own by introducing more geology into where Prof. David Large fantastically supported in this area, giving Sean and I the opportunity to give experimental findings geological meaning. I would like to think that having come into the PhD with little research experience and a lot to learn I have embraced the challenge and can now call myself a research scientist.

In the early stages of the project the support and guidance from Prof. Matthew Hall were invaluable; and also that of Prof. Nino Ripepi during my time at Virginia Polytechnic Institute and State University, as well as for being on hand with any queries regarding shale samples. A huge amount of appreciation also goes to Dr Aleksandra Gonciaruk, who has been consistently available for laboratory equipment training, experimental help, with the best way to process results from each rig and for the occasional, but much needed coffee break.

Without the funding of the NERC CDT in Oil and Gas, and the University of Nottingham I would have been unable to take on the challenge of a PhD which I am very grateful for. In addition to this the support from the CDT through Anna and Lorna has been invaluable, as well as from the other CDT students whom I have relished the opportunity to continue learning from. I am hugely appreciative of the training academy for providing me with so many exceptional courses, and the opportunity to broaden my knowledge in different areas of the oil and gas industry through both class and fieldwork.

I would finally like to show my massive appreciation to my family and Tori who have supported me throughout the four (and a bit) years of the project, especially so in the past year where everyone without exception has been challenged.

Abstract

Seal rocks, also called cap rocks, are a crucial and sometimes overlooked factor (due to not being the primary factor in exploration, having more of a role in the resource evaluation and development) in the evaluation of a potential gas accumulation, and is critical in downhole gasification (enhanced gas recovery) and storage of other gases. Shale rocks are the most common seal rock in conventional reservoirs; currently shales are providing an unconventional oil and gas source which can act as a potential buffer to the energy industry as it transitions towards renewable energies (which are still in their formative years) whilst there is a continued rise in demand for energy globally. Over the past ten years there has been a boom in shale gas production in the United States (Barsotti *et al.*, 2016; Li *et al.*, 2016; Yu *et al.*, 2016), and it is anticipated that this boom may be repeated in the UK (Andrews, 2013).

Downhole gasification (enhanced gas recovery) offers a potential way to produce from these “difficult-to-extract” (as a result of low permeability’s) reservoirs by using carbon dioxide as a displacement gas for methane. At the same time this carbon dioxide can be also be stored resulting in the environment being exposed to less greenhouse gas (Kim, Cho and Lee, 2017; D. Liu *et al.*, 2019). However, it is erroneous to consider shales as a completely impermeable layer, and their ability to retain different fluids is variable (controlled by the capillary entry pressure and/or the permeability and the extent of diffusive losses) which could result in some/all of them being ineffective at retaining carbon dioxide. This is because shales are highly complex and anisotropic containing pores over several orders of magnitude. Typically they have a significantly low permeability and porosity, combined with structural and chemical heterogeneities of shales mean that physical processes are significantly impacted. Importantly the structure-transport relationship is complex resulting in processes such as hydrocarbon migration, methane extraction, gas storage, or carbon sequestration being poorly understood. This project proposes the development of several novel characterisation techniques and combinations of complementary techniques to characterise the multi-scale properties of shales in order to more accurately provide the information needed for secure decisions regarding gas production and storage.

In this work mercury porosimetry, together with mercury thermoporometry, and computerised x-ray tomography (CXT) were performed on post-porosimetry samples containing entrapped mercury, to characterise the pore structure of cap-rocks. However limitations were identified where mercury was trapped in pores too large to sufficiently suppress the bulk melting point (thermoporometry) such that a separate melting peak formed. However, the combined use of mercury porosimetry and computerised x-ray tomography was effective at highlighting the location of trapped mercury, but was ineffective at providing quantitative results regarding the macroporosity of the sample. Further drawbacks of mercury porosimetry based analysis are the potential destruction of experimental material where further analysis cannot be carried out unless mercury forms part of the experimental technique (i.e. thermoporometry and computerised x-ray tomography as described above).

Therefore, gas overcondensation, was proposed as an alternative technique as a bridge between micro-pore characterisation, below the limit of mercury detection, up to macropores which are undetected in conventional sorption experiments, with the additional benefit that the overcondensation method preserves experimental material. In previous work, gas sorption experiments typically consist of a boundary adsorption isotherm up to a restricted maximum pressure (e.g. up to $0.995 \frac{p}{p_0}$). Following this there is a pseudo-

boundary desorption isotherm, which is merely a descending curve since complete pore-filling with liquid-like condensate was not achieved. As a result of this conventional gas sorption alone cannot prove the complete pore size range up to large macro-pores. Gas overcondensation experiments can be expanded with gas sorption scanning curves which have successfully revealed advanced condensation effects, allowing probing of the inter-relationship and spatial juxtaposition of multi-scale porosities. Gas overcondensation and scanning loops were successfully used for the Utica and Bowland samples to reveal where additional percolations knee develop that are characteristic of a particular pore size within the wider pore network (Utica). Work on the Bowland was able to determine that there are some large macro-pores shielded by pore necks of <4nm; complimentary adsorption calorimetry work was able to relate this shielding to pore necks by calculating the mass transfer and thermokinetic properties of the samples.

Prior to the use of gas overcondensation mineralogy was assessed with the use of conventional gas sorption where results (Marcellus and Utica) showed an inverse relationship between carbonate and illite quantities (i.e. an increasing carbonate content was associated to a decreasing illite content). Utica surface areas demonstrated a strong correlation to illite quantity, whereas Marcellus surface areas demonstrated a weaker correlation to illite. For both samples there was good correlation to the total organic carbon. With the new information gained from gas overcondensation it has allowed for additional, and more advanced correlations to be made with other physical properties of shales such as the mineralogy. It was found that for the changeover period (Utica samples), from primarily clay to carbonaceous deposits, there was an associated growth in the disorder of the pore network over particular key length-scales. These length-scales were highlighted by percolation processes in the gas overcondensation and scanning curves. This peaking in disorder was also associated to a peak in total organic carbon content and the accessible porosity was shown to be dominated by the organic carbon phase.

Following the identification of this trend with the use of gas overcondensation and mineralogy, numerical analysis techniques were used to replicate these findings with the use of the homotactic patch model. It was established that with the use of conventional gas sorption (nitrogen) isotherms and isotherms for the pure mineral phases of the sample good results can be generated indicating the associated quantity of each mineral to the sample.

List of Publications

Tang, X., Ripepi, N., Luxbacher, K. and Pitcher, E., 2017. Adsorption models for methane in shales: Review, comparison, and application. *Energy & Fuels*, 31(10), pp.10787-10801.

Rigby, S., Pitcher, E., Large, D. and Fletcher., R. 2021. Multi-scale Pore Structural Change Across a Paleodepositional Transition in Utica Shale Probed by Gas Sorption Overcondensation and Scanning (under review).

Rigby, S., Pitcher, E., Fletcher, R. and Large, D., 2021. Pore Structure-Transport Relationships in Bowland Shale. *Bowland Shale Geological Society Special Publication* (under review).

List of Presentations

Pitcher, E., Rigby, S. and Large, D., 2019, January. Petrographic controls on shale surface area and the novel characterisation of pore structures. In *Geophysical Research Abstracts* (Vol. 21).

Funding Sources

This work was supported by the Natural Environment Research Council [grant number NE/M00578X/1], and the University of Nottingham for the award of a partial PhD studentship.

Contents

| | |
|---|-----|
| Preface..... | i |
| Acknowledgements..... | ii |
| Abstract | iii |
| List of Publications | v |
| List of Presentations..... | v |
| Funding Sources | v |
| Table of Figures..... | ix |
| List of Tables | xx |
| The Thesis Structure..... | xxi |
| 1. Introduction | 1 |
| 2. Review of Literature | 7 |
| 2.1. The Formation of Shales | 7 |
| 2.2. Characterisation Complexity..... | 11 |
| 2.3. Evolution of the Use of Shales..... | 13 |
| 2.4. Essential Pore Characteristics of Shales..... | 17 |
| 2.5. Experimental Techniques..... | 18 |
| 2.5.1. Gas Adsorption | 18 |
| 2.5.2. Mercury Intrusion Porosimetry | 28 |
| 2.5.3. Computer X-ray Tomography (CXT)..... | 30 |
| 2.5.4. Differential Scanning Calorimetry (DSC) | 31 |
| 2.5.5. RockEval Pyrolysis..... | 32 |
| 2.5.6. Scanning Electron Microscopy (SEM) with Mineral Liberation Analysis (MLA)... | 32 |
| 2.5.7. Thermogravimetric Analysis (TGA) | 33 |
| 2.5.8. X-Ray Diffraction (XRD) | 33 |
| 2.5.9. Small Angle X-Ray Scattering (SAXS)..... | 33 |
| 2.5.10. Nuclear Magnetic Resonance (NMR) | 34 |
| 2.6. Numerical Modelling Techniques..... | 34 |
| 2.6.1. Fractal Dimensions (“self-similarity”)..... | 34 |
| 2.6.2. Homotattic Patch (BET, nBET and FHH) | 36 |
| 2.7. Technique Development Thus Far | 37 |
| 2.8. Sample Geological History | 39 |
| 2.8.1. Marcellus..... | 40 |
| 2.8.2. Utica | 40 |
| 2.8.3. Bowland..... | 41 |
| 3. Aims and Objectives | 43 |

| | |
|---|-----|
| 4. Methodology..... | 46 |
| 4.1. Gas Sorption | 46 |
| 4.2. Mercury Intrusion Porosimetry (MIP)..... | 52 |
| 4.3. Differential Scanning Calorimetry (DSC) | 53 |
| 4.4. Computed X-Ray Tomography (CXT) | 54 |
| 4.5. Scanning Electron Microscopy with Mineral Liberation Analysis (SEM MLA)..... | 54 |
| 4.6. Thermogravimetric Analysis (TGA), X-Ray Diffraction (XRD) and RockEval | 55 |
| 4.7. Numerical Modelling | 56 |
| 4.7.1. Fractal Dimensions..... | 60 |
| 4.7.2. Homotattic Patch | 62 |
| 4.7.3. Rationale | 64 |
| 5. The Marcellus Shale..... | 65 |
| 5.1. Methodology | 65 |
| 5.2. Results..... | 65 |
| 5.3. Discussion..... | 84 |
| 5.4. Conclusion | 88 |
| 6. The Utica Shale..... | 89 |
| 6.1. Materials | 89 |
| 6.2. Methodology | 91 |
| 6.3. Results..... | 92 |
| 6.4. Discussion..... | 109 |
| 6.5. Conclusions | 115 |
| 6.6. Additional Work..... | 115 |
| 7. The Bowland Shale | 117 |
| 7.1. Materials | 117 |
| 7.2. Methodology | 117 |
| 7.3. Results..... | 120 |
| 7.4. Discussion..... | 135 |
| 7.5. Conclusions | 137 |
| 8. Shale Treatment | 137 |
| 8.1. Rationale | 137 |
| 8.2. Methodology | 138 |
| 8.3. Results..... | 138 |
| 8.4. Discussion..... | 147 |
| 8.5. Conclusion | 148 |
| 9. Discussion | 149 |

| | |
|-------------------------------|-----|
| 10. Conclusion..... | 156 |
| 10.1. Introduction..... | 156 |
| 10.2. Empirical Findings..... | 156 |
| 10.3. Future Work | 158 |
| 10.4. Summary | 159 |
| Appendix 1..... | 160 |
| Appendix 2..... | 163 |
| Appendix 3..... | 164 |
| Appendix 3.1 | 164 |
| Appendix 3.1.1 | 164 |
| Appendix 3.1.2 | 166 |
| Appendix 3.1.3 | 169 |
| Appendix 3.2 | 175 |
| Appendix 3.2.1 | 175 |
| Appendix 3.2.2 | 179 |
| Appendix 4..... | 184 |
| Appendix 5..... | 186 |
| Appendix 5.1 | 186 |
| Appendix 5.2 | 188 |
| Appendix 6..... | 189 |
| Appendix 6.1 | 189 |
| Appendix 6.2 | 190 |
| Bibliography..... | 191 |

Table of Figures

| | |
|---|----|
| Figure 1: different marine environments and the anoxic, dysoxic or oxic conditions which lead to the preservation or destruction of organic matter respectively (edited from Arthur (1994)). | 8 |
| Figure 2: hydraulic fracturing operations where the well penetrates vertically through the water table to the shale formation and then changes direction to drill horizontally. Following this the formation is hydraulically fractured by injecting water, sand and chemicals into the well forming fissures which allow gas to flow out. | 14 |
| Figure 3: simplified diagram of carbon capture and storage in a saline aquifer with a caprock able to trap stored CO ₂ . CO ₂ is injected via an injection well at the surface which receives captured waste CO ₂ . | 16 |
| Figure 4: flow dynamics of CO ₂ and CH ₄ through a shale formation where CO ₂ preferentially adsorbs forcing CH ₄ to desorb (edit Godec et al., 2014). | 17 |
| Figure 5: between physisorption and chemisorption where there is an absence of covalent bonds in physisorption where adsorption is controlled by van der waals forces. | 18 |
| Figure 6: isotherm with "Point B" labelled for the beginning of the multilayer adsorption starts. | 21 |
| Figure 7: different types of isotherms which can be achieved from gas adsorption. I : Microporous materials (e.g. Zeolite and Activated carbon), II : Non porous materials (e.g. Nonporous Alumina and Silica), III : Non porous materials and materials which have the weak interaction between adsorbate and adsorbent (e.g. Graphite/water), IV : Mesoporous materials (e.g. Mesoporous Alumina and Silica), V : Porous materials and materials that have the weak interaction between the adsorbate and adsorbent (e.g. Activated carbon/water) (Rouquerol et al., 2014). | 24 |
| Figure 8: visualisation of the differences between pore blocking and cavitation where pore blocking occurs at $ppo > 0.5$ and cavitation takes place at approximately $0.5 ppo$. In pore blocking the pore body does not empty until the leading neck has emptied, whereas in cavitation the body empties through the pore neck which remains filled during this time. | 27 |
| Figure 9: ink-bottle pore with a much wider pore body than neck, with mercury trapped in a pore following extrusion when the mercury has become disconnected from the mercury column. | 29 |
| Figure 10: the contact angle of the liquid-gas and liquid-solid interface shown by θ . | 30 |
| Figure 11: differentiating between the adhesive and cohesive forces related to surface tension in capillary action. | 30 |
| Figure 12: a pipe/tube/capillary with radius r , and a pressure difference ΔP , across it. | 30 |
| Figure 13: heterogeneous shale surface showing organic and inorganic minerals. Inorganic minerals are represented by two forms but many more would be present in nature. | 36 |
| Figure 14: schematic of the sample tube setup for Micromeritics 3Flex gas sorption. A, the sample tube. B, the filler rod. C, the ferrule and nut. D, the isotherm jacket used for N ₂ analysis. | 47 |
| Figure 15: iQ isotherm data corrections where a polynomial fitted to the blank data is used to subtract from the sample points for the exact pressure that the points are taken from. | 51 |
| Figure 16: mass transfer kinetics for a blank run, and sample data collected using the same experimental procedure. | 51 |
| Figure 17: cross section of a penetrometer for mercury intrusion where the bulk material penetrometer (A) has no additional features, and the powder penetrometer (B) has an extended neck to stop material entering the penetrometer stem. | 53 |

Figure 18 DSC melting curve where the melting point of mercury has been suppressed such that a separate peak exists (-45°C) before the bulk melting peak (-39°C) (edit Rigby, 2018). 54

Figure 19: fractal BET fit to the Marcellus shale in excel over the relative pressure range 0-0.995 pp_0 . The blue circles (●) are the experimental data and the orange line (---) is the modelled data. Modelling parameters used were V_m (9.4386), C (520.0574) and D (2.738713)..... 57

Figure 20: Langmuir fit to the Marcellus shale in excel of the relative pressure range 0-0.995 pp_0 . The blue circles (●) are the experimental data and the orange line (---) is the modelled data. Modelling parameters used were V_m (12.9055) and b (292.902) 57

Figure 21: 2 part fractal FHH fit to the Marcellus shale in excel of the relative pressure range 0-0.995 pp_0 . The blue circles (●) are the experimental data and the orange line (---) is the modelled data. Modelling parameters used were V_m (9.32866), D_1 (3) and D_2 (3). 58

Figure 22: finite multilater form of the BET fit to the Marcellus shale in excel of the relative pressure range 0-0.995 pp_0 . The blue circles (●) are the experimental data and the orange line (---) is the modelled data. Modelling parameters used were V_m (9.4386) and N (1). .. 58

Figure 23: fractal BET and kerogen fit to the Marcellus shale in excel of the relative pressure range 0-0.995 pp_0 . The blue circles (●) are the experimental data and the orange line (---) is the modelled data. Modelling parameters used were $k - value$ (0.049025), V_m (9.4386), C (235.4792) and D (3). 59

Figure 24: fractal FHH and kerogen fit to the Marcellus shale in excel of the relative pressure range 0-0.995 pp_0 . The blue circles (●) are the experimental data and the orange line (---) is the modelled data. Modelling parameters used were $k - value$ (0.067328), V_m (2.631502) and D (2.95445) 59

Figure 25: finite multilayer form of the BET and kerogen fit to the Marcellus shale in excel of the relative pressure range 0-0.995 pp_0 . The blue circles (●) are the experimental data and the orange line (---) is the modelled data. Modelling parameters used were $k - value$ (0.021917), V_m (9.4386) and N (1)..... 59

Figure 26: decreasing residuals for the Marcellus 7804'-7807' with the fractal BET (blue circles ●), FHH (grey circles ●) and n-BET (orange circles ●) in the homotattic patch using kerogen and illite isotherms against the number of model iterations with a trendline forecast to 1.6 million iterations. The same was done for all samples and it was determined that by 1 million iterations the relative further reduction against processing time was optimum. 64

Figure 27: N_2 gas adsorption results for the grain size study on the Marcellus 7795'-7798' where desorption is depicted by dashed lines, 106-150 μm by blue circles (●), 150-212 μm by orange circles (●), 212-425 μm by grey circles (●) and 425-600 μm by yellow circles (●). 66

Figure 28: CO_2 gas adsorption results for Marcellus 7795'-7798' for grain sizes 106-150 μm (blue circles ●), 150-212 μm (orange circles ●), 212-425 μm (grey circles ●) and 425-600 μm (yellow circles ●). 67

Figure 29: BJH cumulative pore volume pore size distribution for Marcellus 7795'-7798' for the grain sizes 106-150 μm (blue circles ●), 150-212 μm (orange circles ●), 212-425 μm (grey circles ●) and 425-600 μm (yellow circles ●)..... 67

Figure 30: BJH cumulative surface area pore size distribution for Marcellus 7795'-7798' for the grain sizes 106-150 μm (blue circles ●), 150-212 μm (orange circles ●), 212-425 μm (grey circles ●) and 425-600 μm (yellow circles ●)..... 68

| | |
|---|----|
| Figure 31: N ₂ gas adsorption isotherm for Marcellus 7804'-7807' (orange circles ●), 7834'-7837' (grey circles ●) and 7864'-7867' (yellow circles ●) for 106-150um. The desorption braches of the isotherms are represented with dashed lines. | 69 |
| Figure 32: CO ₂ gas adsorption isotherm for Marcellus 7804'-7807' (orange circles ●), 7834'-7837' (grey circles ●) and 7864'-7867' (yellow circles ●) for 106-150um. Isotherms were reversible and so desorption is not included..... | 70 |
| Figure 33: pore size distribution for the BJH cumulative pore volume for Marcellus 7804'-7807' (orange circles ●), 7834'-7837' (grey circles ●) and 7864'-7867' (yellow circles ●) for 106-150um..... | 70 |
| Figure 34: pore size distribution for the BJH cumulative surface area for Marcellus 7804'-7807' (orange circles ●), 7834'-7837' (grey circles ●) and 7864'-7867' (yellow circles ●) for 106-150um..... | 71 |
| Figure 35: normalised mercury intrusion porosimetry results for Marcellus 7804'-7807' (orange circles ●), 7834'-7837' (grey circles ●) and 7864'-7867' (yellow circles ●) for 106-150um identifying that Marcellus 7864'-7867' has the lowest intruded volume and Marcellus 7804'-7807' the greatest intruded volume. | 72 |
| Figure 36: showing a bar chart for the mineral % of chips of the Marcellus shale from SEM MLA. Bars are ordered by depth (left to right) with Marcellus 7795'-7798' represented by the diagonal empty bricks, 7804'-7807' the textured black, 7834'-7837' diagonal stripes and 7864'-7867' the textured grey..... | 74 |
| Figure 37: BSE image and corresponding mineral map for Marcellus 7795'-7798' highlighting an illite dominated matrix (orange), with fine grained quartz (blue) interspersed throughout the matrix and some coarse grains of limestone (turquoise) with a 5mm scale bar..... | 74 |
| Figure 38: BSE image and corresponding mineral map for Marcellus 7804'-7807' highlighting an illite dominated matrix (orange), with fine grained quartz (blue) interspersed throughout the matrix and a coarse grain of pyrite (mustard) with a 5mm scale bar. | 75 |
| Figure 39: BSE image and corresponding mineral map for Marcellus 7834'-7837' highlighting an illite dominated matrix (orange), with fine grained quartz (blue) interspersed throughout the matrix and some coarse grains of limestone (turquoise) with a 5mm scale bar..... | 75 |
| Figure 40: BSE image and corresponding mineral map for Marcellus 7864'-7867' where there seems to be an equal presence of both illite (orange) and quartz (blue); there are also some coarser limestone grains (turquoise with a 5mm scale bar). | 75 |
| Figure 41: SEM images of the Marcellus 7804'-7807' with a clay sized particle matrix dominated by illite. There are non-uniformly distributed coarse grains of quartz and limestone throughout the samples. The second SEM image shows that there are two separate inputs for quartz and limestone, where grains are within the clay dominated matrix they have been transported and deposited. Whereas contiguous grains of quartz and limestone are due to in-situ precipitation/dissolution. These textural and mineral properties are shared by the Marcellus samples 7795'-7798' and 7834'-7837'. | 76 |
| Figure 42: SEM images of the Marcellus 7864'-7867' showing the clay sized particle matrix dominated by illite, and containing slightly coarser quartz grains. In the second SEM image the nature of the limestone can be more clearly seen as a cement or precipitate between the illite-quartz matrix. In the third SEM image the contrast and brightness have been adjusted to highlight the smaller quartz grains within the clay sized particle matrix. | 77 |
| Figure 43: (A) BJH pore volume and the clay content, (B) BJH pore volume and the carbonate and silicate content. The BJH pore volume is shown with a yellow diamond (◆) in (A) and (B), the clay content with a cross (✕), the carbonates with a plus (+) and the silicates with an asterisk (*). | 78 |

Figure 44: (A) BJH pore volume and the total organic content (TOC%), (B) BJH pore surface area and the total organic content (TOC%), (C) BET surface area and the total organic content (TOC%). The BJH pore volume and surface area, and the BET monolayer quantity adsorbed and surface area are shown by a yellow diamond (◆) and the total organic carbon is shown by a cross (×)..... 79

Figure 45: FHH $D1$ (×) and $D2$ (*) for the four grain sizes analysed of Marcellus 7795'-7798' showing an increase in fractal dimension with increasing grain size for both $D1$ and $D2$. Parameters used are listed in Table 5..... 80

Figure 46: fBET (◆), fFHH (▲) and fFHH $D1$ (+) and $D2$ (×) compared with each other for the Marcellus shale samples. Parameters used are listed in Table 6..... 80

Figure 47: (A) the first fractal dimension, $D1$ (+), for the FHH correlated to the BET surface area (◆), (B) the second fractal dimension, $D2$ (+), correlated to the monolayer capacity V_m from the BET model (◆) and (C) the first fractal dimension, $D1$ (+) for the FHH correlated to the TOC% (◆). 81

Figure 48: k -value derived by each of the isotherm models BET (◆), FHH (■) and nBET (▲). Although the specific values vary they are distributed in the same way. Parameters used are listed in Table 7. 82

Figure 49: k -value from the BET model (◆) to the TOC% (+) from RockEval Pyrolysis where there is a correlation between the relative increase and decrease of values..... 83

Figure 50: (A) kerogen modelled data, k -value (■) with the BET model from the 3 part homotattic patch and the TOC% (▲) showing a correlation between Marcellus 7804'-7807', 7834'-7837' and 7864'-7867', however the model underestimates the kerogen for Marcellus 7795'-7798' and (B) the illite modelled data, i -value (■) with the BET model from the 3 part homotattic patch and the clay % (▲) where the same correlation is observed for Marcellus 7804'-7807', 7834'-7837' and 7864'-7867' and the model underestimates the clay for Marcellus 7795'-7798'. Parameters used are listed in Table 8. 83

Figure 51: ratio of TOC% to clay content (■) for experimental and homotattic patch values (◆), where there is a strong correlation between these values showing that the ratio of derived values is equivalent to the ratio of surface area contributions from experimental work..... 88

Figure 52: N_2 gas adsorption branch for all samples, desorption branches are omitted to make the data clearer. Samples are grouped by colour where there are multiple samples from a single 3 foot core. In the N_2 sorption experiments there is no correlation to depth, however samples over the depth range 6102'-6106' consistently have the lowest uptake. 90

Figure 53: CO_2 gas adsorption branch for all samples, desorption branches are omitted to make the data clearer. Samples are grouped by colour where there are multiple samples from a single 3 foot core. In the CO_2 gas sorption experiments there is some correlation to depth at the extreme ends, however the samples between are not as neatly correlated... 90

Figure 54: relationship of carbonates (empty ■), clays (empty ●), silicates (empty ▲) and TOC% (+) with depth. Where there are multiple samples per 3 feet of core the quantities have been averaged in order to show the overall trend as simply as possible. The smaller graph superimposed on the larger graph more clearly shows the trend over 5860'-5900' feet. 91

Figure 55: variation of mineral composition for the Utica shale samples U1 to U5. Carbonates (empty ■) and clays (empty ●) are inversely correlated to each other with increasing carbonate content and decreasing clay content with depth. Silicates (empty ▲)

show an overall decreasing correlation with depth, however there is a spike in U5 where the silicate content is almost twice at any other depth. TOC% (+) also shows an overall decreasing correlation with depth but has a spike at U3 where the TOC% is significantly greater than for any other sample..... 94

Figure 56: (A) the TOC% and BET surface area and (B) the clay content and the BET surface area..... 94

Figure 57: a typical electron micrograph of sample U1, with mud to silt-sized quartz (q) and bioclastic calcite (cc) grains in an illite matrix (d) with intra and inter granular calcite cement (cc). 94

Figure 58: U1 BSE and corresponding mineral map showing the clay sized particle matrix dominated by illite (orange) with interspersed grains of quartz (blue) and carbonate (turquoise), with 5mm scale bar. 95

Figure 59: An electron micrograph of a typical sample U2, with mud to silt-sized quartz (q) and authigenic calcite (cc) grains within an illite (d) matrix with some finer-grained silicate and carbonate material. Some inter-particle calcite cements (cc). 95

Figure 60: U2 BSE and corresponding mineral map demonstrating the same clay sized particle matrix dominated by illite (orange). Compared to U1 there are fewer carbonate (turquoise) grains, and they show no preferential alignment and/or distribution (with 5mm scale bar)..... 95

Figure 61: An electron micrograph of sample U3 with mud to silt-sized quartz (q), bioclastic and authigenic calcite (cc) grains within an illite (d) matrix with some finer-grained silicate and carbonate material. This sample is from close to the transition zone between the Utica shale and Point Pleasant Formation. There is evidence of intra-particle calcite cement (cc) within the bioclastic calcite grains. Within this there is some inter-particle calcite cements (cc). 96

Figure 62: U3 BSE and corresponding mineral map showing the presence of a clay sized grain matrix dominated by illite (orange) as well as grains of quartz (blue), however there is a significantly greater quantity of carbonates (turquoise) in comparison to U1 and U2. These carbonates are present as bands and also in biogenic forms (with 5mm scale bar).. 96

Figure 63: An electron micrograph of a typical sample of U4, being part of the Point Pleasant Formation with coarse silt-grained carbonate zoned minerals which are comprised of calcite (cc) and dolomite (dol) due to the dolomitisation of calcite to form dolomite. There are silt-grained quartz (q) and calcite (cc) grains surrounded by an illite (d) and finer-grained carbonate matrix. Observed post-sedimentation events are some inter-particle calcite cement (cc) and dolomitisation of the calcite. 97

Figure 64: U4 BSE and corresponding mineral map showing the presence, but reduction in the clay sized illite (orange) dominated matrix, within this matrix there are some quartz grains (blue) but far fewer than can be seen for samples U1, U2 and U3. There is a significant quantity of carbonates (turquoise) which take on a biogenic form likely as a result of bioturbation (with 5mm scale bar)..... 97

Figure 65: An electron micrograph of a typical sample of U5, which is part of the Point Pleasant Formation with typical calcite (cc) grains (5-10 μm), with some finer inter-granular illite (d). There are some darker coloured minerals which have been identified as dolomite, and the other grains some inter and intra particle cement. 98

Figure 66: U5 BSE and corresponding mineral map showing a carbonate grain (turquoise), with some fine grained quartz (blue) within it. There are also some areas of dolomite (green) where some mineral alteration has occurred (with 5mm scale bar)..... 98

Figure 67: mercury porosimetry intrusion and extrusion normalised to zero intrusion at 0.7MPa to remove the effect of mercury intruding and moving around the external spacing of the chips for samples U1 (◆), U2 (✕), U3 (✕), U4 (✕) and U5 (⊕) (colours and symbols consistent with Figure 52 and Figure 53 of the N₂ and CO₂ gas sorption isotherms). U2 and U1 have the greatest volume of intruded mercury and U4 and U5 the smallest volume of intruded mercury, however U3 has the greatest volume of trapped mercury. 99

Figure 68: (A) basic ink-bottle pore geometry of a pore which mercury could get trapped in, (B) a simplified example of the possible trapping of mercury in samples U1 and U2 where some mercury has been extruded but a large quantity is still trapped in the sample, (C) a simplified example of the possible trapping of mercury in sample U3 where very little mercury has been extruded and a significant quantity is trapped in the sample, (D) a simplified example of the possible trapping of mercury in samples U4 and U5 where most, if not all, of the intruded mercury has been extruded. Trapped mercury (■), the shale sample (■) and empty space (□). 99

Figure 69: cumulative intra-particle pore size distributions for Utica shale samples U1 (◆), U2 (✕), U3 (✕), U4 (✕) and U5 (⊕) (colours and symbols consistent with Figure 52 and Figure 53 of the N₂ and CO₂ gas sorption isotherms). Results for the pore size distributions are consistent with the intrusion – extrusion curves in Figure 67. 99

Figure 70: 2D reconstructed slice from CXT data-set for a chip of U1 shale following mercury porosimetry (left, scale bar at 1000µm), it is possible to see where mercury has intruded between micro-fractures and potentially between laminations of the shale and an example of 3D reconstruction (right) of CXT images of chip of U1 shale following mercury porosimetry. 101

Figure 71: 2D reconstructed slice from CXT data-set for a chip of U2 shale following mercury porosimetry (left, scale bar at 1000µm), it is possible to see where mercury has intruded between micro-fractures and potentially between laminations of the shale, and an example of 3D reconstruction (right) of CXT images of chip of U2 shale following mercury porosimetry. 101

Figure 72: 2D reconstructed slice of CXT data-set for a chip of U3 following mercury porosimetry (top, scale bar at 1000µm), it is possible to see where mercury has intruded around the edges in a more “cloud-like” way through more accessible pore as opposed to through fractures and laminations in the sample, and an example of a 3D reconstruction (bottom) of CXT images of chip of U3 shale following mercury porosimetry. 102

Figure 73: 2D reconstructed slice from CXT data-set for a chip of U4 shale following mercury porosimetry (left, scale bar at 1000µm), it is possible to see where mercury has intruded along the edges of the sample, and an example of a 3D reconstruction (right) of CXT images of chip of U4 shale following mercury porosimetry. 102

Figure 74: 2D reconstructed slice from CXT data-set for a chip of U5 shale following mercury porosimetry (left, scale bar at 1000µm), it is possible to see where mercury has intruded along the edges of the sample, and an example of 3D reconstruction (right) of CXT images of chip of U5 shale following mercury porosimetry. 103

Figure 75: Conventional nitrogen sorption isotherms (empty ●), overcondensation boundary desorption isotherms, a 0.5 pp0 scanning loop (✕), and a 0.8 pp0 scanning loop (✕) for chip samples of Utica shales (A) U1, (B) U2, (C) U3, (D) U4 and (E) U5. 106

Figure 76: Variation across the shale series U1-5 of the *k*-value (●) from the fits to the homotattic patch models with either fractal BET (◆) (eq.6) or finite multilayer BET (▲)

(eq.7). Also shown is the variation across the Utica shale series U1-5 of the total organic carbon (TOC%). Parameters used to calculate these values are shown in Table 10. 108

Figure 77: compares the conventional sorption isotherms (empty ▲) and overcondensation desorption isotherm (empty ■) for samples of shale U3 in chip (approximately mm particle size, represented by black symbols) and powder form (represented by blue symbols). It can be seen that the ultimate amount adsorbed increased for the powder sample in both conventional and overcondensation experiments. It is also noted that the sharpness of the higher knee in the overcondensation boundary desorption isotherm is slightly reduced for the powder sample. It can also be seen that neither of the conventional desorption isotherms for chip or powder samples have any sign of convexity. 109

Figure 78: schematic depictions of the model pore spatial arrangements probed by scanning loops in samples (a) U1, U2 and U5, and (B) U3 described in the main text. The model in part (A) is a “jam-jar” type arrangement with inter-connections, with the bottom very largest pore shielded by very narrow necks. The model in part (B) has a large macropore surrounded by a disordered “sea” of smaller pores. 110

Figure 79: Schematic diagram of the state of pore-filling with condensate (blue shading) of the model pore system shown in Figure 78A at various positions (indicated by red arrows) around the conventional and overcondensation isotherms of the form found in this work. Regions left white represent vapour-filled pores. It is noted that the multilayer film build-up is omitted for simplicity. 111

Figure 80: schematic diagram of the state of pore-filling with condensate at two positions along the overcondensation desorption isotherm for the pore structural model, given in Figure 78B, for shale sample U3. The blue shading represents pores filled with condensate, while white represent an empty pore. 112

Figure 81: schematic diagram of pore filling via a co-operative pore-pore mechanism, as described in main text. The blue shading indicates the presence of condensate and the arrow indicates the direction of the co-operative pore-filling process originating from the still-filled pore body. The diagram also shows the difference in pore-filling at the springing off point for SL1, compared with the boundary adsorption isotherm at the same pressure. 113

Figure 82: schematic diagram of the seeded percolation process. The blue shading represents the presence of liquid condensate, while regions left white represent vapour-filled pores. The arrow signifies the presence of a free meniscus from which desorption can occur in the direction shown. 114

Figure 83: (A) DSC for U1 where there is some depression of the bulk mercury peak skewing the symmetry of it, however the lack of separate peak means that the determining pore size distributions accurately from this data is not possible, (B) DSC for U2 where there is some depression of the bulk mercury peak skewing the symmetry similar to U1, (C) DSC for U3 where the bulk peak appears significantly more skewed than for U1 and U2, however no separate peak is formed making accurate determination of the pore size distribution not possible and (D) DSC for U5 where there is no skewed symmetry of the bulk peak in comparison to U1, U2 and U3. 116

Figure 84: mineral composition of the above marine band (grey textured), marine band (diagonal empty bricks) and below marine band (textured black) shale samples studied in this work. 121

Figure 85: BSE SEM image (top), and corresponding SE (bottom) SEM image, from the above marine band showing a clay sized particle matrix [denoted d] dominated by illite with courser quartz [denoted q] and carbonate [denoted cc] grains interspersed throughout.

These are aligned bottom left to top right across the image, and the total organic carbon [denoted a] is similarly aligned, the presence of pyrite [denoted py] is indicative of an anoxic environment. In the SE image (bottom) the organic carbon particles have been highlighted with a red border. In the second BSE SEM image (top right) the mineral and organic matter alignment can be seen more clearly. 122

Figure 86: BSE SEM image (top), and corresponding SE (bottom) SEM image, from the marine band showing a clay sized particle matrix [d] dominated by illite. There are coarser grains of carbonate [cc] and quartz [q] which are not preferentially aligned. In the SE image (bottom) the organic carbon particles have been highlighted with a red border. The second BSE SEM image (top right) samples a different field of view..... 123

Figure 87: BSE SEM image (top), and corresponding SE (bottom) SEM image, for the below marine band shale. The images show a clay sized particle matrix [d] dominated by illite, with coarser quartz [q] and carbonate [cc] grains interspersed and showing no preferential alignment. The decrease in total organic carbon [a] and pyrite [py], relative to Figure 85 and Figure 86, potentially indicates a less anoxic environment..... 124

Figure 88: nitrogen adsorption (solid symbols) and desorption (open symbols) isotherms for the marine band shale obtained under a variety of pre-treatment and experimental conditions, namely either no thermal pre-treatment (●) at all (just evacuation to vacuum) and equilibration time (ET) of 20 s, or degassed at 140°C for 3 hours and ET=20 s (●), or degassed at 140°C for 16 hours and ET=20 s (●). The sample was then degassed at 140°C for a further 3 hours after initial degassing and nitrogen sorption experiment before conducting a further nitrogen sorption experiment with ET=60 s (●) in the second figure. 125

Figure 89: conventional nitrogen (top) and carbon dioxide (bottom) adsorption (solid symbols) and desorption (open symbols) isotherms obtained for samples of the above marine band (●), marine band (●), and below marine band shales (●) with equilibration times of 30 s for the micro-pore region, and 20 s for the meso-pore and above region, following degassing at 110°C for 16 hours. 126

Figure 90: a comparison of the conventional isotherm (empty ●) with the overcondensation boundary desorption isotherm (empty ●) with scanning loops SL1 (0.5 pp0 scanning loop ✕) and SL2 (0.8 pp0 scanning loop ✕) for samples of the (A) above marine band, (B) marine band and (C) below marine band shales. The equilibration time for the isotherm points was 20 s. 128

Figure 91: carbon dioxide adsorption isotherms obtained at 273.16 K for the above marine band (●), marine band (⊕), and below marine band (✕) shale samples. Also shown (solid lines) are fits of the adsorption data to the Toth isotherm equation. The resultant fitted parameters are given in Table 14..... 129

Figure 92: mercury intrusion (solid symbols) and extrusion (open symbols) porosimetry data for the above marine band (▲), marine band (●), and below marine band (◆) shale samples..... 129

Figure 93: typical raw data-sets for the eighth adsorption point from an adsorption calorimetry experiment on a sample of above marine band shale, (A) showing heat-flow and (B) mass uptake. Also shown (solid orange lines) are fits of the experimental data to equations 6 (a) and 7 (b)..... 130

Figure 94: comparisons of the mass transfer parameters obtained from the adsorption calorimetry and adsorption-corrected mass uptake methods at different carbon dioxide saturations for adsorption isotherms on the above marine band (●), marine band (●) and

below marine band (●) shales. The dashed lines shown are fits of the data to straight line functions through the origin including data points from 0-730 mbar. Where the straight line fit has not been modelled is indicated with a ● 131

Figure 95: variation of mass transfer coefficient k with fractional carbon dioxide saturation for the above marine band (●), marine band (▲), and below marine band (■) shale samples..... 132

Figure 96: variation of surface fractal dimension $D1$ (◆) from a fit of the fractal FHH model to nitrogen adsorption isotherms over relative pressure ranges of 0.2-0.5 (left), and the clay content (*), for the three shale samples and comparison of the variation of $D2$ (◆), and the carbonate (X) and silicate (+) mineral composition (right), for the three shales. Parameters used are listed in Table 12. 133

Figure 97: BJH pore size distributions for the above marine band (●), marine band (●), and below marine band shales (●). 134

Figure 98: variation of homotattic patch fraction for kerogen (◆), standard BET surface area (X), BJH cumulative surface area (+) (left), and BJH cumulative pore volume between pore sizes of 320-0.7 nm (*) (right), for the three shale samples. Parameters used are listed in Table 13. 134

Figure 99: N₂ isotherm at 77K from Micromeritics 3Flex for the clay rich sample before (●) and after acid treatment (●)..... 139

Figure 100: CO₂ isotherm at 273.15K from Micromeritics 3Flex for the clay-rich sample before (●) and after acid treatment (●). 139

Figure 101: CO₂ isotherm at 283.15K from Autosorb iQ for the clay-rich sample showing before (●) and after (●) acid treatment. 140

Figure 102: CO₂ isotherm at 293.15K from XEMIS for the clay-rich sample showing before (●) and after (●) acid treatment. 140

Figure 103: mass transfer kinetics from Autosorb iQ showing the acid treated sample (●) to have an incredibly slow rate of mass transfer when compared to the untreated sample (●). 141

Figure 104: SEM MLA for the clay-rich samples showing the mineral quantities before (textured grey) and after acid (diagonal stripes) treatment. 141

Figure 105: BSE and mineral maps for the untreated Marcellus sample showing a fine grained illite (orange) matrix with some fine grained quartz (blue) and other material interspersed throughout (with a 0.5mm scale bar). 142

Figure 106: BSE and mineral maps for the acid treated Marcellus sample showing that there have been significant changes to the illite (orange) matrix (with a 0.5mm scale bar). 142

Figure 107: N₂ isotherm at 77K from Micromeritics 3Flex for the carbonate-rich sample, showing the before (●) and after (●) acid treated samples. 143

Figure 108: CO₂ isotherm at 273.15K from Micromeritics 3Flex for the carbonate-rich sample, showing the before (●) and after (●) acid treated samples. 143

Figure 109: CO₂ isotherm at 283.15K from Autosorb iQ for the carbonate-rich sample, showing the before (●) and after (●) acid treated samples. 144

Figure 110: CO₂ isotherm at 293.15K from XEMIS for the carbonate-rich showing the before (●) and after (●) acid treated samples. 144

Figure 111: mass transfer kinetics form Autosorb iQ before (●) and after (●) acid treatment..... 145

| | |
|--|-----|
| Figure 112: SEM MLA for the carbonate-rich samples showing that after acid treatment (textured grey) the relative quantity of carbonate is much lower than before acid treatment (diagonal stripes)..... | 145 |
| Figure 113: BSE and mineral map images for the untreated Utica sample showing predominantly carbonate (turquoise) grains, with some quartz (blue) grains and a dolomite (green) grain. There are some finer quartz (blue) grains within the carbonate (turquoise) grains, however overall the individual grains have a much simpler mineralogy than the corresponding Marcellus sample (with a 0.5mm scale bar)..... | 146 |
| Figure 114: BSE and mineral map for the acid treated Utica shale where there is a considerable increase in the number of quartz (blue) grains and a decrease in the number of carbonate (turquoise) grains in comparison to the untreated sample (with a 0.5mm scale bar). | 146 |
| Figure 115: N ₂ and CO ₂ sorption isotherms with two repetitions to show repeatability of the procedure. | 150 |
| Figure 116: three Marcellus 7864'-7867' N ₂ sorption analysis from different sub-sections. | 150 |
| Figure 117: using the Gurvitsch volume against grain size and using trend line forecasting to predict what the maximum quantity adsorbed may be for larger samples..... | 159 |
| Figure A4. 1: diffractogram for Marcellus 7795'-7798' showing the dominant quartz peak at 27° which causes all other signals to be part of the noise. | 184 |
| Figure A4. 2: diffractogram for Marcellus 7804'-7807' showing the dominant quartz peak at 27° which causes all other signals to be part of the noise. | 184 |
| Figure A4. 3: diffractogram for Marcellus 7834'-7837' showing the dominant quartz peak at 27° which causes all other signals to be part of the noise. | 184 |
| Figure A4. 4: diffractogram for Marcellus 7864'-7867' showing the dominant quartz peak at 27°, there is also a clear carbonate based peak at 29°. Both these dominant signals cause all other signals to be part of the noise. | 185 |
| Figure A6.1. 1: U1 core sample of clay sized grain shale with planar lamination and no evidence of bioturbation at core scale. Cracks in the core are presumed to be as a result of drilling from depth, and transportation from the United States. | 189 |
| Figure A6.1. 2: U2 core sample of clay sized grain shale with predominantly planar lamination, there is some potential evidence of additional mineralogical input between laminations although cannot be confident that this has not been imbibed during the drilling process..... | 189 |
| Figure A6.1. 3: U3 core sample of clay sized grain shale with a mix of planar and wavy laminations. There are visible pore network openings on the surface of the core and a mineralogical transition at 5.5 cm (on the ruler) from a darker to lighter mineral phase. Cracks in the core are presumed to be as a result of drilling from depth, and transportation from the United States. | 189 |
| Figure A6.1. 4: U4 core sample of clay sized grains which are in three phases from 2-3cm, 5-6cm and 10-11cm. These sections have wavy laminations and there is some additional mineral input in 5-6cm and 10-11cm from the underlying parts. From 3-5cm and 6-10cm there is a coarser grained section with some pore openings to the core surface, as well as some vein like mineral phases in wavy laminated layers. | 190 |
| Figure A6.1. 5: U5 core sample of very fine grained sample with no visible laminations, there's some isolated areas of darker sediment, juxtaposed by some more vein like mineral phase. From 3-6cm vertically, half-way across horizontally there is a separation in the lighter grey sediment with a column of darker sediment due to a mud injectite where it's been overpresured and flamed through the overlying section. The areas of lighter colour | |

which are more round in nature are only on the surface and believed to be an artefact of the drilling process. 190

Figure A6.2. 1: examples of reconstructed 2D slice CVT images of fresh samples of (a) U1 and (b) U3, with a 1000 μm scale bar..... 190

List of Tables

| | |
|---|-----|
| Table 1: lists the grain sizes that samples were sieved to in the sample preparation procedure, and the average grain size for used for each grain size in some of the experimental analysis..... | 46 |
| Table 2: the grain sizes used for the grain size study on the Marcellus 7795'-7798'. | 66 |
| Table 3: shows the percentage contribution to the sample mass from moisture, volatiles, ash and fixed carbon calculated using the equation in Appendix 2..... | 73 |
| Table 4: TOC% for the Marcellus shale samples acquired through RockEval Pyrolysis. | 78 |
| Table 5: parameters used to model the values presented in Figure 45..... | 80 |
| Table 6: parameters used to model the values presented in Figure 46..... | 81 |
| Table 7: parameters used to model the values presented in Figure 48..... | 82 |
| Table 8: parameters used to model the values presented in Figure 50..... | 84 |
| Table 9: sample depths, mineral content, TOC% and Ro% the thermal maturity given by (14. 1) (Jarvie et al., 2005) for all Utica samples. Carbonates are comprised of limestone and dolomite; clays are comprised of illite, kaolinite and goethite; silicates are comprised of quartz, muscovite and albite. | 89 |
| Table 10: parameters used to model the values in Figure 76. | 108 |
| Table 11: details of shale samples studied in this work. | 117 |
| Table 12: parameters used for the modelled values presented in Figure 96..... | 133 |
| Table 13: parameters used for modelled values presented in Figure 98..... | 134 |
| Table 14: parameters from fits of Toth isotherm (15. 3) to carbon dioxide adsorption isotherms for shale samples. | 135 |
| Table 15: fractal dimensions for the acid and none acid treated samples using a two part FHH model to derive a fractal dimension for the surface roughness and network complexity. | 147 |
| | |
| Table A1. 1: Composition, surface areas, thermal maturity and sorption capacities of Devonian – Mississippian shales..... | 161 |
| Table A1. 2: Composition, surface areas, thermal maturity and sorption capacities of Jurassic shales. | 161 |
| Table A1. 3: total porosity (vol.%) and mineralogical compositions (wt.%) of shale samples. | 162 |
| | |
| Table A5.1. 1: all SEM MLA data for the samples analysed in this thesis..... | 187 |
| | |
| Table A5.2. 1: BET surface area of various minerals which make up the majority of shales. | 188 |

The Thesis Structure

This thesis is divided into 10 chapters with chapters 1, 2 and 3 providing the rationale and a thorough description of the existing work and methodologies used in the area of shale pore characterisation. The thesis will then move on to outline the methodology used in this study, and how the novel characterisation techniques were introduced and in some cases further developed. The following four chapters (chapters 5, 6, 7 and 8) will show how the methodologies were used with three sets of shale samples and shale samples following acid treatment. There is also an evolution in methodology used as the shale samples were introduced to the sample chronologically, i.e. the Marcellus was sampled first and was used to test methods, while the Bowland was the last sampled and a more refined use of methodologies were used. Finally the thesis is concluded with a detailed evaluation of the methodologies use and proposals for future work in this area.

Chapter 1. Introduction

Chapter 2. The reader is introduced to the need for this work and the importance of shale pore characterisation in the oil and gas industry, as well as the wider environmental implications associated with this. The chapter then moves onto discuss the formation and properties of shales which lead them to be highly complex, and the work carried out by others previously to characterise them.

Chapter 3. Aims and Objectives

Chapter 4. This chapter expands on chapter 2 by unpacking the specific uses of each experimental technique both in theory and in practice. As well as the downfalls and benefits of each experimental technique. Additionally the drawbacks of conventional experimental methods are described alongside the steps taken to overcome these with novel developments. To conclude the chapter the numerical models used are explained in detail with evidence to support the use of certain models and combinations of models over others.

Chapter 5. The Marcellus shale is analysed using gas sorption work, mineralogy, TOC% and numerical modelling (fractal dimensions and the homotattic patch) to understand the pore system of the sample. As the first sample used in this study, the primary workflow used was standard techniques to fully understand the drawbacks of each technique and the complexities involved in fully characterisation the pore systems of shales.

Chapter 6. Work on the Utica shale builds on these findings and starts to introduce novel experimental techniques such as gas overcondensation, post mercury porosimetry computed x-ray tomography and thermoporometry. This chapter also looks into the specific correlations between mineralogy, TOC% and the pore surface area and pore volume. As well as this it investigates the

changeover in mineral regime and how this affects the shale properties.

- Chapter 7. Lastly the Bowland shale uses the most effective methods from chapter 5 and chapter 6 to characterisation the pore systems and mass transport throughout the samples. This chapter specifically looks at samples before, at and after a marine band. Consequently a high degree of variation between samples is expected similar to U3 and U4 in chapter 6.
- Chapter 8. In this final chapter a clay-rich and carbonate-rich shale sample are treated with weak acid in-line with that used in hydraulic fracturing, and by others in literature. Following this treatment the mineralogy and mass transport properties of the samples are assessed to understand how these are affected.
- Chapter 9. All methods used, experimental and numerical, are discussed in detail with the drawbacks and work down to overcome these highlighted to demonstrate the effectiveness of novel characterisation methods development during the thesis.
- Chapter 10. Final conclusions are made on the work in chapters 5, 6, 7 and 8 as well as recommendations for future work to expand on the work presented in the thesis.

1. Introduction

1.2. *The Growing Importance of Shales*

Improved knowledge concerning shale rocks is important because of their involvement in oil and gas production, gas storage, carbon dioxide sequestration, radioactive waste repositories, and civil engineering (Kim *et al.*, 2017; Liu *et al.*, 2019; Liu *et al.*, 2019). Since the industrial revolution (18th and 19th century), the demand for oil and gas has continued to increase and there is now a global dependency. Conventional natural oil and gas reserves are depleted, and renewable energy storage is still in its formative years so cannot be considered as a reliable source. During this transitional stage in global energy unconventional natural oil and gas have become an invaluable resource. In the past 10 years, there has been a boom in shale gas production in the United States (Wang *et al.*, 2015; Barsotti *et al.*, 2016; Li *et al.*, 2016; Yu *et al.*, 2016) due to advancements in technology enabling the development and commercial deployment of hydraulic fracturing. The energy market is moving into a unique period where there is an increase in demand and an increasingly conscientious consumer. In order to meet the increased energy demand, and satisfy the conscientious consumer energy needs to be reliably produced (natural oil and gas) and remediative action performed to limit the environmental impact.

1.3. *Global Agreements and Future Targets*

The Intergovernmental Panel on Climate Change (IPCC) have recommended that global temperatures should not increase more than 2°C from pre-industrial temperatures. Further efforts and recommendations have been made to further reduce this to 1.5°C as laid out by the Paris Agreement. These environmental targets and recommendations need to be met globally and locally by each country, while simultaneously supporting the energy consumption needed for continual economic growth, development and technological innovation. The environmental aspect could partly be dealt with by the deployment of large-scale carbon capture and storage (CCS) projects (Busch *et al.*, 2008; Kang *et al.*, 2011). As well as this additions to CCS technology can be made which could be used to produce more gas, and simultaneously remove CO₂ from the environment. Enhanced recovery using CO₂ is designed as a tertiary production method for increased gas recovery – while also removing CO₂ from the atmosphere by underground storage (White *et al.*, 2005). For the UK to fulfil the recommendations of the IPCC and to meet the domestic carbon targets, it is estimated that almost complete decarbonisation needs to occur by 2050. This has been laid out in the Climate Change Act 2019, although many combined authorities have committed to reach net zero carbon before 2050. To achieve this there is additional pressure for the UK to move away from being a NET energy importer and utilise its own energy resources, to achieve energy independence and stability. Despite this it is likely that 70% of the UK demand will still need to be met by oil and gas imports (HM Government, 2013).

Shales are an important part in this energy transition and development as they have been identified as reservoirs (formations containing organic matter) for unconventional natural gas and oil. They are already fast becoming a major component of natural gas production in the United States (Montgomery *et al.*, 2005; King, 2010; Kuuskraa *et al.*, 2013; Wang *et al.*, 2014) who have been making large shale gas exports. When organic material is buried over a long period of time thermal degradation occurs transforming it into kerogen, oil, and natural gas if high temperatures and pressures are reached and sustained over a substantial period of time (Zhang *et al.*, 2012; Chen *et al.*, 2014). The thermal maturity of the organic

carbon reflects the degree of transformation (thermal degradation) that it has undergone. There are four stages which result in pore changes (Y. Chen *et al.*, 2015) the first is a reduction in meso-pore volume due to the physical compaction of the sample, there is then an increase in the meso-pore volume when kerogen in the sample is thermally degraded, the next step in thermal degradation causes a reduction in meso-pore volume as a consequence of bitumen blocking pore bodies and throats finally when the bitumen is further degraded meso-pore volume increases again. Shales have classically been considered cap rocks in conventional reservoirs due to their tight pore structures retarding the upwards migration of mobile organic matter (oil and gas).

As a result, characterising shales (Ross and Marc Bustin, 2009; Wang *et al.*, 2015; Li *et al.*, 2016; Nia *et al.*, 2016; Kenomore *et al.*, 2017; Kenomore, 2020; Spanakos and Rigby, 2020) is essential for the understanding and estimation of gas-in-place (GIP), storage capacity and cap rock integrity. Shale pores are in the nanometer range and classified as micro-, meso- and macro-pores defined by the ranges <2nm, 2-50nm and >50nm respectively (Li *et al.*, 2016). The proper classification of pore size is essential to understanding the properties of a material and achieving accurate characterisation of it. Some material may have the same apparent porosity, however there could be significant variation in the size and geometry of these pores. Resultantly the materials will react very differently under the same experimental conditions (Zdravkov *et al.*, 2007). Pore width classes correspond to the application of the capillary condensation theory at different relative pressures. Pore widths of 50nm (macro-pores) is related to a relative pressure of 0.96. At relative pressures below 0.39 the N₂ layer is unstable as a result of the tensile strength effect; this relates to pores 2nm in size and the Kelvin equation cannot be applied (Rouquerol *et al.*, 1994). Micro-pores mean that the width between pore walls is such that the adsorbate can interact with both pore walls at the same time and pore filling occurs in a continuous way (Rouquerol *et al.*, 1994). For meso-pores capillary condensation takes place between 0.39-0.96 P/Po. Pores greater than 50nm in size (macro-pores) do not achieve adsorbate condensation through the relative pressure 0-0.995 P/Po and so are characteristic of multilayer adsorption (Zdravkov *et al.*, 2007).

Shales also contain complex fracture structures which are in the micro-meter range. Pores can be further characterised as inter- or intra-particle pores within a matrix or organic and inorganic particles (Li *et al.*, 2016). The properties of shales (pore size, shape, connectivity, pore wall roughness, mineralogical composition) and the adsorbate (wettability, molecular size and polarity) influence the gas adsorption isotherm yet a quantitative understanding has not been fully established (Barsotti *et al.*, 2016). The pore structure of shales is also complex and multi-scale, with pores ranging in size from macroscopic faults and fractures down to atomic-scale gaps between clay layers. Further, the composition and surface chemistry of shales is also similarly complex.

1.4. Multi-Scale Complexity of Shales

This multi-scale complexity presents a challenge to pore structure characterisation which necessitates the development of new methodologies and/or techniques. In particular, it is necessary to know how structures on different scales relate to each other. It is essential to focus on the surface area as this is where the majority of natural gas is stored, 20-85% is adsorbed (on the pore surface) and the rest is stored in the bulk pore volume (Ji *et al.*, 2012). Important minerals to understand for specific surface area characterisation are the organic matter and clay minerals which form the major adsorption components. For organic

matter; quantity, type, maturity, vitrinite reflectance are the key qualities, and in clay; micro-pore structures and mineral composition (Ji *et al.*, 2012).

1.5. Current Experimental Techniques

These properties can be directly measured by fluid intrusion techniques such as nitrogen (N₂), carbon dioxide (CO₂) gas adsorption and mercury (Hg) intrusion porosimetry. Using small-angle x-ray scattering distributions these can be compared with intrusion techniques to assess the differences in open and closed pore space. Mineralogy plays a vital role on the overall characterisation of shales since different minerals have different properties and their quantities within the shale will determine surface area, volume and network. As a result of this integral control it is essential to fully characterise mineral contents and this can be determined with x-ray diffraction (XRD) and scanning electron microscopy mineral liberation analysis (SEM-MLA). SEM-MLA produces a mineral map so it is possible to see how minerals are distributed throughout the sample. Imaging methods, such as computerised x-ray tomography (CXT), focussed ion beam scanning electron microscopy (FIB-SEM), and electron tomography (3D transmission electron microscopy) can be further utilised to visualise pore spaces more directly in three dimensions (Rigby, 2020). These methodologies, strictly, use computer reconstructions that can be subject to artefacts - imaging datasets also require filtering to remove 'noise' and make void-solid interfaces more visible. Additional processing is required to segment void, solid and mineral phases which involve subjective analysis of the individual elements. In addition, the combinations of fields of view and resolutions currently feasible mean that one imaging method alone cannot survey the whole range of length-scales of pores present in shales. For example, Keller *et al.*, (2013) performed representative volume calculations that showed FIB-SEM sample volumes of a maximum of several hundred microns cubed were smaller than the representative length-scale cut-off and many of the structural heterogeneities present in the sample studied. It is simply not possible to use imaging modalities with the finest resolution to study statistically meaningful volumes of a sample with multi-scale heterogeneity and pores.

Hence, multi-scale methodologies, utilising two or more imaging modalities, that can bridge most of the requisite length-scale range have been proposed by workers such as Keller *et al.*, (2013), Ma *et al.*, (2017), Ma *et al.*, (2017), Saif *et al.*, (2017) and Ma *et al.*, (2019). However, given the sample volume limitations at the highest resolution, some sort of scale-up method is required. This often means identifying and classifying a small number (1-10) of characteristic phases (for example organic material or quartz minerals) that are assumed to scale homogeneously across all length-scales. There are a number of issues with this approach since it requires subjective identifications of regions belonging to a particular phase. There are also complications when individual grains making up a larger composite are smaller than the correlation length for the materials from which they are made (Nepryahin *et al.*, 2016).

Alternatively, indirect methods, such as mercury porosimetry, have been used to establish the relative disposition of void-space features seen in images obtained at different length-scales (Hemes *et al.*, 2015). Such a different approach to multi-scale imaging and upscaling for studying structure-transport relationships in multi-scale porosity is to use a 'filtering', or 'sifting', -type approach (Rigby, 2020). In the filtering approach a particular sub-set of a much more complex overall network is isolated or 'knocked-out', and the impact of this on

the process of interest, such as mass transport, is examined. For example, using mercury porosimetry scanning curves, pores of progressively smaller size can be removed by mercury entrapment, and the impact of doing so on mass transport assessed via the rate of adsorption of gas before and afterwards (Nepryahin, *et al.*, 2016; Nepryahin, *et al.*, 2016). Alternatively, nuclear magnetic resonance (NMR) cryodiffusometry can be used to isolate the behaviour of a particular sub-set of pores within a much larger network. However, there are lower limits on the pore sizes that can be probed by mercury porosimetry and cryoporometry.

Conventional gas sorption experiments are one of the very few techniques that can be used to study the pore structure of shales, down to the very smallest nanometre-scale (<2nm) porosity below the resolution limit of many imaging techniques (Rigby, 2020). However, in previous work in the literature, the type of gas sorption experiment conducted, and data thereby obtained, typically consisted just of a boundary adsorption isotherm up to a limited ultimate pressure ($1 \frac{p}{p_0}$), followed by a pseudo-boundary desorption isotherm, that is often really just an unrecognised descending scanning curve because complete pore-filling with condensate was not achieved at the top (high-pressure end) of the adsorption isotherm. Hence, conventional gas sorption alone cannot cover the complete pore size range including macro-pores. Therefore, it cannot deliver information on the inter-relationship between pores over a wide length-scale range. There are adaptations that can be made to conventional gas adsorption analyses which delivers more comprehensive and richer data-sets for shales using overcondensation and sorption hysteresis scanning curves. The upper cut-off in pore size that can be studied with gas sorption is limited by the highest ultimate pressure obtained in the experiment, this ultimate pressure is additionally controlled by the experimental temperature and type of adsorbate used. This is often truncated well before saturation to avoid flooding the apparatus with bulk condensate. However, overcondensation allows the full boundary desorption isotherm to be obtained even for samples where complete pore-filling is not achieved at the top of the adsorption isotherm during conventional gas sorption experiments (Aukett and Jessop, 1996; Murray *et al.*, 1999). In the overcondensation experiments a separate, both high and wide, hysteresis loop was obtained above and beyond that seen in conventional experiments.

1.6. Early Stage Novel Characterisation

Gas sorption scanning experiments enable the spatial inter-relationship between different pore sizes to be determined (Esparza *et al.*, 2004). Sorption hysteresis scanning involves construction of isotherm curves or loops by truncating a series of pressure increments or decrements before they reach the upper or lower hysteresis closure points (Tompsett *et al.*, 2005). As implicitly mentioned above, the simplest type of scanning experiment is a descending scanning curve originating from the boundary adsorption curve created by reversing the direction of pressure step changes before achieving complete pore-filling with condensate (at the Gurvitsch volume). The descending scanning curve can be converted into a scanning loop by once more changing the direction of the pressure step changes, before the descending scanning curve reaches the lower hysteresis closure point, thereby giving rise to an ascending branch in addition to the descending branch. The ascending branch of the loop will then re-join the boundary adsorption isotherm. An ascending scanning curve can also be created springing from the boundary desorption isotherm by changing from pressure decrements to increments part way down the boundary desorption isotherm. This

ascending scanning curve can be converted into a scanning loop by again changing the direction of pressure changes, but from increases to decreases, before the ascending curve reaches the boundary adsorption isotherm. Scanning curves and loops can take a variety of forms and shapes which contain information on the nature of the phase transitions of the adsorbate and pore structure of the adsorbent, as will be described below.

In the past, only very limited use has been made of gas sorption scanning curves and loops to study shales. Seemann *et al.*, (2017) measured a small series of descending water sorption scanning curves for Sichuan 211 shale rock. These curves all converged on the lower hysteresis closure point (or thereabouts, as there was some slight low-pressure hysteresis). Very limited analysis was conducted of these curves. Barsotti *et al.*, (2020) measured scanning curves for n-butane and n-pentane for Middle Eastern gas shales. In both cases, crossing scanning curves were obtained. The interpretation of these data was limited to noting that crossing scanning curves are most often associated with more ordered, templated silica materials, and suggesting that the form of the adsorption isotherm was controlled by pore morphology, and that of the desorption by cavitation. Rigby *et al.*, (2020) also observed crossing behaviour in ascending scanning curves springing from the boundary desorption isotherm obtained for a thermochemically treated shale sample using the aforementioned overcondensation method. This form of the scanning curve, together with the aforementioned wide hysteresis of the overcondensation desorption, was consistent with a void space consisting of large pore bodies shielded by narrow pore windows. From SEM studies, it was observed that the thermochemical treatment of the shale had created ovoid, 'bubble-like' pore bodies, that intersected at circular windows, within the organic/carbon component of the shale that would give rise to the type of scanning curve behaviour described by Rigby *et al.*, (2020). This type of intersecting ovoid pore has also been observed within organic material for a variety of natural shale samples, including marine Longmaxi shales (Chen *et al.*, 2019; Ji *et al.*, 2019), Upper Permian marine-terrestrial transition Longtan Formation shales, and Horn River shale (Curtis *et al.*, 2012).

Gas sorption scanning experiments can be used to upscale nanometre-scale characterisations of complex multiscale porous media. This is because, while the particular pressure at which basic physical processes, such as capillary condensation, arises is controlled by nano-scale characteristics, such as pore size, the pore-pore co-operative effects, such as advanced condensation/adsorption (also known as the 'cascade effect'), network delayed condensation, and pore-blocking, present for complex pore networks operate over length-scales from the neighbouring pore up the size of the sample particle itself (Rigby, 2018, 2020). These pore-pore co-operative effects control the overall shape of the gas sorption scanning curves through their dependencies on the spatial disposition of the pore size distribution and network connectivity. The overall size of the scanning curve or loop is very often related to the volume of sample that the underlying physical processes are affecting. For example, the shape of the boundary desorption isotherm around the percolation knee generally relates to the formation of sample-spanning clusters of emptied pores (Seaton, 1991). The critical pore size controlling desorption for a given set of pores may be a macroscopic (>10 microns) distance away. The pore-pore co-operative process of percolation during gas desorption 'sifts' out the particular pore size at the knee, and, thereby, identifies the rate-limiting pore size, according to critical path analysis theory

(Ambegaokar *et al.*, 1971; Thompson *et al.*, 1987; Seaton *et al.*, 1997), for Knudsen diffusion or permeation of gas moving from the given pores to the exterior (or vice-versa).

2. Review of Literature

2.1. The Formation of Shales

2.1.1. Definition

For the past twenty-five years a key focus of scientific interest has been shales (particularly black shales) as they often contain significant quantities of organic carbon. This makes them potential hydrocarbon source and reservoir rocks. Additionally, they are prevalent throughout geological history and make up around two-thirds of all sedimentary rocks (Arthur, 1994; Dusseault, 2004).

The original definition, by Pettijohn (1957), defined black shales as:

“facies most commonly just black shale. Such shale is thinly laminated, papery and black. Has an abnormally high content of carbon (>5%), rich in pyrite and noted for concentration of rare elements (V, U, Cu). Carbonates are rare except as cone-in-cone layers or as septarian nodules”

By 1980 this definition had been narrowed down to some essential criteria (Curtis, 1980);

“a. high organic carbon content, b. low carbonate content, c. high pyrite content, d. fissility from lamination”

Despite this, the term shale was still poorly constrained and not precisely defined. Within the petroleum industry (Horsrud *et al.*, 1998) shales are understood as sediments, and sedimentary rocks ranging from a weak clay rich “soup” through to a strongly cemented shaly siltstone. More recently (Schön, 2015) this definition has been refined to describe shales as sedimentary rock which contains a mixture of clay-size, silt-size and some sand-size particles. Shales are clastic sedimentary rocks which are not compositionally defined like a carbonate or igneous rock. This results in shales presenting in a range of colours, although they are typically grey. Colours vary from the classically regarded black shales which usually results from a high percentage of carbonaceous material (Arthur, 1994), red due to hematite (iron oxide), brown from the presence of goethite, yellow from the presence of limonite (iron hydroxide), and green from having a dominant micaceous clay content (chlorite, biotite and illite) (Grim, 1951). They are commonly made up of 59% clay minerals (<0.002 mm), 20% quartz, 7% carbonates, 3% iron oxides, 2% other minerals and 1% organic material (Schön, 2015). Since the dominant particle size is <0.002mm it results in a very tight pore structure giving shales very low porosities (<5%) and permeabilities (0.001mD) which can be compared to an unfractured metamorphic or igneous rock (Schön, 2015).

2.1.2. Composition

Shales are abundant in the sedimentary sequence (Lynch, 1997) making up about two-thirds (Arthur, 1994; Dusseault, 2004) of all sedimentary rocks, extending throughout geological time. They are significant to the petroleum industry as their low porosity and permeability have historically seen them used for their sealing properties when overlying conventional reservoirs. Unlike an evaporite seal, however, they have more recently been considered as a source and reservoir themselves as a result of their high organic carbon content. The organic carbon content of the shales is most often due to kerogens which have been thermally degraded into oil and gas; though some may be as a result of upwards migration from the conventional reservoir below.

As a result of their complexity the pore size distributions, pore networks and mass transfer kinetics of shales are poorly understood and are not well measured with any one technique. Due to the disconnectedness of pores, shales cannot be conventionally produced by depletion, the primary production technique in conventional reservoirs, and often require mechanical processes which aim to improve the network connectivity.

2.1.3. Depositional Environments

In the same way that shales are not well defined compositionally, they are also not well defined by a formation process which can account for the structural heterogeneities and complexities across different shales globally. Despite this, past research was focused on trying to apply uniformitarian principles to depositional models of shales (Arthur, 1994). However, we will see throughout literature and in this thesis that these uniformitarian principles are not easily applied.

The “Deep Sea Drilling Project” (Arthur, 1994) produced a wealth of data which made it evident how widespread black shale sequences were spatially and across geological time. Early hypotheses up to this point thought shales were formed in restricted and/or isolated basins, but the discovery that some of these shales were deposited both globally and synchronously meant that these hypotheses needed to be re-evaluated. The primary consequence of this is that local bathymetry can no longer provide the main explanation for black shale formation (Arthur, 1994).

It is widely accepted that black shales are black because of the increased content of carbonaceous material. The preservation of this material is associated to anoxic conditions preventing oxidation and consequent carbonate production. Due to this accepted understanding it allowed the focus of the debate to move onto the shallow- versus deep-water argument for shale deposition (Arthur, 1994). Research aims from this point have moved on to focus on which environments are the most conducive to organic matter preservation, and the different factors which may inhibit or support organic matter preservation (Figure 1).

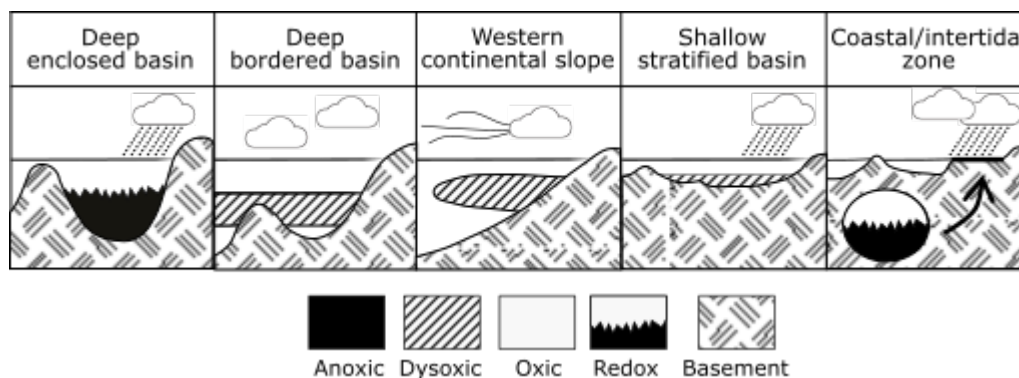


Figure 1: different marine environments and the anoxic, dysoxic or oxic conditions which lead to the preservation or destruction of organic matter respectively (edited from Arthur (1994)).

Four key depositional processes have been outlined (Stow *et al.*, 2001) to describe shale formation. These processes can occur singularly or together - when they occur together this can happen sequentially or simultaneously. Also outlined are the main factors allowing preservation of organic matter during and after these processes.

The first depositional process is *pelagic settling* which is the vertical settling of grains (usually biogenic or fine-grained terrigenous material) under the influence of gravity, from surface waters through the water column. In the open ocean this is a continuous process and results in a slow accumulation of sediment. In the ocean margins however, the process is more cyclical where sediment is often deposited during the onset of eutrophic periods.

The next process is *hemipelagic deposition* which combines both vertical and lateral settling of sediment due to gravity and an additional horizontal inertia. Examples of environments with horizontal inertia are rivers, plumes, glacial melt water diffusion, turbidity layer plumes and internal tides and waves. This depositional environment, like *pelagic settling*, is continuous but sedimentation rates vary with the volume of sediment input.

These first two depositional processes are more closely related to specific sedimentary environments, whereas the following examples characterise the processes by which these fine-grained sediments are transported.

Turbidity currents are one of the main ways fine-grained material is transported from shallow to deep water. These fine-grained materials are carried in a dilute turbulent suspension, propelled by the downslope component of gravity leading to *hemiturbiditic sedimentation*. This fine-grained material is often carried beyond the final turbidity current as a consequence of negative buoyancy and upward dispersion from the dilute suspension. This fine-grained material is then deposited as part of the background pelagic and/or hemipelagic material. *Debris flows (slides and slumps)*, are high-concentration mixes of sediment and water which are able to move large volumes of material downslope in single large events. Plastic flow is associated with these events where fine-grained materials form a thick slurry which acts like a cohesive material able to support larger clasts. The fine-grained material from these events will then be deposited by *pelagic settling* and/or *hemipelagic deposition*.

These processes result in heterogeneities throughout a sedimentary section as a result of the very fine-grained sediment in pelagic and hemipelagic flows, when grain sizes are small the resultant permeability of the sediment is very low. Additionally the slow settling through the water column allows for a greater sedimentary mix, and for sediment grains to undergo any chemical or microbial interactions before deposition. The resultant fine-grained and chemically altered sediment results in a very heterogeneous rock in the future. For the turbidity currents the high energy flow in the early stage of transport can lead to a wide variety of materials to be included in the flow, the fine-grained material is often carried beyond the final turbidity current and forming a part of the water column where it settles similarly to pelagic and hemipelagic flows.

2.1.4. Organic Matter Supply and Preservation

The main debate now surrounds primal productivity versus preservation mechanisms, i.e. the organic matter supply and the mechanisms by which this is preserved before oxidation occurs. The preservation process of organic matter has several requirements (environmental and mechanical) needed to minimise the oxidation process i.e. water column anoxia and high sedimentation rates.

Before preservation mechanisms can be considered a sufficient supply of organic matter must be secured. A sufficient supply is not a fixed number that must be reached; but a rate where supply is greater than the rate of degradation (Arthur, 1994; Stow *et al.*, 2001). Degradation processes are most often oxidation (Arthur, 1994; Stow *et al.*, 2001) into carbonates, but also acidification from the microbial content within the water column (Stow *et al.*, 2001).

Organic matter is primarily supplied by terrestrial transportation (Arthur, 1994) of seaward moving rivers carrying large volumes of organic detritus and/or nutrients (Stow *et al.*, 2001). Additionally, organic matter can be input into marine sediments by photosynthetic production of marine phytoplankton undertaking a full respiratory process (Arthur, 1994).

Once a sufficient supply has been secured preservation mechanisms must be in place in order for organic matter to be preserved within the sedimentary record. The main environmental requirement is anoxia – which will minimise the volume of organic matter degraded by conversion into carbonate material (Stow *et al.*, 2001). Additionally, this anoxia must extend from surface waters, through the water column to bottom-waters (Stow *et al.*, 2001).

The main mechanical process needed for preservation is rapid burial (usually) due to a high sedimentation rate (Arthur, 1994; Stow *et al.*, 2001). This burial rate similarly to organic matter

supply is not a fixed threshold number but is determined by occurring faster than the rate of degradation. Betts and Holland, (1991) more specifically determined sedimentation rates of less than 60cm/ky required an increased burial rate to preserve organic matter, i.e. if burial for these sediments was not rapid the organic matter would be degraded before it could be preserved – the upper oxic part of the sediment column is especially aggressive in the rate of degradation so organic matter needs to be quickly removed (Stow *et al.*, 2001). For sedimentation rates greater than 60cm/ky the rate is high enough such that the length of time spent in the oxic zone is reduced (due to gravity driven settling) promoting a greater amount of preservation. A greater supply of sediment will likely contain a greater amount of organic matter which will, overall, lead to a larger volume being preserved despite some degradation in this oxic zone.

A second key mechanical element that needs to be considered is the grain size of the sediment. A fine-grained sediment will have a low permeability which will inhibit oxygenated waters from circulating in the upper layer (Stow *et al.*, 2001). The other impact of grain size is the increased surface area of the overall sediment where a finer grain provides a larger surface area for organic matter to adsorb on (Keil *et al.*, 1993 from Arthur, 1994). This specific mechanism is sensitive to the grain mineralogy, where certain minerals will have a greater or lesser affinity for organic matter adsorption.

Finally, the extent of preservation is also affected by the type of organic matter. There are three main types of organic matter Type I (lacustrine/algae), Type II (marine) and Type III (humic/non-marine) which are variably resistant to degradation. Organic matter with larger proportions of resistant biopolymers can lead to improved preservation over organic matter with lower proportions (Stow *et al.*, 2001).

2.1.5. Diagenetic Processes

Following the depositional processes and preservation mechanisms sediments then undergo diagenesis which is a combination of both physical and/or mechanical processes. Diagenesis is the process which turns sediments into a rock. Diagenesis can also vastly alter the physical and mineralogical properties of the rock, for shale this often increases the complexity and heterogeneities of a sample, and also the differences between samples.

Physical diagenetic processes are primarily concerned with the compaction of the sediment and the development of fissility within shale. It was thought that shale fissility was mostly as a result of clay mineral orientation (Curtis, 1980), however it was seen that shales do not show any greater level of clay mineral orientation than some mudrocks and siltstones. However, in thin-section it was seen that shales when compared to other rock types had a perfect preservation of very fine scale lamination and there was very intricate layering of organic sulphide-rich layers with clays, despite clay mineral orientation not being perfect. Fissility can also be linked to anoxic environments which support organic matter preservation as they highlight a lack of life due to there being no evidence of bioturbation (Curtis, 1980).

During burial there is a great deal of diagenesis in the clay minerals (usually a thermogenic reaction) turning them from smectite to illite (Lynch, 1997), these processes also create differentiation between swelling and non-swelling clays. This process of diagenesis has a significant impact on the reduction of porosity and permeability of the shale (Dutta, 1985; Katsube and Williamson, 1994; Lynch, 1997) due to compromises in the microstructures and pore networks of the shale. These structures play a crucial role in fluid flow, and a greater level of complexity impedes the ability of fluids to move within the shale. This is the primary process required for hydrocarbon recovery and/or carbon dioxide storage (Dræge *et al.*, 2006). Both physical and chemical diagenetic processes are universally influenced by the rate of burial. A slower burial rate allows for a higher degree of

diagenesis, where a faster burial leads to a reduced degree of diagenesis (Curtis, 1980). Chemical diagenetic processes are significantly more complicated than physical processes, where fine-grained material is particularly affected by chemical diagenesis. When unstable mineral assemblages are deposited together by sedimentary processes, the least stable components will begin to react with the environmental conditions (e.g. pH and Eh). These environmental conditions can be broken down into three key zones present in the early diagenetic process occurring in the first 1-2km of the water column depth. Curtis, (1980) identifies the three key zones as follows; zone 1 - aerobic oxidation conditions, zone 2 – sulphate reduction zone and zone 3 – fermentation zone.

2.2. Characterisation Complexity

This vast difference in depositional sedimentary environments, diagenetic processes, organic matter supply and preservation mechanisms leads to a poorly constrained understanding of shales. As well as vastly heterogeneous mineralogies which significantly affect the acquisition of results, behaviour of the reservoir and the methods by which it can be produced from. Table A1. 1, Table A1. 2 and Table A1. 3 show a summary of results from Ross and Marc Bustin (2009) and Chen *et al.*, (2015) identifying a range in TOC%, vitrinite reflectance and mineralogy of a range of shale samples which differ spatially and chronologically.

2.2.1. “Typical” Characteristics

Chen *et al.*, (2011) outlined the typical characterisation of a shale gas reservoir determined by the Basset Sample Analysis; this process aims to characterise the geochemical, petrographical, mineralogical and petrophysical properties of the shale. These four components are concerned with the lithologic data of the rocks including mineral types, porosity, permeability, formation thickness etc. Additionally, the organic matter needs to be considered; the quantity or richness, maturity and the gas content associated to this. Further heterogeneity is introduced through the pore types, Cao *et al.*, (2015) investigate a different way to characterise pores as inter-particle, intra-particle and organic – instead of organic, inorganic and micro-fractures.

Work by Ross and Bustin (2009) summarised that;

“...resource evaluations are complicated by the structurally heterogeneous nature of fine-grained strata and their intricate pore networks, which are interdependent on many geologic factors including TOC, mineralogy, maturity and grain size”

The studied examined two data sets of samples, the first Devonian-Mississippian in age and the second Jurassic. The key and specific discoveries which were made were that despite correlations between organic matter and the micro-porosity within individual datasets these correlations did not extend across both datasets. The Jurassic dataset was more organically enriched than the Devonian-Mississippian but did not show an increase in the quantity adsorbed (nitrogen and carbon dioxide gas adsorption), this is thought to be reflective of the physical changes in organic matter with increased maturity. Thermal maturity leads to some degradation which results in the opening of more micro- and meso-porosity; as a result, discrete datasets can be compared however caution must be taken when they range over several geological timescales. This range over time can mean that different depths, length spent at depth and organic matter types are present making correlations between different datasets insignificant in their conclusions. Investigations into the inorganics (aluminosilicate-rich and silica-rich phases) identified that aluminosilicates contributed to the micro-pore volume resulting in the micro-pores not being solely controlled by the organic matter (Ross and Bustin, 2009). Silicate rich shales on the other hand have micro-pore volume contributions solely from the organic matter. To add further complexity to this problem the micro-porosity of the aluminosilicates is variable based on the degree, type of packing and crystal size.

2.2.2. Pore Types

The pore type can be associated with the specific mineral but can also be more generally defined by where they occur in the sample (Cao *et al.*, 2015). Intra-particle pores have the highest degree of heterogeneity and generally provide the lowest pore volume to a sample. They are not very abundant within the shale and are poorly connected. Inter-particle pores occupy the mid-range of heterogeneity, and are more abundant and better connected than the intra-particle pores. Organic pores have the lowest level of heterogeneity and are the best connected providing the most volume within a shale sample. One of the key properties in these different pores is the variation in aperture range and connectivity to the rest of the sample. Organic pores have the lowest range in aperture, through to the inter-particle pores with the highest range in aperture; this aperture range impacts on the ability of the pores to connect within the shale matrix and form probable volume within the sample.

2.2.3. Engineering Properties

Permeability anisotropy needs to be determined so that the ability of a fluid to flow through a reservoir is understood. Permeability is a key parameter controlling the producibility of a reservoir, as reservoir fluids must be able to flow to be produced (Tan *et al.*, 2019). Although shales are considered to be naturally fractured, the fractures are not well-connected like in coals. They are irregular and poorly connected resulting in permeability values often within the order of nano- to milli-Darcy's. Permeability is also strongly sensitive to the changes in effective stress which can lead to several orders of magnitude variation in permeability across a formation (Tan *et al.*, 2019). In silicate rich zones where shales are more brittle, they will fracture well and this is an essential characteristic for permitting hydraulic fracturing and maintaining a productive permeability (L. Chen *et al.*, 2015). Whereas aluminosilicate rich (clay) zones are more ductile and less prone to fracture and remain open (unless well propped). The mineralogical heterogeneities outlined above will cause a large order of magnitude difference in the permeability baffling the flow of reservoir fluids.

Fathi and Akkutlu (2009) outline why anisotropic effects are significant to the development of shales as reservoirs to produce from. The current approach is to describe the gas-matrix interactions deterministically, assuming all formations will act similarly. Work to date has determined these anisotropies to be non-trivial in their impact on the fluid transport and mass transfer kinetics within the formation. The consequence of this is that the formation anisotropy is over-looked and the nature of the rock to retain gas within the matrix is not well-understood leading to large volumes of gas not being produced from the reservoir.

In addition to the internal heterogeneities of shales (Chen *et al.*, 2011), there is an additional complexity introduced when samples are unloaded from depth (borehole samples specifically). As this happens the pressure and temperature with which they are under is significantly reduced leading to further damage and alteration of the samples (Horsrud *et al.*, 1998). The main structural impact of the unloading process is expansion of the rock creating micro-cracks, dinking and reducing fluid saturation – experimentally the consequence of this expansion is the over-estimation in porosity, permeability and the pore size distributions.

It is not possible to simply adapt current techniques for reservoir production from conventional reservoirs to unconventional reservoirs due to the complex properties of shales, and the heterogeneity of their constituents (Josh *et al.*, 2012). Although in some cases ideal basins can be well understood (often the U.S.), it is not possible to arbitrarily apply these models to other shale formations (Chen *et al.*, 2011). There is a high degree of variability, heterogeneity and anisotropy vertical and horizontally within one formation – without the additional differences between separate basins (L. Chen *et al.*, 2015). Since shales can range from silt-rich to carbonate-rich and even transition into “tight gas sands” their physical and mechanical properties are fundamentally

different and require a unique systematic workflow for thorough characterisation (Josh *et al.*, 2012). Having a thorough understanding and way to deal with these problems is significant for the oil and gas industry as shales can make up the difference between supply and demand in the current energy climate. They could also bridge the gap while renewables are developed.

2.3. Evolution of the Use of Shales

2.3.1. Historically

Shales were first used as a marker in geological maps associated with having underlying coal measures (Tourtelot, 1960). It was later identified that shales possess the ideal properties to form caprocks to oil and gas in conventional reservoirs mitigating the upwards migration of hydrocarbons out of a reservoir (Tourtelot, 1960; Palchik, 2003; Appels *et al.*, 2017). More recently interest and the use of shales has transitioned from a caprock in conventional reservoirs to unconventional oil and gas reservoirs themselves. Production of these unconventional reservoirs now occurs on a global scale working to meet demand where conventional reservoirs are becoming increasingly depleted (Smith and Young, 1967; Brendow, 2003; Dooley, Dahowski and Davidson, 2009; Keating *et al.*, 2011; Latham, 2011; Wang, Ryan and Anthony, 2011; Liu *et al.*, 2013; Godec *et al.*, 2014; Nichols and Victor, 2015).

2.3.2. Presently

Shales are being investigated for their potential use, and effectiveness as cap rocks (seals) in carbon capture and sequestration processes (Dooley, Dahowski and Davidson, 2009; Orr, 2009; van den Broek *et al.*, 2010; Dalhoff *et al.*, 2011; Liu *et al.*, 2013; Jiang and Bhattacharyya, 2016; Szabó *et al.*, 2016). Further developments to this are the use of shales as stores for carbon dioxide (CO₂) by using CO₂ in a competitive adsorption process to fix CO₂ on the pore surface, and at the same time releasing methane (CH₄) from the surface for production (Brendow, 2003; Orr, 2009; Godec *et al.*, 2013, 2014; Liu *et al.*, 2013). This process is known as enhanced gas recovery and is a relatively new area of engineering research.

There are other uses of shales which are being investigated on a more local scale where there is a specific need for the engineering technology, and the shale formation is physically and mechanically suitable. Some formations are investigated for their potentials as using spent shales to treat surface waters (Fox *et al.*, 1980), heavy mineral stores (Smith and Young, 1967; Appels *et al.*, 2017), as novel sources for hydrogen (H₂) in the coal-biomass to liquid (CBTL) process (Dooley, Dahowski and Davidson, 2009; Jiang and Bhattacharyya, 2016) and it is also considered that they can act as sufficient barriers to maintain oxidation conditions above and below by stopping the upwards movement of oxygen from a reservoir resulting in supporting the acid-generating potential in a reservoir (Appels *et al.*, 2017).

2.3.3. Shale Use in the Oil and Gas Industry

Methane (natural gas) stored in shales is considered the best option to extend the life of fossil fuels for infrastructures currently not equipped for renewables. Most commonly in shale oil and/or gas formations where organic carbon content in the rock has thermogenically degraded over time creating smaller molecules of oil and gas (natural gas); shale (when a seal to a conventional reservoir) additionally traps gas which has migrated out of the underlying conventional reservoirs (Zoback *et al.*, 2010). Methane is also wrongly perceived to be a cleaner alternative to carbon dioxide released from conventional oil and gas activities, however methane has a 100-year global warming potential of 28-36 but carbon dioxide is just 1 (Stocker *et al.*, 2014).

2.3.3.1. Horizontal Drilling

Horizontal drilling (Figure 2) is the method used for production from unconventional reservoirs and is the process of drilling at a non-vertical angle (Speight, 2015; Lehr *et al.*, 2016). The idea of

horizontal drilling was first introduced in the 1930s as a method to optimise conventional reservoir production (Zoback *et al.*, 2010; Hossain and Islam, 2018), and is now the method used for unconventional reservoir production. The evolution of horizontal drilling now sees the use of multi-lateral drilling where several horizontal wells are drilled off of a primary vertical well (Speight, 2015). Horizontal drilling is often used to reduce costs by drilling from land to a target not directly below the penetration point (Speight, 2015), an example of this is Witchfarm (Dorset), where drilling takes place on-shore, but the reservoir is primarily off-shore. Horizontal drilling is primarily used for production, however the associated benefits of this technology are that there is a smaller footprint at the surface (Hossain and Islam, 2018) and also allows for ecological sensitive areas to be avoided (Speight, 2015) as drilling does not need to occur directly above the reservoir.

As with any new technology horizontal drilling faces several challenges; these are predominantly social and environmental. Social challenges are mainly to do with the mineral rights (Hossain and Islam, 2018) and people not wanting drilling operations to take place, “not in my backyard”. Environmental challenges are focused on subsurface contamination of ground water (greater surface area of wells below ground), blowouts, seismic risks if there are unmapped faults which are re-activated by the drilling process, surface water, soil contamination and other surface impacts as a result of surface drilling operations at the well pad (Zoback *et al.*, 2010).

2.3.3.2. Hydraulic Fracturing

The most important role that horizontal drilling has played is in the development of natural gas shale plays through the addition of hydraulic fracturing (Lehr *et al.*, 2016). Hydraulic fracturing, or ‘fracking’, is the high-pressure injection of fracturing fluid which is comprised mostly of water, some chemicals (e.g. acids and viscosity modifiers) and proppant. This mixture is injected during horizontal drilling in shale deposits in order to improve network connectivity to produce oil and gas which is trapped within the rock, shown in Figure 2 below (Andrews, 2013; Bažant *et al.*, 2014).

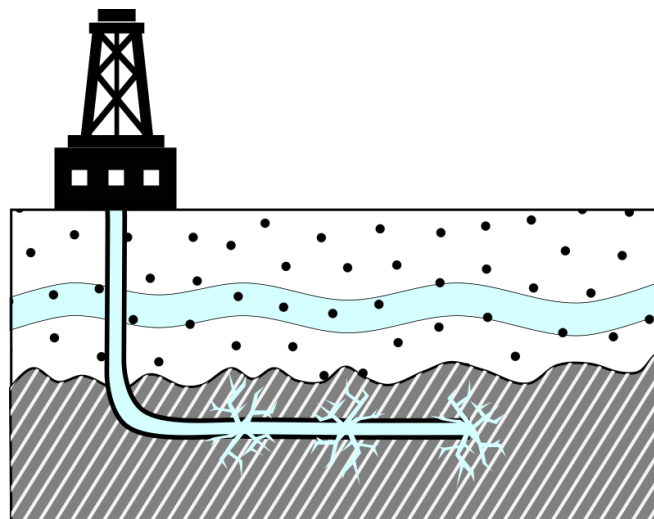


Figure 2: hydraulic fracturing operations where the well penetrates vertically through the water table to the shale formation and then changes direction to drill horizontally. Following this the formation is hydraulically fractured by injecting water, sand and chemicals into the well forming fissures which allow gas to flow out.

This process of horizontal drilling creates new pathways from which gas can flow, which optimises production (Bažant *et al.*, 2014) and provides a number of unconventional reservoirs previously not considered as economically viable. In the US where there are a number of shale gas reservoirs it has been estimated that there are several thousand trillion cubic feet (tcf) of gas. If only a fraction of this is extracted it will still satisfy the demand for energy in the US for a number of years (Burnett, 2013), this is an energy supply which would not have been available were it not for hydraulic fracturing. In Britain alone the British Geological Survey (BGS) have estimated that there are possibly 1,300 tcf of

gas trapped in the rocks beneath Lancashire, Yorkshire and the surrounding counties. Britain's current energy demand is 3tcf per year, and so if only 10% of the current estimate was able to be economically extracted it would provide 40 years' worth of energy. Though these are promising figures it still needs to be established how much of this estimate is both technically and commercially recoverable (Gosden, E. and Clancy, 2013).

Like any new technologies hydraulic fracturing faces many challenges; it shares the same social and environmental challenges that horizontal drilling faces with some additions. The risk to ground water contamination is increased due to mobilisation of formation fluids or escaping methane (Kissinger *et al.*, 2013; Lange *et al.*, 2013; Hoffman *et al.*, 2014), earthquakes and other surface contamination accidents (Kissinger *et al.*, 2013; Lange *et al.*, 2013). Diffuse methane emissions which could contaminate groundwater may also escape into the atmosphere and contribute to the greenhouse gas emissions (Kissinger *et al.*, 2013). This means that hydraulic fracturing activities need to take place within the framework of the appropriate groundwork (regulation) for activities to go ahead (Andrews, 2013). Regulation of the hydraulic fracturing industry vary by the country operations are taking place in; consequently, under-regulation can lead to a lot of operations taking place but at a lower safety level, or over-regulated where regulations make it close to impossible for operations to take place.

2.3.3.3. Carbon Capture and Sequestration (Storage)

There are additional challenges in the operations associated with the caprock characteristics. Caprocks (commonly shale) are highly heterogeneous in pore system, mineralogy and fracture networks – with all these properties varying with the relative stress and strain regime the system is currently in (Lange *et al.*, 2013). This is further complicated by the lack of continuity between units meaning it is not possible to replicate the same process from one formation to the next in the same way that a conventional sandstone reservoir will often have similar properties across several different reservoirs (Lange *et al.*, 2013). Additionally, the lack of specific knowledge can lead to uncertainty on whether the resulting product is saleable (Andrews, 2013).

This research also aims to be transferrable to carbon capture and storage (CCS) by aiding in the understanding of pore network connectivity of shales, which commonly occur as a “caprock” (or impermeable seal) above depleted oil and gas reservoirs that are being targeted for geological storage of CO₂.

CCS is the process of sequestering waste carbon dioxide (CO₂) from power plants into storage sites where it cannot escape to the atmosphere. The most commonly proposed storage sites are geologic sinks, deep-ocean, deep saline aquifers, active and/or depleted oil and gas reservoirs, un-minable deep coal seams and salt domes (Herzog and Golomb, 2004; Raza *et al.*, 2018).

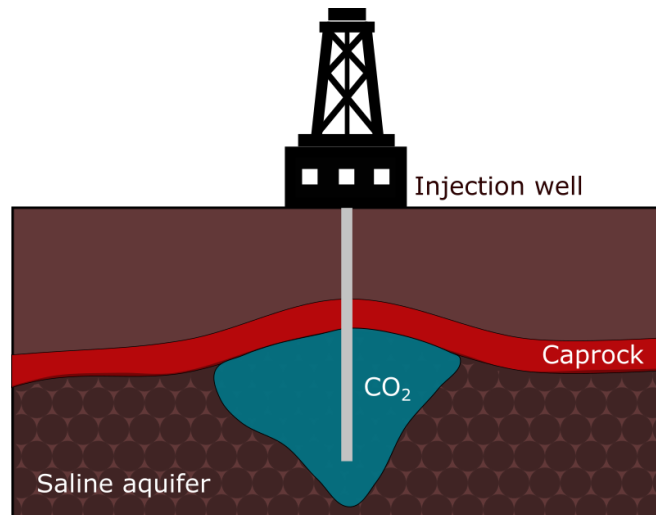


Figure 3: simplified diagram of carbon capture and storage in a saline aquifer with a caprock able to trap stored CO₂. CO₂ is injected via an injection well at the surface which receives captured waste CO₂.

In order for effective geological storage of carbon dioxide to occur there are several formation requirements to ensure storage beneath the surface of the earth. There needs to be adequate porosity, permeability and formation thickness, a satisfactory sealing rock (e.g. shale), a stable geological environment (not tectonically active – its integrity can be “guaranteed” over a long timescale) and a minimum depth which ensures carbon dioxide can remain in its supercritical state where its increased density forces it to sink (Zhang and Huisingsh, 2017).

Fractured shale formations which are depleted of oil and natural gas are attractive repositories because fracture networks which propagate horizontally along the bedding planes provide good storage sites for carbon dioxide (Bielicki *et al.*, 2018). CO₂ can also be used as an alternative to water in the fracturing process, which can reduce capillary trapping and lead to higher yields (Bielicki *et al.*, 2018), also in secondary production in enhanced gas recovery (EGR). The concept of enhanced gas recovery (EGR) is centred on the idea of reinjecting a waste gas, often carbon dioxide or nitrogen, back into a reservoir in order to stimulate further production (Khan *et al.*, 2013). This is viewed favourably when carbon dioxide is the reinjected gas as it offers an opportunity to both re-pressurise the reservoir and also mitigate any environmental impacts in the removal of carbon dioxide from the environment. The main mechanism responsible for the success of EGR due to carbon dioxide is displacement of the reservoir gas (methane) and by re-pressurisation of the reservoir facilitating further production beyond primary production (Moghadas *et al.*, 2018).

CCS is highly dependent on the carbon dioxide gas properties; pressure – volume – temperature relationship, solubility, viscosity, thermodynamics and chemical reactivity (Harding *et al.*, 2018). This is because the storage step is multi-faceted; once the storage formation has been selected the physical mechanism of how the CO₂ will be trapped must be considered. There are five main storage mechanisms for CO₂ storage; super-critical CO₂, caprock/structural/stratigraphic trapping, dissolution of carbon dioxide into the formation brine, from a reaction with the formation brine where it forms a weakly acidic solution and by capillary trapping as a result of water displacement (Blunt, 2010). It has also been recognised that CO₂ could be stored by sorption on the surface of organic and clay minerals surfaces (Song and Zhang, 2013).

The challenge is to understand the long-term integrity of these caprocks to ensure integrity over long timescales. The main leakage processes to be considered are diffusion through water saturated caprocks, the capillary entry pressure being exceeded and gas flowing through the pore network and fracture flow (Edlmann *et al.*, 2013). Caprocks are very tight and their pore neck sizes are such that the capillary entry pressure is incredibly high, further increased if the surface mineralogy is non-

wetting to the supercritical carbon dioxide; however if this pressure can be exceeded then the carbon dioxide will be able to flow freely throughout the rock (Edlmann *et al.*, 2013).

Formation chemistry also needs to be very well understood as the primary composition will chemically react in very different ways and result in different trapping outcomes (Alemu *et al.*, 2011). Work by Alemu *et al.*, (2011) identified two main formation compositions, carbonate-rich and clay-rich. It was observed that the carbonate-rich rock showed significant dissolution when the carbon dioxide was introduced increasing the porosity and enabling better transport of the carbon dioxide through the sample. On the other hand, it was observed in the clay-rich rock that matrix alteration led to a reduction of permeability and porosity further limiting the movement of carbon dioxide throughout the sample.

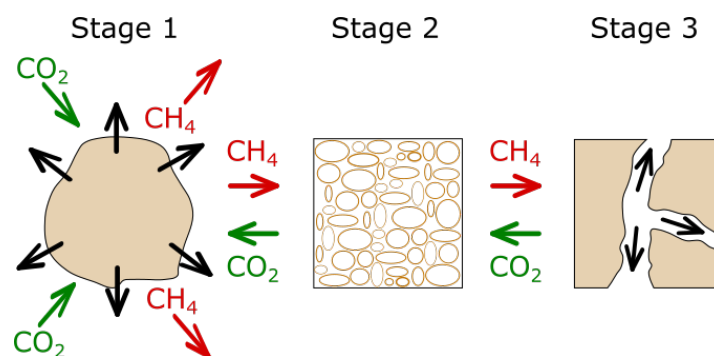


Figure 4: flow dynamics of CO₂ and CH₄ through a shale formation where CO₂ preferentially adsorbs forcing CH₄ to desorb (edit Godec *et al.*, 2014).

2.4. Essential Pore Characteristics of Shales

The research being carried out in this project is relevant to both fracking and CCS since it is aiming to offer methods in which the characterisation of pore size distributions can be enhanced. This is beneficial as shale is an ultra-tight rock with a low pore connectivity and permeability (Shiko *et al.*, 2013; Zhang and Huisingh, 2017). An extensive understanding of pore size distributions, pore networks and connectivity is required to make accurate estimations and develop a thorough understanding of the flow dynamics of carbon dioxide and methane within a formation (Figure 4).

2.4.1. Pore Networks, Porosity and Permeability

Since the permeability of shales is extremely low, possessing the ability to more fully understand micro-structural controls (on porosity and permeability) is necessary in aiding the effective delivery of gas (Curtis, 2010; Sondergeld *et al.*, 2010). Porosity and permeability characterisation in shales is complex, however more simple measurements like the pore volume are still elusive. There are two measurement techniques to do this, either directly or indirect (Sondergeld *et al.*, 2010; Cao *et al.*, 2015; Liu *et al.*, 2016). Direct measurements include physical observations of the sample and can only offer a two-dimensional view of the pore structure. Indirect methods are most commonly fluid intrusion techniques which intrude the pore volume and infer a porosity from that (Sondergeld *et al.*, 2010). In both direct and indirect methods, the shale is observed on a lab-scale and not reservoir scale – making large scale pore network connectivity almost impossible to determine. As well as this the enhanced understanding of pore networking and connectivity will help to quantify the integrity of a shale as a seal for CCS in stopping the upwards migration of stored carbon back into the environment.

2.4.2. Mineralogy

Curtis, (2010) have investigated a number of different American gas bearing shales on the micro- and nano-scale. They have reconstructed the shales using focused ion beam milling and scanning electron microscopy – the results show a significant variation in the micro-structures. The micro-

structures are comprised of mineral content, micro-texture, clay distribution and the porosity, and these are significant to the connectivity of the shale (Sondergeld *et al.*, 2010). In gas shales, clay content is highly variable, as well as other mineral content such as quartz and calcite. During deposition and compaction pore space is reduced, however this can align clay minerals leading to more anisotropic qualities (Sondergeld *et al.*, 2010).

2.4.3. Organic Matter Content

The most significant characteristics to potential gas production in shales is organic matter content and porosity – especially when organic matter is connected by the pore network, it is therefore necessary to understand where porosity is situated. It is reported that the porosity in shales exist in either the organic matrix, inorganic matrix, or it exists within both. This is significant as the producibility of gas bearing shales relies on the connectivity of the pore network to the organic matter. Due to these complexities, it makes the estimation of gas-in-place (GIP) difficult (Sondergeld *et al.*, 2010; Shiko *et al.*, 2013).

2.5. Experimental Techniques

2.5.1. Gas Adsorption

Gas adsorption is universally utilised as a method to determine the specific surface area, volume and pore size distribution (with density functional theory models) of fine powders and porous solids (Rouquerol *et al.*, 2014). It is a fluid intrusion method, where a given adsorbate intrudes the pore network under a constant temperature. The sorption which we have used in this project is physisorption which utilises the Van der Waals interaction between the adsorbate and the adsorbent (Figure 5). Chemisorption takes place with covalent bonding between the adsorbate and adsorbent making it an irreversible process.

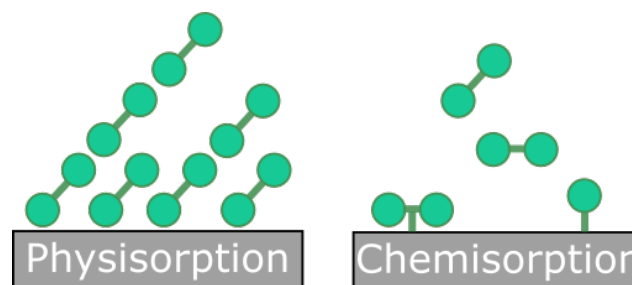


Figure 5: between physisorption and chemisorption where there is an absence of covalent bonds in physisorption where adsorption is controlled by van der waals forces.

Analysis of gas sorption data is complicated by the heterogeneity of material surfaces (roughness) and the porosity of the sample (“openness” of the pore networks) which will both limit the area available for adsorption. The adsorbate used will additionally impact the derived results since a larger molecule will not “fit” on some portions of a rough surface, through the same portions of a pore network (Rouquerol *et al.*, 2014). The analysed experimental data allows correlations to be drawn between the dominant pore sizes, surface area and pore volume. Most materials which are of technological importance and have research carried out on them are in some way heterogeneous, and this heterogeneity is often the property of interest.

2.5.1.1. Langmuir Model

The Langmuir model deals with monolayer adsorption on an idealised surface, and assumes that the adsorbate behaves like an ideal gas under isothermal conditions, defined by the ideal gas equation, (1. 1) (Rouquerol *et al.*, 2014).

$$pV = nRT \quad (1. 1)$$

Where p is the pressure, V the volume, n the amount of substance, R the ideal gas constant and T the temperature. The original derivation of the Langmuir model (Langmuir, 1916) treated the model kinetically and stated that adsorption takes place on a homogeneous surface which has the same surface chemistry and only allows each space to hold one molecule. When the Langmuir model is dealt with in this way some additional assumptions are made about the adsorbate and adsorbent (Rouquerol *et al.*, 2014; Singh and Kumar, 2016); that the adsorbent is a flat surface (homogeneous), when the adsorbate adsorbs it is immobilised, each adsorption site is equivalent to the next, each adsorption site can only be occupied by one molecule (monolayer) and that there is no interaction between adsorbate molecules on different sites.

The model has also been proposed for a number of other mechanisms which include more than one kind of adsorbing site, a surface which is not homogeneous, where each site can adsorb more than one molecule, adsorption is dissociative and occurs in multiple layers (Langmuir., 1918).

Mathematically the Langmuir model is derived in the following way when the adsorbent is viewed as a series of equivalent and independent sites available for adsorption, N^s . A number of these sites will become occupied when molecules adsorb on them, N^a giving the fraction of occupied sites, θ as;

$$\theta = \frac{N^a}{N^s} \quad (1. 2)$$

For the kinetic theory the rate of adsorption depends on the pressure and fraction of unoccupied sites ($1 - \theta$), and the rate of desorption depends on the number of occupied sites and the activation energy (E) required to overcome the physical bonds between the adsorbate and adsorbent. Equilibrium occurs when the adsorption and desorption are equal, and the net rate of adsorption can be equated to zero;

$$\frac{dN^a}{dt} = \alpha p(1 - \theta) - \beta \theta e^{-\frac{E}{RT}} = 0 \quad (1. 3)$$

Here the constants α and β are characteristic of the gas-solid system being analysed and p is the analysis pressure. If assuming the case is the first addressed by Langmuir and the adsorbate does not interact with any other adsorbate molecules then the desorption of these molecules is independent of the surface coverage; assuming this the value of E becomes constant as the activation energy is between one type of adsorbate-adsorbent pairing for the adsorption system. This assumption, when applied to (1. 3) (above), allows simplification and re-arrangement to the classically accepted Langmuir isotherm equation;

$$\theta = \frac{bp}{(1 + bp)} \quad (1. 4)$$

b is the adsorption coefficient which can be exponentially related to the positive energy of adsorption when K , the pre-exponential factor is equal to the ratio of $\frac{\alpha}{\beta}$

$$b = K e^{\frac{E}{RT}} \quad (1. 5)$$

When analysing data with use of the Langmuir model it is necessary to highlight that since it is concerned with monolayer adsorption, only the first few points ($0-0.035 \frac{p}{p_0}$) are taken from the isotherm.

Langmuir model is only relevant for cases where a monolayer is formed. At pressures about this where a multi-layer region begins to form it is no longer able to describe the characteristic behaviour of the adsorbate-adsorbate interaction (Nagy, 2012). At low pressures where the rate of adsorption is described by;

$$rate = \frac{kbp}{1 + bp} \quad (1.6)$$

If you take $rate = k\theta$ and equate this to (1.6), the term $bp \ll 1$ resulting in the denominator of (1.6) being equal to 1 and thus the $rate$ being expressed as;

$$rate \approx kbp \quad (1.7)$$

This term is a first order reaction where the $rate$ is controlled both by k and p . However, in the high-pressure case where $bp \gg 1$ the denominator in (1.6) becomes bp and so $rate$ can be expressed as;

$$rate \approx k \quad (1.8)$$

In the low-pressure case the $rate$ is controlled by both k and p , a pressure exponent. Whereas in the high-pressure case the $rate$ is controlled only by k and no longer contains a pressure dependency.

2.5.1.2. Brunauer-Emmett-Teller (BET) Model

The appearance of Langmuir's comprehensive treatment of monolayer adsorption (Langmuir, 1916; Langmuir., 1918) prompted several investigators to consider the possibility of using gas adsorption for surface area determination. The first significant advances were made by Brunauer and Emmett (Brunauer and Emmett, 1935; Emmett and Brunauer, 1937) and their work prepared the way for the development of the Brunauer–Emmett–Teller (BET) theory in 1938 (Brunauer *et al.*, 1938). In Figure 6 "Point B" (designated by Emmett and Brunauer, 1937) indicates the beginning of the linear section which marks the completion of monolayer adsorption and the beginning of multilayer adsorption. From the amount adsorbed at "Point B", the surface area could be calculated assuming that the monolayer was complete at this point (Emmett and Brunauer, 1937).

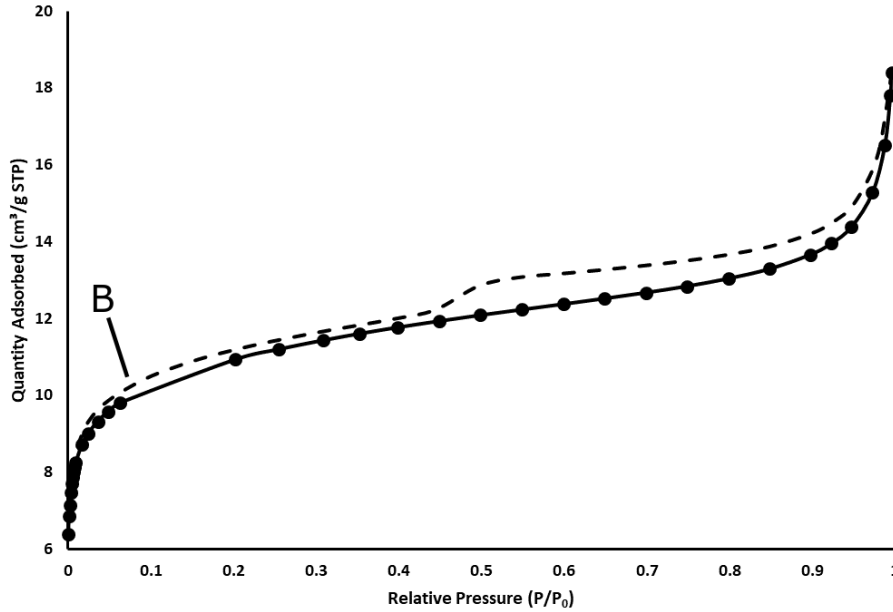


Figure 6: isotherm with “Point B” labelled for the beginning of the multilayer adsorption starts.

Brunauer *et al.*, (1938) developed the isotherm equation for multilayer adsorption (BET equation) by introducing a number of assumptions to the problem in order to simplify it. The initial BET equation was developed to handle Type II character isotherms which are representative of non-porous materials (Rouquerol *et al.*, 2014). This is most commonly carried out using gases which are unreactive to the surface of the adsorbent. The gas most commonly used is nitrogen carried out at 77K.

BET is primarily used most to quantify the specific surface area of a sample, which is defined by the total surface area of a material per unit of mass (e.g. m²/kg). This is therefore a scale-dependent property which has no single true value. Values of specific surface area calculated by BET theory are therefore heavily dependent on the adsorptive used (Rouquerol *et al.*, 2014).

The three main assumptions made for the BET theory are listed below (Rouquerol *et al.*, 2014);

1. Gas molecules physically adsorb on the adsorbate in layers infinitely – i.e. equivalent to the sample being surrounded by a liquid phase (Sing, 1998)
2. There is no interaction between each layer of adsorbed molecules, but to act as an adsorption site for a molecule of the upper layer (Sing, 1998)
3. Langmuir theory can be applied to each layer

The first step moving on from the Langmuir theory which dealt with only monolayer adsorption was to assume that an infinite number of molecular layers could adsorb up to a saturation pressure p_0 . In this scenario the adsorbate molecules in the monolayer provide an adsorption site to the next layer of molecules and so on until the saturation pressure is reached. Mathematically this is represented by $\theta_0, \theta_1, \theta_2, \dots, \theta_i$; the fraction of the surface covered by 0, 1, 2, ..., i layers of adsorbed molecules - θ_0 represents the fraction of bare surfaces where the monolayer is incomplete and so θ_1 the fraction of “empty sites” in the next layer and so on. This assumption indicates the expectation that adsorbed layers will not be uniformly thick, but instead be made up of molecular stacks of varying height.

If, however it is assumed the fractions of bare (θ_0) and covered (θ_1) surface remain constant at the equilibrium pressure p , then the rate of condensation on the bare and rate of evaporation from the covered layer can be equated and expressed as;

$$a_i p \theta_{i-1} = b_i \theta_i e^{-\frac{E_i}{RT}} \quad (2.1)$$

In this instance a_i , b_i and E_i represent the adsorption, desorption and activation energy for the i^{th} adsorption layer. In order to calculate the total amount adsorbed it can be said that the sum of surface fractions is equal to unity such that;

$$\sum_0^{\infty} \theta_i = 1 \quad (2.2)$$

And,

$$V_m \sum_0^{\infty} i \theta_i = V \quad (2.3)$$

V_m is the monolayer adsorbed on the surface, and V is the total amount adsorbed. Principally the constants a_i , b_i and E_i should be different for each layer but Brunauer, Emmett and Teller handled this by making two key assumptions;

1. In the second layer, and all layers above the activation energy E_i has the same value as the liquefaction energy (E_L) of the adsorbate
2. The multilayer has an infinite thickness at $\frac{p}{p_o} = 1$, when $i = \infty$

Given the first assumption we can let,

$$\frac{b_2}{a_2} = \frac{b_3}{a_3} = \dots = \frac{b_i}{a_i} = g \quad (2.4)$$

Since all subsequent layers after the first are assumed to have the same properties. The result is that $\theta_1, \theta_2, \dots, \theta_i$ can be expressed in terms of θ_0 ;

$$\theta_i = y x^{i-1} \theta_0 \quad (2.5)$$

By defining a constant C to be;

$$C = \frac{y}{x} = \frac{a_1}{b_1} g e^{\left(\frac{E_1 - E_L}{RT}\right)} \quad (2.6)$$

Then,

$$\theta_i = C x^i \theta_0 \quad (2.7)$$

By rearrangement of (2.1), and the substitution of θ_i for θ_0 it can be written;

$$\frac{V}{V_m} = \sum_0^{\infty} i \theta_i = C \sum_0^{\infty} i x^i \theta_0 \quad (2.8)$$

Where V is the quantity adsorbed, and V_m is the monolayer capacity. This can then be expanded to give the commonly recognised BET equation;

$$\frac{V}{V_m} = \frac{Cx}{(1-x)(1-x+Cx)} \quad (2.9)$$

And by assuming that the adsorbed layer is of infinite thickness when at saturation pressure i.e. $\frac{p}{p_0} = 1$, it follows that for pressures up to saturation, $x = \frac{p}{p_0}$ and (2.9) can be written;

$$\frac{V}{V_m} = \frac{C \frac{p}{p_0}}{\left(1 - \frac{p}{p_0}\right) \left(1 - \frac{p}{p_0} + C \frac{p}{p_0}\right)} \quad (2.10)$$

It is still common however for the BET model to significantly over-estimate the true monolayer capacity of the material (Gómez-Gualdrón *et al.*, 2016). More specifically work carried out by McMillan and Teller (1951) highlight that the BET model often predicts adsorption which is too small at low pressure (monolayer) and too large at higher pressures (multilayer). This statement was refined by Gómez-Gualdrón *et al.*, (2016) that the overestimation of a true monolayer capacity tended to be more significant in materials that combined meso- and large micro-pores (about 1.5-50nm). Additionally, pressure sensitivity causes different ranges to yield different results despite attempts to implement consistency. This then impacts on the application of BET to more complex materials with multimodal pore size distributions, pore shapes and pore sizes (Gómez-Gualdrón *et al.*, 2016). Extensive adsorption measurements (Beebe and Young, 1954; Isirikyan and Kiselev, 1961; Grillet *et al.*, 1979), and simulations (Nicholson *et al.*, 1982; Seri-Levy and Avnir, 1993) on a wide range of adsorbate-adsorbent systems have shown that for systems where physisorption is the only mechanism taking place they do not behave in the way the assumptions state they do.

There are three main types of isotherm which are derived from gas sorption experiments (**Error! Reference source not found.**). The first of these, Type I, is an example from a microporous material where most of the uptake takes place in the low relative pressure region. The second of these, Type II, is representative of a non-porous material and Type III a material where the interaction between adsorbate and adsorbent is weak (this can also be a macro-porous sample). Isotherm types, Type IV and V include the desorption branch of the sorption experiment and provide additional information regarding the texture of a meso-porous material (ALothman, 2012; Rouquerol *et al.*, 2014).

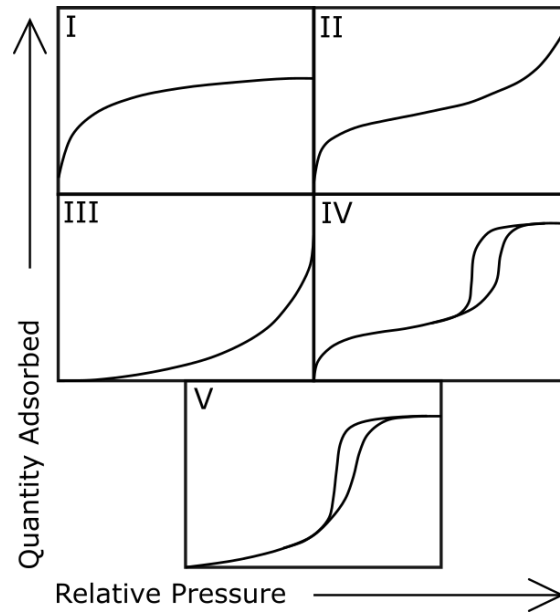


Figure 7: different types of isotherms which can be achieved from gas adsorption. I : Microporous materials (e.g. Zeolite and Activated carbon), II : Non porous materials (e.g. Nonporous Alumina and Silica), III : Non porous materials and materials which have the weak interaction between adsorbate and adsorbent (e.g. Graphite/water), IV : Mesoporous materials (e.g. Mesoporous Alumina and Silica), V : Porous materials and materials that have the weak interaction between the adsorbate and adsorbent (e.g. Activated carbon/water) (Rouquerol et al., 2014).

2.5.1.3. Frenkel-Halsey-Hill (FHH) Theory

Brunauer *et al.*, (1969) pointed out a key weakness in their own model that an infinite number of molecular layers may not always be achieved at the saturation pressure. A theory was put forward by Frenkel, Halsey and Hill which was initially proposed in the 1940s and 1950s (Pomonis and Tsaousi, 2009), and takes the form;

$$\frac{V}{V_m} = RT \ln \left(\frac{p_0}{p} \right)^{-\left(\frac{1}{s}\right)} \quad (3.1)$$

Where $\frac{V}{V_m}$ is the surface fractional coverage, R the gas constant, T temperature, and p and p_0 the pressure and saturation pressure respectively; s is a parameter which describes the shape of the isotherm.

The FHH theory states that as an adsorbate reaches a thickness of several molecular layers the surface heterogeneity is considerably reduced. This idea was later revisited in the 1980s and 1990s by Pfeifer and Neimark (Pfeifer *et al.*, 1989; Neimark, 1990; Pfeifer and Liu, 1997) who introduced the fractal dimensionality D (Pomonis and Tsaousi, 2009), since early approaches were limited by the assumption that the pore surface and morphology are simple. Real solid surfaces are very complex in both the pore surface (roughness) and the pore network (connectivity) (Avnir and Jaroniec, 1989).

By re-examining the FHH equation with respect to a fractal dimension D , Pfeiffer suggested two additional forms for the FHH equation depending on the adsorbate-adsorbent interactions. For the case where the adsorbate-adsorbent interactions are dominated by the van der Waals attraction then the isotherm can be written as;

$$\frac{V}{V_m} = RT \ln \left(\frac{p_0}{p} \right)^{-\left(\frac{3-D}{3}\right)} \quad (3.2)$$

The second case describes when capillary forces are in effect and the adsorbate surface tension is the dominating factor, this is expressed as;

$$\frac{V}{V_m} = RT \ln \left(\frac{p_0}{p} \right)^{-(3-D)} \quad (3.3)$$

The first case is more sensitive to surface roughness and occurs at lower relative pressures, the second case is more sensitive to network complexity and occurs at higher relative pressures. Despite this pressure range dependency there is not a clear switch over point and the threshold between the two models is dependent on the properties of the specific adsorbate-adsorbent system.

2.5.1.4. Barret-Joyner-Teller (BJH) Model

Over the 1940s to the 1970s several different methods were proposed for deriving pore size distributions from gas adsorption isotherms. These methods were considered “classical” as they based themselves on the Kelvin model of pore filling and the assumptions made by Kelvin (Rouquerol *et al.*, 2014). In the early work, it was customary to assume the pore shape to be cylindrical, but now the slit-shaped and packed sphere models are considered to be more suitable for some systems.

The BJH model evaluates the pore size distribution of the pores within the adsorbent; however, to do this you must decide which branch of the isotherm to take i.e. adsorption or desorption. Desorption is controlled by percolation effects within the network, so if you have a broad distribution of interconnected pores the adsorption branch would be a better option since the percolation effect would skew the pore size distribution towards larger pores.

Where the Langmuir model takes the relative pressure from 0-0.035 $\frac{p}{p_0}$, the BET model from 0.035-0.5 $\frac{p}{p_0}$, the FHH from about 0.025-0.8 $\frac{p}{p_0}$ the BJH is able to extend this to the full isotherm. The assumption made by Frenkel-Halsey-Hill that near saturation the adsorbate will behave like a bulk liquid leads to the BJH model taking the first step to remove condensate from the larger pores. Then each subsequent step down the desorption branch sees the thinning of the multilayer in larger pores (where the condensate has already emptied), and the removal of condensate from smaller pores.

2.5.1.5. Density Functional Theory (DFT)

The density functional theory (DFT) is a powerful method for the investigation of adsorption in pores and generation of a pore size distribution for the sample from experimental isotherms. It uses the pore size distributions gathered from the adsorption or desorption branch of the adsorption isotherm which are key descriptors of the void space in materials (Rigby *et al.*, 2008). The DFT can only be considered as a theoretical model (Ravikovitch *et al.*, 1995), and is most effective in slit shaped pores.

Towards the end of the 1980s Seaton *et al.*, (1989) adapted a statistical mechanical approach to the formally known field theory in order to develop a revised form for the density functional theory when dealing with the interpretation of gas adsorption data (Balbuena and Gubbins, 1992, 1993; Lastoskie *et al.*, 1993; Cracknell *et al.*, 1995; Maddox and Gubbins, 1995; Ravikovitch and Neimark, 2001; Neimark *et al.*, 2003).

At saturation the bulk fluid is considered homogeneous where its properties can be determined more simply by pressure and temperature. Due to the adsorption forces within the pore walls however the density of the fluid is not constant and must instead be viewed as a “layer-wise”

distribution. As a result of this the density distribution is expressed as a function of the distance r from the pore wall – the free energy is then taken from the Helmholtz free energy equation which allows expression in terms of the density profile r which can be minimised with constant m , V and T , to obtain the equilibrium density profile.

This initial density functional theory is considered the “local” approach and was developed by Seaton *et al.*, (1989) for use in nitrogen isotherms, but only holds for fluid-fluid interactions and fails to describe the fluid-solid interactions. This led to the development of the non-local density functional theory (NLDF) which involves the incorporation of short-range smoothing approximation of the fluid density and weighting functions (Rouquerol *et al.*, 2014). The NLDF takes the gas adsorption results which correspond to all the possible states of the system at a fixed volume, temperature and chemical potential (Landers *et al.*, 2013). This allows the minimum possible state to be presented as a function of the adsorbed fluid density, the NLDF then minimises this over all possible states of the system (Landers *et al.*, 2013).

Although satisfactory results are derived from this theory for phase transition in slit-shaped and cylindrical mesopores and can also be applied to different isotherm types it is limited by several factors (Rouquerol *et al.*, 2014). In very narrow pores the theory fails as well as being unable to predict solid-liquid adsorbate transitions – this is in part due to the fact the non-local density functional theory (NLDF) assumes a flat structure-less surface (Landers *et al.*, 2013; Rouquerol *et al.*, 2014).

Neimark and others have addressed this problem by proposing the Quenched Solid DFT (QSDFT), which accounts for surface roughness of the adsorbent (Gor *et al.*, 2012; Landers *et al.*, 2013). The QSDFT, unlike the NLDF does not assume a homogenous surface so accounts for surface roughness. It does this by considering the grand potential of both the solid and fluid in the system. Differently to the NLDF the QSDFT considers the process to be made up of a two-component density functional with the fluid molecules interacting with the solid (modelled as hard spheres) in an attractive pairwise potential (Neimark *et al.*, 2009; Landers *et al.*, 2013). QSDFT uses the Lennard-Jones pairwise potentials, as opposed to the integrated Lennard-Jones potentials used by the NLDF (Landers *et al.*, 2013), therefore accounting for intermolecular interactions. The Lennard-Jones potential is a simple mathematical model which is used to approximate the interaction between two neutral atoms or molecules. Where the QSDFT considers a pair of separate points at a distance r from each other, and the NLDF considers a range of distances which can be integrated less specifically. By making these changes in the QSDFT method the PSD gained is significantly improved. Compared to the NLDF the PSD produced is much more accurate since the assumption that the surface is smooth and homogeneous causes the adsorption isotherm steps (first layer, second layer etc.) to be represented in the NLDF PSD as pore sizes which may not be present (Neimark *et al.*, 2009; Landers *et al.*, 2013).

The NLDF and QSDFT in essence generate a series of hypothetical isotherms for individual pore ranges and wall potentials (Rouquerol *et al.*, 2014). When generating a PSD using a DFT it is also important to select the correct branch of the isotherm. As a result of pore blocking and cavitation effects forming hysteresis in the isotherm – it is most accurate to use the adsorption branch of the isotherm (Landers *et al.*, 2013).

2.5.1.6. Gas Sorption Experimental Effects

All the methods used for pore size analysis of gas adsorption isotherms detailed above start from the assumption that pores are rigid and of a well-defined shape throughout the sample. The pore shapes most commonly assumed are either cylindrical or slit-shaped pores – the reality however is that very few adsorbents can be represented by these idealised properties (Rouquerol *et al.*, 2014).

Consequently, a number of experimental effects are introduced which need to be considered such as pore networking, pore blocking, capillary condensation and cavitation (Thommes *et al.*, 2006).

Keeping in mind that most adsorbents of any technological importance, are often so because of their complexity in connectivity, shape and surface properties (Rouquerol *et al.*, 2014). This complexity impacts the shape of the gas adsorption isotherms and will affect the results derived from this e.g. specific surface area, pore surface area, pore volume, pore size distributions etc. (Thommes *et al.*, 2006). On the scale of a single pore with a given shape the hysteresis is as a result of the co-operative effects which reflect the pore network connectivity. This is considered to be a property which is intrinsic of the vapour-liquid-phase transition in a finite volume system (Thommes *et al.*, 2006).

Ink-bottle pores are a common example of a non-idealised pore type which contribute to the evaporation of capillary condensation which obstructs the pore necks and can be seen on the experimentally measured hysteresis loop (Figure 8). The pore body will empty at the point in which the relative pressure is the relative pressure at which the pore neck will desorb – until this point the pore body is blocked (Thommes *et al.*, 2006). This is often seen as a steep step in the desorption branch of the isotherm around $0.5 \frac{p}{p_0}$.

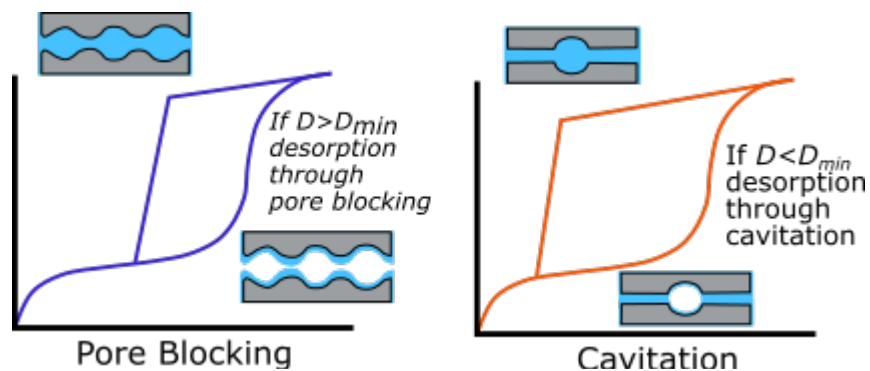


Figure 8: visualisation of the differences between pore blocking and cavitation where pore blocking occurs at $\frac{p}{p_0} > 0.5$ and cavitation takes place at approximately $0.5 \frac{p}{p_0}$. In pore blocking the pore body does not empty until the leading neck has emptied, whereas in cavitation the body empties through the pore neck which remains filled during this time.

The lower limit of hysteresis has been correlated to the cavitation effect of the desorption branch of the isotherm. This has been coupled with the tensile strength hypothesis of the adsorbate. It was believed that the tensile strength of the fluid, indicated by cavitation, is not dependent on the pore structure of the adsorbent but is a quality of the adsorptive (Thommes *et al.*, 2006).

Cavitation permits the desorption of larger pore bodies through a pore throat without the pore throat emptying, pore blocking however only allows the emptying of pore bodies once the pore throat has emptied (Figure 8). By changing the adsorption gas some effects of pore blocking are removed because a smaller molecule will block a smaller range of pore necks (Rigby *et al.*, 2008). The different molecule sizes in the gases will cause pore blocking effects to be observed at different relative pressures allowing the pore throat size to be determined (Thommes *et al.*, 2006). Cavitation however takes place around $0.5 \frac{p}{p_0}$ and represents the emptying of pore throats $< 4\text{nm}$, therefore the hysteresis closure at this point indicates the number of pore throats $< 4\text{nm}$ that are present in the sample but not how much smaller than 4nm they are.

Capillary condensation in larger pores is predicted by the Kelvin equation (Mason, 1982):

$$\ln\left(\frac{p}{p_0}\right) = \frac{-k\gamma V_M \cos\phi}{RT(r_p - t)} \quad (4.1)$$

where $\frac{p}{p_0}$ is the relative pressure at which condensation occurs in a cylindrical pore of radius r_p , t is the multilayer thickness, k is a geometry parameter and depends on the pore type (for a cylindrical pore open at both ends $k = 1$; and for a pore with one dead end, or for desorption from a hemispherical meniscus, $k = 2$), γ is the surface tension and V_M is the molar volume of the condensed liquid phase, ϕ is the contact angle with which the liquid meets the wall, and T is the absolute temperature. In small pores, with a high radius of surface curvature, the multilayer, or t -layer, thickness will be greater than for large pores. (Broekhoff, 1967, 1968) have provided equations for the thickness of the t -layer for adsorption and desorption processes in small pores, which will be used to determine pore sizes in this work.

It is noted from (4.1) that capillary condensation will occur earlier (lower pressure) for a hemispherical meniscus compared to a cylindrical sleeve-shaped meniscus. This can lead to the operation of a pore-pore co-operative adsorption process within pores of underlying geometries akin to the so-called through 'ink-bottle' arrangement (Rigby, 2018, 2020). For a regular, through ink-bottle pore geometry, access to a larger diameter pore body is only through smaller diameter pore necks (or windows) that are located at the two ends of, and are co-axial with, the pore body. Pore-filling during adsorption in such a system is initiated by condensation via cylindrical-sleeve shaped menisci in the necks. The filling of the pore necks completes the hemispherical menisci located at the ends of the pore body, meaning condensation in the body can be initiated from them, before that from the cylindrical-sleeve shaped meniscus along the length of the pore wall. Hence, the pore necks adjoining the pore body can co-operate in lowering the filling pressure for the latter. The ink-bottle pore model can also illustrate the pore-pore co-operative effect known as pore-blocking or pore-shielding that can occur during desorption. Evaporation of the condensate from a pore can only occur when the pressure drops below the critical value given by the Kelvin equation if there is a free meniscus with the vapour phase. In the case of the pore body in the ink-bottle, when the external vapour pressure drops below the critical value to destabilise the condensate in it, there is no free meniscus because the condensate in the necks is still above its critical pressure. The liquid in the pore body thus enters a metastable liquid state until the pressure is reduced sufficiently for the liquid in the necks to evaporate. Then the meniscus will advance to the junction of the neck and body and the metastable liquid in the body can finally evaporate.

These pore-pore co-operative effects will also operate in much more complex, disordered networks consisting of many more inter-connected pores. The advance of condensate or vapour phase through the network, upon pressure changes one way or another, is controlled by the numbers of different pathways possible, which, in turn, depends upon the overall size and connectivity of the pore network. This network penetration process for highly disordered systems can be analysed using percolation theory, which is explained in more detail elsewhere (Seaton, 1991).

2.5.2. Mercury Intrusion Porosimetry

Mercury porosimetry is a fluid intrusion technique which is used for the characterisation of porous media. Unlike gas adsorption mercury porosimetry is able to characterise pore sizes >50nm well and can also be extended to the characterisation of large meso-pores (Rigby and Edler, 2002). Mercury porosimetry is unique in its ability to characterise materials over several orders of magnitude (0.004-100 μ m), where most can only cover a couple orders of magnitude (Giesche, 2006). The principle of mercury intrusion porosimetry is to exploit the non-wetting properties of the fluid which require an external force to be applied in order for pores to be intruded. It is possible from this to correlate the pressure required for intrusion with the correlating pore throat which has been intruded (Rigby and

Edler, 2002; Giesche, 2006). This is primarily determined by the external pressure needed to overcome the opposing force of the liquid surface tension into the pore (Giesche, 2006).

Porous media should be viewed as a network of different pores, which are interconnected by pore channels of varying size – the transition from a channel into a pore is known as the pore throat and this is the property measured by mercury intrusion porosimetry (Giesche, 2006). This property of the technique can cause pore size distributions derived solely from mercury intrusion porosimetry to underestimate the pore sizes as it is a measure of the throat which is often narrower than the body (Figure 9) (Wardlaw and McKellar, 1981); in combination with other techniques however (e.g. small-angle x-ray scattering) this technique is capable of assessing the connected pore space and network complexity of the material (Giesche, 2006). Results from mercury intrusion porosimetry are additionally used comparatively with other methods (e.g. gas adsorption) where the experimental techniques overlap their measurement ranges (Giesche, 2006). In the instance of nitrogen gas adsorption this is for the period of 50-100nm. This technique is limited by the maximum pressure than can be achieved in order to measure the smallest pore sizes – consequently it cannot measure pores which can be accessed by gas adsorption, though is capable of measuring larger pores beyond the limit of gas adsorption. Mercury intrusion porosimetry, as well as pore size distribution, is able to provide information on the total (accessible) pore volume/porosity, the skeletal and apparent density and the specific surface area (Giesche, 2006).

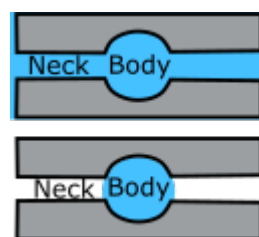


Figure 9: ink-bottle pore with a much wider pore body than neck, with mercury trapped in a pore following extrusion when the mercury has become disconnected from the mercury column.

The derivation of the Washburn equation is based on the Hagen-Poiseuille equation for fluid motion (5. 1) which relates the fluid flow rate to a measured pressure drop (Washburn, 1921; Szekely *et al.*, 1971).

$$\Delta P = \frac{8\mu l Q}{\pi r^4} \quad (5. 1)$$

In (5. 1) ΔP is the pressure difference, Q the volumetric flow rate, l the length of the pipe, μ the dynamic viscosity and r the radius of the pipe. Washburn specifically derived his equation for capillary flow in a cylindrical tube in the absence of a gravitational field (Washburn, 1921). Although issues have been raised about the physical meaning of the calculated pore radius and the accuracy in using this to determine the contact angle, it has proved accurate in enough cases that it is still used. Several additional mathematical steps are taken and (5. 2) is derived that relates the motion of the meniscus in a capillary with respect to r , to the pressure;

$$\Delta P = \frac{2\gamma_L}{r} \cos \phi \quad (5. 2)$$

Which is the commonly known Washburn equation when γ_L is the interfacial tension and ϕ the contact angle (Washburn, 1921; Szekely *et al.*, 1971). The contact angle is where the liquid–gas interface meets the solid–liquid interface for the adsorbent (Figure 10).

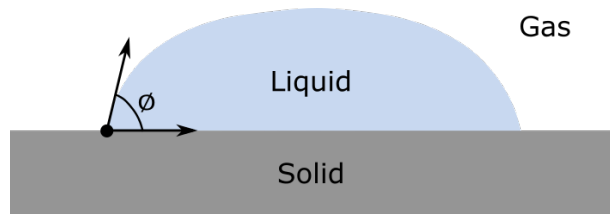


Figure 10: the contact angle of the liquid-gas and liquid-solid interface shown by ϕ .

The surface tension of the adsorbate is determined by the attractive/cohesive force of the surface adsorbate molecules with each other. This takes place in order for them to occupy the least possible surface area and can be more simply described as a measure of how much force it takes to keep the adsorbate together. For mercury in capillary action the surface tension preferentially forms a convex meniscus (Figure 11) over a concave meniscus (Figure 11) as a result of the adhesive forces between the adsorbate and adsorbent surface.

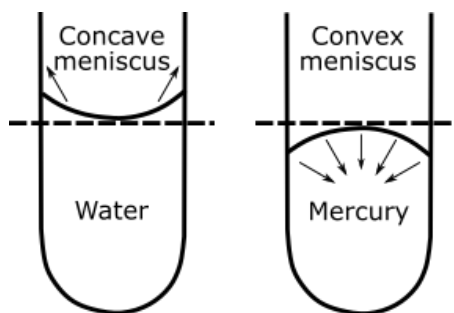


Figure 11: differentiating between the adhesive and cohesive forces related to surface tension in capillary action.

Figure 12, shows the pressure difference across a schematic of a capillary where the pressure is applied left to right resulting in the pressure at $P_1 > P_2$. The difference in these values ΔP , the pressure difference is indicative of a pore or radius r , given the liquid properties γ_L and ϕ .

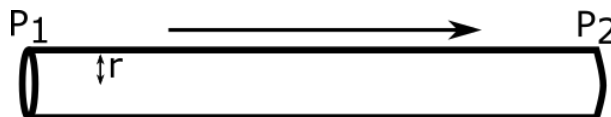


Figure 12: a pipe/tube/capillary with radius r , and a pressure difference ΔP , across it.

The most commonly referred to physical property of a pore network are “ink-bottle pores” (Good and Mikhail, 1981; Lowell and Shields, 1981; Lowell and Shields, 1981; Wardlaw and McKellar, 1981; Moro and Böhni, 2002) and refers to pores where the pore throat/neck to pore body ratio is such that the body is significantly larger with respect to the throat/neck. The consequence of this is that the mercury empties from the neck before the body when depressurised; the result is that mercury in the pore body is no longer connected to the mercury column in the sample and becomes trapped in the body (Lowell, 1980) – a phenomenon known as “snap-off”. This leads to the total volume of intruded mercury not equalling the total volume of extruded mercury and results in hysteresis/trapping. Additional reasons identified by Wardlaw and McKellar (1981) suggest that in addition to the pore throat to pore body ratio the throat to pore coordination number (number of pore throats connected with each pore i.e. connectivity), random and non-random heterogeneities and the surface conditions of pores and throats will impact on hysteresis/trapping in mercury intrusion porosimetry results.

2.5.3. Computer X-ray Tomography (CXT)

Computed x-ray tomography (CXT), also known as x-ray CT, was the first non-invasive imaging technique which allowed the direct visualisation of internal micro-structures (Toga, 2002; Farber, 2019). Early uses of CXT were in the medical field for imaging brains which revolutionised the

treatment of patients with neurological and neurosurgical disorders (Toga, 2002). It has gone on to serve several other uses in the medical field where drug testing and stimuli sensitive drug delivery systems exploit the x-rays ability to distinguish between densities allowing them to carry out contrast imaging (Nair *et al.*, 2018). This density distinguishing can be exploited in shales by using CXT to assess the three-dimensional distribution of density within a shale sample, density contrasts are derived from the minerals and microstructural details which CXT allows to be visualised (Farber, 2019). In most experimental processes a sample is rotated through 180° or 360° whilst a series of x-ray images are acquired, by applying a Fourier transform to these two-dimensional images it is possible to create a set of images which form a three-dimensional map of the sample (Farber, 2019).

CXT offers a digitised method for taking sequential thin sections through a sample to analyse the density contrasts between various minerals. When applied to geosciences these contiguous images are compiled to produce three-dimensional models of the sample which can be digitally manipulated to produce both qualitative and quantitative data (Ketcham and Carlson, 2001). In geosciences the variation in x-ray attenuation depends on the material density which in rock samples corresponds to boundaries between mineral phases and often produces data analogous to thin section analysis (Ketcham and Carlson, 2001). It is possible to exploit this x-ray attenuation by combining mercury intrusion porosimetry with computed x-ray tomography and build a three-dimensional model showing where trapped mercury is located within the sample (Moro and Böhni, 2002).

2.5.4. Differential Scanning Calorimetry (DSC)

Differential scanning calorimetry (DSC) is a thermal analysis technique which measures the heat flow in or out of a sample measured against temperature or time. The melting and/or freezing point depression of a liquid confined within a pore (Landry, 2005) is analysed, and can be used to determine pore properties. When used in this way it is known as thermoporosimetry and determines the pore size distributions by measuring the small temperature shifts due to the liquid being confined in the internal structures of the sample (Ishikiriya and Todoki, 1995). For liquid confined in a smaller pore the melting point is decreased such that it will melt at a lower temperature compared to the bulk liquid – as the pore size increases the melting point depression move further towards the bulk melting point (Charmas and Skubiszewska-Zięba, 2017). The solid-liquid transition is strongly determined by the radius of curvature between the solid-liquid interfaces, a liquid confined in a porous material has only a small division between the solid-liquid interfaces resulting in the radius of curvature being closely related to the pore size (Landry, 2005). This technique is able to determine pore size distributions (Ishikiriya and Todoki, 1995) for pore radii up to 1000nm before the melting depression joins the bulk melting point. Work carried out by Charmas and Skubiszewska-Zięba (2017), on silicas found good agreement between DSC and nitrogen gas adsorption results.

Data obtained from DSC analysis is mathematically handled to produce pore size distribution results by the following equation;

$$R_p(nm) = 0.68 - \left(\frac{k_{GT}}{T_m - T_{m0}} \right) \quad (6.1)$$

Where T_m and T_{m0} are the melting temperature of ice confined in pores and outside of pores respectively and k_{GT} is the Gibbs-Thomson constant for the analysis liquid.

By combining DSC analysis with mercury intrusion porosimetry it is possible to “de-shield” pores which have mercury trapped within them (Rigby, 2018). Mercury intrusion porosimetry is only able to measure the pore throat, and not the pore body; by combining this with DSC it is possible to “de-

shield” the pore body of these pores and combine the two methods to more fully determine the pore size distribution of the sample.

2.5.5. RockEval Pyrolysis

RockEval pyrolysis is used to characterise the organic matter within sample (Sonibare *et al.*, 2005), specifically the quantity, quality, type and thermal maturity. These organic characteristics provide significant information on the potential generation process and to identify which maturity stage the organic matter has achieved (Wood and Hazra, 2017). RockEval pyrolysis thermally decomposes the organic matter (Behar *et al.*, 2001; Sonibare *et al.*, 2005; Franco *et al.*, 2010) in the absence of oxygen, and can be with or without the presence of liquids. Samples are heated to 850°C (Lafargue *et al.*, 1998; Behar *et al.*, 2001) to fully decompose the organic content in the samples, this takes place in the temperature range 300-570°C (Sonibare *et al.*, 2005); sometimes terrestrial organic matter does not fully decompose until 600°C (Lafargue *et al.*, 1998).

Three main measurements are taken (S1, S2 and S3) which are used to characterise the organic matter type. S1 represents hydrocarbons already present and are stripped at temperatures around 300°C, S2 represents hydrocarbons generated by thermal decomposition and takes place between 300-550°C, S3 represents the CO₂ generated during the thermal decomposition (Lafargue *et al.*, 1998; Behar *et al.*, 2001; Sonibare *et al.*, 2005). The temperature at the maximum peak (S2) gives T_{max} (T_{max} helps to determine sample maturity) for the sample. The TOC% is determined by oxidation of the residual organic carbon after pyrolysis under air in a second oven and is known as the S4 peak (Lafargue *et al.*, 1998).

The peaks are formed by a flame ionisation detector (FID) analysing the hydrocarbons as they are released during the heating process (Behar *et al.*, 2001; Franco *et al.*, 2010). The main elements to be detected are hydrogen, oxygen and carbon – it is the ratio of these respective elements that help to determine the organic matter type (Wood, 2017). Type I organic matter has a very high liquid generating potential and are identified by having a higher initial H/C atomic ratio and lower O/C ratio. Type II organic matter has slightly less liquid generating potential and are seen to be moving towards the gas window, they are identified by having relatively equal ratios of H/C and O/C. Type III organic matter has gas generation potential and are identified by a lower initial H/C ratio and a higher O/C ratio (Wood, 2017).

Additionally, markers in organic matter (chemical and isotopic) are used to identify where the original source rock may have been and to better understand the migration path (Wood, 2017). As well as this samples are now often analysed under reflected white fluorescent light to determine the relative quantities of maceral groups (i.e. liptinite, vitrinite and inertinite) (Dang, 2017). This method allows for visual assessment of the organic matter type, and the vitrinite reflectance ($R_0\%$) measure enables modelling for thermal and burial history reconstructions. Vitrinite reflectance values 0.5-1% indicate the oil window, 0.8-2% the wet gas window and 1-4% the dry gas window (Wood, 2017).

2.5.6. Scanning Electron Microscopy (SEM) with Mineral Liberation Analysis (MLA)

Scanning electron microscopy mineral liberation analysis (SEM-MLA) is a scanning electron microscopy technique with additional software able to take x-ray spectra from multiple energy dispersive x-ray (EDX) points. These EDX points are associated with a specific dispersive x-ray spectra and can be matched with an inventory of known mineral spectra. This identification allows the modal mineralogy (area % of the sample) to be calculated by the computer software (Sylvester, 2012). Scanning electron microscopy (SEM) allows areas of approximately 1 cm to 5 microns to be viewed, and see features at a detail of 50 to 100 nm (Swapp, 2017). Shale mineralogy is an integral control on these properties and can be determined by XRD and MLA-SEM. Mineralogy plays a vital role on the overall characterisation of shales since different minerals have different properties and

their quantities within the shale will determine surface area, volume and network. The use of XRD and MLA-SEM characterises the mineralogy of the sample, and with the use of MLA-SEM a modal mineralogy is produced, and a mineral map so it is possible to see how minerals are distributed throughout the sample.

2.5.7. Thermogravimetric Analysis (TGA)

Thermal gravimetric analysis was carried out using a TGA Q500, it is a compositional technique which puts the sample under high temperatures initially using nitrogen to 920°C. Under this temperature there is an initial mass loss from moisture and the volatiles. At the peak temperature, the gas is changed from nitrogen to oxygen and the mass loss measured at this point is due to fixed carbon (Gabbott, 2008). Thermal gravimetric analysis looks at the composition of a sample. It is a method of thermal analysis which measures the change in physical and chemical properties of the material as a function of weight with increasing temperature. For the shale composition characterisation, it enables us to measure the amount of water lost in the shale, the volatiles, fixed carbon and ash (Gabbott, 2008).

2.5.8. X-Ray Diffraction (XRD)

X-ray diffraction (XRD) is a tool to identify the crystallography and mineralogy of a sample by producing a unique diffractogram which can be matched against known records in the Inorganic Crystal Structure Database (ICSD) (Stanjek, 2004). XRD uses an x-ray beam aimed at the sample over a range of angles. The receiver/sensor then detects the intensity given from the sample at the respective angle. This produces a diffraction pattern which is then used to identify the minerals and elements present in the sample. In relation to pore size characterisation it is necessary to understand the mineralogy of the sample since it could influence the affinity that the gas used in gas adsorption has on the sample surface (Stanjek, 2004). TGA and XRD are complementary techniques to the different techniques mentioned previously. In relation to shales they are significant in work similar to (Chalmers and Bustin, 2015; Li *et al.*, 2016; Zhong *et al.*, 2016), where the affinity of different adsorbates to the pore surface is considered.

Bragg's law is used to resolve the detected x-rays and is defined below;

$$n\lambda = 2d \sin \theta \quad (7.1)$$

Where n is a positive integer, λ is the wavelength of the incident wave, d the interplanar distance and θ the scattering angle. When x-rays of a known wavelength are projected at the sample at an angle, θ , diffraction takes place when the x-rays which are reflected from different crystal planes differ by an integer, n , of wavelength, λ . During an XRD experiment the angle that the x-rays are projected at the sample are varied such that Bragg's law is satisfied by different d -spacings.

2.5.9. Small Angle X-Ray Scattering (SAXS)

Small angle x-ray scattering (SAXS) utilises the scattering effect of x-rays as a result of electrons in an irradiated material (Rigby and Edler, 2002). Throughout a sample the distribution of electrons is heterogeneous, resulting in variations in electron density which when spaced similar to the x-ray wavelength of the incident beam, λ , produces scattering at angles greater than 10°. This is the minimum angle used for conventional x-ray scattering analysis, however when these heterogeneities extend over ranges between 0.5-400nm then the scattered x-rays are detected at small angles – it is for these samples that the SAXS technique must be utilised (Rigby and Edler, 2002). SAXS provides information on much larger internal structures than normal inter-atomic distances, as well as probing the properties of closed pore space such as shape and size.

2.5.10. Nuclear Magnetic Resonance (NMR)

Nuclear magnetic resonance (NMR) spectroscopy uses the magnetic properties of a given atomic nuclei, which are influenced by the physical and/or chemical properties in which the molecule is contained. Nuclear magnetic resonance (NMR) can characterise an entire structure using only one analytical technique. Recently NMR is being increasingly used in inorganic chemistry and biochemistry, as well as other disciplines – where it is able to provide structural information about the sample (Levitt, 2002).

NMR exploits the natural property of an atoms nucleus by manipulating the spin to produce a detectable resonance. The most exploitable nuclear spin is a spin $\frac{1}{2}$, the spin of a proton (^1H), when spin $\frac{1}{2}$ nuclei are placed within a magnetic field they align to the field (low energy) or to oppose the field (high energy) (Levitt, 2002). When the electromagnetic field is applied across the sample nuclei aligned to the field absorb energy and move to a higher energy state, nuclei opposed to the field release energy and return to a lower energy state. This process occurs in two steps by first aligning the nuclei, and by then perturbing this alignment by altering the magnetic field (Levitt, 2002). This returns the sample nuclei to their initial state in a process known as “relaxation” which produces two measureable values T_1 and T_2 . The energy difference between T_1 and T_2 corresponds to the applied external magnetic field.

Deuterium can be used in NMR when a samples pore network is saturated with it, the dominant relaxation process occurs because of the interactions between the spins of the solid surface and the molecules intruding the pore space. By using deuterium the connectivity of pore networks can be probed, where it has been found a high level of diffusivity affects T_2 by diffusive pore coupling (Fleury and Romero-Sarmiento, 2016). This can only be used with pores greater than 800nm, and those smaller than 800nm are grouped in one relaxation time. Resultantly in very small spaces there may not be a strong enough signal since the length scale of NMR interactions is comparable to the potential thickness of pore walls.

Hyperpolarised xenon-129 can diffuse within a sample and enable the study of microscopic porous systems. The chemical shift in xenon-129 is studied and used to selectively image gas within pores (Pavlovskaya *et al.*, 2015). By imaging xenon-129 in MRI it is possible to alter the frequency/energy of the xenon-129 being imaged by the specific pore size in which it resides. The nature of xenon-129 is “floppy” meaning it can be relaxed and depolarised easily, this should promote a difference in the Knudsen regime which should be larger than the molecular diffusivity. This difference is determined by the pore space in which the xenon resides, from this it is then possible to identify the pore spaces in the sample (Pavlovskaya *et al.*, 2015).

2.6. Numerical Modelling Techniques

2.6.1. Fractal Dimensions (“self-similarity”)

Natural rock surfaces are often rough on the molecular scale. This roughness is neglected in conventional models of gas sorption, such as the standard BET equation (Rouquerol *et al.*, 2014). Concavities in the surface mean that the space for adsorbing the second and subsequent layers of an adsorption multi-layer declines with distance from the surface, and the maximum molecular capacity of each successive layer decreases. For surfaces that exhibit the particular property of self-similarity over several length-scales, and are, thus, fractals, the decrease in the capacity of each layer of adsorbate is given by the equation (Avnir *et al.*, 1983):

$$\frac{A_i}{A_1} = i^{2-d} \quad (8.1)$$

where A_1 is the area in the first adsorbed layer, A_i is the area in the i th adsorbed layer, and d is the surface fractal dimension ($2 < d < 3$). For values nearer 2 the surface is interpreted as being smoother, and in essence a 2-dimensional object; for values nearer 3 this represents a rough surface which occupies 3-dimensional space. Fractal theory, proposed by Mandelbrot (1982), has allowed easier quantification of complex self-similar geometry which Euclid geometry struggled to characterise. – Fractal theory is additionally unique in its applicability to more than one material (Song *et al.*, 2004). This effect can be incorporated into the standard BET model such that a fractal version thereof is obtained. BET fractal equation has one dimension and is calculated over the pressure range $0.035-0.5 \frac{p}{p_0}$ and is most frequently used for analysis in the multi-layer region (Vajda and Felinger, 2014). It is given by (Mahnke and Mögel, 2003):

$$V_{BET} = V_m \times \frac{Cx}{1 + x(C - 1)} \times (1 - x)^{D-3} \quad (8. 2)$$

where V is the amount adsorbed, V_m is the monolayer capacity, C is the BET constant, and x is the relative pressure. The effect of the fractal roughness, as described by (8. 2) is to lead to a decline in the amount adsorbed in each successive layer of adsorbate. The FHH can also be used for fractal dimensions and gives D_1 and D_2 (Pfeifer *et al.*, 1989; Pfeifer and Liu, 1997); which are indexes of surface roughness and structural irregularity of solid materials, respectively (P. Zhang *et al.*, 2018).

$$V_{FHH} = V_m \times e^C \times \left(\ln \frac{1}{x} \right)^{D-3} \quad (8. 3)$$

D is the fractal dimension and D_1 or D_2 are calculated at the relative pressure range $0.25-0.5 \frac{p}{p_0}$ and $0.5-1.0 \frac{p}{p_0}$ (P. Zhang *et al.*, 2018), respectively. V_{FHH} , the quantity adsorbed at the given relative pressure; V_m , the volume of the monolayer derived from the BET equation and e^C , a constant.

Fractal dimensions are defined between the values of $2 < d < 3$. 2 defines a material that has a low amount of surface roughness and a regular structure (Vajda and Felinger, 2014), 3 defines a material with a high amount of surface roughness and an irregular structure.

Fractal dimensions derived from gas adsorption isotherm results define and quantify the internal surfaces porous media (Watt-Smith *et al.*, 2005), specifically surface roughness and pore network complexity. More recently simulations have identified that the degree of surface roughness strongly influences the rate of mass transfer and diffusion (Watt-Smith *et al.*, 2005), this has consequently driven research in the area to quantitatively characterise these fractal properties (Song *et al.*, 2004; P. Zhang *et al.*, 2018).

The investigation into microporous structures are necessary for the comprehensive characterisation of shale gas reservoirs (P. Zhang *et al.*, 2018). The main direction of this investigation has been into qualitative identification of shale pore types (organic matter pores, intra-particle pores, inter-particle pores and micro-fractures). It has been determined that micro-pore properties are predominantly affected by D_1 and not D_2 because it is known from PSDs that micro-pores seem to be unaffected by grain size variation (Y. Chen *et al.*, 2015), by extension they will not strongly be affected by network complexity. This is also the case for surface area properties which are predominantly affected by the surface roughness factor. This is identified by the positive correlation between D_1 and these properties. Zhang *et al.*, (2018) have deployed fractal geometry theory to analyse the complexity and heterogeneity of porous media where imaging and fluid intrusion techniques cannot do this alone. Another study by Zhang *et al.*, (2018) assessed the impact on particle size with fractal dimensions derived from nitrogen gas adsorption. They found that with

decreasing particle size D_1 increased and D_2 decreased – the physical implications of this are that there are more surface area irregularities but less complexity within the pore network. The physical properties of the samples were altered as follows; specific surface area decreased with decreasing particle size whilst the average pore diameter and total pore volume increased.

2.6.2. Homotattic Patch (BET, nBET and FHH)

Rocks are complex mixtures of different minerals which all have very different material properties, including, and crucially, adsorption capacities. Adsorption capacities describe the capacity a material has, and is able to have, an adsorbate adsorb on it. This is a property which is complex and dependent upon both physical and chemical properties. If a material has a considerably rough surface compared to a material with a smooth surface, the additional space the rough surface occupies in three-dimensional space will provide more surface area for the adsorbate to adsorb upon. However, the actual adsorption critically relies on the chemical property of the material such that they are suitably attractive to the adsorbent, e.g. the same 1cm^2 area of quartz and organic matter would not adsorb the same quantity since the surface chemistry of organic matter makes it much more attractive to the adsorbent in comparison to the inert surface of quartz.

To overcome the complex surface chemical heterogeneity of shale samples the homotattic patch model was introduced (Walker and Zettlemoyer, 1948). This model considers the surface of the adsorbent to consist of a patchwork of different types of site (Figure 13), perhaps corresponding to different mineral grains, each with their own characteristic adsorption behaviour.

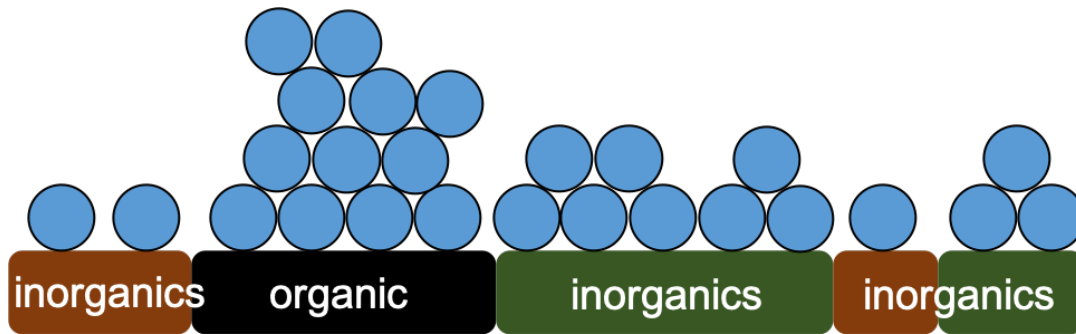


Figure 13: heterogeneous shale surface showing organic and inorganic minerals. Inorganic minerals are represented by two forms but many more would be present in nature.

The model assumes that each of these patches is large, such that edge effects, where they neighbour other patches, are negligible (Watt-Smith *et al.*, 2005). The resulting overall adsorption is thus a composite of the behaviour of the set of patches, such that:

$$V = V_m(p_1I_1 + p_2I_2 + \dots + p_iI_i + \dots) \quad (8.4)$$

where I_i is the isotherm equation describing adsorption on the i th patch, and p_i is the fraction of the surface occupied by patches of type I_i , such that the various p_i -values obey:

$$p_1 + p_2 + \dots + p_i + \dots = 1 \quad (8.5)$$

The homotattic patch is based on the understanding that different materials will have different sorption behaviours based on their surface chemistry (Rigby *et al.*, 2008). Shales have a very heterogeneous surface formed of organic and inorganic minerals. In this work, the homotattic patch theory will be used to separate the contributions to adsorption from each of the organic and inorganic matter phases in the shale. The homotattic patch models used represented adsorption on the inorganic phase using the fractal BET equation, or the BET equation with a finite number of

adsorbed layers (n) in the multilayer, while the organic phase was represented by an empirical fit to an experimental isotherm for a pure kerogen sample.

2.7. Technique Development Thus Far

Much of the experimental work has been guided and developed from work existing in literature, this was done such that experimental results with conventional techniques would be comparable to pre-existing results. Additionally, samples were prepared in-line with the preparation methods of others so that should any physical changes be taking place, they take place similarly to others samples.

Shales are universally prepared for gas adsorption analysis by degassing at a temperature of about 110°C for a time period of 12-14 hours (Chen *et al.*, 2014; Holmes *et al.*, 2017; Zhang *et al.*, 2018). The current standard is established by achieving the following; samples do not lose any additional wet weight and the temperature is not increased such that any morphological changes will occur to the minerals. Investigations with TGA determined that that degassing to 110°C was sufficient to remove pore water, and studies which degassed samples for different periods of time at 110°C showed that for an increased time period no additional changes were introduced to the sample. To remain in line with literature (Chen *et al.*, 2014; Holmes *et al.*, 2017; Zhang *et al.*, 2018) sample preparation was carried out at 110°C for 16 hours (16 hours was selected by default to fit around lab access hours). Degas parameters were maintained for all samples despite any physical changes such as grain size (P. Zhang *et al.*, 2018), thermal maturity and type of adsorbate (Chen *et al.*, 2014), these may affect the degas process since a larger grain size will possess longer pore networks which are likely to have imbibed a greater volume of pore fluid that could be more timely to remove.

Determination of total organic carbon (TOC%) content is a multi-faceted problem, it is widely accepted that a large portion of pores within shale samples are associated to TOC% (Wang *et al.*, 2016; P. Zhang *et al.*, 2018). However, TOC% can be of several types; Types I, II and III (Zhang *et al.*, 2012), and even within these classes can be of variable maturity levels (Zhang *et al.*, 2012; Chen *et al.*, 2014). Organic matter types are designated by the origin of the carbon; Type I organic matter is derived from mainly algal and amorphous origins, Type II are derived from mixed terrestrial and marine source material, and Type III is derived from woody terrestrial material. These different organic matter types have different sorption capacities. Type III has the greatest sorption capacity, while Type II falls in the middle, with Type I having the lowest sorption capacity (Zhang *et al.*, 2012). Implications of this finding are most relevant to the shale-gas storage industry where a Type III organic matter would be able to store the largest volume of CO₂.

The implications of thermal maturity within shales has been crudely summarised as 'more mature equals more pore space'. However Chen *et al.*, (2014) have considered in more detail the link between the thermal decomposition process and the consequent impact on pores within shale. A decrease in meso-pore volume is observed when there has been a transition from immature to early mature TOC% wherein physical compaction and preferential crushing of meso-pores occurs due to the overburden pressure. The meso-pore volume increases moving into the early oil window (where organic matter has just started to crack, beginning around 60°C) where generation of new pores occurs as a result of thermal degradation. Meso-pore volume decreases, as shales approach the late mature stage, due to blocking and filling of pore bodies and throats by bitumen restricting flow. Once higher thermal maturities have been reached the meso-pore volume increases again when hydrocarbons are produced as a result of cracking the bitumen and oil.

Although most work is focussed on the effect of organic matter on the pore network, the inorganic mineralogy of the shale cannot be overlooked since its composition will also influence the pore structure (Wang *et al.*, 2016; P. Zhang *et al.*, 2018). Specific minerals which have been observed to impact the pore volume and surface area are clay, quartz, carbonates and feldspar. Results of

mineralogical investigations have found that micro- and meso-pore volumes increase with clay content (Chen *et al.*, 2014; Wang *et al.*, 2016), decrease with increasing feldspar content and show no clear relationship with quartz and carbonates (Chen *et al.*, 2014). Specific implications of mineralogy and organic matter are to do with the location of the organic matter within the inorganic mineral matrix (Wang *et al.*, 2016; Afsharpoor and Javadpour, 2018). Wang *et al.*, (2016) found that the most commonly developed pores were micro- and meso-pores within organic matter and inter-particle pores between, and/or within, clay minerals. Additionally to this, micro-fractures, which provide gas transport channels within shales, commonly occur at the mineral interface between organic matter and clay minerals.

The internal physical structures of pore systems in shales are also a consequence of depth and burial history, independent of organic matter and mineralogy. When rocks are formed they undergo a burial process which primarily determines the overburden pressure (Smith, 1971). Investigations looking specifically into shale compaction have identified that due to the very low permeability of these rocks the loss of water due to the accumulated overburden, can lag behind what is expected over a coarser grained rock (Smith, 1971). As samples are buried and compacted the porosity decreases to a minimum, determined by the differential vertical stress (overburden) and the pore-water pressure. The vertical stress acts externally on the pore walls whilst the pore-water pressure acts internally to support them (Smith, 1971). Pore-water pressure can become over-pressured in comparison to the surrounding sediments, this has implications for the rock properties are that porosity and inter-connectivity of pores is significantly affected (Katsube and Williamson, 1994). It has been observed that larger porosities and pore sizes exist at shallower depths and the effective porosity then decreases with burial depth where sediments have been under more pressure.

As a result of the above, the decompression of samples when brought to the surface must be considered, one must question whether micro-fractures are an artefact of decompression or a “real” structure which exists at depth (Ougier-Simonin *et al.*, 2016). This question is of great significance since micro-fractures are included in many models and during experiments. Micro-fractures have been shown to be a controlling factor in gas transport through shales and greatly influence the mechanical properties of the shale. Factors which can cause this decompression micro-fracturing are primarily due to gaseous expulsion of pore fluids (Ougier-Simonin *et al.*, 2016).

A lot of work has been carried out investigating the grain size dependence on isotherm results. Work by Chen *et al.*, (2014) and Zhang *et al.*, (2018) have identified that with a decreasing grain size the adsorbed volume increased. Changes were specifically identified where there was enhanced accessibility to meso-pores (L. Chen *et al.*, 2015; Y. Chen *et al.*, 2015) and there was a more variable result with micro-pores. It is supposed that the crushing the shale into smaller fractions results in more positioned nearer the surface of grains increasing the number of accessible pore networks.

By analysing the changes in nitrogen gas adsorption isotherms it is possible to see that hysteresis loops decrease in size with decreasing particle size as a result of the lattice size effect (Seaton, 1991; P. Zhang *et al.*, 2018). Since the shape of the isotherm remains consistent it shows that the grain size variation does not alter pore shape or the resulting adsorption mechanism – additionally supported by pore size distributions which produce the same modality but with a variable quantity (P. Zhang *et al.*, 2018). Comisky *et al.*, (2011) have carried out analysis with mercury intrusion porosimetry to determine what the optimal sample size is for the determination of porosity.

Fractal analysis carried out by Zhang *et al.*, (2018) shows that D_1 increases with decreasing particle size and D_2 decreases with decreasing particle size. Larger particle sizes have more total pore volume as a result of the presence of a greater number of macro-pores, consequently the volume to surface area ratio is greater than for a smaller particle size. This is demonstrated with a larger D_2 and

a smaller D_1 indicating more network complexity and surface roughness, the opposite is true for smaller particle sizes. The correlation between D_1 and surface area suggests that these samples would provide more adsorption sites (Wang *et al.*, 2016) and are likely to have higher adsorption capacities compared to samples with lower D_1 values. Additionally, increasing D_1 values are correlated to increasing TOC% values (Yang *et al.*, 2014; Wang *et al.*, 2015; Ji *et al.*, 2016) which further supports the widely accepted view that surface area and sorption are strongly related to the TOC%. The effect of D_2 on sorption capacity has been seen to be negligible (Wang *et al.*, 2016), and there also appears to be no relationship with clay content (Yang *et al.*, 2014). D_2 however has a strongly negative correlation with the average pore diameter (Ji *et al.*, 2016) i.e. as the average pore diameter decreases the complexity of the pore network increase.

By combining different techniques it enables you to probe different scale levels and characterise pore systems over a wider range of scales (Anovitz and Cole, 2015). Abell *et al.*, (1999) combined mercury intrusion porosimetry (MIP) with scanning electron microscopy (SEM) to image a more complete picture of the pore systems. The SEM was carried out under pressured conditions so that mercury did not extrude before imaging. Rigby *et al.*, (2003) combined nitrogen gas adsorption with MIP and repeated nitrogen gas adsorption in order to calculate the volume of mercury trapped in the sample by calculating the differences in nitrogen gas adsorption results. Watt-Smith *et al.*, (2005) combined gas adsorption, SAXS and MIP in an attempt to deconvolve surface patches of samples.

2.8. Sample Geological History

The shale samples used in this thesis are the Marcellus shale (Preston County, WV), Utica shale (Portage County, OH) and Bowland shale. The geologic history of each sample is included below, but a summary is given here.

The Marcellus is found in Pennsylvania east of West Virginia, and parts of New York, Ohio and Maryland and spans an area of 240,000km² (Popova, 2017). It is Middle Devonian in age with total organic carbon (TOC) content in the range of 1-20% (Popova, 2017) and falls in the dry gas range for thermal maturity (Kargbo *et al.*, 2010). The dominant mineralogy of the Marcellus can be described as carbonaceous silty, black shale that encloses scattered pyrite, carbonate concretions, and contains scarce fossils.

The Utica shale underlies the Marcellus shale spanning 440,300km² across New York, Pennsylvania, Ohio and West Virginia; as well as this it extends under adjacent parts of Ontario and Quebec in Canada and Kentucky, Maryland, Tennessee and Virginia. Underlying the Marcellus the Utica is older in age and dated to be Upper Ordovician in age, despite this it is a slightly less mature reservoir falling in the lower middle part of oil window into the dry gas window. Where the reservoir underlies the Marcellus it is part of the dry gas window, but in other areas (not underlying the Marcellus) the Utica has not reached burial depths sufficient for thermal maturation into the dry gas window. The average organic content for the Utica is approximately 3.5% (Patchen and Carter, 2015) and the mineralogy has been summarised as being calcite rich which lower percentages of clay, quartz and feldspar than the surrounding rock.

The Bowland shale, often referred to as the Bowland-Hodder shale runs across the central part of the UK (Kaufman, 1993; Andrews, 2013). It was deposited in a series of tectonically active basins (Kaufman, 1993; Andrews, 2013) during the Carboniferous period (Andrews, 2013). The formation can be broken into four section called the Upper Bowland-Hodder Shale Gas Unit, Upper Bowland-Hodder Shale Oil Unit, Lower Bowland-Hodder Shale Gas Unit and the Lower Bowland-Hodder Shale Oil Unit (in order of increasing depth) (Kaufman, 1993). Individual units are not laterally continuous across the entire central UK, but are cumulatively continuous. Upper shale units are 900m thick and are comprised of Type II organic matter, lower shale units are up to 3000m thick and are comprised

of Type II and Type III organic matter (Kaufman, 1993). The overall organic content for the Bowland-Hodder shale is in the range of 1-3%, however in places can reach as much as 8% (Andrews, 2013). The formation is comprised of the Bowland Shale and Hodder Mudstone (Kaufman, 1993), and then transitions laterally into shallow-water shelf limestones and deltaic sandstones (Andrews, 2013).

2.8.1. Marcellus

The Marcellus is part of the Appalachian Basin (Popova, 2017) and belongs to a group of black, organic-rich shales that are deposited in the foreland basin roughly parallel to the structural front of the Appalachian Mountains. Stratigraphically the Marcellus shale represents the lowest unit of the Hamilton Group in the Devonian age and is divided into sub-units which are dominated by black shale but also contain lighter shales and are interbedded with limestone – the lithological heterogeneity within the Marcellus is as a result of depositional and diagenetic processes (Ver Straeten *et al.*, 1994; Popova, 2017). The Middle Devonian Marcellus formation was deposited in a thickening wedge of shallow marine claystone and limestone (exposed as a result of NE-trending faults) (Harper, 1999).

By paleogeographic reconstruction it is believed that the organic-rich deposition of the Marcellus occurred in a large, nearly enclosed embayment. The implications of this geometry restricted marine circulation within the basin (Ver Straeten *et al.*, 1994; Popova, 2017) which leads to a more anoxic environment facilitating better organic matter preservation (Laughrey, Billman and Canich, 2004; Engelder and Lash, 2008).

The thermal maturity of the Marcellus increases in the SE direction, and the formation overall falls within the dry gas window (Kargbo, Wilhelm and Campbell, 2010; Popova, 2017). Within the Marcellus formation the natural gas occurs in three different ways. Within the pore spaces of the shale, the vertical fractures of the shale formed by different stress and strain regimes over time, and by adsorption on mineral grains and organic matter. Most of the recoverable gas is contained within the pore spaces of the shale (Milliken *et al.*, 2013).

2.8.2. Utica

The Utica and Point Pleasant Formations are a major shale gas play in the Appalachian Basin (Brinkley, 2016). The Utica Formation consists of dark grey to brown calcareous shale often laminated and bioturbated, with an organic content of approximately 3.5% (Smith, 2013). The samples from the Utica shale are calcite rich which lower percentages of clay, quartz and feldspar than the surrounding rock. Below the Utica Shale to the lower part there is a general upwards decreasing calcite content and an increasing clay content, this is then inverted for the middle portion of the unit (Wickstrom, 2013; Patchen and Carter, 2015). Then once again inverted (to the initial trend) for the upper part of unit into the overlying units (Lavoie *et al.*, 2014).

This transition from carbonates into clay rich sediments occurs alongside a cyclic series of authigenic and bioclastic calcite grains identified as being part of a storm-dominated area. At this transition point the storm-dominated region is identified to be part of an epicontinental sea where there is little sediment input (clay) which results in the sediment forming processes being authigenic carbonate cements (Patchen and Carter, 2015).

The Utica shale is a black, calcereous, organic-rich shale. Similarly, to most shale reservoir formations the organic content of the unit is highly variable both laterally and vertically as a result of its diachronous nature (Wickstrom, 2013; Chen *et al.*, 2014). It is believed that several factors could have contributed to this variability; where the region is believed to have been subject to seasonal anoxia as a result of algal blooms (Patchen and Carter, 2015) and as a result of the deepening

foreland basin causing the area to be overwhelmed and the carbonate environments drowned (Wickstrom, 2013).

Although the transformation ratio of kerogen has been calculated to indicate the thermal maturity (oil window into the dry gas window) of the area, it cannot be relied upon since the T_{max} derived from rock pyrolysis contains little information on the maturity level (Chen *et al.*, 2014). Vitrinite reflectance is the measure commonly used to indicate thermal maturity however the Utica is made up of Type III organic matter which pre-date vitrinite.

2.8.3. Bowland

The Bowland Shale was deposited during the Carboniferous (Visean to Bashkirian) time period, and makes up a part of the Craven Group, it overlies the Pendleside Formation and is overlain by the Millstone Grit. Data on the Bowland Shale is known from a combination of outcrop data and subsurface borehole data across the north of England, Isle of Man, parts of North Wales and the Midlands.

During the Asbian period of the Carboniferous palaeomagnetic evidence suggests Britain was located at near-equatorial latitudes (Słowakiewicz *et al.*, 2015). At this time there was likely to have been glacial eustasy with fluctuating sea levels (Gross *et al.*, 2015) likely to have had a significant impact on sediment deposition. Deposition of shales and marine shales occurred from hemipelagic flows (Hough *et al.*, 2014; Gross *et al.*, 2015) moving laterally into basins and moving across the platform carbonates of the East Midlands and Derbyshire high. These platforms and basins were formed by a period of north-south regional extension in the early Carboniferous providing the beginnings of the shelf-type structural geology of the region. The area continued to be tectonically active over the period (Visean to Namurian) in which these shales were deposited, towards the late Carboniferous there was the start of a compressive regime which will have provided the necessary depth needed for the transformation of organic matter (Słowakiewicz *et al.*, 2015).

Despite the tectonically active basins shales are laterally continuous across the basins and platforms, as opposed to enclosed within basins and lacking on the platforms. The result however is shale deposits in the basins are significantly thicker and richer in organic material because of the presence of a stratified water column, and also means these marine shales have a higher total organic carbon content than the non-marine shales. The total organic carbon content ranges from 0.37-2.45%, and is predominantly made up of Type III organic matter (humic), with some input from Type II organic matter (planktonic) (Słowakiewicz *et al.*, 2015). This organic matter make-up is likely due to the transport of terrestrial material in a hemipelagic flow into the basins and across the carbonate platforms, where planktonic organic matter is seen this is as a result of organic matter in the water column of the basinal deposits. In other areas of the Craven Group the Bowland Shale only contains Type III and Type IV (inert/residual organic matter which will not produce hydrocarbons) organic matter with no evidence of Type II organic matter which have been observed in other areas of the Bowland (Hough *et al.*, 2014). It is likely that of the samples analysed there were none which represented a period where a stratified water column was able to develop as a result of the detrital carbonate supply being cut-off. Since this has not been cut-off it can be assumed that in samples with no evidence of Type II organic matter they are taken from one of the carbonate platform where the overlying mudrocks are thinner and less rich in organic matter (Hough *et al.*, 2014).

Due to the sea level fluctuations the sedimentary successions have developed in a cyclical fashion with non-marine and marine shales. Marine shales make up the minor bands in the sequence and are associated with maximum flooding surfaces and the maximum rate of sea level rise (Hough *et al.*, 2014; Gross *et al.*, 2015). The sea level fluctuations have been attributed to repeated glaciation and melting in the southern hemisphere (Hough *et al.*, 2014).

As a result the Bowland Shale is comprised of a series of non-marine and marine shales occurring cyclically throughout deposition. There is significant interest in this cyclicity and the consequential variations in total organic carbon throughout the cycle because of where certain areas may be of a greater or lesser prospect for oil or gas production. Research suggests that the Bowland Shale may have not reached the required depths and temperatures to move from the oil to the gas window (Hough *et al.*, 2014).

3. Aims and Objectives

The principal aim of this thesis is to develop a set of novel characterisation techniques which are able to measure a greater range of pore sizes than is possible with current techniques where only a few orders of magnitude can be measured by one technique. There are several reasons why this is both inefficient and problematic for research and industry. Firstly, the need to utilise several techniques for one sample characterisation is costly in terms of time and money – secondly, each experimental technique is susceptible to their own physical limits and contain a series of independent artefacts which require post analysis corrections. As a result each set of data needs independent analysis and therefore it cannot be guaranteed that the corrections made will produce a synchronous description of the pores and pore system within a sample. An example is the combined use of gas adsorption and mercury intrusion porosimetry which are often used to measure the smaller pores and then larger pores, however the pore property measured by each method is different (gas adsorption measures the pore body and mercury intrusion porosimetry measures the pore throat) and so the combination of these results does not result in a synchronous set of data. The ultimate aim is to therefore achieve pore characterisation more simply (with fewer individual experiments) over a wider range of pore sizes which produce a synchronous set of data, or to reveal additional characteristics previously missed by standard techniques.

This principal aim can be subdivided into three separate aims each with their own set of objectives needed to achieve these aims. The following lists and explains each aim in more detail and expands on the individual objectives required to meet these aims and why they are necessary.

3.1. First Aim

The first aim of the project is to characterise the samples with a set of basic characterisation techniques in-line with current literature and industry standards to understand the samples at the currently accepted and industrially used level of detail. It is essential to do this at the outset so that any results derived by novel techniques can be compared to results from standard techniques. Without this initial basic characteristic it is not possible to confidently conclude whether the novel techniques were successful or not in measuring a wider pore range or revealing any other characteristic properties not seen by standard characteristic methods. The initial basic characterisation carried out are detailed below explaining their significance and the specific pore characteristic they are used to measure.

The main physical characteristics that need to be measured to characterise pore systems are the pore size distribution, pore surface area, pore volume and the network connectivity. Additionally it is important to consider the degree of complexity, or the pore hierarchy in the pore system since this will strongly control the ability of fluids to flow through the reservoir. Gas adsorption and mercury porosimetry are fluid intrusion techniques which are the most common methods used to measure these properties. Since both use fluid intrusion they are only capable of measuring the open pore space within a sample, resulting in a large portion of the pore volume in the sample unmeasured as it is closed and inaccessible to probe fluids. A further technique used to measure this closed pore space is small-angle x-ray scattering (SAXS), however in use with shales there are often issues reducing the signal to noise ratio enough such that results of value can be obtained. The other main physical property to characterise is the ratio of organic to inorganic minerals within the sample – and

more specifically what the component parts of the inorganic fraction are. The techniques utilised to obtain the ratio of organic and inorganic components are thermogravimetric analysis and RockEval which are both pyrolysis techniques that burn off components of the sample at a designated temperature ramping rate. Thermogravimetric analysis measures the weight lost at certain temperatures, whereas RockEval is used specifically for measuring organic matter properties such as the quantity, quality and type of organic matter. To characterise the components of the inorganic fraction x-ray diffraction can be used and the diffractogram peaks matched to those of known minerals, due to the complexity of shales and the number of complex minerals they contain this method can be weak when minerals such as quartz and calcite dominate the vertical scale. An additional method to resolve the inorganic components is scanning electron microscopy equipped with mineral liberation analysis to pick individual mineral grains and match the energy dispersive x-rays to those of known minerals.

3.2. Second Aim

The second aim is to introduce a more rigorous approach to the numerical analysis and modelling carried out in literature. Current practice is most often to use excel, sometimes utilising the solver function. However, the analysis is generally prone to some level of subjective discretion with regards to selecting the pressure range or the key parameters needed. Although often unintentional, when analysing data like this subconscious bias can often lead to data being handled in a way to produce the best results despite not covering enough data points, or by making non-physical assumptions.

The first objective therefore is to develop a method to determine the fractal dimensions of gas adsorption data which reduces the extent to which the researcher makes any decisions pertaining key parameters i.e. pressure ranges. This will be conducted using R. where a series of steps must be completed, e.g. contain at least two-thirds the data points, and produce physically reasonable results. By doing this it allows a critical review between other numerical models and enables an assessment to take place where applications in their former may have fallen short. It is possible to also see if despite the greater objectivity in analysis if the correlation between fractal behaviours and other physical properties remains consistent. By using R. it has been identified as a novel innovation on an existing technique making it more rigorous and less prone to unconscious bias. The second objective is to build on this numerical analysis technique and address a modelling component in R. to produce a homotactic patch that enables the separation of organic and inorganic components in terms of their contribution to the overall sample properties. This information is valuable to further determining the economic value of a reservoir for production or storage since adsorbates will preferentially adsorb on some adsorbent surfaces and not others.

3.3. Third Aim

The last aim of the project is to transition this knowledge into the novel development of experimental techniques which will probe the physical properties of the samples. To measure more orders of magnitude in one technique than was previously possible it is necessary to enhance certain experimental methods, and also combine methods to enhance the resolution of imaged pores by introducing contrast fluids. It has been identified that it is necessary to quantify the network connectivity more precisely than has previously been achieved since this will control the flow of fluids during production and/or storage.

Additionally attempts will be made to assess the impact of formation mineralogy on production techniques using acidic fracking fluids.

The novel techniques attempted, and the use for which they were developed follow below. Mercury intrusion porosimetry is only capable of measuring the pore throat of a pore and so additional experiments need to be carried out after this to “de-shield” the pore bodies. The nature of mercury intrusion porosimetry is such that if the pore throat is significantly smaller than the pore body mercury will be trapped in the body after completion of the experiment. At this point differential scanning calorimetry and computed x-ray tomography can be utilised to measure and visualise (respectively) the pore bodies containing trapped mercury. The limiting factor for nitrogen gas adsorption is that it does not condense in larger pore bodies so systematically underestimates the pore size distribution where there may be some much larger pores. Forcing condensation in this method and analysing the desorption it is possible to reveal larger pore bodies and additional levels of hysteresis. Other techniques developed relate more specifically to industry and assess the production/storage potential of shales; heat of adsorption, rate of adsorption and sample acidisation.

4. Methodology

4.1. Gas Sorption

4.1.1. Sample Preparation

Samples were provided by Virginia Polytechnic University, drilled in conjunction with the United States Department of Energy (USDOE) - samples were sent as two-thirds cores, in 6 inch (average) height sections. More detailed sample information is provided in 2.8. Sample Geological History. The majority of the experimental techniques used required samples in powder form, although some were able to take larger pieces of sample and for these 3-5mm “chips” of sample were used. To prepare powdered and chipped sample from core they were initially broken down using a sledge hammer and chisel to remove smaller pieces. After this samples were pulverised using a Humboldt pulveriser with grinding rings, in order to maintain control over the particle size produced pulverising only occurred for 1-3 seconds at a time to retain enough coarser material. Between each round of pulverising the material was manually sieved in pans of varying size (Table 1) to remove the fine grained powder from the bulk material, included is also the average grain size based on work by EL-Sayed and Mostafa (2014) where histograms show no skewed particle size distribution. This process was repeated until there was only a small amount of coarse material remaining and then the sieves were placed in the mechanical sieve shaker to separate out each particle fraction.

| Sieve Size (μm) | Average Grain Size (μm) |
|------------------------------|--------------------------------------|
| <75 | - |
| 75-106 | 90.5 |
| 106-150 | 128 |
| 150-212 | 181 |
| 212-425 | 318.5 |
| 425-600 | 205 |
| >600 | - |

Table 1: lists the grain sizes that samples were sieved to in the sample preparation procedure, and the average grain size for used for each grain size in some of the experimental analysis.

Before gas adsorption experiments were conducted samples were degassed using a Micromeritics VacPrep at 110°C for 16 hours to remove any pore water or other gases trapped within the pores. These degas parameters were guided by literature (Chen *et al.*, 2014; Holmes *et al.*, 2017; Zhang *et al.*, 2018) and preliminary investigations into the nature of the samples where it was noted that above 110°C some significant changes may occur to the sample; such as morphological changes in the clay mineral, degradation of more volatile minerals which are broken down at higher temperatures and the over-drying of the sample such that it becomes more brittle than it would naturally be. However, the degas temperature still needed to exceed 100°C to remove water from the samples. Additionally the time under vacuum and temperature was evaluated in order to maximise the degassing process whilst not changing the structure of the sample. Using a degasser in-situ it was possible to identify that after 4 hours the weight of the samples had stabilised, but to remain in line with literature (Chen *et al.*, 2014; Holmes *et al.*, 2017; Zhang *et al.*, 2018), and make results comparable to those reported by others in literature, then a thermal pre-treatment time of 16 hours was selected. During the investigation of sample degas preparation it was seen that between the period from 4-16 hours there was no additional change in sample mass, however 16 hours was used for consistency.

4.1.2. Micromeritics 3Flex

Nitrogen (N_2) and carbon dioxide (CO_2) gas sorption was carried out using a Micromeritics 3Flex (volumetric gas adsorption) to determine the surface area, pore space and pore size distribution for large micro-pores (<2nm), meso-pores (2-50nm) and small macro-pores (>50nm). Nitrogen gas

adsorption was carried out over the relative pressure range of $0-0.995 \frac{p}{p_0}$ at 77 K, and carbon dioxide was carried out over the relative pressure range $0-0.035 \frac{p}{p_0}$ at 273.15K. Since carbon dioxide sorption was carried out at a lower relative pressure range, this enables a more detailed probing of the micro-pore region of the sample.

For the adsorption branch of the isotherm, dosing of the adsorbate occurs in prescribed pressure increments up to $0.995 \frac{p}{p_0}$ with a defined tolerance for each step i.e. 3% above or below the prescribed pressure point. The quantity adsorbed for this step is recorded as cm^3/g and makes up the y-axis of the isotherm plot. The desorption branch of the isotherm is measured in a similar way with prescribed pressure steps moving back towards $0 \frac{p}{p_0}$ with a defined tolerance – commonly the pressure tolerance in the desorption pressure steps is broader than in the adsorption steps. The combination of the adsorption and desorption branches make up the sorption isotherm for the material which is then used for several analysis techniques e.g. Langmuir, BET, BJH, DFT and additional mathematical analysis such as fractal dimensions and FHH.

The experimental procedure for gas adsorption on the Micromeritics 3Flex is as follows;

- The experimental setup for the sample (Figure 14) comprises a sample cell with a bulb at the end (to contain the sample) and a narrower neck, the neck of the sample tube is closed off with a filler rod, a sample tube cap, ferrule and nut which contains an O-ring to ensure a tight closure



Figure 14: schematic of the sample tube setup for Micromeritics 3Flex gas sorption. A, the sample tube. B, the filler rod. C, the ferrule and nut. D, the isotherm jacket used for N_2 analysis.

- The empty cell is weighed (to 4 decimal places), and then re-weighed (to 4 decimal places) with the fresh sample i.e. wet sample. Where enough material was available the target weight was approximately 2g to ensure that the minimum BET surface area was met for analysis; this is 20m^2 total area i.e. 0.1g of sample is required if the sample area is around $200\text{m}^2/\text{g}$.
- The sample is then degassed in a Micromeritics VacPrep under vacuum for 16 hours at 110°C in order to remove the moisture in the sample. The length of time is determined based on previous experiments with similar samples under gravimetric experiments where after 16 hours at 110°C the mass of the sample remained constant
- Once the 16 hour treatment period has been completed the sample is cooled to room temperature and brought back to atmospheric pressure by backfilling with helium

- The sample and cell are re-weighed (to 4 decimal places) to establish the dry weight of the sample
- Samples are then loaded into the Micromeritics 3Flex ports for analysis

If N₂ is being used as the analysis gas the experiment is carried out at 77K with the sample cells being lowered into a dewar filled with liquid nitrogen. In order to keep the temperature constant throughout the cell, an isothermal jacket is fitted around the neck of the sample cell. A thermocouple is used to monitor the temperature of the sample tube as liquid nitrogen will evaporate over the course of an experiment. If CO₂ is being used as the analysis gas, the experiment was carried out at 273.15K and the isothermal jackets and thermocouple are not required. A sub-ambient, thermoelectric cooled dewar is used to maintain the temperature.

The Micromeritics 3Flex was the principle machine used for the majority of the experimental gas adsorption analysis. With this piece of equipment I investigated the relationship between sample depth and physical properties, how these properties are affected by changing grain size and also to establish the heat of adsorption for some samples.

4.1.3. XEMIS

The Hiden Isochema XEMIS is a gravimetric sorption analyser which is designed for use with a range of gases up to vapour pressures of 200 bar (our XEMIS is limited to 60 bar as the transducers are not installed to reach 200 bar), the high level of accuracy and microbalance technology enables high resolution measurements for exceptionally small quantities of material. For shales, this allows highly accurate measurements across a larger range of pore sizes with carbon dioxide since this equipment is able to reach (closer to) saturation pressure than the 3Flex, and also investigate the sorption kinetics and produce equilibrium isotherms.

The XEMIS consists of a microbalance which has the counterweight and sample suspended from it within twin thermostats so that they are separate units i.e. the sorption of the sample is not impacted by anything that happens to the counterweight. As both the counterweight and sample are suspended from the microbalance by fine metal wires there is an element of buoyancy which needs to be accounted for by the symmetric geometry and design of the microbalance. The microbalance has been designed to minimise buoyancy effects and, thereby, maximise sensitivity; however, despite this, corrections must still be made in cases where uptake quantity is small such that buoyancy is not negligible.

Samples do not undergo any pre-preparation as samples are degassed in-situ allowing for less sample handling throughout the experimental procedure compared to 3Flex. Samples are weighed in a small quartz crucible with a small loop on top, allowing the sample to be suspended on the microbalance, and an opening to the side just below the centre. This opening position allows the top of the sample to be covered such that the carbon dioxide dosing cannot directly reach the sample and potentially displace it from the crucible; as a result sample integrity (in terms of not being blown away when gas is dosed, or sucked into the rig when brought under vacuum) can be ensured throughout the experimental process.

To perform a sample degas, a furnace is attached externally to the twin thermostats and held by arms which rotate out beneath the twin thermostats to hold the external heating systems. The degas procedure and equipment status are all controlled from the Isochema HIsorp software to the specific requirements of the experiment. In order to maintain consistency all samples were degassed at 110°C for 16 hours under vacuum. The benefits of this in-situ degas on a gravimetric sorption analyser are that the weight lost by the sample can be monitored in real time, and thus, if a sample

weight had not stabilised after 16 hours, then the degas procedure could be extended until this point had been reached.

After the sample weight has stabilised, the analysis procedure can be written into the software. Depending on the analysis temperature, it may be necessary to change from the furnace to the water bath for the analysis, all experiments were carried out at 20°C. This temperature was selected as the analysis temperature, as it enabled the full pressure range of XEMIS to be utilised, whilst also maximising the relative pressure range ($\frac{p}{p_0}$) possible for carbon dioxide (saturation pressure at 20°C is 57.29 bar) in order to achieve close to $0.995 \frac{p}{p_0}$.

For the experimental procedure for XEMIS, a pressure step and ramping rate is selected such that the rate of pressure increase can be accurately controlled. This level of control allows for adjustments to be made if the ramping rate for the pressure is too high, such that it creates buoyancy in the analysis material. Once the target pressure has been achieved, it will maintain this for a designated period of time, or until the sample mass stabilises depending on the experimental conditions. If the pressure does not stabilise over this period of time it is indicative of a leak within the system which means that the pressure level cannot be sustained by XEMIS. If the sample mass is showing oscillatory behaviour outside of reasonable fluctuations ($\pm 0.0010\text{g}$) then it is possible this is a result of a “valve effect” where the apparent bouncing is as a result of the slow valve response (Brandani *et al.*, 2016), if the weight continues to increase and does not plateau then the sample likely has a very slow rate of uptake, or a really high adsorptive capacity, however if the weight increases and then begins to decrease this likely shows a very weak adsorptive capacity and the sample is beginning to desorb during the time given to the pressure step.

4.1.4. Autosorb iQ

Autosorb iQ – Chemisorption (& Physisorption) Gas Sorption Analyser (iQ-C/MP/Kr/MS) from Quantachrome Instruments was coupled to an in-situ mass spectrometry and calorimetry system (Setaram SenSys EVO 3D TG-DSC). The coupling of these two instruments enables the kinetics of each adsorption point to be measured and the heatflow calculated for each dosing. iQ measures adsorption enthalpy by calorimetry at a constant temperature, where the isotherm method uses isotherms measured at different temperatures and involves a large number of assumptions to be made. A crucial use for this is to further distinguish between two samples which may produce very similar isotherms separated by minutiae detail; when kinetics and heatflow are included it is possible to differentiate samples by their rate of uptake i.e. how quickly the sample adsorbs the analysis adsorbate.

The Autosorb iQ is a volumetric sorption analyser like the Micromeritics 3Flex, but the additional kinetics information allows the instrument to provide much more detailed information about the analysis sample. It contains two analysis stations and a P_0 cell (to measure the adsorbate saturation pressure) connected to the manifold, and two additional stations which were used for sample degassing. Sample preparation was therefore carried out the same way as Micromeritics 3Flex where the samples are weighed before and after degassing to establish the dry weight of the sample. After this the sample is loaded into the analysis station using the same set-up described for Micromeritics 3Flex of a ferrule and nut containing an O-ring. This station is connected to the manifold and the experimental procedure is set up in the computer software as with Micromeritics 3Flex and XEMIS.

The Autosorb iQ experimental setup commences with the defining of the dosing quantity across the required pressure range e.g. x amount of points between $0-0.1 \frac{p}{p_0}$ dosing at $3 \text{ cm}^3/\text{g}$. As a consequence, the time of the experiment is not well defined since the transition to the next step is

taken based on a tolerance criterion relating to a plateau/equilibrium being reached at the current dosing step. The sensitivity can be controlled such that the perceived plateau/equilibrium is accepted at a lower or higher tolerance. Difficulties associated with this experimental setup are that for comparison between some samples the same dosing quantity may or may not work if a sample has a particularly high or low uptake.

In the experimental setup used, only one of the analysis stations connected to the manifold is available for analysis as the other is a reference cell. The Setaram SenSys EVO 3D TG-DSC is connected to the Autosorb iQ such that the TG-DSC is able to measure the heatflow at each pressure point. This allows for direct comparison between the kinetics data for each pressure point from Autosorb iQ and the heatflow of each pressure point from Setaram SenSys EVO.

Kinetics data from Autosorb iQ was analysed using the linear driving force proposed by Glueckauf (1955), and used recently in this application by Sircar and Hufton (2000) which uses the equation below to derive the k -value (mass transfer, s^{-1} , or the diffusion coefficient) for each adsorption point.

$$M(t) = M_0(1 - e^{-kt}) \quad (9. 1)$$

Where $M(t)$ is the changing mass of the sample with respect to time, M_0 the mass of the sample where it reaches a plateau and t the time duration for that adsorption point. For the heat flow data the following equation is used to derive τ the thermokinetic parameter in s (Auroux *et al.*, 2009).

$$D(t) = D_m e^{(-\frac{t}{\tau})} \quad (9. 2)$$

Where $D(t)$ is the deviation of the heat flow with time, D_m the maximum deviation and t the time duration for that adsorption point.

Corrections were made to the data based on the adsorption of CO_2 to the surface of the sample tube. An experiment was run using non-porous white quartz under the experimental conditions needed for the experiment, for every new experimental procedure an additional blank run was needed so that adsorption points correlated.

For the isotherm corrections a best-fit polynomial was fit to the blank sample data associated to the sample, and this was used as a baseline to subtract from the sample data as shown in Figure 15. This procedure was carried out again for the desorption branch of the isotherm.

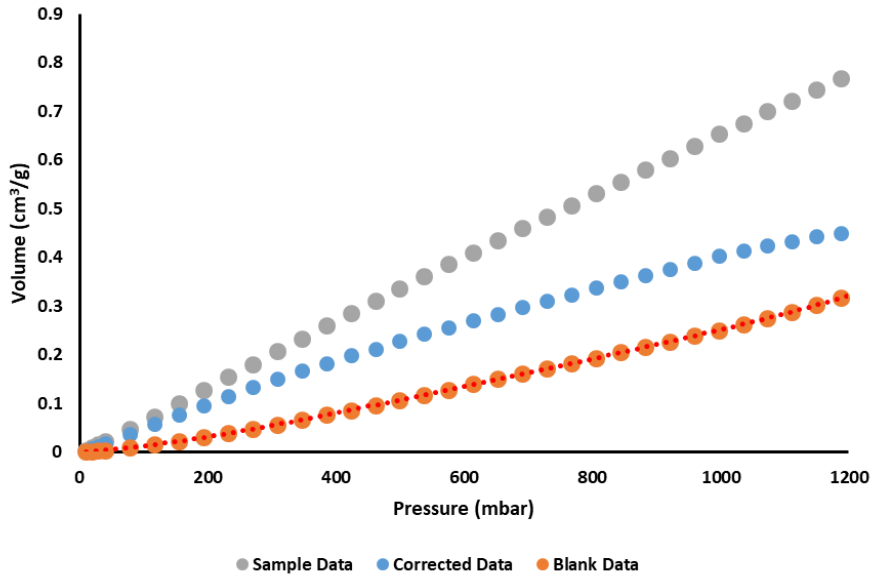


Figure 15: *iQ* isotherm data corrections where a polynomial fitted to the blank data is used to subtract from the sample points for the exact pressure that the points are taken from.

The kinetics data did not require blank corrections due to the short time it takes for the chamber to equilibrate relative to the length of time that data is collected over. The result of this is that any adsorption on the analysis tube surface would not have been measured and included in the analysis. The mass transfer k (Glueckauf, 1955; Sircar and Hufton, 2000), needed correction with Henry's Law to account for the variation in the mass transfer which is as a result of the dissolved gas phase with respect to the partial pressure. Henry's constant (H) is calculated by taking the differential of the trendline for the sorption isotherm to calculate H at each pressure point. Corrections were then made to k by multiplying it by $H + 1$ for the respective pressure point ($+1$ ensures that the value of k is maintained and then fractionally altered by H).

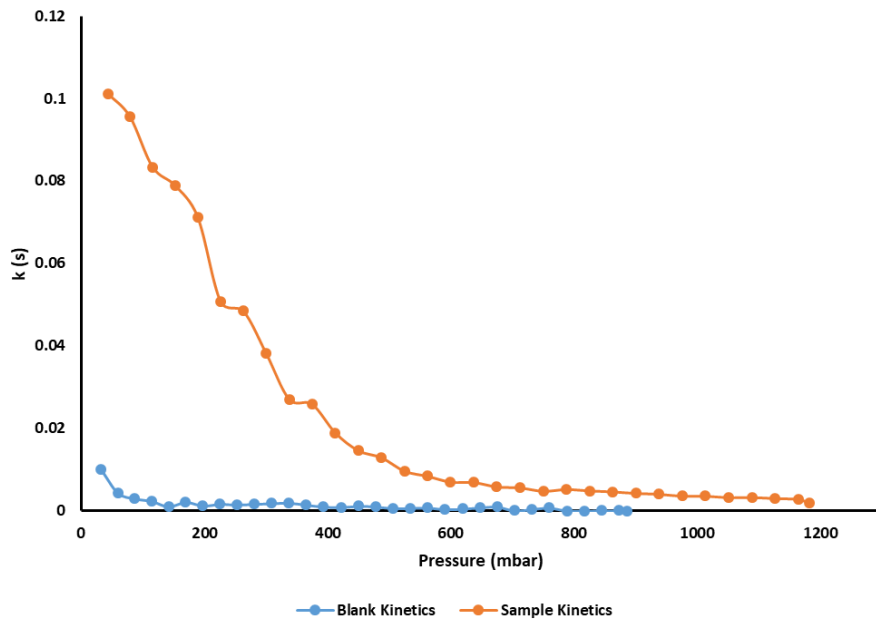


Figure 16: mass transfer kinetics for a blank run, and sample data collected using the same experimental procedure.

4.1.5. Over Condensation

Nitrogen gas adsorption overcondensation was carried out on samples of Marcellus, Utica and Bowland shale to probe the larger pore sizes and any additional levels of hysteresis. Overcondensation experiments were carried out on a Micromeritics ASAP 2020 physisorption analyser using a method similar to that described by Murray *et al.*, (1999). In the overcondensation experiment, the first stage is to increase the pressure in the sample tube to higher than the saturation vapour pressure of nitrogen. This pressure increase should facilitate sufficient condensation such that even the biggest pores are filled with liquid nitrogen at the start of the overcondensation desorption isotherm, which will also involve some bulk condensation in the sample tube. This bulk condensation is what is avoided in the conventional experiment. The required period to reach this stage is dependent upon the sample size and the pore volume. While it does not matter if the volume of condensate is much higher than that needed for complete pore filling, the total duration of the experiment would be much longer in that case. Once complete pore-filling had been achieved, the pressure was lowered to just below the saturated vapour pressure of nitrogen such that the bulk condensate vaporized completely while keeping all the sample internal porosity liquid-filled. Once this stage has been accomplished, the first data point on the overcondensation desorption isotherm can be measured. This point corresponds to the total pore volume of the sample. The pressure is then progressively lowered in small steps, and the rest of the desorption isotherm was obtained in the usual way.

4.2. Mercury Intrusion Porosimetry (MIP)

4.2.1. MIP Sample Preparation

Prior to mercury intrusion porosimetry experiments samples were oven dried overnight at 70-100°C depending on the requirements of the other oven users. Due to the high pressure nature of mercury intrusion porosimetry it was found that any differences in those temperatures were negligible when samples had undergone prior degas for gas adsorption experiments.

4.2.2. Experimental Procedure

After sample preparation the analysis material can be prepared for mercury intrusion porosimetry which is carried out on a Micromeritics AutoPore IV 9500. Mercury intrusion porosimetry consists of low- and high- pressure analysis at ambient temperature and constant volume. The AutoPore IV 9500 consists of two analysis ports for low- and high- pressure, which take the sample from atmospheric pressure to under vacuum and then to 207MPa and 414MPa respectively.

Samples are analysed in penetrometers based on the material type i.e. powder or chips, the penetrometers consist of a thinner stem where mercury enters the analysis system and a bulb which holds the sample (Figure 17). Penetrometer bulbs vary by material type, when chips are used the bulb contains no additional features so long as the chip size is larger than the throat size of the penetrometer stem (Figure 17A); for a powder the penetrometer stem extends into the bulb such that the analysis material cannot enter the stem (Figure 17B). Analysis material must be kept out of the penetrometer stem so that the movement of mercury into the bulb is not impeded, and so during extrusion analysis material is not pulled back into the porosimeter. Once the sample has been put in the penetrometers bulb and weighed it is sealed with high vacuum grease around the rim of the bulb and a cap is affixed with a locking ring so that the system is air tight and can be taken under vacuum.

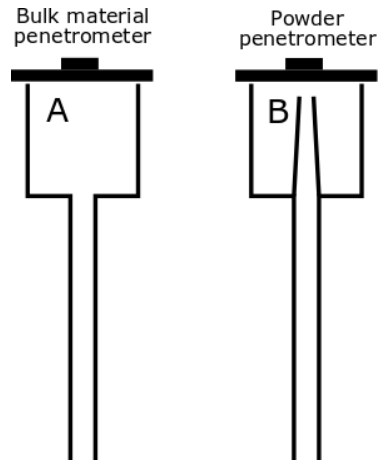


Figure 17: cross section of a penetrometer for mercury intrusion where the bulk material penetrometer (A) has no additional features, and the powder penetrometer (B) has an extended neck to stop material entering the penetrometer stem.

The AutoPore IV 9500 works similarly to 3Flex where a set of pressure targets are prescribed in the experimental setup along with a tolerance for each step. The quantity intruded is calculated based on the difference in volume between what is injected into the system and the space in the bulb this takes up, the difference between these values is the quantity of mercury intruded into the sample, e.g. if 5mL of mercury are pushed into the system but only 4mL occupy the bulb volume then the quantity intruded would be 1mL. When moving from low- to high- pressure analysis the whole system is weighed so that the intrusion curve can continue from the correct intruded quantity.

After intrusion has completed and the maximum pressure is reached and the mercury is extruded when the system is taken back down to atmospheric pressure. Resultantly the extrusion curve does not return under vacuum where the intrusion started so there will always appear to be an incomplete curve, however this is the convention of mercury intrusion porosimetry. Analysis of data takes place in excel with a report file exported from the system software.

4.3. Differential Scanning Calorimetry (DSC)

4.3.1. DSC Sample Preparation

As with other experimental work samples all underwent the crushing and sieving process prior to any other experiment specific preparation. For Hg-DSC chips of sample were used so the analysis material could be easily recovered from the mercury intrusion porosimetry work. To recover analysis material mercury is safely drained from the penetrometer in-line with safety standards and placed in a steel DSC pan (aluminium reacts with mercury) which is sealed with an O-ring to ensure that it is fixed in place. These pans are loaded into the DSC and the experimental procedure setup on the analysis software.

4.3.2. Experimental Procedure

Differential scanning calorimetry was carried out on a TA Instruments DSC2500 and is used here as a thermoporometry technique using an intruded fluid within an analysis material to reveal pore size distributions based on the depression of the fluid melting point (Figure 18), using the relevant form of the Gibbs-Thomson equation;

$$\Delta T_m = \frac{k}{x} \quad (10.1)$$

Here, $\Delta T_m = T_m^\infty - T_m(x)$, the difference in the bulk melting temperature of the intruded fluid and the melting temperature in a pore of diameter x ; k is the Gibbs-Thomson constant and x is the pore diameter. When conducted after mercury intrusion porosimetry DSC has the specific use to un-

shield pore bodies with mercury trapped inside by using the depressed melting point to calculate the corresponding pore size.

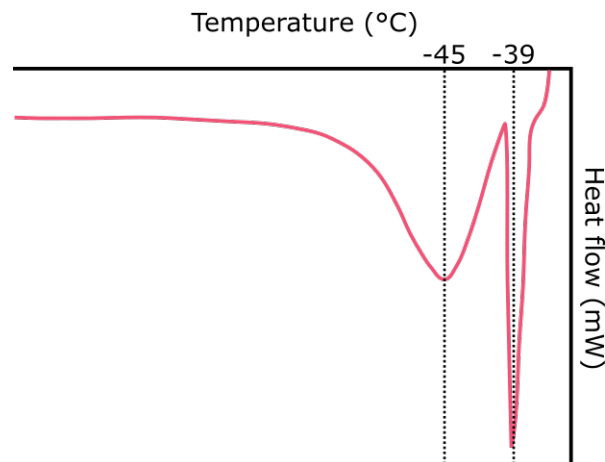


Figure 18 DSC melting curve where the melting point of mercury has been suppressed such that a separate peak exists (-45°C) before the bulk melting peak (-39°C) (edit Rigby, 2018).

The experimental procedure was set up on the TRIOS software associated with the DSC and is included in more detail. The parameters used for study of the mercury intruded samples was to decrease the sample temperature to -80°C and hold it at this temperature for 30 minutes to ensuring freezing of the trapped mercury and supercool the sample. The sample temperature is then increased to -60°C at a rate of 2°C/minute, the sample is held at this temperature for a further 30 minutes before the temperature is increased again to -30°C at a ramping rate of 0.1°C/minute. The melting point of mercury is -38.83°C so beyond this point once the mercury has all melted no more information can be learnt since it will all be in a liquid state.

4.4. Computed X-Ray Tomography (CXT)

4.4.1. Hg-CXT Sample Preparation

As with other experimental work samples all underwent the crushing and sieving process prior to any other experiment specific preparation, for Hg-CXT chips of sample were used so that analysis material could be easily recovered from the mercury intrusion porosimetry work. To recover analysis material mercury is safely drained from the penetrometer in-line with safety standards and material is recovered for DSC analysis. These samples were then safely transferred for CXT analysis where samples were mounted with some blue tack to hold them in place.

4.4.2. Experimental Procedure

CXT was carried out by Martin Corfield (University of Nottingham, Department of Electrical & Electronic Engineering) on an Xradia Versa XRM-500. The Xradia Versa XRM-500 is a high-resolution 3D X-ray CT system capable of submicron resolution. The samples were scanned with source parameters 140 kV and 71 μ A with a resulting pixel size of 6.7997 μ m.

4.5. Scanning Electron Microscopy with Mineral Liberation Analysis (SEM MLA)

4.5.1. SEM MLA Sample Preparation

As with other experimental work samples all underwent the crushing and sieving process prior to any other experiment specific preparation, for SEM MLA chips of sample were used. Samples were embedded in epoxy resin in different orientations, i.e. parallel and perpendicular to the bedding plane. They were placed in a vacuum oven until the air bubbles were removed from the samples and left to set overnight. These were then polished with decreasing coarseness of polishing pads in order to expose the sample and produce a smooth surface in order to obtain the best energy dispersive X-rays. Before analysis occurs, samples are carbon coated in a 10-20nm thick coat of carbon.

4.5.2. Experimental Procedure

SEM MLA was carried out on an FEI Quanta 600 (operated at 20kV, working distance of 13mm and spot size 7) equipped with mineral liberation analysis software which enables the quantification of sample mineralogy by taking several energy dispersive X-ray (EDX) points. These EDX points are associated with a specific dispersive X-ray spectra which can be matched to known (from a mineral database) minerals. There are several identification and quantification techniques can be carried out in order to establish mineral phases within the sample. This identification allowed the modal mineralogy (area % of the sample) to be calculated by the computer software (Sylvester, 2012).

After the acquisition of the backscattered electron (BSE) image several processing steps are taken before producing the mineral map and modal mineralogy for the sample. The processing steps that need to be are de-agglomeration/segmentation of chips, phase segmentation of minerals and mineral identification by x-ray analysis of the EDX points. Particles are de-agglomeration to remove potential bias where grains may be touching and mineral fractions in contact with each other which would not usually be. Phase segmentation is carried out to maximise the contrast in grey-scale between minerals so that phase boundaries defined as clearly as is possible; doing this enables mineral phases to be picked out in different grey-scales, with lighter elements appearing darker and heavier elements appearing brighter. Mineral identification is carried out by matching the EDX points from SEM to a known mineral database; colours are associated to minerals and the process repeated until as many of the minerals are identified. In samples with complex mineralogies, or mixed phase there are often a large number of un-resolved areas – although it is good to reduce this as much as possible one must be pertinent to not over-analyse the image.

4.6. Thermogravimetric Analysis (TGA), X-Ray Diffraction (XRD) and RockEval

4.6.1. Sample Preparation

Prior to thermogravimetric analysis, x-ray diffraction and RockEval experiments no additional preparation was carried out beyond the previously described crushing of the samples. This is because none of the following experimental techniques probe the pore networks of the sample, they instead investigate the mineralogical make-up of the samples by a combination of pyrolysis and x-ray diffraction techniques.

4.6.2. Thermogravimetric Analysis (TGA)

Thermogravimetric analysis (TGA) was carried out on a TA Instruments Q600 SDT to indicate what the basic composition of the analysis material was i.e. volatiles, water, fixed carbon and ash, by measuring the change in physical and chemical properties as function of weight and increasing temperature. This was carried out as an early analysis technique to establish what temperature samples could be safely degassed up to without changing the nature of the sample. Using the computer software associated with the instrument experimental conditions were defined such that the sample was heated through 110°C (moisture) to 920°C (volatiles) using nitrogen – an inert gas. The gas then changes to oxygen as the temperature decreases and the components of fixed carbon and ash (600°C) can be determined. The contributions from the moisture, volatiles, ash, fixed carbon, dry volatiles, dry ash and dry fixed carbon can be calculated with the equations in Appendix 2.

4.6.3. X-Ray Diffraction (XRD)

A Bruker Advance Series 2 X-Ray Diffractometer was used to analyse the mineral composition of the analysis material. An x-ray beam is aimed at the sample over a range of pre-defined angles, θ and the receiver/sensor detects the intensity of the diffracted beam at the respective angle. Diffraction takes place when these x-rays of a known wavelength, λ are diffracted by the crystal lattice spacing

of different minerals. The different crystal lattice spacing between minerals differs by an integer, n . The experimental angles are pre-defined such that Bragg's law is satisfied by different d -spacings.

$$n\lambda = 2d \sin \theta \quad (11. 1)$$

Fourier transforms are used during data analysis to resolve the values and produce a unique diffractogram for the sample. The unique diffractogram produced can be matched against known records with the Inorganic Crystal Structure Database (ICSD), and analysis is carried out in EVA to do this. The XRD results derived from the Bruker Advance Series 2 are qualitative and cannot specify the quantity of each mineral present.

4.6.4. RockEval

RockEval pyrolysis was carried out by Dr. Christopher Vane (British Geological Society, Head of Organic Geochemistry BGS Keyworth). This technique is used to determine the hydrocarbon generation potential of rocks, the type of organic matter and the maturity of this. The experimental procedure is similar to that of thermogravimetric analysis however there is an additional detector which allows for the characterisation of specific carbon types. Samples are heated like in TGA through a pre-defined set temperatures which will determine the amount of hydrocarbons (S1 and S2 peaks) and the CO₂ content (S3 peak), the temperature reached when the S2 peak occurs is known as T_{max} the maximum temperature the sample reached.

A standard experimental procedure would heat the sample in nitrogen using flame ionisation detection to detect and quantify the hydrocarbonaceous products. During this process the S1 peak is determined by heating up to 300°C, which corresponds to free hydrocarbons (gas and oil); the S2 peak is determined by continued heating and will be present between 300-650°C and represents the hydrocarbons generated by organic matter cracking. The temperature at which this occurs i.e. maximum hydrocarbon quantity resulting from organic matter cracking, is known as T_{max} and will be different across samples. The S3 peak is derived during the cooling period after the S2 peak has been established and corresponds to the quantity of carbon dioxide within the sample. After pyrolysis in nitrogen has completed the residual organic and inorganic carbon content is pyrolysed by combustion in air from 300-850°C. By establishing this parameters, the total organic carbon content (TOC %) can be calculated as the sum of the pyrolysed organic content and residual organic content. The hydrogen index corresponds to the quantity of pyrolysable organic compounds (S2 peak) relative to the total organic carbon; the oxygen index corresponds to the quantity of CO₂ (S3 peak) relative to the total organic carbon.

4.7. Numerical Modelling

Prior to in-depth numerical modelling the different models available were evaluated to assess their fit to shale sorption data and refine the pressure range over which the model holds.

The fractal BET (Wang *et al.*, 2015) (8. 2) was fitted to the Marcellus shale and can be seen below in Figure 19.

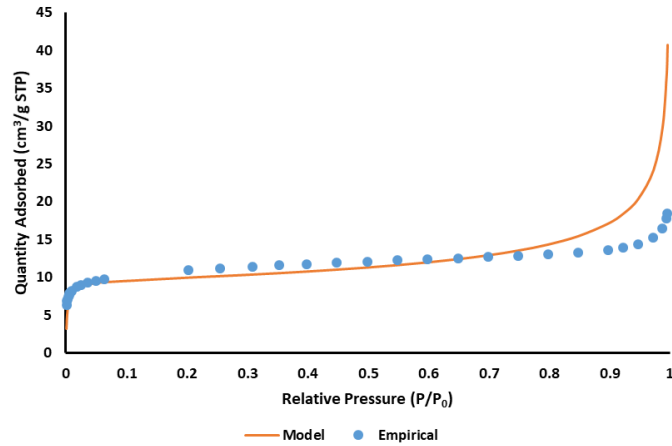


Figure 19: fractal BET fit to the Marcellus shale in excel over the relative pressure range $0-0.995 \frac{p}{p_0}$. The blue circles (●) are the experimental data and the orange line (---) is the modelled data. Modelling parameters used were V_m (9.4386), C (520.0574) and D (2.738713).

The model fits in the lower pressure range however ascends too steeply through the mid-range of the graph before overestimating the quantity adsorbed at the high relative pressure range. This is because the BET model does not account for the physical occurrence of capillary condensation.

The Langmuir model (Rouquerol *et al.*, 2014) produced a poor fit over the data (Figure 20), even when the pressure range was reduced. Resultantly the Langmuir was not used for any further analysis of N_2 sorption data.

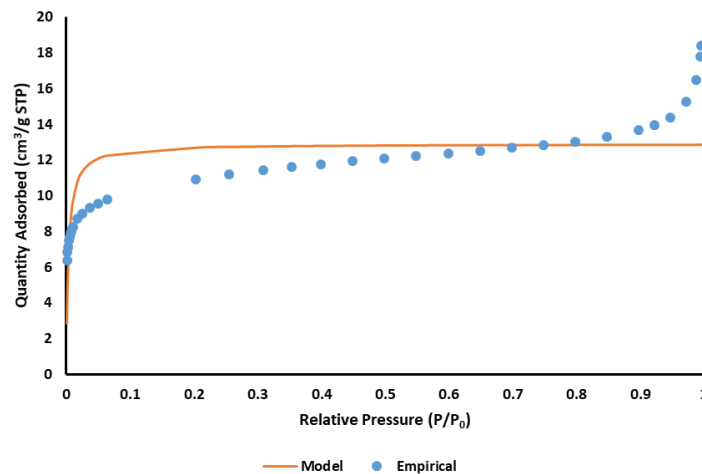


Figure 20: Langmuir fit to the Marcellus shale in excel of the relative pressure range $0-0.995 \frac{p}{p_0}$. The blue circles (●) are the experimental data and the orange line (---) is the modelled data. Modelling parameters used were V_m (12.9055) and b (292.902)

The fractal FHH (Tang *et al.*, 2003; S. Zhang *et al.*, 2018) (8. 3) was fitted to the Marcellus shale (Figure 21), where it can only be used to model beyond approximately $0.3 \frac{p}{p_0}$ and only up to $0.8 \frac{p}{p_0}$ making it difficult to model a dataset with solely this model.

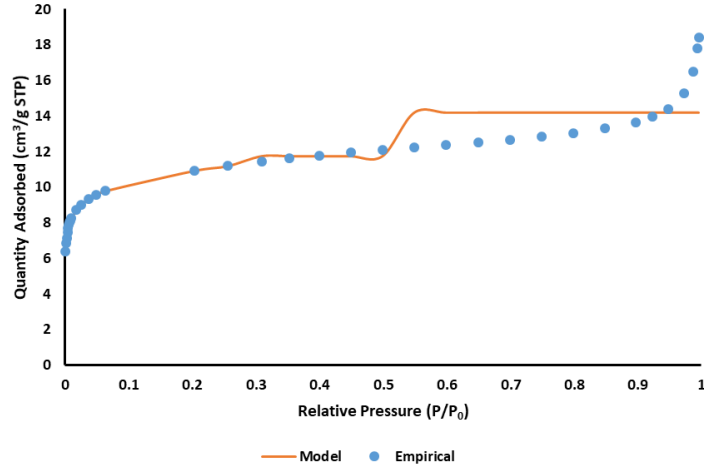


Figure 21: 2 part fractal FHH fit to the Marcellus shale in excel of the relative pressure range 0-0.995 $\frac{p}{p_0}$. The blue circles (●) are the experimental data and the orange line (---) is the modelled data. Modelling parameters used were V_m (9.32866), D_1 (3) and D_2 (3).

The finite multilayer form of the BET equation (Rigby et al., 2008);

$$V_{n-BET} = V_m \times \frac{C}{\frac{1}{x} - 1} \times \frac{1 - (N + 1)x^N + Nx^{N+1}}{1 + (C - 1)x - Cx^{N+1}} \quad (12. 1)$$

Where V_m , C and x are the same as for the fractal BET equation, V_{n-BET} is the quantity adsorbed modelled by the n-BET and N is the number of adsorption layers. The n-BET was used where the fit to the lower relative pressure was comparable to the fractal BET and FHH, however the fit through the mid-range up to the higher relative pressures was much better (Figure 22).

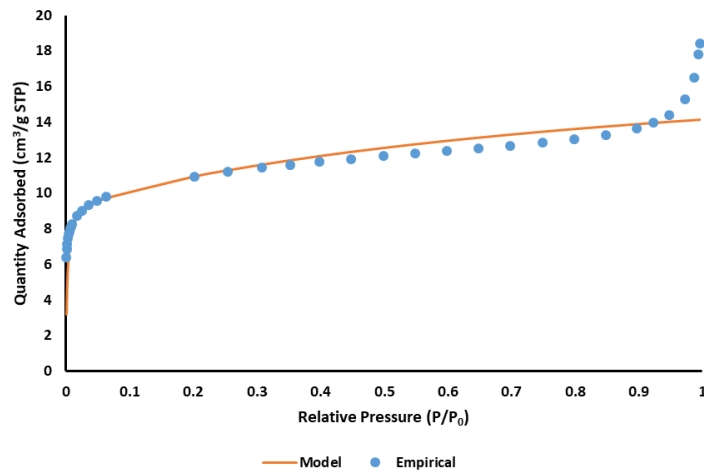


Figure 22: finite multilayer form of the BET fit to the Marcellus shale in excel of the relative pressure range 0-0.995 $\frac{p}{p_0}$. The blue circles (●) are the experimental data and the orange line (---) is the modelled data. Modelling parameters used were V_m (9.4386) and N (1).

After this homotattic model fits were carried out using the kerogen data (12. 11) provided by Schlumberger and one of the fractal models, or the finite multilayer form of the BET. By doing this the fit to the shale sorption data was greatly improved (Figure 23, Figure 24 and Figure 25).

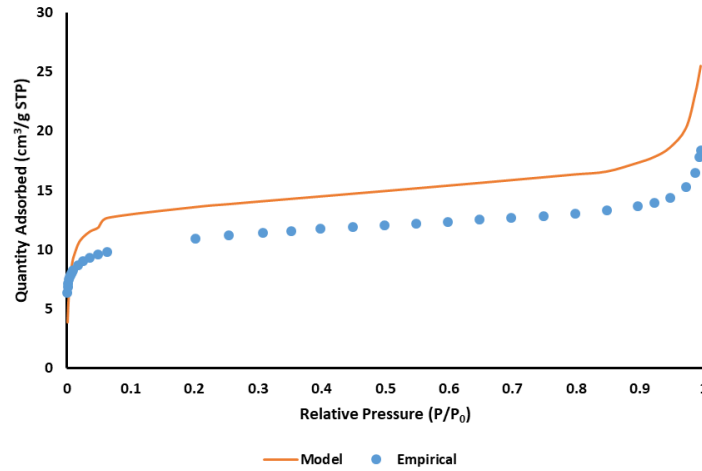


Figure 23: fractal BET and kerogen fit to the Marcellus shale in excel of the relative pressure range $0-0.995 \frac{p}{p_0}$. The blue circles (●) are the experimental data and the orange line (---) is the modelled data. Modelling parameters used were k – value (0.049025), V_m (9.4386), C (235.4792) and D (3).

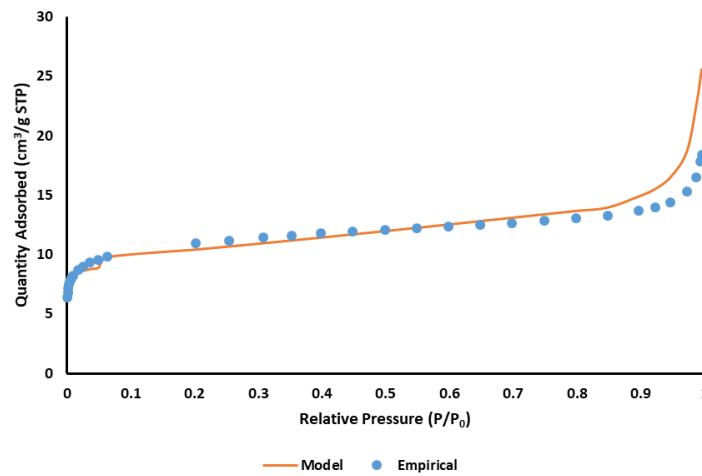


Figure 24: fractal FHH and kerogen fit to the Marcellus shale in excel of the relative pressure range $0-0.995 \frac{p}{p_0}$. The blue circles (●) are the experimental data and the orange line (---) is the modelled data. Modelling parameters used were k – value (0.067328), V_m (2.631502) and D (2.95445)

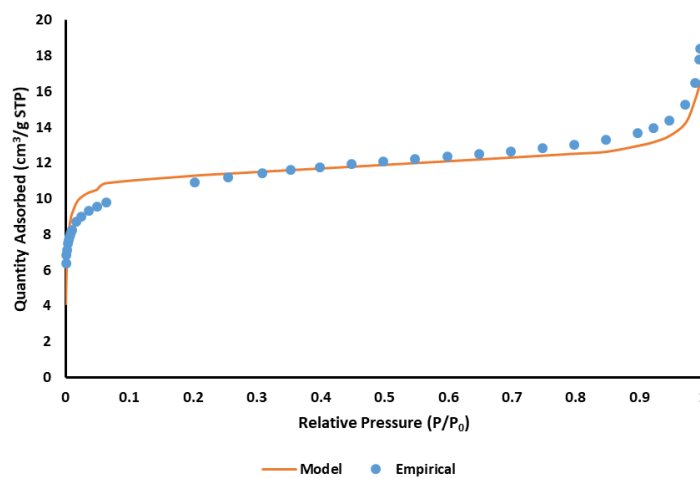


Figure 25: finite multilayer form of the BET and kerogen fit to the Marcellus shale in excel of the relative pressure range $0-0.995 \frac{p}{p_0}$. The blue circles (●) are the experimental data and the orange line (---) is the modelled data. Modelling parameters used were k – value (0.021917), V_m (9.4386) and N (1).

The methodology for this is explained in the rest of the chapter, and the analysis was moved from Excel to R. where code was written to describe the model parameters exactly.

4.7.1. Fractal Dimensions

Two different fractal regimes were used to analyse the surface and pore network properties of the samples from gas adsorption isotherms; the Brunauer-Emmett-Teller (BET) and Frankel-Halsey-Hill (FHH).

4.7.1.1. Brunauer-Emmett-Teller (BET)

BET fractal dimension (Wang *et al.*, 2015) tells us about the surface roughness of the sample with a value between 2 and 3; where values near 2 indicate a smoother surface, and values near 3 indicate a rougher surface. The BET fractal dimension is only relevant for the BET region of the isotherm (multi-layer) which is generally taken from 0.035-0.5 $\frac{p}{p_0}$. The fractal form of the BET equation takes the following form:

$$V = V_m \times \frac{Cx}{1 + x(C - 1)} \times (1 - x)^{D-3} \quad (12. 2)$$

Where V is the quantity adsorbed, V_m the monolayer capacity, C a BET constant, x the relative pressure ($\frac{p}{p_0}$) and D the fractal dimension.

Initially excel was used to carry out this analysis by using the solver function to minimise the residuals between the experimental and modelled data. C and V_m are constants which were taken from the analysis software associated with Micromeritics 3Flex when the BET model is fitted for the gas adsorption isotherm data, along with the quantity adsorbed and the associated relative pressures. When the solver add-in is used for analysis the aim is to minimise the sum of the residuals which is:

$$\sum_{i=1}^i (V_{i,exp} - V_{i,mod})^2 \quad (12. 3)$$

Where $V_{i,exp}$ is the quantity adsorbed by the experimental results for the i th adsorption point, and $V_{i,mod}$ is the calculated quantity adsorbed by the BET model for the i th adsorption point; the residuals were only summed over the relative pressure range for which the BET model is relevant (0.035-0.8 P/Po). To minimise the sum of the residuals the values V_m , C and D are able to vary under predefined conditions; $V_m > 0$, $C > 1$ and $2 \leq D \leq 3$.

4.7.1.2. Frankel-Halsey-Hill (FHH)

FHH fractal dimension (Tang *et al.*, 2003; S. Zhang *et al.*, 2018) can be applied over a broader relative pressure range than the BET fractal dimension, with D_1 taken from 0.25-0.5 $\frac{p}{p_0}$ and D_2 from 0.5-0.995 $\frac{p}{p_0}$.

$$V = V_m \times e^C \times \left(\ln \frac{1}{x} \right)^{D-3} \quad (12. 4)$$

In the FHH equation V is the quantity adsorbed, V_m the monolayer capacity, C a constant, x the relative pressure ($\frac{p}{p_0}$) and D the fractal dimension. The FHH fractal dimensions can be resolved by taking the $\ln(V(x))$ of the equation to produce a two stage linear graph of $\ln\left(\frac{V}{V_m}\right)$ against $\ln\left(\ln\left(\frac{1}{x}\right)\right)$. This version of the equation puts it in the form $y = mx + c$ and the fractal dimension can be calculated from the straight line gradient.

$$\ln\left(\frac{V}{V_m}\right) = C + (D - 3) \ln\left(\ln\left(\frac{1}{x}\right)\right) \quad (12. 5)$$

Initial analysis was carried out by plotting the graph in the form of $y = mx + c$ over the full pressure range, it is then possible to identify where the regime changes from surface roughness to pore network complexity by a change in the straight line gradient making it appear like a step in the graph. The point that this change occurs should be around the relative pressure point, $0.5 \frac{p}{p_0}$; however due to sample variation it is likely that this point will vary slightly above and below. By marking this gradient change it then makes it possible to plot the two lines as separate datasets so that a linear trendline can be fitted to each part, e.g. a trendline over pressure range $0.25-0.5 \frac{p}{p_0}$ and another trendline over the pressure range $0.5-0.995 \frac{p}{p_0}$.

The equation for each of these respective trendlines is added to the graph, along with the R-squared value as a measure of goodness of fit. From the straight line equation it is possible to calculate the fractal dimensions by:

$$D_n = 3 - m_n \quad (12. 6)$$

Where D_n is the FHH fractal dimension for the first or second part and m_n is the gradient of the line for the first or second part. This process is carried out for all samples and the fractal dimensions collected and used to compare with other material characteristics such as the pore surface area and pore volume.

Excel was then used to carry out this analysis by using the solver function to minimise the residuals between the experimental and modelled data. V_m is a constant taken from the analysis software associated with Micromeritics 3Flex when the BET model is fitted for the gas adsorption isotherm data, along with the quantity adsorbed and the associated relative pressures; C is a dimensionless value which is not associated to the properties of the sample. (12. 5) is solved for V to the form:

$$V = V_m e^{(C+(D-3) \ln\left(\ln\left(\frac{1}{x}\right)\right))} \quad (12. 7)$$

Solver is then used to minimise the sum of the residuals between the experimental and modelled quantity adsorbed by:

$$\sum_{i=1}^i (V_{i,exp} - V_{i,mod})^2 \quad (12. 8)$$

Where $V_{i,exp}$ is the quantity adsorbed by the experimental results for the i th adsorption point, and $V_{i,mod}$ is the calculated quantity adsorbed by the BET model for the i th adsorption point; the residuals were only summed over the relative pressure range for which the BET model is relevant ($0.25-0.5$ and $0.5-0.995 \frac{p}{p_0}$). To minimise the sum of the residuals the values C , V_m and D are able to vary under predefined conditions; $C > 0$ $V_m > 0$, and $2 \leq D \leq 3$.

4.7.1.3. R Analysis

The code and a description of the code is included in Appendix 3.1.

The next evolution of the fractal analysis was to implement the use of coding for the purpose of minimising the summed residuals further as it was felt that the degree to which excel did this could be improved. Using R. also enables a greater degree of control over the specific maths in place, thus ensuring that the process still derives a physically possible model fit i.e. the modelled isotherm should not go above the experimental isotherm. R. was also used to remove any potential subjective bias in the selection of a pressure range for the data to be analysed over.

For the FHH fractal analysis there is a one part and two part analysis that can be carried out. Using R. code was created for both analysis types where the biggest difference was in the data handling to establish the pressure ranges over which to carry out the fractal analysis.

4.7.2. Homotattic Patch

The code and a description of the code is included in Appendix 3.2.

The homotattic patch is based on the understanding that different materials will have different sorption capacities based on their surface chemistry - shales have a very heterogeneous surface formed of organic and inorganic minerals. This theory is used to de-convolve the organic and inorganic matter contributions in the experimental isotherms. It is widely accepted that organic matter has a stronger affinity with the adsorbate which could result in a build-up of the adsorbate over this patch. In the same way quartz is understood to have a very low affinity for adsorption (in pure quartz samples this should effectively be zero) so patches of quartz may not have a lot of adsorbate adsorbed on them. Heterogeneity of pore surface can lead to “daisy patches” of adsorbate leading to under- or over-estimation, where there are multiple layers in one area and a mono-layer in others.

The homotattic patch theory was used to separate the contributions from organic and inorganic matter in the conventional nitrogen isotherms using the fractal BET, n-BET (Rigby et al., 2008) and FHH equations, combined with data from an empirical kerogen isotherm (12. 9). Further work allowed for the incorporation of illite from an experimental isotherm of illite from Imperial College University who were provided with the material by the Clay Minerals Society. To ensure accurate fitting an equation fit was applied to the kerogen isotherm so that it could be fit to the same pressure points as the sample isotherm (12. 12).

$$model_{iso} = (V_{eq.} \times p) + (kerogen_{iso} \times (1 - p)) \quad (12. 9)$$

The same process was carried out for the illite isotherm and (12. 10) resulted where, $p + q + r = 1$.

$$model_{iso} = (V_{eq.} \times p) + (kerogen_{iso} \times q) + (illite_{iso} \times r) \quad (12. 10)$$

For this simplified form of the homotattic patch $V_{eq.}$ is the quantity adsorbed calculated by either the BET (12. 2), n-BET (12. 1) or FHH (12. 4) equation. The $kerogen_{iso}$ and $illite_{iso}$ are equations from trendline fits of the experimental isotherms such that the isotherm can be derived from any distribution of relative pressure ranges.

$$kerogen_{iso} = \left[\sum_{x>0}^{x \leq 0.025} 6.8705 \cdot \ln(x) + 92.807 \right] + \left[\sum_{x>0.025}^{x \leq 0.7} -34.08x^2 + 110.81x + 76.7 \right] \quad (12. 11)$$

$$+ \left[\sum_{x>0.7}^{x \leq 0.925} 56.209e^{1.2458x} \right] + \left[\sum_{x>0.925}^{x \leq 1} 67470x^2 - 128284x + 61174 \right]$$

$$illite_{iso} = \left[\sum_{x>0}^{x \leq 0.00125} 15.795x^{0.2645} \right] + \left[\sum_{x>0.00125}^{x \leq 0.01} 10.37x^{0.2047} \right] \quad (12. 12)$$

$$+ \left[\sum_{x>0.01}^{x \leq 0.915} 23.882x^3 - 28.421x^2 + 15.257x + 4.085 \right]$$

$$+ \left[\sum_{x>0.915}^{x \leq 1} 1824.5x^2 - 3348x + 1549.6 \right]$$

Data was analysed over the range of $0-0.8 \frac{p}{p_0}$ for the BET and n-BET model since only the multi-layer region of the isotherms are modelled with these theories. Pressure was analysed up to $0.8 \frac{p}{p_0}$ however to ensure that no data was missed. The FHH model was analysed over the pressure range gained by the `Pressure_Op` <- function used for the one part FHH in the fractal dimension analysis.

The specific code used is included, but the general workflow used is described below;

- Dataframe creation
 - Import data to .R as a .csv file
 - Cut data into the relative pressure range needed for analysis
 - Use the relative pressure values to generate the matching kerogen (and illite for three part analysis) isotherm
 - Use `data.frame()` to make a dataframe of the relative pressure quantity adsorbed and kerogen data (and illite if three part analysis)
- Define the parameters
 - Define the parameters needed for each theory
 - BET – C, V_m, D and p (q and r for three part)
 - n-BET – C, V_m, N and p (q and r for three part)
 - FHH – C, V_m, D and p (q and r for three part)
 - The parameters have their respective boundaries defined for each theory
 - C ; within 10% of the experimentally generated value for the BET and n-BET, for the FHH C is an arbitrary constant that can vary without restraint
 - V_m ; within 10% of the experimentally generated value
 - D ; between the values of 2 and 3
 - N ; a positive integer value
 - p ; between the values of 0 and 1 (for three part $p + q + r = 1$)
- Produce modelled data
 - Using the relevant equation a number of modelled isotherms are produced with the different generated parameters
 - These modelled isotherms are compared to the experimental isotherm to assess the best-fit
 - Modelled isotherms which sum to a greater value than the sum of the experimental data are disregarded as this is not a physically possible solution to the problem
- Select optimised parameters

- Calculate the residuals of the physically possible data compared to the experimental data
- Return the parameters associated to the modelled dataset with the smallest residual value

4.7.3. Rationale

The choice of K was made by selecting a series of increasing values and analysing the changes in the residuals with this increase. After several values had been attempted the residual was plotted against the value of K and a trendline applied to forecast where a plateau would be reached (Figure 26). For all samples, by K equal to one million there was a plateau and so this was selected as the minimum analysis value. The decision was made to select K in this way as the analysis time increases significantly with greater K values and this needed to be established as quickly as possible. One million iterations were used as a minimum and where processing was quicker increased this value accordingly but remained consistent throughout the models i.e. all of the fractal BET were analysed by the same number of iterations. The `replicate()` function was used to check the repeatability of the code. By doing this the continuity and repeatability of the code was established from ten repetitions and by studying the variance of the residuals from the model. When the variance of the residual is a minimum this was considered to be an optimised solution, in instances where the residual value is large with respect to the residual of other datasets it is concluded that for these samples there is a significant part of the isotherm contributed by another input which was not include in the model. This “check step” is what dictated the number of code iterations required to achieve minimal variance in the residuals, by increasing the number of iterations the computation time increases and so iterations were also decided based on a reasonable computation time.

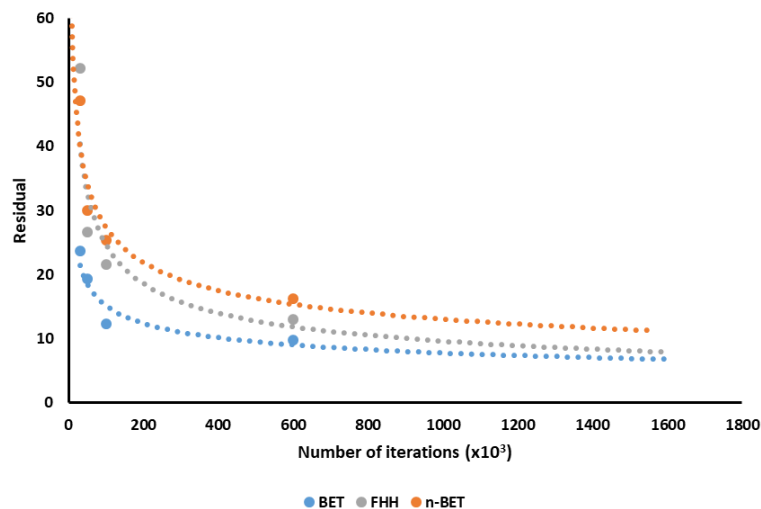


Figure 26: decreasing residuals for the Marcellus 7804'-7807' with the fractal BET (blue circles ●), FHH (grey circles ●) and n-BET (orange circles ●) in the homotatic patch using kerogen and illite isotherms against the number of model iterations with a trendline forecast to 1.6 million iterations. The same was done for all samples and it was determined that by 1 million iterations the relative further reduction against processing time was optimum.

5. The Marcellus Shale

5.1. Methodology

5.1.1. Thermogravimetric Analysis

Thermogravimetric analysis experimental conditions were defined such that the sample was heated through 110°C (moisture) to 920°C (volatiles) using nitrogen – an inert gas. The gas was then changed to oxygen as the temperature decreased, at 600°C (when decreasing) the components of fixed carbon and ash can be determined.

5.1.2. Gas Adsorption

Samples were prepared for nitrogen (N₂) and carbon dioxide (CO₂) gas adsorption by the sample preparation standards outlined in 4.1. Gas Sorption. Gas adsorption was used to analysis Marcellus 7795'-7798' over a range of grain sizes (Table 2), and for Marcellus 7804'-7807', 7834'-7837 and 7864'-7867' to analyse the relationship with depth. Experiments are carried out isothermally at 77K for N₂, and 273.15K for CO₂ analysis. In N₂ analysis the relative pressure steps are carried out between 0-0.995 $\frac{p}{p_0}$ and measure a range of pore sizes from 2-50nm, larger micro-pores and meso-pores, although results are often quoted to include small macro-pores also (100nm). CO₂ analysis is carried out over a relative pressure range 0-0.035 $\frac{p}{p_0}$ and probes pores in the range 0.4-2.0nm (micro-pores).

5.1.3. Mercury Intrusion Porosimetry

As a result of the high pressures and vacuum involved in mercury porosimeter fine grained material can be susceptible to entering the analysis rig. As a result of this chips (3-5mm) of sample was used to ensure no analysis material enters the analysis rig, this also enables material to be more easily recovered for additional analysis. Samples were oven dried overnight to remove any physisorbed water on the pore walls and then prepared for low- and high- pressure, which take the sample from atmospheric pressure to under vacuum and then to 207MPa and 414MPa respectively (results quoted to 310MPa to avoid any false data relating to crushing of the sample).

5.1.4. X-Ray Diffraction (XRD)

A Bruker Advance Series 2 X-Ray Diffractometer was used to carry out XRD on powdered samples from 10° 2θ.

5.1.5. Scanning Electron Microscopy, Mineral Liberation Analysis

SEM MLA was carried out on an FEI Quanta 600 (operated at 20kV, working distance of 13mm and spot size 7) equipped with mineral liberation analysis software which enables the quantification of sample mineralogy.

5.1.6. Numerical Modelling

Numerical modelling was carried out as per the procedure outlined in 4.7. Numerical Modelling for the determination of fractal dimensions and fitting the homotattic patch model. The code is included in Appendix 3 which was used to derive the fractal dimensions, *k* values and *i* values.

5.2. Results

5.2.1. Gas Sorption Grain Size Analysis

The first sample material analysed was the Marcellus shale from depth 7795'-7798' in pre-crushed particle sizes listed in Table 2.

| |
|--|
| 7795'-7798' |
| 106-150μm |
| 150-212μm |
| 212-425μm |
| 425-600μm |

Table 2: the grain sizes used for the grain size study on the Marcellus 7795'-7798'.

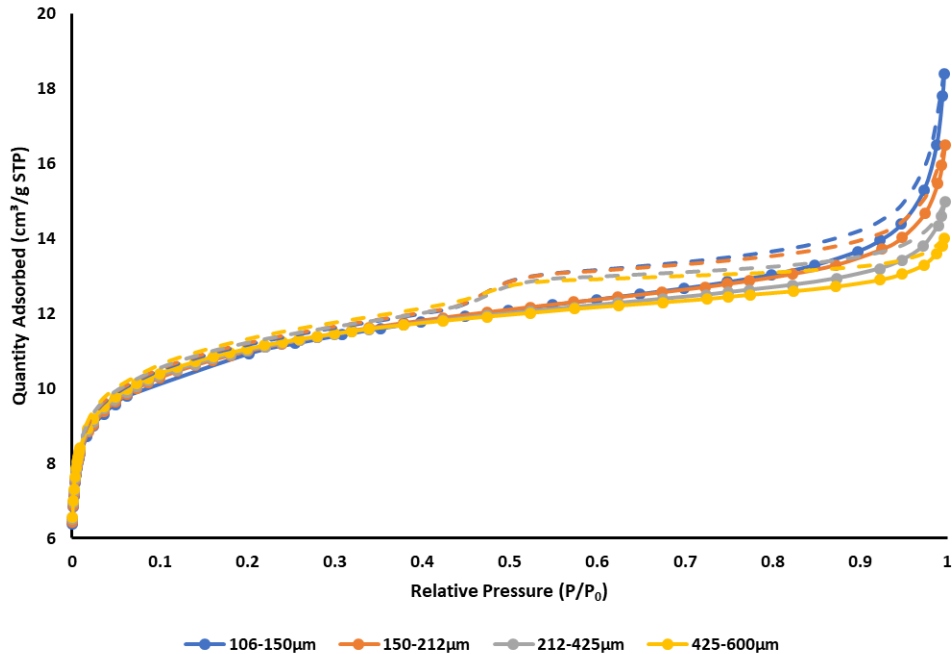


Figure 27: N_2 gas adsorption results for the grain size study on the Marcellus 7795'-7798' where desorption is depicted by dashed lines, 106-150 μm by blue circles (\bullet), 150-212 μm by orange circles (\bullet), 212-425 μm by grey circles (\bullet) and 425-600 μm by yellow circles (\bullet).

N_2 isotherms generated for each particle size of the same sample are the same isotherm type/shape since they originate from the same sample. Figure 27 shows the variation in the form of the N_2 adsorption isotherm, with increasing grain size. It can be seen that there is a decreasing quantity adsorbed and slight increase in the size of the hysteresis loop as grain size increases. During the crushing process pore space is made more accessible to ingress and results in an increased quantity adsorbed. As there is also some decrease in the hysteresis loop size with increasing particle size there has been a decrease in sample complexity i.e. fewer leading small neck sizes.

The hysteresis loops for each grain size were obtained to determine the emptying mechanisms of the pore network; pore-blocking occurs when hysteresis closure takes place at pressures $>0.5 \frac{p}{p_0}$ as a result of leading pore necks $>4\text{nm}$, cavitation takes place at $0.5 \frac{p}{p_0}$ and includes all leading neck sizes $<4\text{nm}$, this is explained in more detail in 2.5.1.6. Gas Sorption Experimental Effects. For the varying grain size the pressure that the hysteresis loop closes at remains consistent at $0.5 \frac{p}{p_0}$, this shows that throughout the varying grain sizes the leading pore necks controlling the desorption of N_2 from larger pores are $<4\text{nm}$.

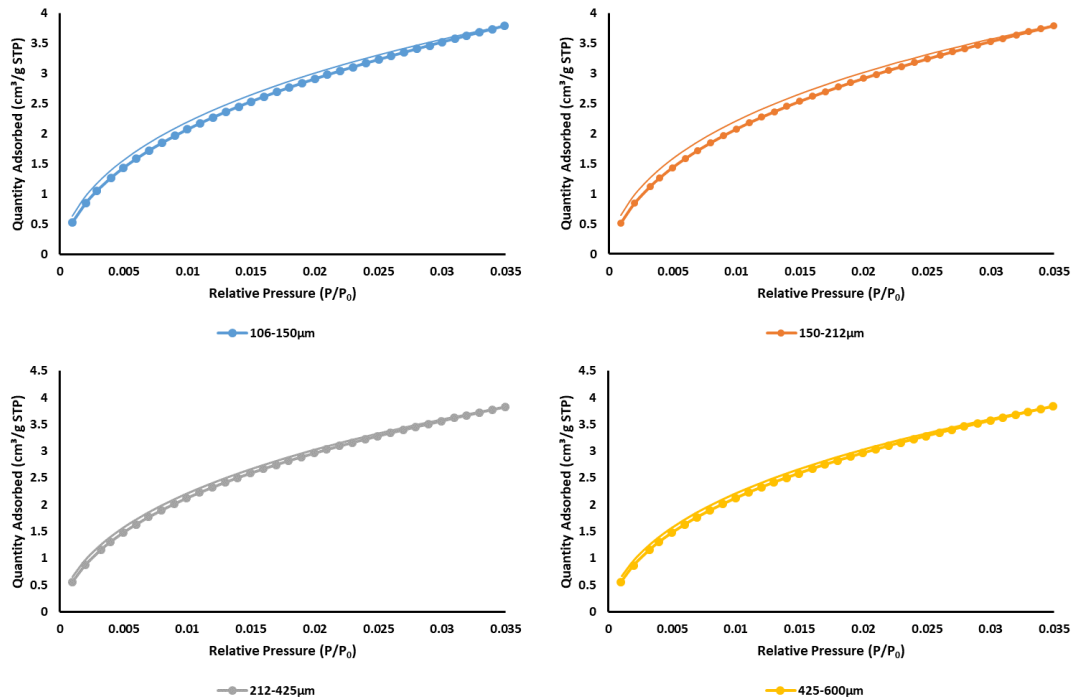


Figure 28: CO₂ gas adsorption results for Marcellus 7795'-7798' for grain sizes 106-150µm (blue circles ●), 150-212µm (orange circles ●), 212-425µm (grey circles ●) and 425-600µm (yellow circles ●).

The CO₂ gas adsorption results for Marcellus 7795'-7798' (Figure 28) show very little difference in the maximum quantity adsorbed. Variations which do exist between isotherms are comparable to variations which would be seen from repeated analysis of the exact same sample, or of different analysis material from the same depth and the same grain size. This result is in line with the findings of (Y. Chen *et al.*, 2015) who have carried out similar tests and found that, with changing particle size, there is little to no difference in the micro-pore volume of the sample. This is further supported by the low pressure range (associated with micro-pores) in the N₂ gas adsorption isotherms (Figure 27) where there is little to no variation between samples.

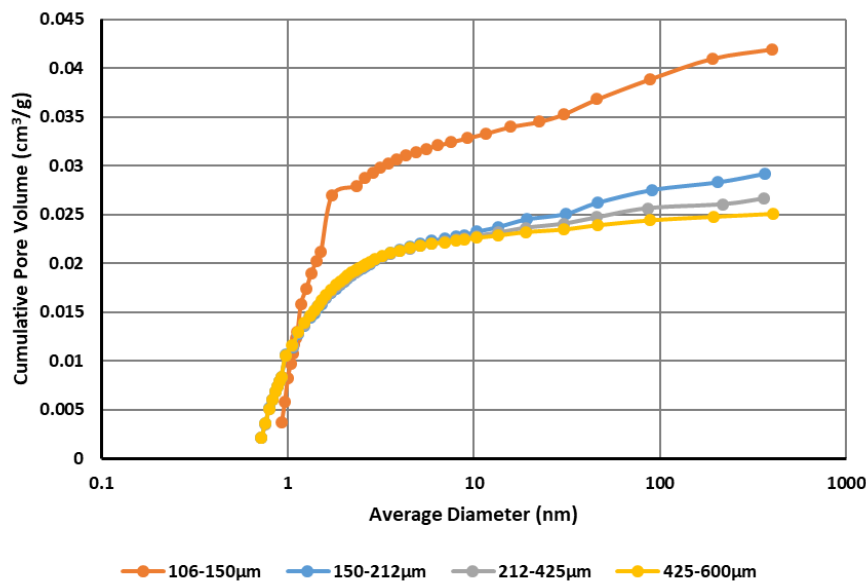


Figure 29: BJH cumulative pore volume pore size distribution for Marcellus 7795'-7798' for the grain sizes 106-150µm (blue circles ●), 150-212µm (orange circles ●), 212-425µm (grey circles ●) and 425-600µm (yellow circles ●).

The cumulative pore volume distributions obtained using the BJH adsorption (Figure 29) model demonstrate a grain size dependency where the finest grain size has a significantly greater cumulative pore volume. There is a smaller degree of separation in the cumulative pore volume curves between the largest three grain sizes, however these are still correlated by depth.

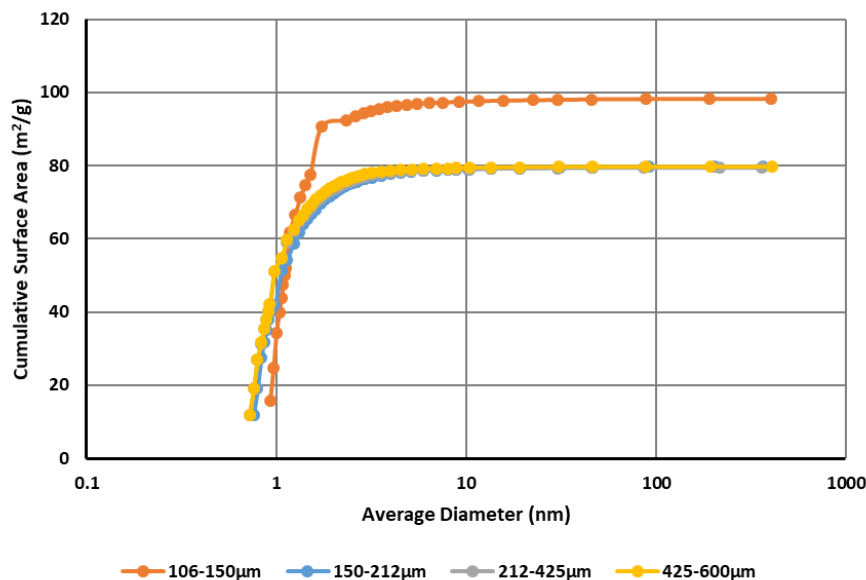


Figure 30: BJH cumulative surface area pore size distribution for Marcellus 7795'-7798' for the grain sizes 106-150µm (blue circles ●), 150-212µm (orange circles ●), 212-425µm (grey circles ●) and 425-600µm (yellow circles ●).

The cumulative pore surface area (from BJH adsorption) is also correlated to grain size, although the deviation between the larger grain sizes is almost indistinguishable (Figure 30) due to the surface area to volume ratio. For example, if you were to take a cube with 1cm length sides the surface area is 6cm² and the volume is 1cm³ resulting in a surface area to volume ratio of 6cm⁻¹. If you change the 1cm cube to a 2cm cube you end up with a surface area of 24cm² and a volume of 8cm³ and a surface area to volume ratio of 3cm⁻¹.

As a result of this micro-pores contribute significantly to the total surface area of a sample, but do not contribute greatly to the pore volume. Conversely macro-pores do not contribute significantly to the total surface area, but do contribute greatly to the pore volume. For this reason the separation between grain sizes 150-212µm, 212-425µm and 425-600µm in the cumulative surface area (Figure 30) is indistinguishable when compared to the cumulative pore volume (Figure 29). More generally the surface area measurements will be more strongly influenced by the presence of micro-pores, and the pore volume by the presence of macro-pores.

It can be seen that the pore sizes most affected by crushing are the larger pores because of the increase in quantity adsorbed at higher relative pressures (larger pores) for the N₂ sorption isotherms (Figure 27), and the lack of change in the CO₂ sorption (Figure 28) isotherms. This is additionally reflected in the cumulative pore size distribution plots where the cumulative pore volume (Figure 29) shows the greatest difference between grain sizes (associated to macro-pores), and there is no significant change in the cumulative surface area distribution (Figure 30) associated to micro-pores.

5.2.2. Gas Sorption Depth Analysis

An additional three Marcellus samples were later provided (from depths 7804'-7807', 7834'-7837' and 7864'-7867') from the same well, but different to 7795'-7798'. Having previously established the impact that varying grain size has on experimental results these samples were analysed for depth

dependence. Samples were crushed to 106-150 μ m and gas adsorption analysis previously described was carried out.

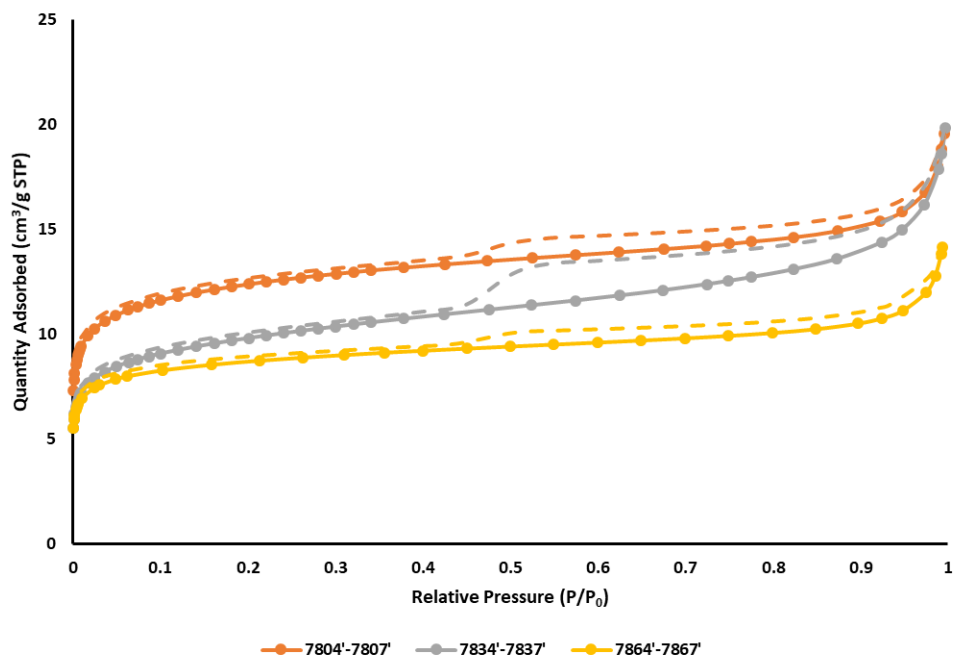


Figure 31: N_2 gas adsorption isotherm for Marcellus 7804'-7807' (orange circles ●), 7834'-7837' (grey circles ●) and 7864'-7867' (yellow circles ●) for 106-150 μ m. The desorption branches of the isotherms are represented with dashed lines.

Results from N_2 gas adsorption (Figure 31) show that there is some correlation between depth and the maximum quantity adsorbed, where deeper samples adsorb a smaller quantity, and shallower samples a greater quantity. However, the size of the hysteresis loops is inconsistent with depth and is controlled by a different sample property influencing the pore network complexity. Specifically in this case the number of leading pore necks <4nm in size controlling desorption of N_2 from larger pores.

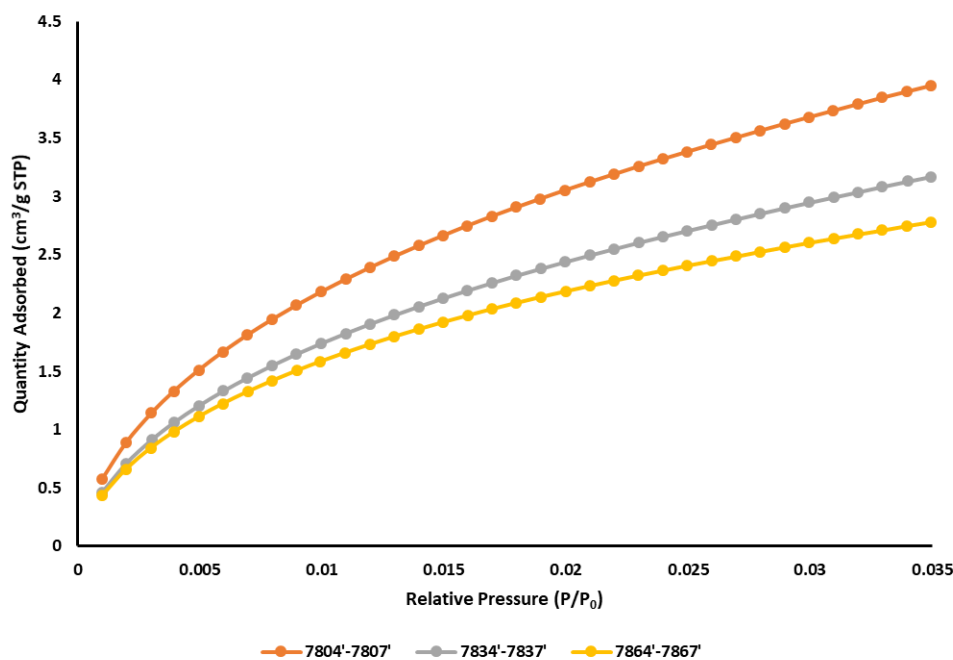


Figure 32: CO₂ gas adsorption isotherm for Marcellus 7804'-7807' (orange circles ●), 7834'-7837' (grey circles ●) and 7864'-7867' (yellow circles ●) for 106-150um. Isotherms were reversible and so desorption is not included.

The CO₂ gas adsorption results (Figure 32) also show a depth correlation, although the variability between samples is different to those observed for N₂ gas sorption (Figure 31). In N₂ gas sorption Marcellus 7834'-7837' adsorbs almost the same as 7804'-7807', however in CO₂ gas sorption the quantity adsorbed by Marcellus 7834'-7837' is much closer to the quantity adsorbed by 7804'-7807'.

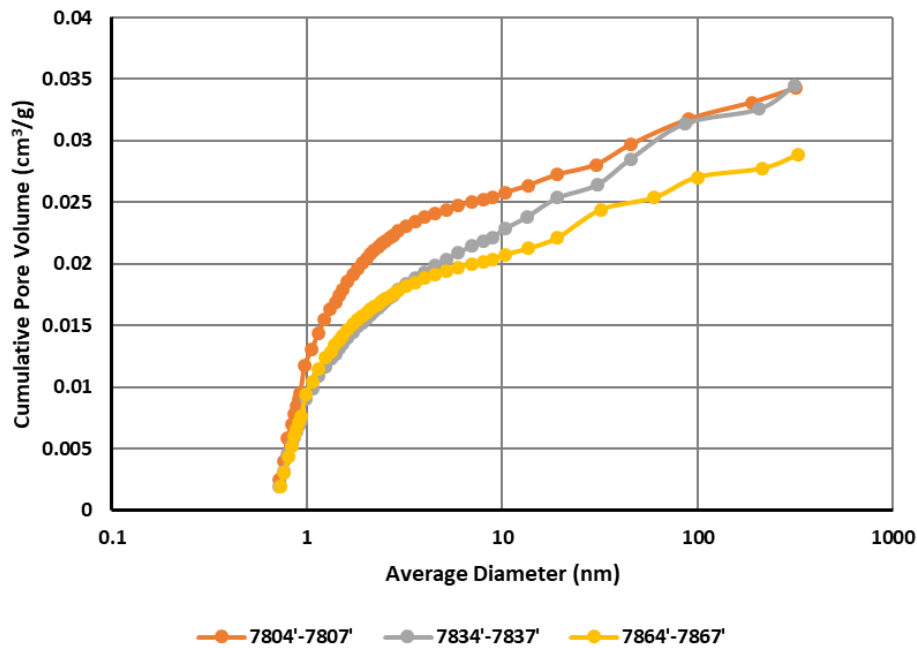


Figure 33: pore size distribution for the BJH cumulative pore volume for Marcellus 7804'-7807' (orange circles ●), 7834'-7837' (grey circles ●) and 7864'-7867' (yellow circles ●) for 106-150um.

The cumulative pore size distribution for pore volume (Figure 33) shows the same distribution as the N₂ isotherm does (Figure 31). From these two results it is possible to say that the quantity of larger pores in Marcellus 7804'-7807' and 7834'-7837' is the same. However the quantity of larger pores for the Marcellus 7864'-7867' is much less as shown by the N₂ isotherm (Figure 31) and cumulative pore size distribution for pore volume (Figure 33) where it adsorbs significantly less and higher relative pressures and has a much lower total pore volume.

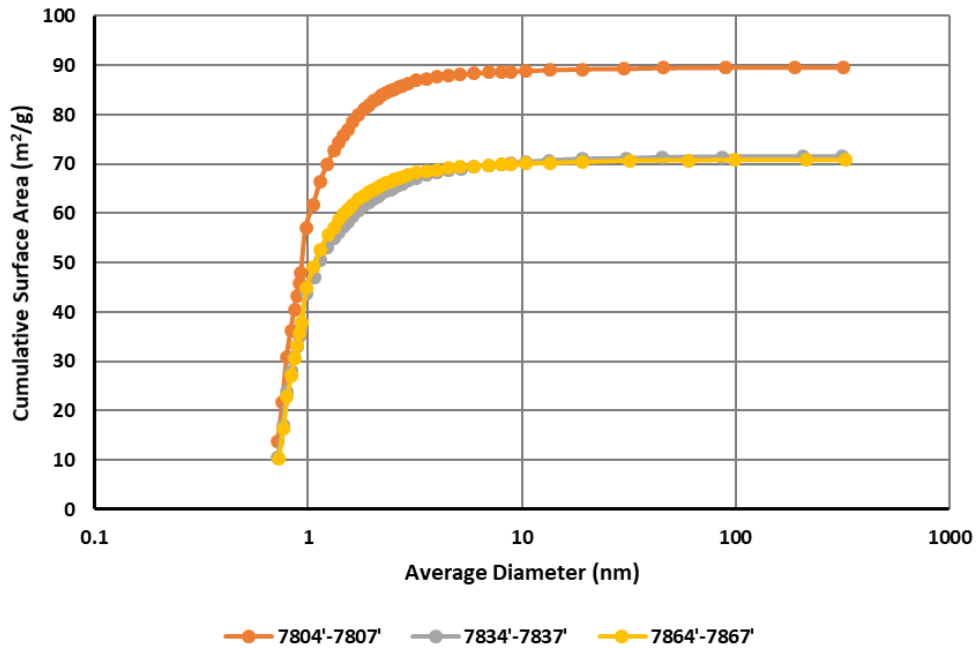


Figure 34: pore size distribution for the BJH cumulative surface area for Marcellus 7804'-7807' (orange circles ●), 7834'-7837' (grey circles ●) and 7864'-7867' (yellow circles ●) for 106-150um.

For the cumulative pore surface area (Figure 34) there is a significant difference between Marcellus 7804'-7807' and 7834'-7837' where surface area is more influenced by the presence of micro-pores and it would be expected for the distribution to be more similar to the CO₂ isotherm (Figure 32).

5.2.3. Mercury Intrusion Porosimetry (MIP)

The mercury intrusion porosimetry (MIP) results for the Marcellus shale (Figure 35) show the same correlation to depth as the N₂ and CO₂ gas sorption results. Marcellus 7804'-7807' and 7834'-7837' have the greatest intra-particle intrusion showing that they have a greater quantity of larger pores. Marcellus 7864'-7867' on the other hand has a very small intra-particle intrusion in comparison to Marcellus 7804'-7807' and 7864'-7867' and reaches a plateau at 1.5MPa where it ceases to intrude any more mercury. This results shows that Marcellus 7864'-7867' has a great number of pores which are too small for mercury to intrude (<4nm) and much of the pore network is not intruded by mercury.

Results were normalised from 0.07MPa (10 psia) which is where mercury intrusion ceases to be a result of inter-particle intrusion, pressures >0.07MPa are as a result of intra-particle intrusion and so tell us about sample properties. Normalisation was achieved by discarding points up until 0.07MPa and then setting that pressure point to zero by subtraction of the perceived intruded volume at that point. This same value is subtracted for all pressure points and results in a normalised intrusion/extrusion graph which only contains intra-particle intrusion. Marcellus 7804'-7807' and 7834'-7837' have a significantly greater intra-particle intrusion volume compared with 7864'-7867'. This is in agreement with N₂ gas adsorption where 7804'-7807' and 7834'-7837' were observed to have a greater number of larger pores.

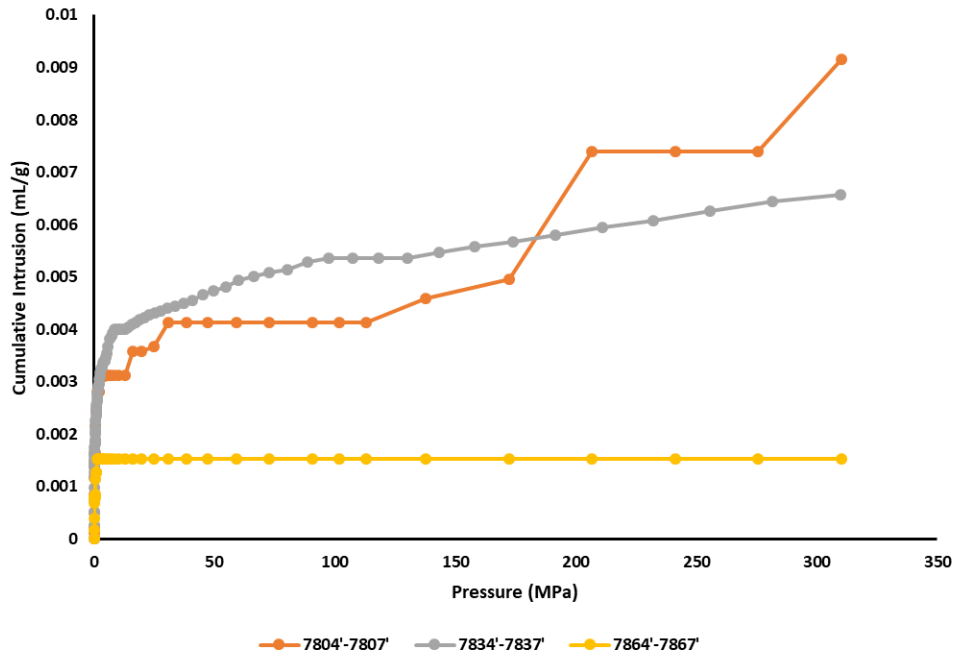


Figure 35: normalised mercury intrusion porosimetry results for Marcellus 7804'-7807' (orange circles ●), 7834'-7837' (grey circles ●) and 7864'-7867' (yellow circles ●) for 106-150um identifying that Marcellus 7864'-7867' has the lowest intruded volume and Marcellus 7804'-7807' the greatest intruded volume.

5.2.4. Mineralogy

The sample composition and mineralogy, were investigated with several methods to characterise different components of the sample. Several methods were used for the Marcellus in order to find the best combination of methods to characterise the mineralogy; thermogravimetric analysis (TGA) was used initially however more specific mineral knowledge was required. As a result, x-ray diffraction (XRD) was used for specific mineral identification but it was concluded the particular mineral percentages were required for accurate characterisation. Since the XRD available to us was qualitative, scanning electron microscopy equipped with mineral liberation analysis (SEM MLA) was used to derive the specific mineral percentages by area of the studied sample. Further to this specific knowledge of the total organic content (TOC%) was required to completely characterise the sample composition and RockEval pyrolysis was used to do this. The sample mineralogy is significant as the pore surface area for minerals vary greatly (Table A5.2. 1) and will consequently impact the overall physical properties of the sample.

5.2.4.1. Thermogravimetric Analysis (TGA)

The first technique used was TGA with an experimental atmosphere of N₂. TGA constantly records the sample weight, experiment time and experiment temperature; the specific temperature at which weight loss occurs indicates the quantity of the component associated to that temperature. The temperature at which each contribution is calculated was advised by Leco Corporation (2010), moisture mass was taken at 110°C, volatile mass at 920°C and ash mass at 600°C (after the gas changes to oxygen).

Using Appendix 2 the constituents in Table 3 can be calculated. In Table 3 where there is a negative value for the fixed carbon %, this corresponds to an increase in mass where oxidation of a mineral has occurred after the TGA experimental atmosphere changes from N₂ to O₂. Dry amounts indicate where the moisture contribution has been removed from the initial values. Where negative values are seen, this indicates as weight gain related to some form of oxidation during the second burning process where the gas is changed.

| Component | Quantity (%) |
|-------------------------|---------------------|
| Moisture | 0.0658 |
| Volatiles | 41.7183 |
| Ash | 58.5209 |
| Fixed Carbon | -0.3051 |
| Dry Volatiles | 41.7458 |
| Dry Ash | 58.5595 |
| Fixed Dry Carbon | -0.3053 |

Table 3: shows the percentage contribution to the sample mass from moisture, volatiles, ash and fixed carbon calculated using the equation in Appendix 2.

5.2.4.2. X-Ray Diffraction (XRD)

X-ray diffraction (XRD) of the Marcellus shale did not start to produce a signal until 20° (2θ), and then continued to produce a signal until 70° (2θ) irrespective of sample. This 2θ range is thus characteristic of all of the samples and shows that there is similarity in their composition where scattering does not begin until 70°. XRD results are shown in Appendix 4 where the largest peak at 26-27° (2θ) present throughout all samples is quartz (Taylor *et al.*, 1970; Stanjek, 2004; Whittig, 2015). The signal for quartz is very strong and as a result makes other minerals more difficult to identify and separate from the noise. Other identifiable minerals carbonates (29°) and pyrite (25°). The presence of these minerals is as a result of the common depositional settings. The counts for an identified mineral do not correlate to the quantity of the mineral within the sample, as a result of this although quartz has the greatest number of counts it does not mean that it will be the primary component of any or all samples.

5.2.4.3. Scanning Electron Microscopy Mineral Liberation Analysis (SEM MLA)

As a result of the qualitative nature of XRD results and highly variable BET surface areas, a more precise quantitative analysis technique is required to determine the quantities of each mineral since this will affect the properties of the samples (Table A5.1. 1).

A scanning electron microscope equipped with mineral liberation analysis software (SEM MLA), allows the mineral phases in the samples to be quantified, and mineral maps produced. To reduce bias analysed chips were taken from a range of points across the respective core (i.e. from different points along the core for Marcellus 7804'-7807' etc); samples were also analysed in different orientations with respect to the bedding plane (i.e. looking parallel and perpendicular to the bedding plane). Table A5.2. 1 shows the mineral types measured by SEM-MLA for each sample based on a shared primary chemical composition; broken down as carbonates (CaCO_3), clays ($\text{SiO}_2 \cdot \text{Al}_2\text{O}_3 \cdot \text{H}_2\text{O}$), silicates (SiO), sulphides (Su) and oxides (O) (Carbonates; limestone and dolomite. Clays; illite, kaolinite and goethite. Silicates; quartz, muscovite and albite. Sulphides; pyrite, chalcopyrite and sphalerite. Oxides; apatite and rutile).

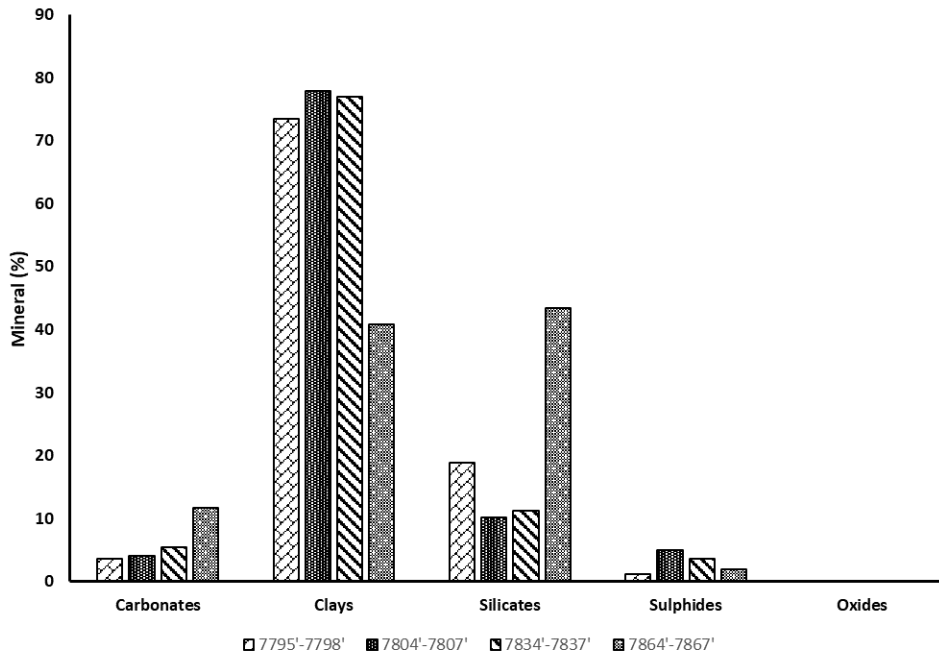


Figure 36: showing a bar chart for the mineral % of chips of the Marcellus shale from SEM MLA. Bars are ordered by depth (left to right) with Marcellus 7795'-7798' represented by the diagonal empty bricks, 7804'-7807' the textured black, 7834'-7837' diagonal stripes and 7864'-7867' the textured grey.

Figure 36 shows that for Marcellus 7795'-7798', 7804'-7807' and 7834'-7837' the mineralogy is very similar and they are all clay dominated samples with about 5% carbonates and 10% quartz. Marcellus 7864'-7867', on the other hand, has a 1:1 ratio of clays and quartz (40%) and about 10% carbonates. SEM MLA also produces mineral maps of the samples colour coded (**Error! Reference source not found.**) to clearly show the distribution of minerals throughout the sample. The diagrams in Figure 37, Figure 38 and Figure 39 are predominantly coloured in orange showing that for the surfaces imaged Marcellus 7795'-7798', 7804'-7807' and 7834'-7837' are clay dominated, with fine-grains of quartz interspersed and coarse inputs of limestone/pyrite. Marcellus 7864'-7867' (Figure 40) is coloured equally with orange (clay) and blue (quartz) with some limestone (pale blue) present in some chips of sample. The mineral maps allow this to be seen visually with the shift from orange (illite) to blue (quartz) in the last sample.

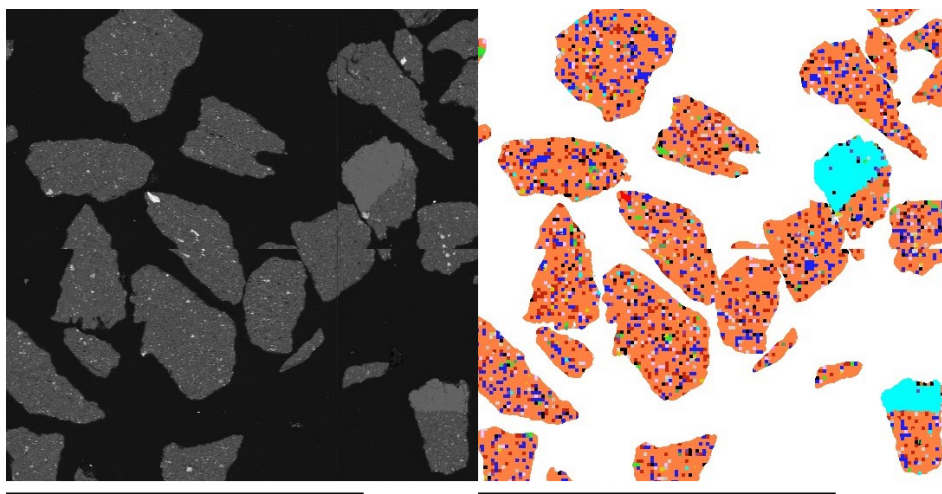


Figure 37: BSE image and corresponding mineral map for Marcellus 7795'-7798' highlighting an illite dominated matrix (orange), with fine grained quartz (blue) interspersed throughout the matrix and some coarse grains of limestone (turquoise) with a 5mm scale bar.

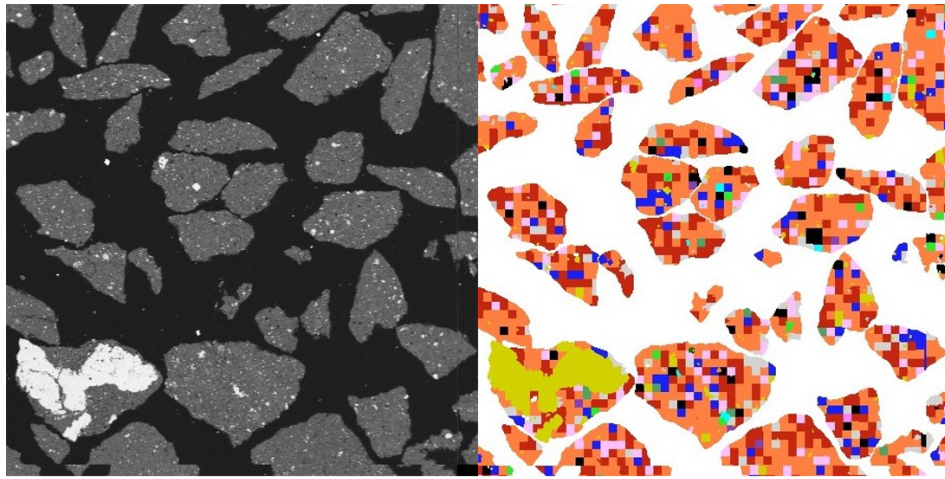


Figure 38: BSE image and corresponding mineral map for Marcellus 7804'-7807' highlighting an illite dominated matrix (orange), with fine grained quartz (blue) interspersed throughout the matrix and a coarse grain of pyrite (mustard) with a 5mm scale bar.

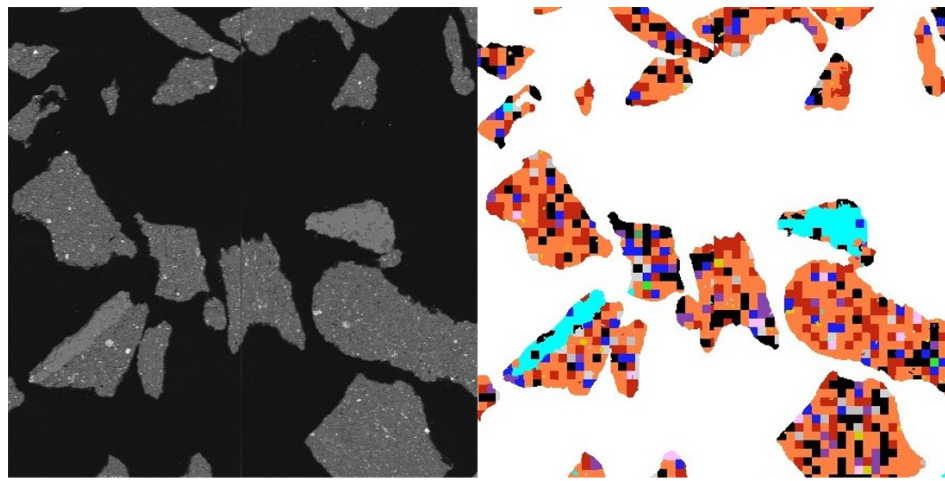


Figure 39: BSE image and corresponding mineral map for Marcellus 7834'-7837' highlighting an illite dominated matrix (orange), with fine grained quartz (blue) interspersed throughout the matrix and some coarse grains of limestone (turquoise) with a 5mm scale bar.

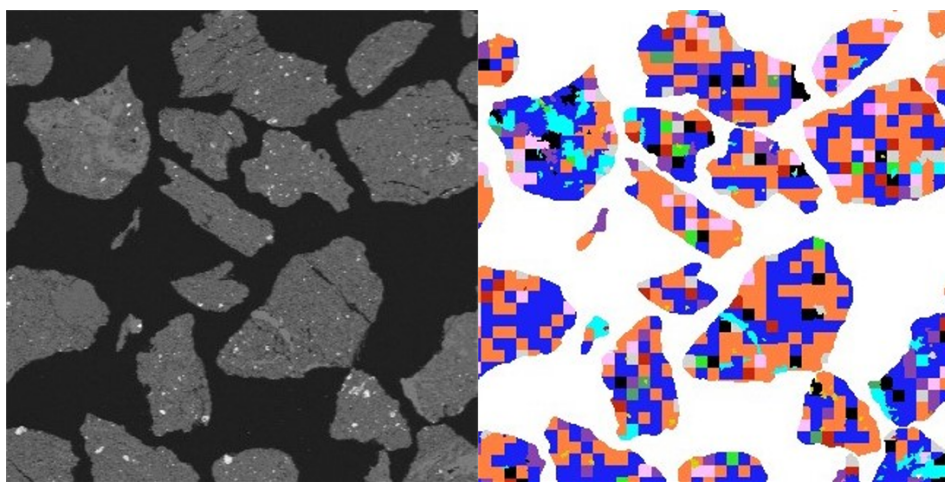


Figure 40: BSE image and corresponding mineral map for Marcellus 7864'-7867' where there seems to be an equal presence of both illite (orange) and quartz (blue); there are also some coarser limestone grains (turquoise with a 5mm scale bar).

All samples show consistency in the average grain size they are made up of, specifically, clay sized particles making up an illite dominated matrix. Samples 7795'-7798', 7804'-7807' and 7834'-7837' are composed of similar ratios between minerals and can be seen in more detail in Figure 41, scanning electron microscopy (SEM) images of 7804'-7807' representative of 7795'-7798' and 7834'-7837'. In these figures coarser limestone grains can be identified which are significantly larger than the surrounding illite matrix. In addition to this there are quartz and pyrite grains which are finer grains than the limestone, but significantly larger than the clay sized particles.

Further mineralogical and textural detail can be gained from scanning electron microscopy (SEM) images of the samples at greater magnification than SEM MLA is carried out. At this magnification specific forms of the minerals can be identified, such as biogenic or authogenic carbonates, as well as the particular grain sizes and any preferential alignment. Figure 41 show these details with the sample described in more detail in the caption.

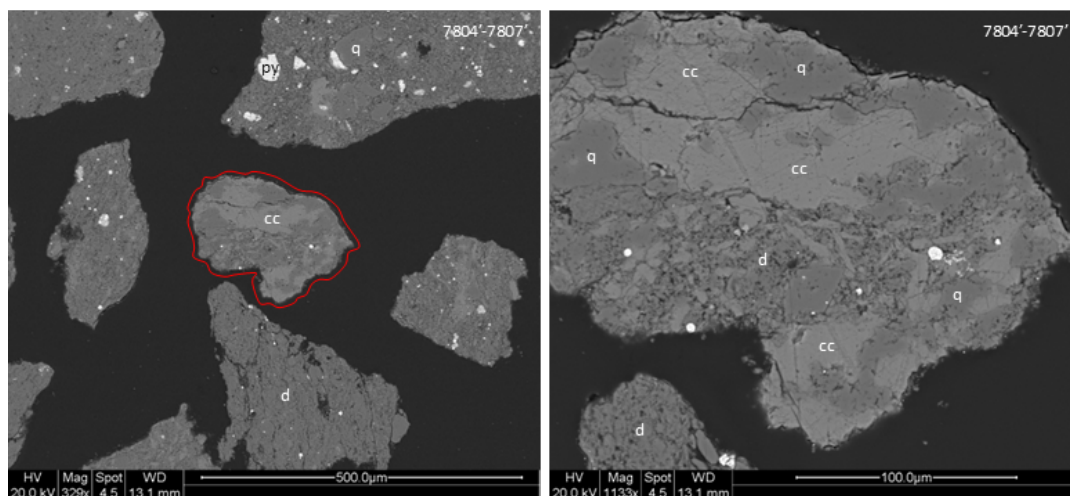


Figure 41: SEM images of the Marcellus 7804'-7807' with a clay sized particle matrix dominated by illite. There are non-uniformly distributed coarse grains of quartz and limestone throughout the samples. The second SEM image shows that there are two separate inputs for quartz and limestone, where grains are within the clay dominated matrix they have been transported and deposited. Whereas contiguous grains of quartz and limestone are due to in-situ precipitation/dissolution. These textural and mineral properties are shared by the Marcellus samples 7795'-7798' and 7834'-7837'.

Marcellus 7864'-7867' is distinct among the samples and contains a significantly greater quantity of quartz. In the mineral maps (Figure 40) this is visible from the significantly greater amount of blue pixels in comparison to the other Marcellus samples. The mineral map (Figure 40) indicates that the quartz is a part of the sample matrix, and not as coarser grains within the matrix and identified by larger isolated sections on the mineral map. Figure 42 is the SEM images for Marcellus 7864'-7867' and more clearly shows the nature of the quartz and limestone.

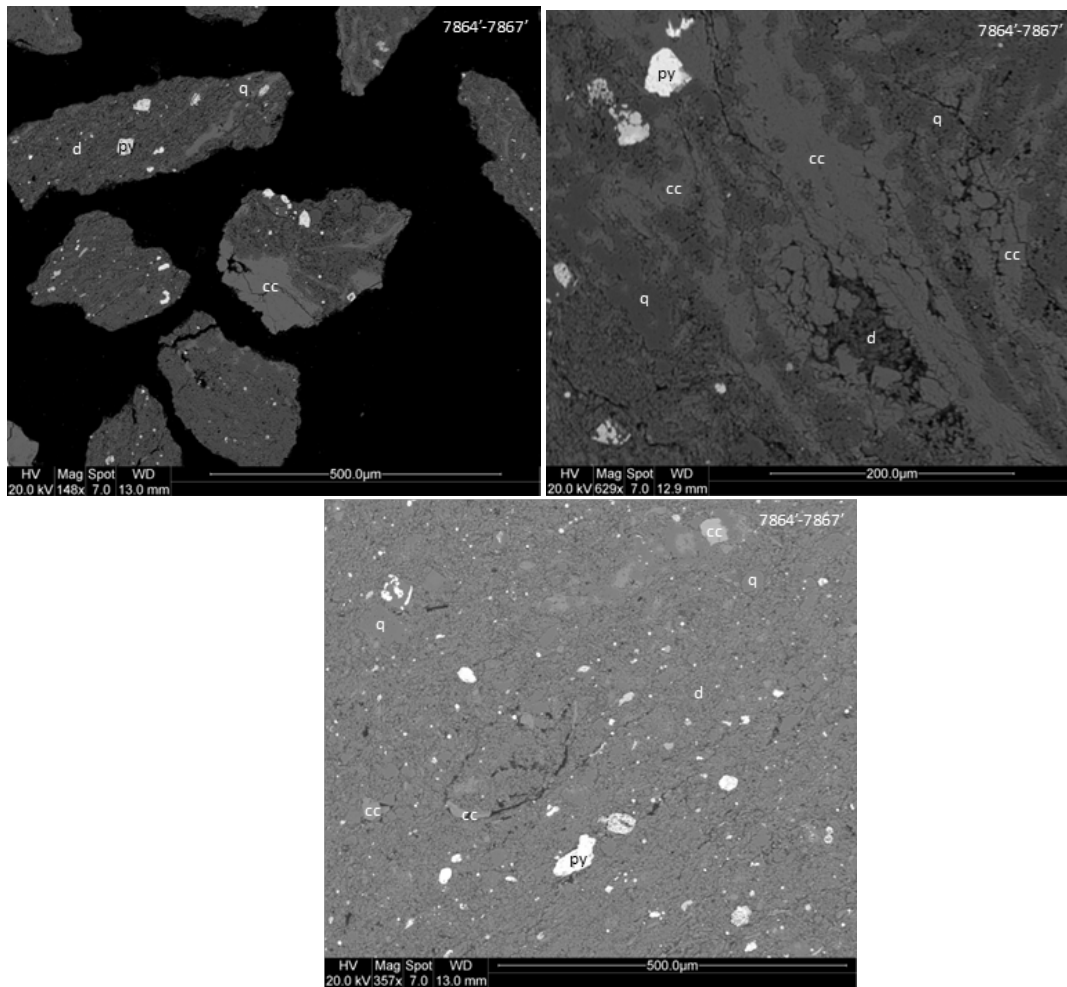


Figure 42: SEM images of the Marcellus 7864'-7867' showing the clay sized particle matrix dominated by illite, and containing slightly coarser quartz grains. In the second SEM image the nature of the limestone can be more clearly seen as a cement or precipitate between the illite-quartz matrix. In the third SEM image the contrast and brightness have been adjusted to highlight the smaller quartz grains within the clay sized particle matrix.

The data from SEM MLA was correlated to the gas sorption results to identify if there are any mineral dependencies with properties such as pore surface area and pore volume. It can be seen in Figure 43A that there is a positive correlation between the BJH pore volume and the clay content, and an inverse correlation with the carbonates and silicates as shown in Figure 43B. This however is a general trend and there is some variation where some minerals are more influential than another, i.e. in the presence of a significantly large clay content the influence of any carbonate or silicate may become less.

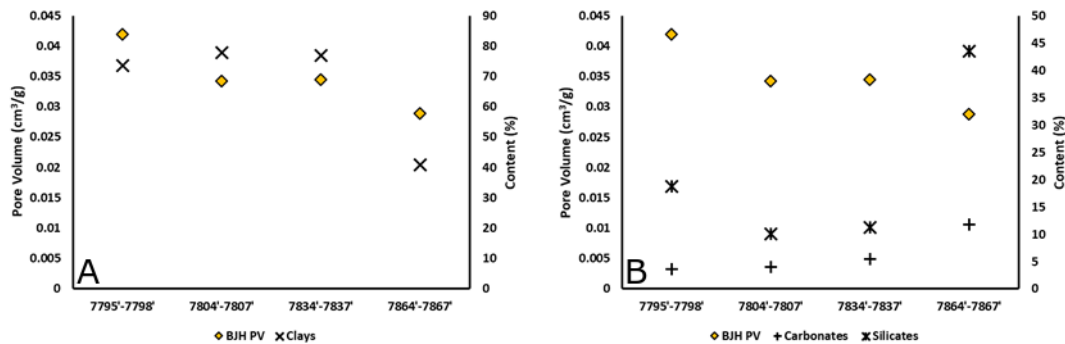


Figure 43: (A) BJH pore volume and the clay content, (B) BJH pore volume and the carbonate and silicate content. The BJH pore volume is shown with a yellow diamond (♦) in (A) and (B), the clay content with a cross (X), the carbonates with a plus (+) and the silicates with an asterix (*).

5.2.4.4. Total Organic Carbon Content (TOC%)

The total organic carbon (TOC%) was measured with RockEval pyrolysis and the results are displayed in Table 4, these results do not correlate to sample depth.

| Sample | TOC (%) |
|-------------|---------|
| 7795'-7798' | 6.88 |
| 7804'-7807' | 7.22 |
| 7834'-7837' | 4.39 |
| 7864'-7867' | 6.11 |

Table 4: TOC% for the Marcellus shale samples acquired through RockEval Pyrolysis.

The TOC% is plotted alongside the BJH pore volume (Figure 44A), the BJH surface area (Figure 44B), the BET monolayer capacity (Figure 44D) and the BET surface area (Figure 44D). From these results it can be seen that the TOC% correlates best to the properties derived from the BET model, and do not correlate well to the properties derived from the BJH model. As previously discussed (2.5.1.2. Brunauer-Emmett-Teller (BET) Model) the BET model takes into account data over the relative pressure range $0-0.35 \frac{p}{p_0}$ and best characterise smaller pores, whereas the BJH model takes into account data up to $0.995 \frac{p}{p_0}$ and better characterise the full pore range up to the largest pores. Consequently this correlation to the BET model shows that the TOC% has a greater impact on smaller pores, and does not correlate well when larger pores are involved in the comparison model. Resultantly it is likely that the TOC% is predominantly comprised of micro- and meso-pores, when there are a larger number of pores in this size range the sample surface area (overall) is considerably greater than a sample comprised predominantly of macro-pores.

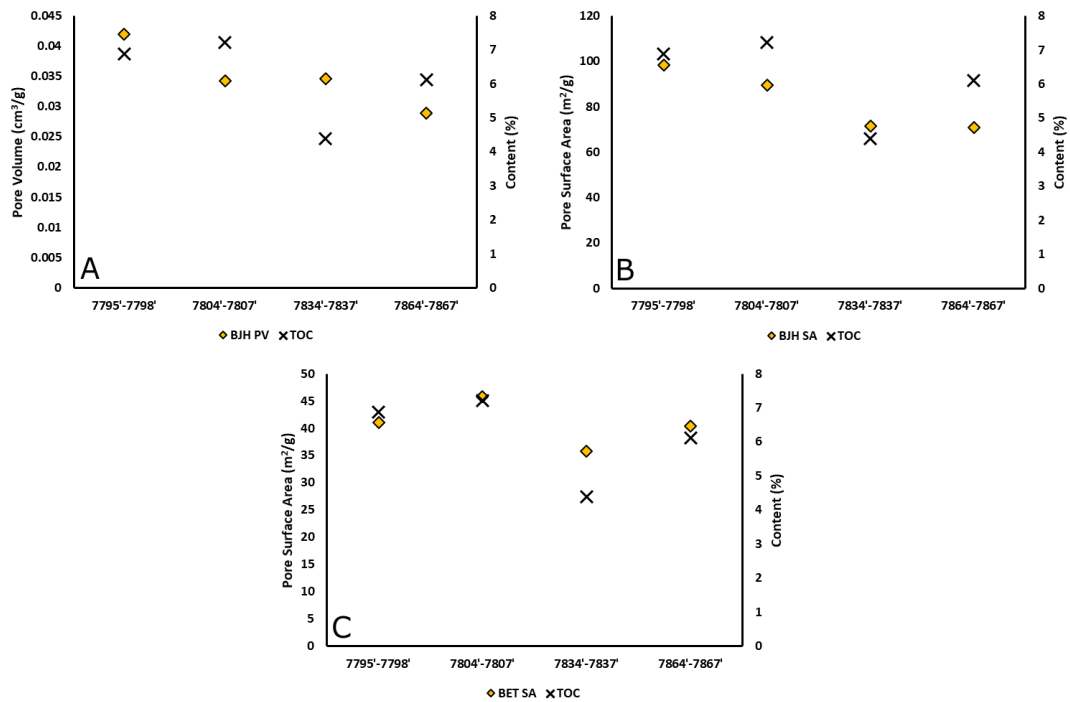


Figure 44: (A) BJH pore volume and the total organic content (TOC%), (B) BJH pore surface area and the total organic content (TOC%), (C) BET surface area and the total organic content (TOC%). The BJH pore volume and surface area, and the BET monolayer quantity adsorbed and surface area are shown by a yellow diamond (♦) and the total organic carbon is shown by a cross (X).

5.2.5 Numerical Modelling

5.2.5.1. Fractal Dimensions

Surface fractal dimensions take values between 2 and 3. A fractal dimension near 2 describes a material which has a small degree of surface roughness, while 3 describes a material with a large degree of surface roughness when analysing isotherms in the lower pressure range.

The fractal Brunauer-Emmett-Teller (fBET), one part fractal Frenkel-Halsey-Hill (fFHH) and two part fFHH as described in, 4.7.1. Fractal Dimensions, were used to calculate the fractal dimensions for the Marcellus shale (Figure 46). The specific values given by the models vary slightly, but the distribution of values for each sample is the same. Looking at Figure 46 it can be seen that the fBET and fFHH D_2 are roughly equal to each other, and that fFHH and Ffhh D_1 are roughly equal to each other; as a result of this the two part fFHH will be used for all further analysis.

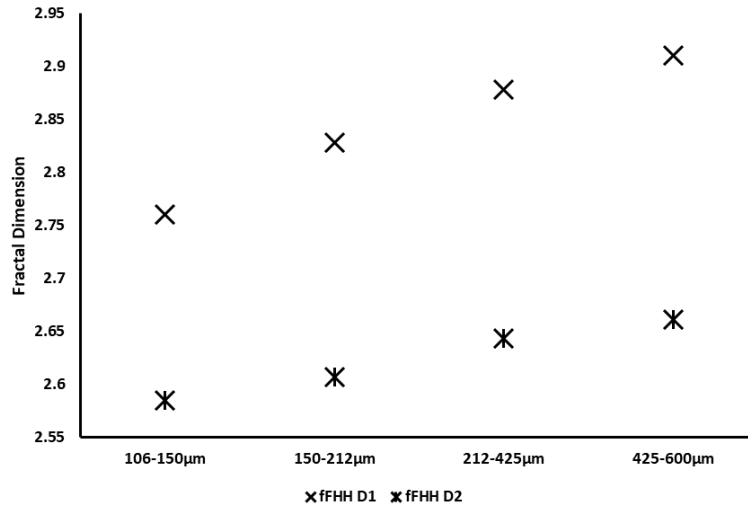


Figure 45: FHH D_1 (X) and D_2 (*) for the four grain sizes analysed of Marcellus 7795'-7798' showing an increase in fractal dimension with increasing grain size for both D_1 and D_2 . Parameters used are listed in Table 5.

| | D_1 | V_{m1} (cm ³ /g STP) | D_2 | V_{m2} (cm ³ /g STP) |
|------------------|--------------------------|-----------------------------------|--------------------------|-----------------------------------|
| 106-150µm | 2.584957 ± 0.00533 | 9.677809 ± 0.36481 | 2.760251 ± 0.00126 | 9.415164 ± 0.54008 |
| 150-212µm | 2.606905 ± 0.0052 | 9.662674 ± 0.46947 | 2.828004 ± 0.00136 | 9.185609 ± 0.36605 |
| 212-425µm | 2.64314 ± 0.00678 | 9.745059 ± 0.52893 | 2.877996 ± 0.00237 | 9.815396 ± 0.56182 |
| 425-600µm | 2.661345 ± 0.00475 | 9.781104 ± 0.30326 | 2.91078 ± 0.00138 | 9.381315 ± 0.63974 |

Table 5: parameters used to model the values presented in Figure 45.

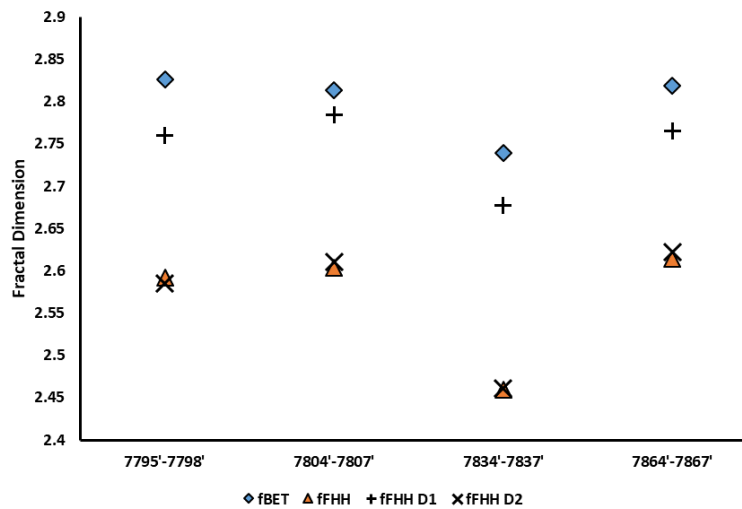


Figure 46: fBET (♦), fFHH (▲) and fFHH D_1 (+) and D_2 (X) compared with each other for the Marcellus shale samples. Parameters used are listed in Table 6.

| | fBET | | | fFHH 1 part | | fFHH 2 part | | | |
|--------------------|------------|--------------------------------|------------|--------------------------------|------------|-----------------------------------|------------|-----------------------------------|------------|
| | C | V_m (cm ³ /g STP) | D | V_m (cm ³ /g STP) | D | V_{m1} (cm ³ /g STP) | D_1 | V_{m2} (cm ³ /g STP) | D_2 |
| 7795'-7798' | 593.6277 | 10.36327 | 2.826387 | 9.751444 | 2.591414 | 9.677809 | 2.584957 | 9.415164 | 2.760251 |
| | ± | ± | ± | ± | ± | ± | ± | ± | ± |
| | 0.2328406 | 0.00962596 | 0.00126545 | 0.44490339 | 0.00250265 | 0.36480926 | 0.00533078 | 0.54008336 | 0.00126411 |
| 7804'-7807' | 939.3546 | 11.50698 | 2.813069 | 10.46507 | 2.603534 | 10.70661 | 2.610574 | 10.91071 | 2.784031 |
| | ± | ± | ± | ± | ± | ± | ± | ± | ± |
| | 3.3710178 | 0.00477268 | 0.00057855 | 0.58654607 | 0.0020235 | 0.57495926 | 0.00711447 | 0.6792774 | 0.00193069 |
| 7834'-7837' | 723.3531 | 9.057219 | 2.739446 | 8.762789 | 2.459025 | 7.973042 | 2.460745 | 8.082057 | 2.677463 |
| | ± | ± | ± | ± | ± | ± | ± | ± | ± |
| | 0.67809634 | 0.00877738 | 0.0017639 | 0.28077085 | 0.00360379 | 0.48374232 | 0.00329368 | 0.40722256 | 0.00127199 |
| 7864'-7867' | 947.6474 | 10.03812 | 2.818605 | 9.127238 | 2.614363 | 9.578161 | 2.622338 | 8.833256 | 2.76576 |
| | ± | ± | ± | ± | ± | ± | ± | ± | ± |
| | 0.67501327 | 0.0062052 | 0.00133906 | 0.36212667 | 0.00242908 | 0.49931534 | 0.0054801 | 0.45560395 | 0.00147689 |

Table 6: parameters used to model the values presented in Figure 46.

When the grain size increases for Marcellus 7795'-7798' the surface roughness (D_1) and network complexity (D_2) both increase (Figure 45) and are correlated to each other. This same trend is observed for the other Marcellus samples and it can be seen in Figure 46 that the surface roughness and network complexity are correlated to each other, e.g. where a surface is rougher, the pore network is also more complex.

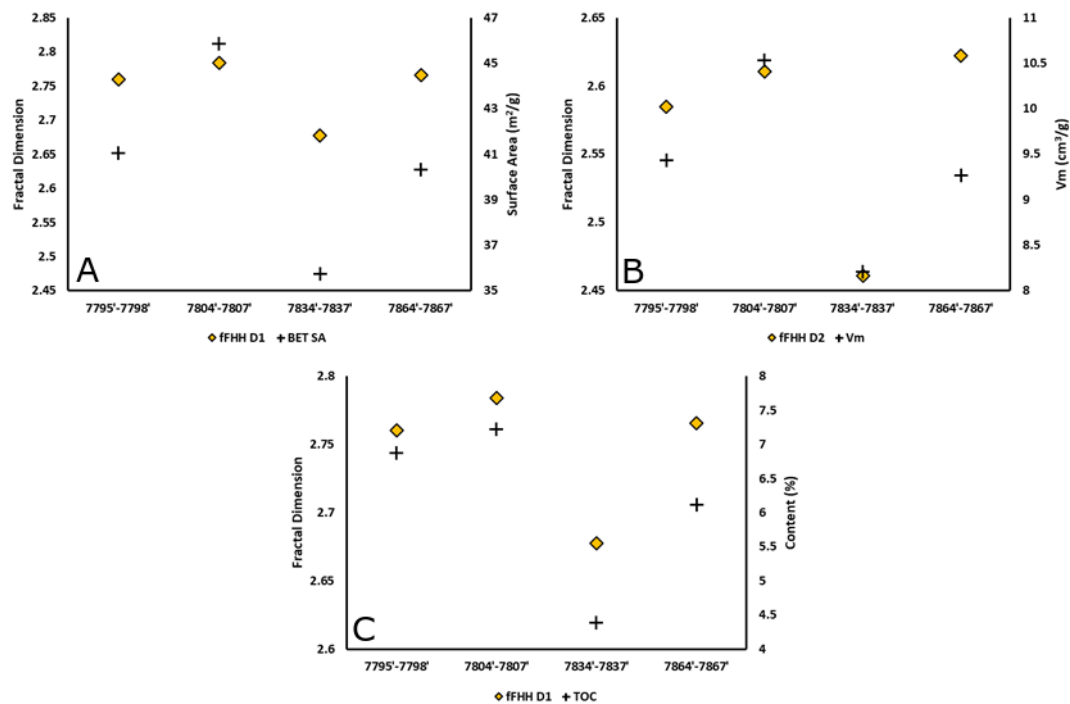


Figure 47: (A) the first fractal dimension, D_1 (+), for the FHH correlated to the BET surface area (♦), (B) the second fractal dimension, D_2 (+), correlated to the monolayer capacity V_m from the BET model (♦) and (C) the first fractal dimension, D_1 (+) for the FHH correlated to the TOC% (♦).

When compared with mineralogy the only component which correlates to the fractal dimensions is the TOC% (Figure 47C). So for an increased TOC% there is an increase in surface roughness denoted by the fractal dimension moving nearer 3 than 2.

5.2.5.2. Homotattic Patch

The trend between fFHH D_1 and TOC% (Figure 47C), is not as close a correlation as would be ideal since values of D_1 and TOC% for Marcellus 7834'-7837' and 7864'-7867' are significantly different. By

introducing the homotattic patch it is possible to model an organic portion of the isotherm and deconvolve this from the inorganic components contribution to the isotherm (inorganic components are jointly determined by the isotherm model at this point). Results show that (Figure 48) the k -value derived by the BET, FHH and nBET model, although inconsistent in value are consistent in distribution. Due to the previous correlation between fBET and fFHH D_1 (Figure 46) continued analysis will be made using the fBET model for analysis of the k -value.

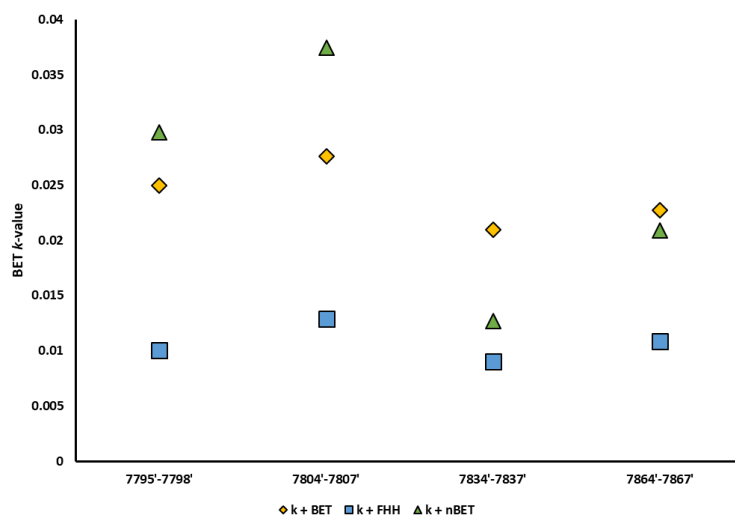


Figure 48: k -value derived by each of the isotherm models BET (♦), FHH (■) and nBET (▲). Although the specific values vary they are distributed in the same way. Parameters used are listed in Table 7.

| | fBET | | | | fFHH 1 part | | | | nBET | | | |
|--------------------|-----------------------------|--------------------------------|-----------------------------|-----------------------------|--------------------------------|-----------------------------|-----------------------------|-----------------------------|--------------------------------|-----|-----------------------------|--|
| | C | V_m (cm ³ /g STP) | D | k - value | V_m (cm ³ /g STP) | D | k - value | C | V_m (cm ³ /g STP) | N | k - value | |
| 7795'-7798' | 590.3138 ± 5.78451984 | 8.568361 ± 0.05056075 | 2.943722 ± 0.01732893 | 0.026183 ± 0.00143396 | 9.69434 ± 0.46005809 | 2.78117 ± 0.02796478 | 0.010015 ± 0.00458627 | 581.9901 ± 10.6377837 | 8.510361 ± 0.03006026 | 1 | 0.029965 ± 0.00047774 | |
| 7804'-7807' | 962.7471 ± 26.7429152 | 9.600161 ± 0.04825956 | 2.893206 ± 0.01259514 | 0.026731 ± 0.00095337 | 10.89604 ± 0.69354482 | 2.82521 ± 0.0585842 | 0.012862 ± 0.00828137 | 1032.309 ± 24.599136 | 8.505335 ± 0.02567783 | 1 | 0.042721 ± 0.0004918 | |
| 7834'-7837' | 928.5334 ± 14.7491158 | 8.414324 ± 0.05874202 | 2.898567 ± 0.01026656 | 0.022341 ± 0.00104109 | 8.302725 ± 0.47243446 | 2.684808 ± 0.04063623 | 0.009021 ± 0.00792398 | 721.908 ± 4.98886345 | 7.555324 ± 0.11913595 | 2 | 0.01244 ± 0.00150975 | |
| 7864'-7867' | 938.4165 ± 11.507666 | 8.384414 ± 0.08105509 | 2.908261 ± 0.01618001 | 0.022691 ± 0.00161758 | 9.054042 ± 0.49608852 | 2.7957 ± 0.02736852 | 0.010838 ± 0.00337037 | 921.7164 ± 15.4005075 | 8.344631 ± 0.01572368 | 1 | 0.02751 ± 0.00028998 | |

Table 7: parameters used to model the values presented in Figure 48.

From Figure 49 it can be seen that the correlation between the k -value and TOC% is improved in comparison to the correlation between fFHH D_1 and TOC% in figure Figure 47C.

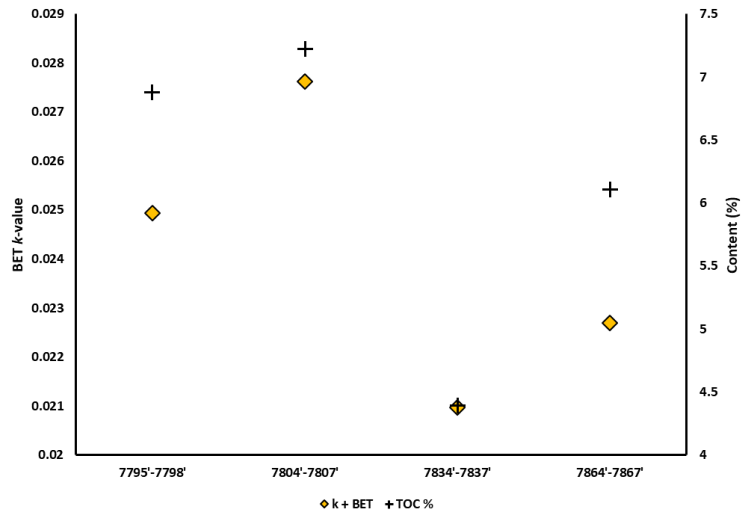


Figure 49: k -value from the BET model (♦) to the TOC% (+) from RockEval Pyrolysis where there is a correlation between the relative increase and decrease of values.

Extensions to the homotattic patch model can be made to include other models, and/or mineral phases where isotherm data is available, and the mineralogy known. From SEM MLA it is known that the dominant clay fraction in these Marcellus shale samples is illite, which also makes up the primary mineral phase of the samples. An N_2 gas adsorption isotherm for illite (Clay Mineral Society) was shared by Imperial College London to enable the development of the homotattic patch model.

The modelled illite constituent, i , produces a strong correlation to the clay content in the Marcellus samples (Figure 50B), similarly to the k -value the actual clay content value is not derived however the same distribution and relationship between the samples is demonstrated. Importantly the k -value when modelled alongside the i -value still maintains its correlation with the TOC% (Figure 50A).

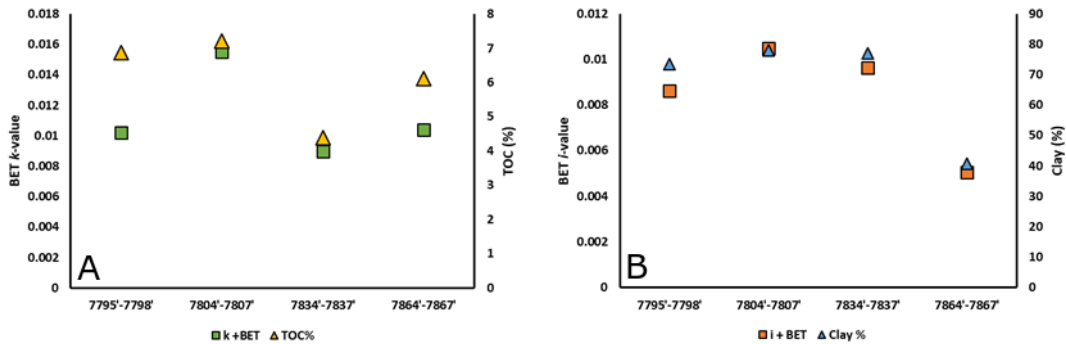


Figure 50: (A) kerogen modelled data, k -value (■) with the BET model from the 3 part homotattic patch and the TOC% (▲) showing a correlation between Marcellus 7804'-7807', 7834'-7837' and 7864'-7867', however the model underestimates the kerogen for Marcellus 7795'-7798' and (B) the illite modelled data, i -value (■) with the BET model from the 3 part homotattic patch and the clay % (▲) where the same correlation is observed for Marcellus 7804'-7807', 7834'-7837' and 7864'-7867' and the model underestimates the clay for Marcellus 7795'-7798'. Parameters used are listed in Table 8.

| | <i>C</i> | <i>V_m</i> (cm ³ /g STP) | <i>D</i> | <i>k – value</i> | <i>i – value</i> |
|--------------------|---------------------------|---|---------------------------|---------------------------|---------------------------|
| 7795'-7798' | 567.3987 ± 21.94609 | 9.003215 ± 0.473736 | 2.874483 ± 0.045858 | 0.010221 ± 0.00494 | 0.008612 ± 0.005623 |
| 7804'-7807' | 909.5686 ± 52.41047 | 9.874094 ± 0.249313 | 2.911871 ± 0.031874 | 0.015531 ± 0.007135 | 0.010493 ± 0.004964 |
| 7834'-7837' | 643.7726 ± 35.49937 | 7.813869 ± 0.358566 | 2.823984 ± 0.047003 | 0.008961 ± 0.00577 | 0.009643 ± 0.006108 |
| 7864'-7867' | 846.9443 ± 49.11641 | 8.699595 ± 0.513204 | 2.891237 ± 0.039122 | 0.010401 ± 0.006621 | 0.005056 ± 0.006247 |

Table 8: parameters used to model the values presented in Figure 50.

5.3. Discussion

5.3.1. Grain Size

Since the quantity adsorbed increases with decreasing particle size it is likely that the process of crushing has enhanced accessibility to the larger pore sizes by opening the pore network and reducing the complexity. For an increase in average grain size of four times (106-150µm to 425-600µm) there is only a reduction in quantity adsorbed of 0.78, this suggests that although quantity adsorbed decreases it is by an order of magnitude less than the grain sizes differ by. As a result of this finding, it may be possible to upscale to reservoir/formation scale with the use of a much smaller analysis sample than previously anticipated so long as the magnitude by which the quantity adsorbed varies continues to decrease with respect to the magnitude difference between changing sample size. It may also be possible to use the variation in quantity adsorbed with grain size to determine a potential spatial distribution of pores in the samples. Across grain sizes where there is little change to the maximum quantity adsorbed it can be inferred that over these ranges the pore network is very similar and the process of crushing does not create any significant physical changes. For example, if across the grain sizes 150-212µm and 212-425µm there was no variation to the measured isotherms it would indicate that there are no pore network variations which occur over the range from 150µm to 425µm which allows us to picture what the level of heterogeneity is within the sample. Where large changes to the maximum quantity adsorbed are observed it indicates that over that range of grain sizes there is significant variability in the distribution of pores and so results in significant changes to the pore network. By making these observations it is possible to determine an indication for the network complexity of the sample without conduction of fractal dimension analysis.

The same analysis can be done for the size of the hysteresis loop allowing a more precise understanding of the physical changes that have taken place in the pore network. In the isotherms for Marcellus shale all hysteresis closure takes place at $0.5 \frac{p}{p_0}$ which relates to cavitation and the emptying of larger pores through pore necks <4nm. When there is a large change in the hysteresis loop it means that the process of crushing has removed a lot of pore blocking within pore networks. By observing where this significant change occurs it allows you to define a threshold over which the pore network becomes more accessible i.e. large hysteresis at 212-425µm which significantly reduces at 150-212µm tells us that the pore network is more complex for grains larger than 212µm due to the presence of many pore necks which are <4nm in size, compared to grains smaller than 212µm where alternative routes around the neck sizes <4nm have been exposed allowing the adsorbate to desorb more easily from the sample. If there is little change to the hysteresis loop this would signify that although more pores have been made accessible there is no alteration to the leading neck size of the pores and there remains the same quantity of <4nm pores. For the Marcellus 7795'-7798' the hysteresis across all grain sizes is consistent showing that over the size range 106-

600 μm there is no significant change to blocking by pore necks of sizes <4nm and these exist pervasively throughout all samples.

By analysing the isotherms more broadly it is possible to identify at which particular point pore sizes are opened and made more accessible. For the Marcellus 7795'-7798' all isotherms overlay each other until just over $0.5 \frac{p}{p_0}$ the hysteresis closure for cavitation. Beyond this point isotherms begin to separate with 106-150 μm and 150-212 μm separating from 212-425 μm and 425-600 μm at $0.6 \frac{p}{p_0}$ (separation 1). 212-425 μm and 425-600 μm do not diverge from each other until $0.75 \frac{p}{p_0}$ (separation 2), then 106-150 μm and 150-212 μm do not diverge until $0.9 \frac{p}{p_0}$ (separation 3). This relates to pores >3nm for separation 1, >5nm for separation 2 and >11nm for separation 3. When the BET model is used for the analysis of sorption data, only relative pressure values up to $0.35 \frac{p}{p_0}$ are used. As a result of this the differences in the isotherms for grain size are not reflected in the BET surface area and monolayer capacity because isotherms do not diverge until relative pressures $>0.6 \frac{p}{p_0}$. Taking this into account it is clear that results must be evaluated across the entire range of relative pressures due to variations which do not necessarily present at the lower pressure ranges.

The pore size distributions show a consistent dependence on grain size, when the grain size is smaller there is an overall larger pore surface area and pore volume. However, the relationship between grain size and the pore size distributions is influenced by the surface area to volume ratio of pores, where larger pores have a greater impact on the pore volume than the surface area, and smaller pores have a greater impact on the surface area than the pore volume. For example, if you were to take a cube with 1cm length sides the surface area is 6cm² and the volume is 1cm³ resulting in a surface area to volume ratio of 6cm⁻¹. If you change the 1cm cube to a 2cm cube you end up with a surface area of 24cm² and a volume of 8cm³ and a surface area to volume ratio of 3cm⁻¹. In application to pore sizes macro-pores have a much smaller surface area to volume ratio compared to micro-pores which have a larger surface area to volume ratio. Consequently the grain size differences are only truly reflected in the cumulative pore volume pore size distribution at the greater pore sizes since the process of crushing more greatly impacts accessibility to larger pores. For the cumulative surface area only the finest grain size shows any difference to the other samples.

5.3.2. Depth

Although the isotherm results (Figure 31 and Figure 32) are correlated to depth there is variation in the pore size distribution (Figure 33 and Figure 34) and hysteresis which are not depth correlated. Marcellus 7834'-7837' has a similar quantity of larger pores as Marcellus 7804'-7807' but a lot fewer smaller pores, although hysteresis loops are not solely dependent on the pore size, the wider hysteresis loop for Marcellus 7834'-7837' does signify the presence of many pores >4nm spatially arranged such that cavitation takes place. At very low relative pressures ($<0.05 \frac{p}{p_0}$) the isotherm for Marcellus 7804'-7807' (Figure 31) immediately diverges from Marcellus 7834'-7837' and 7864'-7867' showing it has a considerably larger number of micro-and fine meso-pores. After this initial divergence, the isotherms for 7804'-7807' and 7834'-7837' run parallel to each other until $0.6 \frac{p}{p_0}$ when 7834'-7837' converges on 7804'-7807' and they resultantly reach $\frac{p}{p_0} = 0.995$ at the same quantity adsorbed. The result of this is that Marcellus 7834'-7837' has a greater number of large meso- and small macro-pores than Marcellus 7804'-7807'. Marcellus 7864'-7867' diverges from both samples at low relative pressure and does not converge again like 7834'-7837' did demonstrating a lower quantity of all pore sizes.

The mercury intrusion porosimetry also reflects this variation in pore size distribution where the intrusion curves for 7804'-7807' and 7834'-7837' cross each other. At lower pressures Marcellus 7834'-7837' has a greater volume of intruded mercury (Figure 35) demonstrating that there is a greater number of larger pores accessed easily by mercury, at higher pressures Marcellus 7804'-7807' intrusion increases above Marcellus 7834'-7837' (Figure 35) where more smaller pores have been filled in comparison.

Due to the variability with depth across gas sorption isotherms (Figure 31 and Figure 32), pore size distributions (Figure 33 and Figure 34) and mercury intrusion porosimetry (Figure 35), it is likely that data is better correlated to factors such as depositional environment, structural history and mineralogy.

5.3.3. Mineralogy

Since clays have a much greater surface area than minerals like quartz and carbonates the expectation is that surface area could directly correlate to clay content, however the Marcellus results do not support the hypothesis that surface area is correlated to clay content. Marcellus 7864'-7867' has the smallest quantity of clay (40.805%), but does not have the smallest BET surface area (40.33 m²/g). On the other hand Marcellus 7834'-7837' has the greatest quantity of clay (79.96%), but the smallest BET surface area (35.726 m²/g). Despite the large surface areas associated to clays (>20 m²/g) (Diamond and Kinter, 1956; Kini *et al.*, 2005; Macht *et al.*, 2010; Lammers *et al.*, 2017), the BET surface area does not correlate with clay content. Additional investigation shows that the BET surface area for the Marcellus samples, instead, correlates to TOC% (Figure 44D). From this it is clear that the primary influence on shale surface area is the TOC% however the correlation in Figure 44D shows some variation. The variations identified are where the TOC% for Marcellus 7804'-7807' plots below the BET SA, where for the other samples the TOC% plots above the BET surface area. As a consequence of this it is hypothesised that although TOC% is the primary influence on the BET surface area, in the presence of a large quantity of a low surface area mineral the resultant BET surface area will be altered to reflect this.

Figure 36 (Table A5.1. 1) for the mineralogy of the Marcellus shale shows that Marcellus 7804'-7807' in addition to having the greatest TOC% (7.22%) also has the lowest quantity of silicates (10.095%) which are known to have a very low surface area (Meloni *et al.*, 2012; Pennell, 2016), and one of the largest clay quantities (77.945%) known to have a large surface area. This may explain, and demonstrates how although TOC% has the primary influence on BET surface area, other minerals are still impactful to these correlations. The surface area of organic matter however is highly variable depending on the type and maturity of the specific kerogen in the sample.

The surface area is considered to be the most significant property with respect to reservoir production as the majority of methane is stored by adsorption on the pore walls. Since most methane is stored by adsorption the accurate evaluation of sample pore surface area is necessary to industry so accurate gas-in-place estimations can be made. However, the pore volume and minerals which are known to retard or create buffers to flow are mechanically important to understand since they will impact the producibility of a reservoir.

5.3.4. Numerical Modelling

Wang *et al.*, (2015) have identified the fractal dimensions results to be significant to the understanding of material surface properties, since samples with a larger D_1 (the surface fractal dimensions) will have a rougher surface and provide more adsorption sites and consequently own relatively higher adsorption capacities. D_1 is most greatly impacted by the presence of micro- and fine meso-pores as a result of their large surface area to volume ratio, since macro-pores have a small surface area to volume ratio they do not significantly impact D_1 . Results show that for an

increased TOC% (Figure 47C) there is an increase in surface roughness denoted by the fractal dimension moving towards 3 and further away from 2. The significance of this is that with an increased TOC% the increase in surface roughness results in more adsorption sites for either methane production or for carbon storage. Marcellus 7834'-7837' is the only sample with a fractal dimension, D_1 , less than 2.5 suggesting that it may have an overall smoother surface than the other samples. Given this low value for the fractal dimension, combined with the lowest surface area it is clear that there is a physical difference to this sample which lead to variations from the sample population.

It is also necessary to consider the second fractal dimension, D_2 , taken at higher pressures and describing the pore network complexity. At values near 2 the pore network is open and easily accessed by the adsorbate, for values near 3 the network is complex and not easily accessible. Although D_1 was impacted by the presence of micro- and fine meso-pores, D_2 is not impacted by macro-pores within the sample. D_2 is concerned with the complexity of pore neck sizes where a greater degree of heterogeneity is likely to result in more narrow neck sizes. Where the ratio between the neck size and pore body is near 1:1 it suggests that there is a low level of heterogeneity and so the network complexity should be low ($D_2 = 2$). As the ratio of the pore neck to pore body moves from unity the heterogeneity in the pore network increase and so the complexity is likely to increase reflected in a fractal dimension of $D_2 = 3$.

The pore filling properties are most affected by D_2 since a large value suggests a complex pore network with a high degree of heterogeneity in the size difference between pore necks and pore bodies. Consequently, samples with a large value of D_2 may not be easily accessible, as a result even if a sample has a large value for D_1 (greater adsorption capacity) but the value of D_2 is also large (complex network) it is likely that production or storage in this sample could be very difficult. Although D_2 correlates to the monolayer capacity from the BET model it is not necessarily the case that D_2 will correlate to all pore filling (volume) properties. For example the pore volume may be large but easily accessed due to a near 1:1 ratio of the pore neck and body resulting in a sample with low level of heterogeneity, on the other hand the volume could be small but not easily accessed resulting in a large fractal dimension. In this instance the graph would demonstrate an inverse relationship to the fractal dimension and pore volume.

When the grain sizes are varied the changes to the fractal dimensions can be observed (Figure 45), for an increasing grain size both fractal dimensions increase, although D_2 is most affected. This is the expected result for D_2 as for a smaller grain size you would anticipate the degree of network complexity to be reduced due to the opening of previously closed pores, and additional networks being provided to the desorbing adsorbate. Larger grain sizes however have more closed pore space and fewer alternative paths for the adsorbate to desorb via, so this results in an increasing value for D_2 with increasing grain size. For D_1 however this result shows that it is not solely dependent on the quantity of micro and fine meso-pores opened by the process of crushing and increasing the accessibility of the adsorbate to these pores. This shows that surface roughness is also correlated to the grain size which was not previously hypothesised, and so it must be considered whether D_1 is a true measure of the internal surface roughness, or if it is also a measure of the external surface roughness. If this is the case then this is a systematic error which will need to be investigated further and considered in future fractal dimension analysis.

The fractal dimension results (Figure 47C) indicate that the TOC% has the greatest impact on D_1 , by using the homotattic patch it is possible to derive a value (k -value) which represents the contribution of the kerogen phase to the isotherm. When the k -values are plotted with the TOC% (Figure 49) it can be seen that the distribution between more closely reflects that of the actual TOC%. As a result of this it may be possible in future to use the homotattic patch as an indication for

relative TOC% within a formation where experimental analysis is not available. When a second mineral phase (illite) was introduced to the model the results (*i*-value) of this mineral phase correlated to the mineralogy results from SEM MLA (Figure 50B), without affecting the correlation of the *k*-value to the TOC% (Figure 50A).

Although the *k*- and *i*-values derived from the homotattic patch are not the same as the values from SEM MLA it is possible that the model provides a “measure of influence” of the mineral on the overall isotherm. For example, the Marcellus 7795’-7798’ has an *i*-value (illite contribution) of 0.0086 and *k*-value (kerogen contribution) of 0.0102, despite having a clay content and TOC% of 73.515% and 6.877% respectively. When the ratio of the mineral content from SEM MLA multiplied by the BET SA (illite 33.7202 m²/g and kerogen 342.2751 m²/g) is compared to the ratio of the *k*- and *i*-value (13. 1) they are the same (Figure 51).

$$\frac{\text{mineral}_1\% \times \text{BET SA}_1}{\text{mineral}_2\% \times \text{BET SA}_2} = \frac{n_1}{n_2} \quad (13. 1)$$

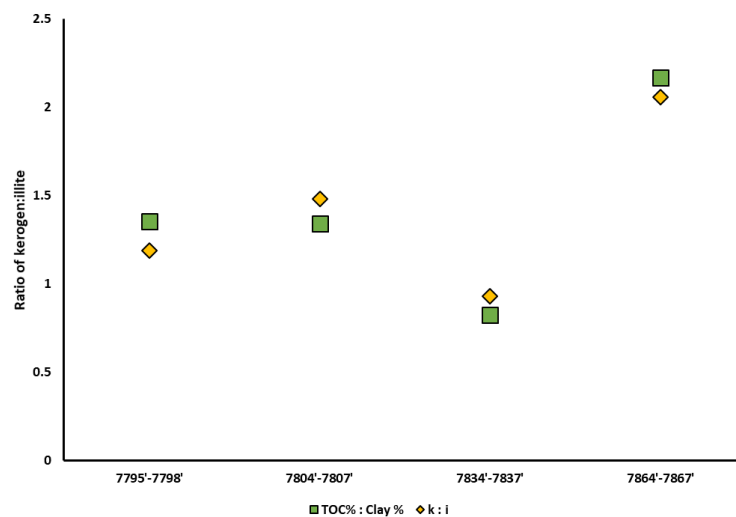


Figure 51: ratio of TOC% to clay content (■) for experimental and homotattic patch values (◆), where there is a strong correlation between these values showing that the ratio of derived values is equivalent to the ratio of surface area contributions from experimental work.

This extension to the homotattic patch analysis is not yet fully proved however the success so far of the homotattic patch at this early stage is encouraging for future developments to the model.

5.4. Conclusion

The process of crushing a sample creates more pore volume, but does not have an impact on the pore surface area as micro-pores are not significantly altered by the process of crushing. It has been shown that with study of more grain sizes forecasting could be used on the quantity adsorbed to predict the results of much larger samples. Marcellus samples 7804’-7807’, 7834’-7837’ and 7864’-7867’ are depth correlated by their isotherms however not correlated by BET surface area and monolayer capacity. It is likely that samples correlate more strongly with mineralogy than they do with depth. TOC% and clay content have the strongest correlation to surface area and pore volume of the samples, where carbonates and quartz can have a negative correlation to these properties. Mineralogy is not simply defined and the ratio of various minerals has a greater impact than the presence and quantity of one mineral independently. By using the fractal dimensions and homotattic patch it is possible to deconvolute some of the constituents of the samples and derive values which describe the surface and network properties of the samples which produce a good correlation to the surface area and volume.

6. The Utica Shale

6.1. Materials

Fifteen samples of the Utica shale were provided by Virginia Polytechnic Institute and State University, drilled by CNX Gas Company in July 2012. Samples were drilled in Potage County, Ohio and span the depth range from 5800' to 6106' (306') in a series of 3 feet steps (Table 9), for some core from each foot of the 3 foot section were provided and for others just one section of the 3 foot section was provided. All samples were analysed as 106-150µm grains (powder), or as 3-5mm chips where grains were unsuitable for the experimental technique.

| Sample | Carbonates | Clays | Silicates | TOC% | Ro% |
|---------------|------------|--------|-----------|------|-------|
| 5800'-5803' | 24.9 | 50 | 19.115 | 2.97 | 0.796 |
| 5860'-5863' | 25.115 | 58.985 | 12.025 | 2.33 | 0.958 |
| 5869'-5872' | 29.945 | 49.955 | 17.025 | 1.36 | 0.922 |
| 5872'-5875' 1 | 15.565 | 58.925 | 19.385 | 1.79 | 0.94 |
| 5872'-5875' 2 | 22.265 | 55.325 | 17.985 | 1.65 | 0.85 |
| 5875'-5878' | 41.285 | 33.68 | 20.93 | 1.27 | 0.904 |
| 5899'-5902' 1 | 33.015 | 44.755 | 16.385 | 1.2 | 0.958 |
| 5899'-5902' 2 | 30.8 | 44.855 | 17.72 | 1.38 | 0.958 |
| 5899'-5902' 3 | 28.45 | 49.765 | 16.74 | 1.46 | 0.976 |
| 5998'-6001' 1 | 53.96 | 28.02 | 15.265 | 2.67 | 0.976 |
| 5998'-6001' 2 | 55.865 | 25.375 | 13.96 | 4.33 | 0.976 |
| 6102'-6103' | 79.56 | 10.015 | 5.41 | 0.28 | 0.94 |
| 6103'-6106' | 62.35 | 0.565 | 32.91 | 0.27 | 0.76 |
| 6102'-6106' 1 | 78.75 | 9.41 | 8.185 | 0.39 | 1.048 |
| 6102'-6106' 2 | 86.29 | 4.28 | 6.67 | 0.18 | 1.048 |

Table 9: sample depths, mineral content, TOC% and Ro% the thermal maturity given by (14. 1) (Jarvie et al., 2005) for all Utica samples. Carbonates are comprised of limestone and dolomite; clays are comprised of illite, kaolinite and goethite; silicates are comprised of quartz, muscovite and albite.

$$R_o\% = 0.018T_{max}(^{\circ}C) - 7.16 \quad (14. 1)$$

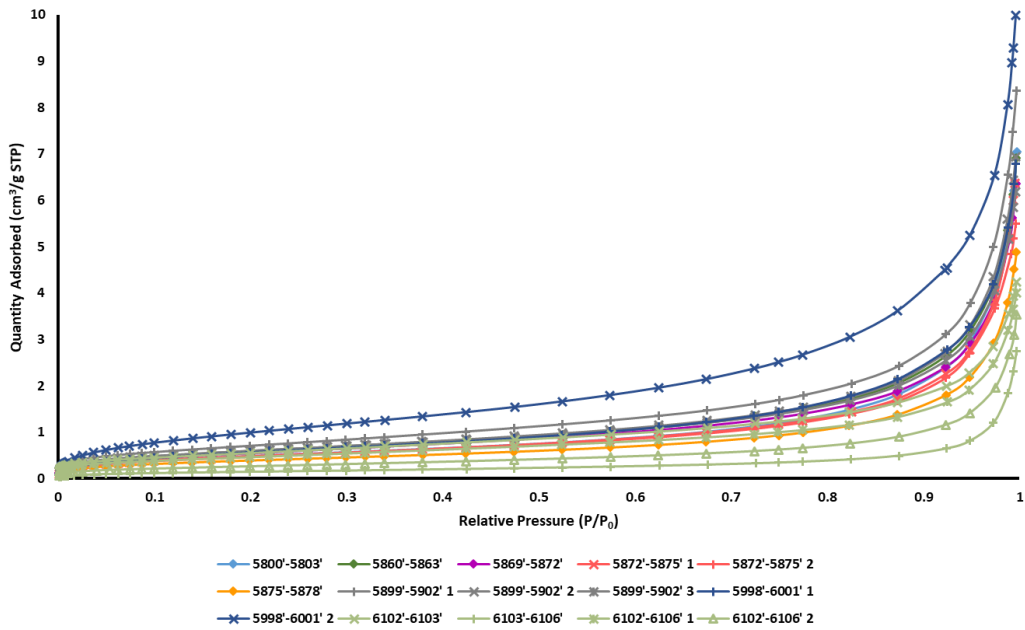


Figure 52: N_2 gas adsorption branch for all samples, desorption branches are omitted to make the data clearer. Samples are grouped by colour where there are multiple samples from a single 3 foot core. In the N_2 sorption experiments there is no correlation to depth, however samples over the depth range 6102'-6106' consistently have the lowest uptake.

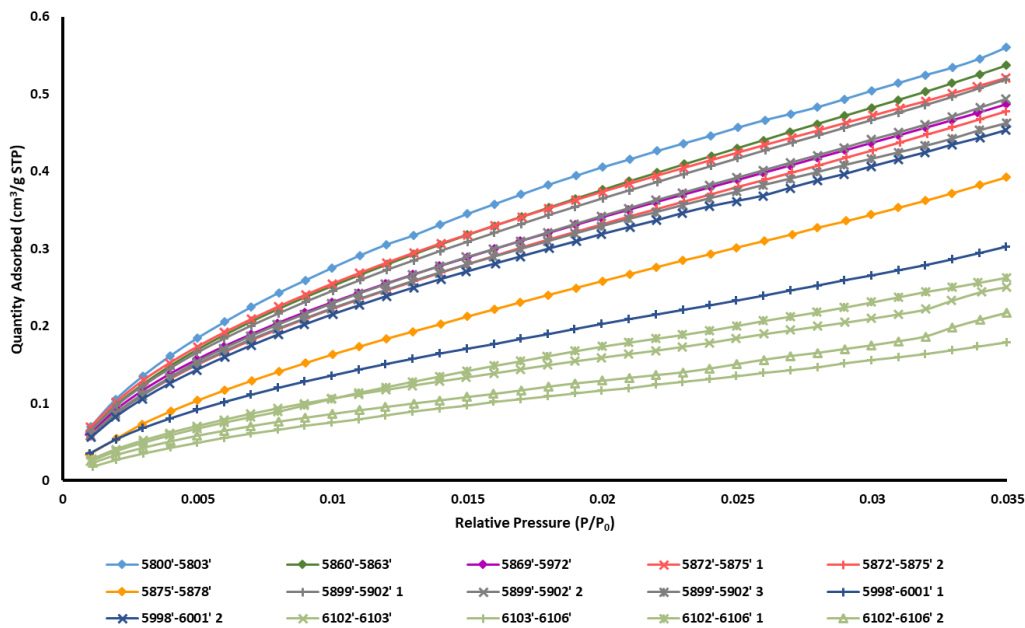


Figure 53: CO_2 gas adsorption branch for all samples, desorption branches are omitted to make the data clearer. Samples are grouped by colour where there are multiple samples from a single 3 foot core. In the CO_2 gas sorption experiments there is some correlation to depth at the extreme ends, however the samples between are not as neatly correlated.

Samples were collected from the Upper Ordovician Utica and Point Pleasant Formations, major shale gas plays, in the Appalachian Basin (Colton, 1961; Brinkley, 2016; Sweda, 2019), where the Utica shale accumulated in a deepening foreland basin (Colton, 1961; Sweda, 2019). Deposition of this transgressive sequence (Wickstrom, 2013) is characterised by the transition from shallow marine carbonates of the Point Pleasant Formation to siliciclastic mudstones of the Utica Formation (Patchen and Carter, 2015) which transition between formations marked by generally elevated total organic carbon (TOC%) concentrations (Hickman *et al.*, 2015), Figure 54. The Utica Formation samples are fine grained light to dark grey calcareous mudstones. As the depth decreases the quantity of carbonates also decreases resulting in reduced evidence of bioturbation and more clearly

defined laminations, from 6102' and deeper it is believed to be the Point Pleasant Formation which is a calcareous grey mudstone with abundant thin 0.5-4cm interbedded light grey limestone.

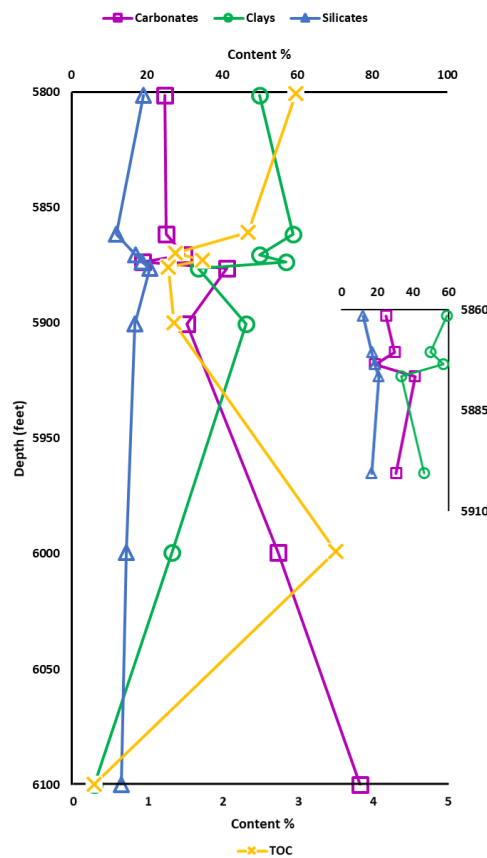


Figure 54: relationship of carbonates (empty \blacksquare), clays (empty \bullet), silicates (empty \blacktriangle) and TOC% (\times) with depth. Where there are multiple samples per 3 feet of core the quantities have been averaged in order to show the overall trend as simply as possible. The smaller graph superimposed on the larger graph more clearly shows the trend over 5860'-5900' feet.

Due to the conclusions made in 5. The Marcellus Shale that shale properties are more strongly correlated to depositional environment than they are depth, five Utica samples were selected for more detailed analysis based on Figure 54 so that the transition of carbonate-rich to clay-rich lithotype is captured and comparisons can be made.

The five selected samples were from depths 5800'-5803', 5872'-5875', 5998'-6001', 6102'-6103' and 6103'-6106' and will be referred to as U1, U2, U3, U4 and U5 respectively. Samples U1 and U2 are from the Utica Formation, U3 from the base of the Utica Formation where it transitions into the Point Pleasant Formation, and samples U4 and U5 represent the Point Pleasant Formation. They are defined such that there is an increasing carbonate content with increasing depth, and a decreasing clay content with increasing depth. These five samples were also chosen to capture the variation in TOC% which is not depth correlated and to observe the impact that this has on the overall properties of the shale such as surface area, pore volume and connectivity.

6.2. Methodology

All samples underwent conventional nitrogen (N_2) (Figure 52) and carbon dioxide (CO_2) (Figure 53) gas sorption analysis at 77K and 273.15K respectively using a Micromeritics 3Flex physisorption analyser. Analysis was carried out over the relative pressure ($\frac{p}{p_0}$) range 0-0.995 (N_2) and 0-0.035 (CO_2). As well as scanning electron microscopy mineral liberation analysis (SEM MLA), carried out on an FEI Quanta 600 (operated at 20kV, working distance of 13mm and spot size 7) equipped with

mineral liberation analysis software by JKTech/FEI which enables the quantification of sample mineralogy by taking several energy dispersive X-ray (EDX) points. RockEval pyrolysis (carried out by the British Geological Survey) was additionally used to determine the mineralogy and total organic carbon content (TOC%). Analysis was carried out in line with that described in 4. Methodology.

Following the completion of these analysis results were analysed and this provided the information to guide selection of the five samples based on previously recognised rationale. The five selected samples then underwent the further methodology (experimental and numerical) described in the rest of the chapter.

6.2.1. Mercury Intrusion Porosimetry

Samples were oven dried overnight at 100°C in order to remove any pore water that may be present within the sample. Once dried, samples were prepared for mercury intrusion porosimetry (MIP) where they underwent low- and high- pressure analysis at ambient temperature and constant volume. Low-pressure analysis was carried out up to 207 MPa, and high-pressure to 414 MPa on a MicroMeritics AutoPore IV 9500, before mercury was extruded and the system returned to ambient pressure.

6.2.2. Computerised X-ray Tomography (CXT)

Following mercury porosimetry, CXT was carried out on an Xradia Versa XRM-500. The Xradia Versa XRM-500 is a high-resolution 3D X-ray CT system capable of submicron resolution. The samples were scanned with source parameters 140kV and 71µA with a resulting pixel size of 6.7997µm.

6.2.3. Nitrogen Overcondensation

The overcondensation experiments were carried out on a Micromeritics ASAP 2020 physisorption analyser using a method similar to that described by Murray *et al.*, (1999). The equilibration times used were 20s and 60s. Two different times were tested to ensure that the sample isotherm was fully equilibrated. The samples were outgassed at 140°C for 2 hours under vacuum prior to analysis. In the overcondensation experiment, the first stage is to increase the pressure in the sample tube to higher than the saturated vapour pressure of nitrogen. This pressure increase should facilitate sufficient condensation such that even the biggest pores are filled with liquid nitrogen at the start of the overcondensation desorption isotherm, which will probably inevitably also involve some bulk condensation in the sample tube. This bulk condensation is what is avoided in the conventional experiment. The required period to reach this stage is dependent upon the sample size and the pore volume. While it does not matter if the volume of condensate is much higher than that needed for complete pore filling, the total duration of the experiment would be much longer in that case. Once complete pore-filling had been achieved, the pressure was lowered to just below the saturated vapour pressure of nitrogen such the bulk condensate vaporized completely while keeping all the sample internal porosity liquid-filled. Once this stage has been accomplished, the first data point on the overcondensation desorption isotherm can be measured. This point corresponds to the total pore volume of the sample, following this the pressure is decreased in small steps before desorption then continues in the usual way.

6.3. Results

6.3.1. Sample Petrology

The major mineral composition of the samples as determined using MLA varies as expected (Figure 55 with the Point Pleasant Formation samples U4 and U5 enriched in carbonate and the Utica Formation samples enriched in clay. The Utica Formation ranges from 25-59% illite content and the Point-Pleasant Formation 0.5-10%. Less than 1% kaolinite was observed in all samples and any other clay fractions were too small to resolve. Carbonate minerals identified are limestone and dolomite, the latter associated with localised fracturing. In the Utica Formation carbonates make up 15-56%

with no dolomite. In the Point Pleasant formation carbonates make up 63-80% with 2% and 10% dolomite in samples U5 and U4 respectively. The silicates present in the samples are primarily quartz and muscovite with some small quantities of albite identified; for the Utica Formation (U1, U2 and U3) silicates comprise 13-20% and 5-33% for the Point Pleasant Formation (U4 and U5). Several sulphides and oxides were also identified however these do not contribute more than 2% in any sample when combined. TOC% peaks in sample U3 from the base of the Utica Formation and is generally higher in samples (U1, U2) from the Utica Formation than those in the Point Pleasant Formation (U4, U5).

Detailed examination of sample textures (Figure 57, Figure 59, Figure 61, Figure 63 and Figure 65) indicates that the Utica Formation samples are characterised by bioclastic carbonates with intra-particle calcite cement in a fine grained illite and quartz grain matrix. Organic carbon is observed as discrete particles running parallel to bedding compacted around neighbouring siliciclastic grains. However the Point Pleasant samples are characterised by authigenic carbonates which have undergone some dolomitisation. In U5 there is some fine grained illite, however U4 is made up of a fine-grained illite matrix with coarse grained authigenic carbonate cement within it. Organic carbon is not observed in U5, but is observed in discrete particles in U4.

The Utica Formation consists of dark grey to brown calcareous shale often laminated and bioturbated, with a TOC% of approximately 3.5% (Smith, 2013). Samples (U1 and U2, Figure 58 and Figure 60 respectively) are predominantly siliclastic siltstones with lesser amounts of bioclastic material (Table 9). The matrix is dominated by illite with lesser amounts of calcite cement. Whether the illite is primary or secondary was not determined. Organic matter is present as discrete particles or agglomerations (Figure 59). U3 (Figure 62) is taken from the base of the Utica Formation which is defined to be organic and carbonate rich (Hickman *et al.*, 2015).

The underlying Point Pleasant Formation is overall defined by an organic-rich, calcareous shale with interbedded limestone. The Upper interval of the Point Pleasant Formation (such as samples U4 and U5 in Figure 64 and Figure 66, respectively), however, is an organic-poor grey shale with abundant thin limestone beds. A TOC% of <1% (Figure 55) is typical of this interval with low organic carbon and intermediated composition in terms of the balance between siliclastic and bioclastic material. The lower interval of the Point Pleasant Formation (below the samples studied here) is much more carbonate rich, with an average TOC% of 4%–5%, is a storm-influenced formation, and has common burrows, even in the organic-rich facies (Luft, 1971; McDowell, 1986; Hickman *et al.*, 2015). In the locations of the borehole, from which the samples studied here were obtained, the formations were deposited on a storm dominated shelf, hypothesised to have been part of a semi-enclosed epicontinental sea (Popova, 2017).

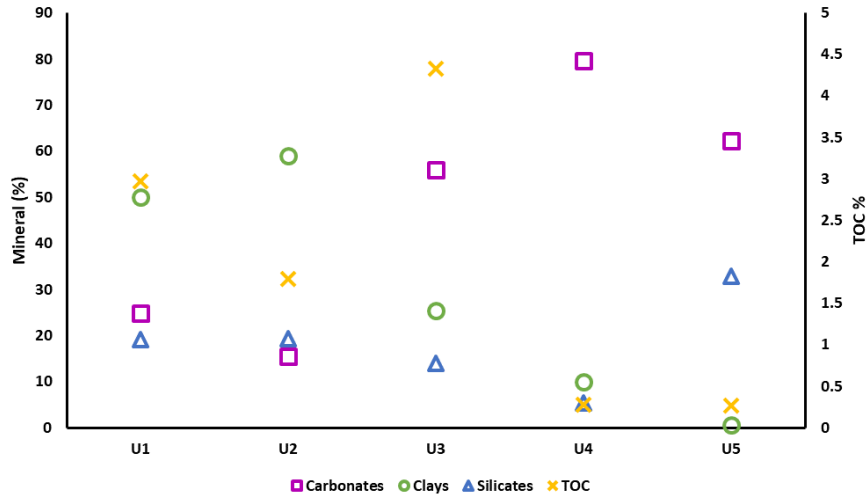


Figure 55: variation of mineral composition for the Utica shale samples U1 to U5. Carbonates (empty \square) and clays (empty \bullet) are inversely correlated to each other with increasing carbonate content and decreasing clay content with depth. Silicates (empty \triangle) show an overall decreasing correlation with depth, however there is a spike in U5 where the silicate content is almost twice at any other depth. TOC% ($+$) also shows an overall decreasing correlation with depth but has a spike at U3 where the TOC% is significantly greater than for any other sample.

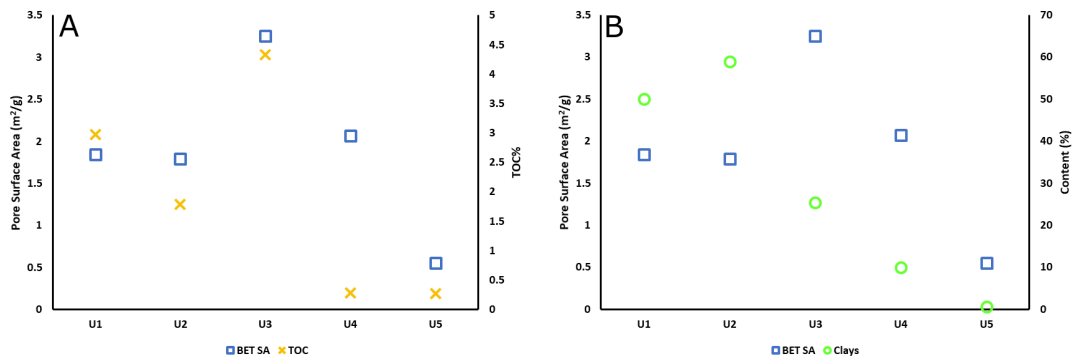


Figure 56: (A) the TOC% and BET surface area and (B) the clay content and the BET surface area.

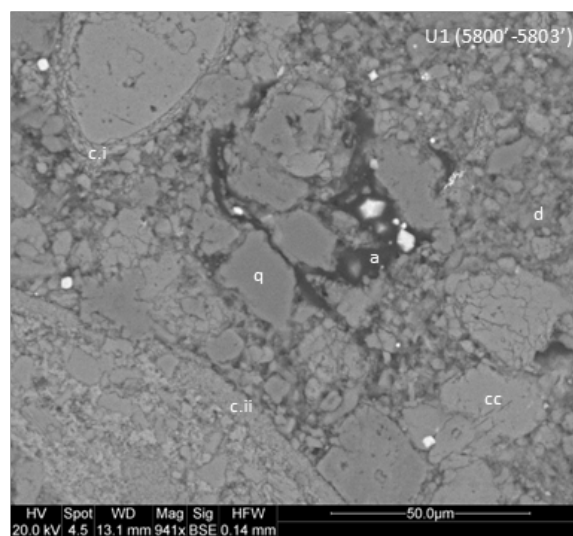


Figure 57: a typical electron micrograph of sample U1, with mud to silt-sized quartz (q) and bioclastic calcite (cc) grains in an illite matrix (d) with intra and inter granular calcite cement (cc).

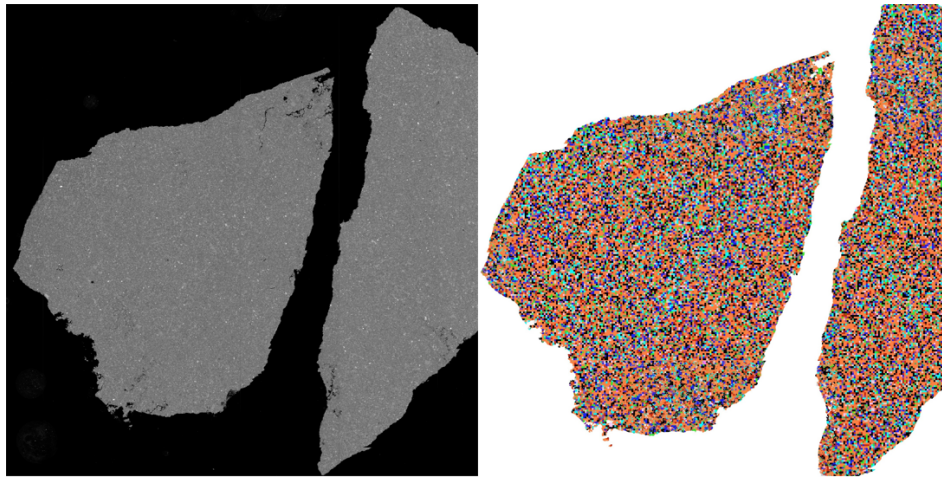


Figure 58: U1 BSE and corresponding mineral map showing the clay sized particle matrix dominated by illite (orange) with interspersed grains of quartz (blue) and carbonate (turquoise), with 5mm scale bar.



Figure 59: An electron micrograph of a typical sample U2, with mud to silt-sized quartz (q) and authigenic calcite (cc) grains within an illite (d) matrix with some finer-grained silicate and carbonate material. Some inter-particle calcite cements (cc).

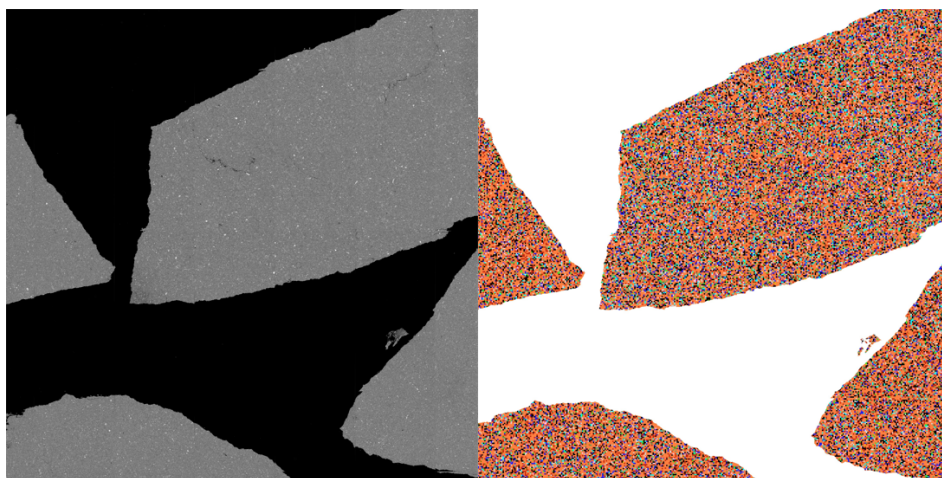


Figure 60: U2 BSE and corresponding mineral map demonstrating the same clay sized particle matrix dominated by illite (orange). Compared to U1 there are fewer carbonate (turquoise) grains, and they show no preferential alignment and/or distribution (with 5mm scale bar).

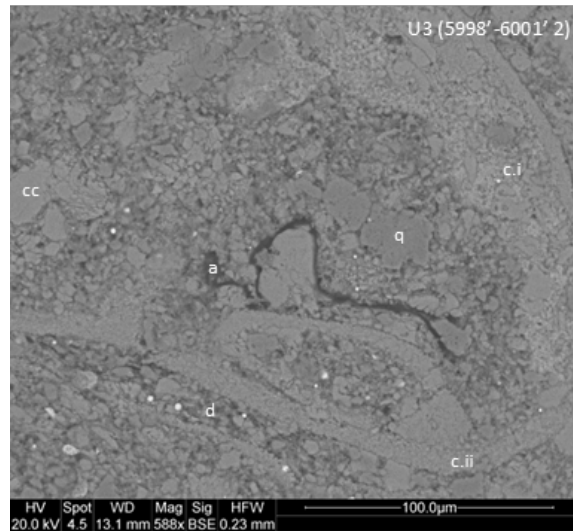


Figure 61: An electron micrograph of sample U3 with mud to silt-sized quartz (q), bioclastic and authigenic calcite (cc) grains within an illite (d) matrix with some finer-grained silicate and carbonate material. This sample is from close to the transition zone between the Utica shale and Point Pleasant Formation. There is evidence of intra-particle calcite cement (cc) within the bioclastic calcite grains. Within this there is some inter-particle calcite cements (cc).

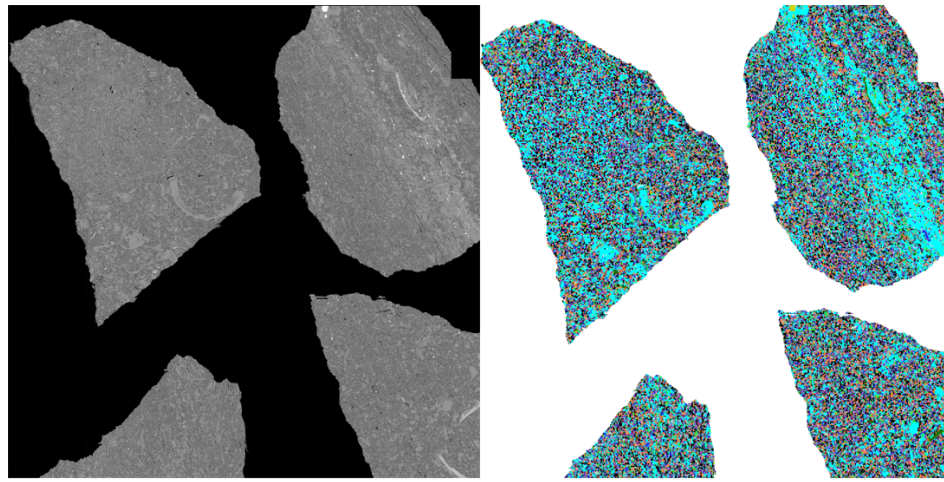


Figure 62: U3 BSE and corresponding mineral map showing the presence of a clay sized grain matrix dominated by illite (orange) as well as grains of quartz (blue), however there is a significantly greater quantity of carbonates (turquoise) in comparison to U1 and U2. These carbonates are present as bands and also in biogenic forms (with 5mm scale bar).

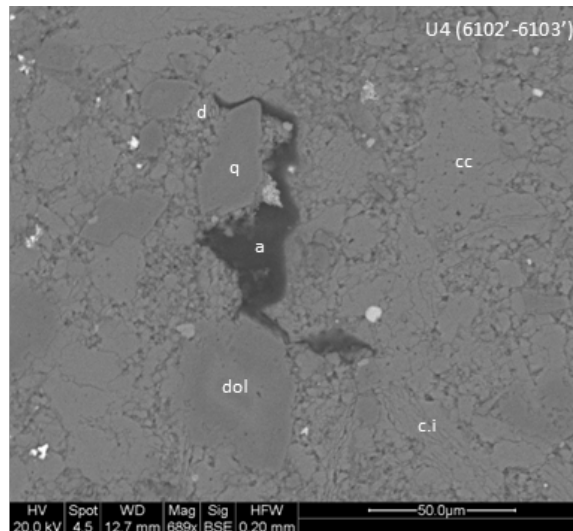


Figure 63: An electron micrograph of a typical sample of U4, being part of the Point Pleasant Formation with coarse silt-grained carbonate zoned minerals which are comprised of calcite (cc) and dolomite (dol) due to the dolomitisation of calcite to form dolomite. There are silt-grained quartz (q) and calcite (cc) grains surrounded by an illite (d) and finer-grained carbonate matrix. Observed post-sedimentation events are some inter-particle calcite cement (cc) and dolomitisation of the calcite.

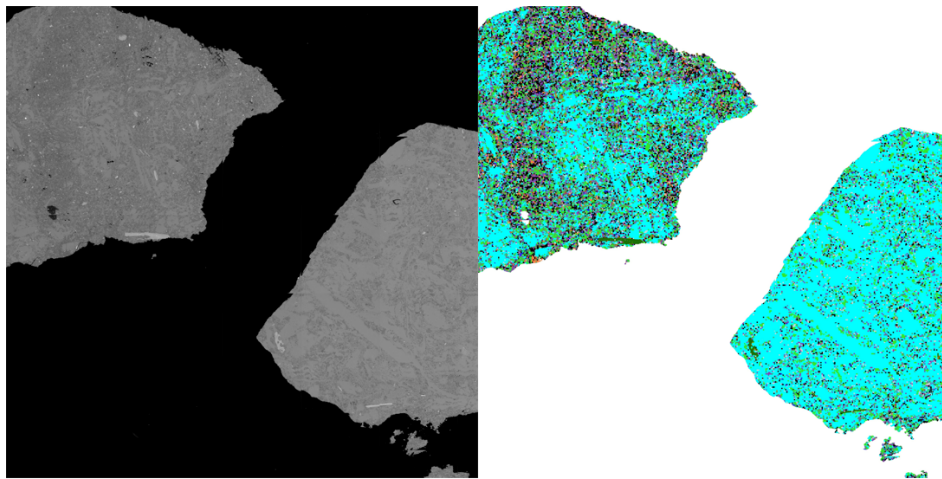


Figure 64: U4 BSE and corresponding mineral map showing the presence, but reduction in the clay sized illite (orange) dominated matrix, within this matrix there are some quartz grains (blue) but far fewer than can be seen for samples U1, U2 and U3. There is a significant quantity of carbonates (turquoise) which take on a biogenic form likely as a result of bioturbation (with 5mm scale bar).

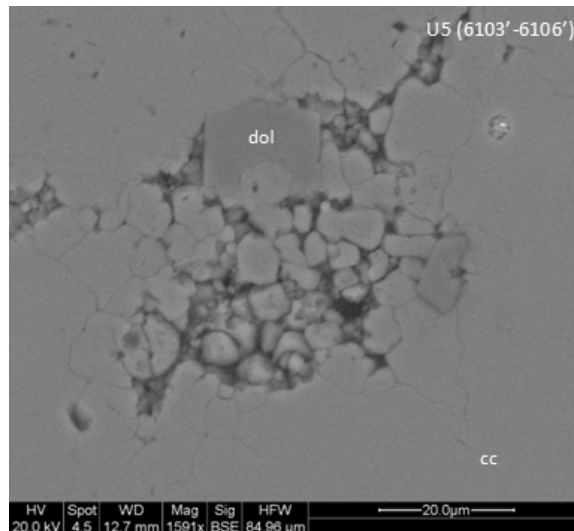


Figure 65: An electron micrograph of a typical sample of U5, which is part of the Point Pleasant Formation with typical calcite (cc) grains (5-10 μm), with some finer inter-granular illite (d). There are some darker coloured minerals which have been identified as dolomite, and the other grains some inter and intra particle cement.

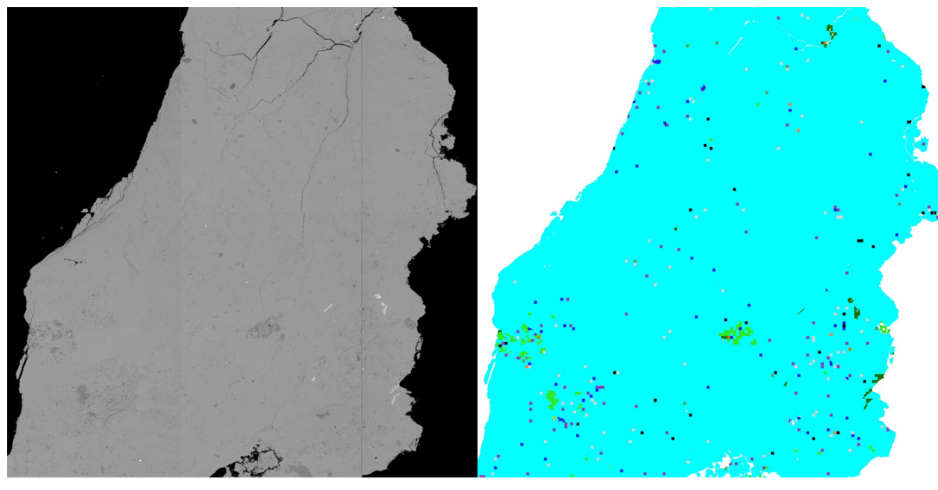


Figure 66: U5 BSE and corresponding mineral map showing a carbonate grain (turquoise), with some fine grained quartz (blue) within it. There are also some areas of dolomite (green) where some mineral alteration has occurred (with 5mm scale bar).

6.3.2. Mercury Intrusion Porosimetry (MIP)

Figure 67 shows the raw mercury intrusion and extrusion curves for samples U1 to U5. It can be seen that, for some samples (U1-3), the mercury intrusion curves are of a hyperbolic form at the highest pressure, thereby suggesting that mercury has not been able to fill the entire void space. It is noted that, typically, very little of the mercury extruded when the pressure was reduced, and thus mercury entrapment is apparently high. Simple pore geometries are shown in Figure 68 to visually depict the possible trapping of mercury in samples U1-U5. The high pressure that mercury intrusion porosimetry is carried out at can result in crushing of the sample which results in the appearance of entrapment. The distinction of trapping or crushing will be made and confirmed by analysis of the CXT data.

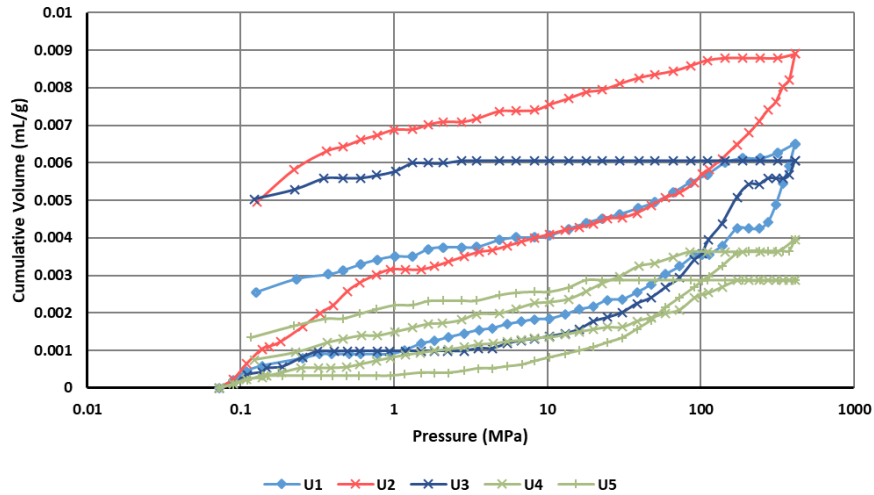


Figure 67: mercury porosimetry intrusion and extrusion normalised to zero intrusion at 0.7MPa to remove the effect of mercury intruding and moving around the external spacing of the chips for samples U1 (♦), U2 (×), U3 (×), U4 (×) and U5 (+) (colours and symbols consistent with Figure 52 and Figure 53 of the N₂ and CO₂ gas sorption isotherms). U2 and U1 have the greatest volume of intruded mercury and U4 and U5 the smallest volume of intruded mercury, however U3 has the greatest volume of trapped mercury.

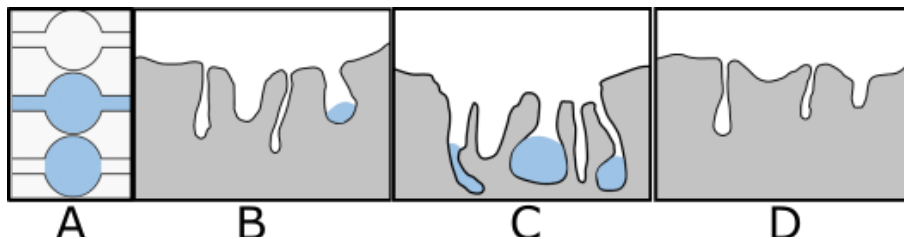


Figure 68: (A) basic ink-bottle pore geometry of a pore which mercury could get trapped in, (B) a simplified example of the possible trapping of mercury in samples U1 and U2 where some mercury has been extruded but a large quantity is still trapped in the sample, (C) a simplified example of the possible trapping of mercury in sample U3 where very little mercury has been extruded and a significant quantity is trapped in the sample, (D) a simplified example of the possible trapping of mercury in samples U4 and U5 where most, if not all, of the intruded mercury has been extruded. Trapped mercury (■), the shale sample (■) and empty space (□).

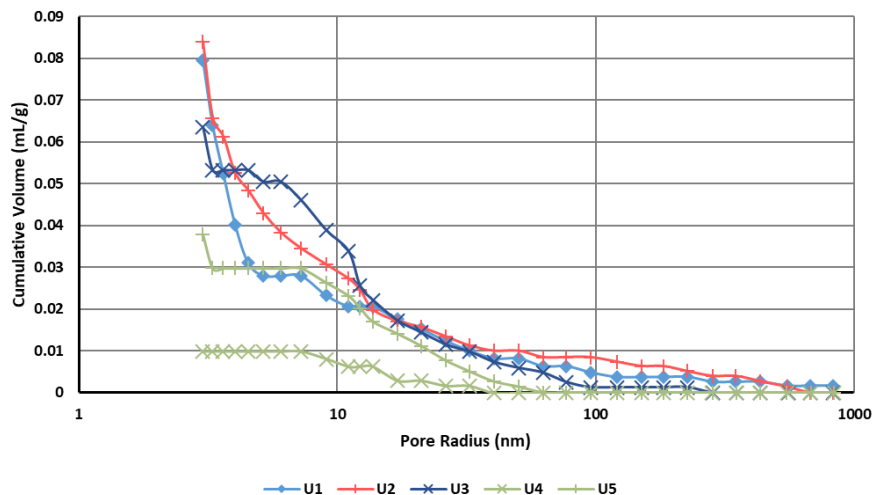


Figure 69: cumulative intra-particle pore size distributions for Utica shale samples U1 (♦), U2 (×), U3 (×), U4 (×) and U5 (+) (colours and symbols consistent with Figure 52 and Figure 53 of the N₂ and CO₂ gas sorption isotherms). Results for the pore size distributions are consistent with the intrusion – extrusion curves in Figure 67.

6.3.3. Computerised X-Ray Tomography (CXT)

Figure 72 shows typical examples of reconstructed 2D slices from the CXT imaging of sample U3 following mercury porosimetry (examples for U1, U2, U4 and U5 are included in Figure 70, Figure 71, Figure 73 and Figure 74 respectively). Some 2D slice images of samples of fresh mercury shale chips before mercury porosimetry are included in the Figure A6.2. 1. Since mercury has a much higher electron density than the surrounding shale it absorbed many more x-rays, and appears as bright white in the images, while the rock is mid-grey (and empty space is black). However, electron-dense minerals such as iron pyrites would also strongly adsorb x-rays and also be expected to appear as bright white pixels. However, the CXT images of fresh samples given in Figure A6.2. 1 show that the spatial incidence of strongly x-ray adsorbing minerals is very low before porosimetry. Hence, virtually all the bright white pixels in Figure 72 are due to entrapped mercury. The presence of mercury within the sample suggests that the entrapment in the porosimetry extrusion curves is real and not just apparent, due to sample compression. The high mercury entrapment during porosimetry means that the mercury provides a good tracer for the intruded volume.

The high contrast between entrapped mercury and the rock means the images can be unambiguously gated to show only the entrapped mercury phase. Figure 70, Figure 71, Figure 72, Figure 73 and Figure 74 shows a 3D reconstruction of chips of sample U1-U5 containing entrapped mercury. From Figure 70 and Figure 71, it can be seen that the pores intruded in mercury porosimetry are generally parallel to the bedding planes in the shale for sample U1, though there is some more intrusion at the edge of the sample. From Figure 71, for sample U2, the residual mercury also picks out fainter, smaller macro-pores/fractures not directly visible otherwise, and the “cloud-like” entrapped mercury around them. It is possible that some cracks may have formed during the drilling and transportation of the cores from the United States, and further cracking may have occurred when the cores were reduced to millimetre-sized chip samples for mercury porosimetry. The CXT images of fresh samples given in Figure A6.2. 1, suggest that visible cracking for these materials is limited to the edge of the chips and the pervasiveness of these cracks (Figure 71) is low such that the order of the typical lattice size for the nanoscopic pore network will not have been affected. Resultantly the relative accessibility of the meso-pore network will not have been greatly affected.

In contrast, from Figure 72, the entrapped mercury in U3 suggests more pervasive and homogeneous mercury penetration and entrapment, but only up to a particular front in the shale. The entrapped mercury in U3 is located in broad bands and extended regions, rather than being more closely associated with fractures and adjacent borders along fractures, as for U1 and U2. This greater spatial prevalence of entrapped mercury away from defined planes or fractures also suggests greater disorder. The dark regions of the chips in the CXT images represent areas with pore necks too small to permit mercury intrusion and/or low voidage fraction. From a consideration of the grey-scale it looks most likely to be the carbonate phases that have been intruded in U3, since intrusion was in the lighter coloured mineral phases. The greater pervasiveness of mercury intrusion in U3, compared to U1 and U2, would then be consistent with the data in Figure 54 which shows that U3 has much more carbonate than U1 and U2. Clays, which are more abundant in U1 and U2, are likely to have more pores too small for mercury to intrude. This is also consistent with the more pervasive distribution of entrapped mercury across the chip of U4, shown in Figure 73, which, from Figure 54, has the highest carbonate content of all samples. However, the intensity of the bright regions in Figure 73 are lower than for Figure 72 for U3 suggesting less mercury intrusion for U4 consistent with the lower intruded volumes for U4, compared with U3, in Figure 67. The spatial distribution of entrapped mercury in U5, seen in Figure 74, is less pervasive than for samples U3 and U4, and back to more like U2. Overall, the aforementioned findings from CXT suggests that, across the series U1-U5, also shows an evolution in the amount and spatial distribution of entrapped mercury.

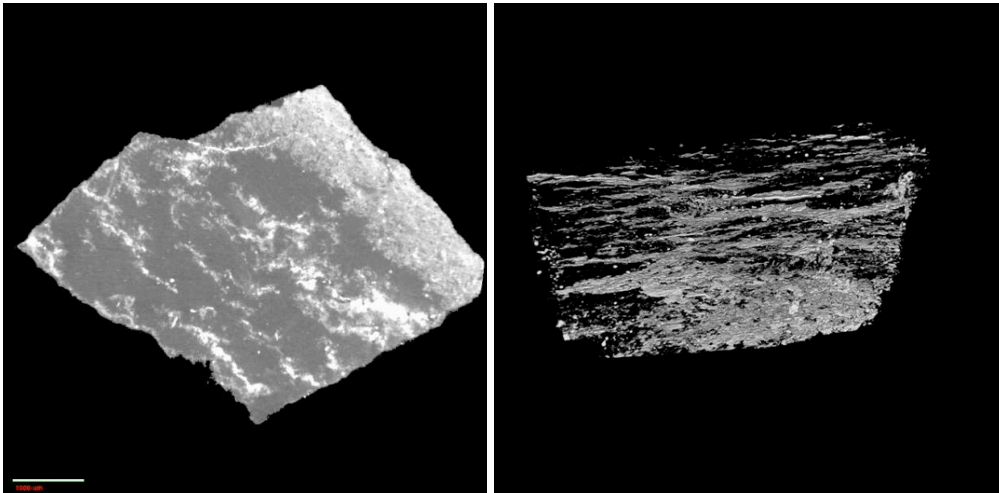


Figure 70: 2D reconstructed slice from CXT data-set for a chip of U1 shale following mercury porosimetry (left, scale bar at 1000 μ m), it is possible to see where mercury has intruded between micro-fractures and potentially between laminations of the shale and an example of 3D reconstruction (right) of CXT images of chip of U1 shale following mercury porosimetry.

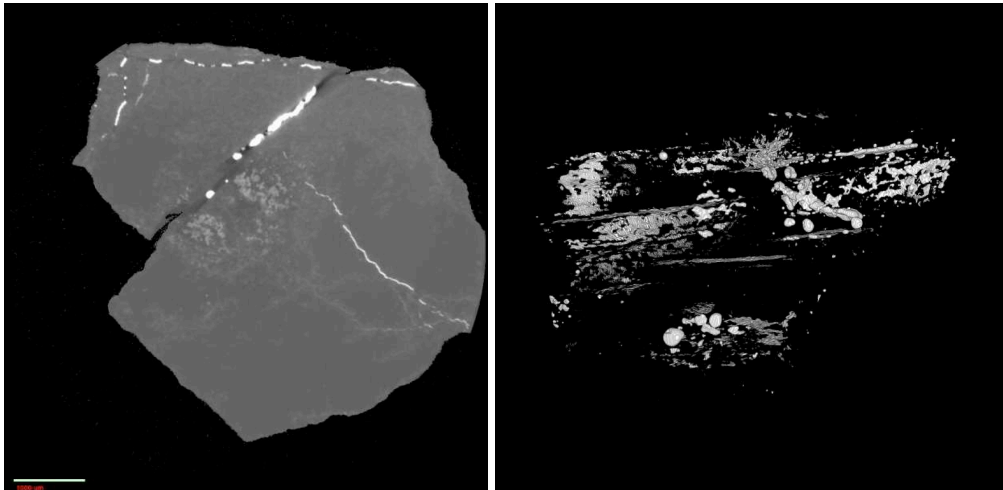


Figure 71: 2D reconstructed slice from CXT data-set for a chip of U2 shale following mercury porosimetry (left, scale bar at 1000 μ m), it is possible to see where mercury has intruded between micro-fractures and potentially between laminations of the shale, and an example of 3D reconstruction (right) of CXT images of chip of U2 shale following mercury porosimetry.

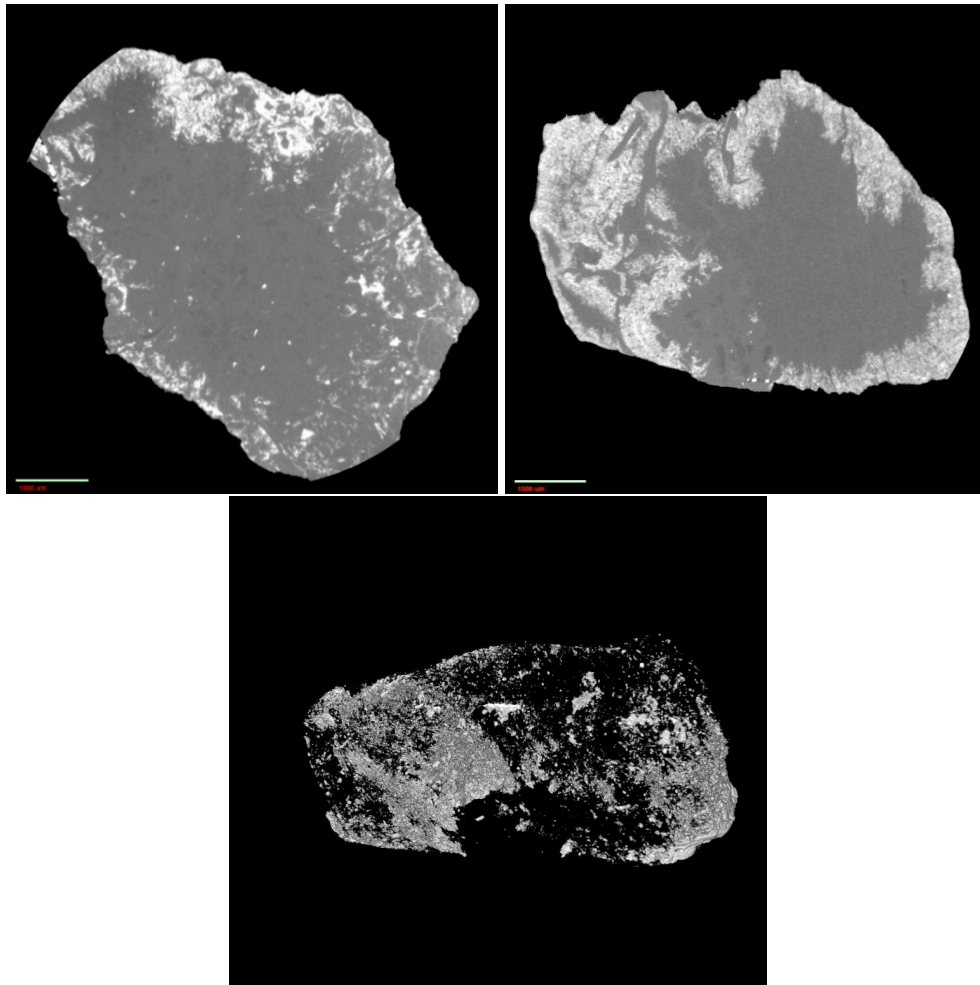


Figure 72: 2D reconstructed slice of CXT data-set for a chip of U3 following mercury porosimetry (top, scale bar at $1000\mu\text{m}$), it is possible to see where mercury has intruded around the edges in a more “cloud-like” way through more accessible pore as opposed to through fractures and laminations in the sample, and an example of a 3D reconstruction (bottom) of CXT images of chip of U3 shale following mercury porosimetry.

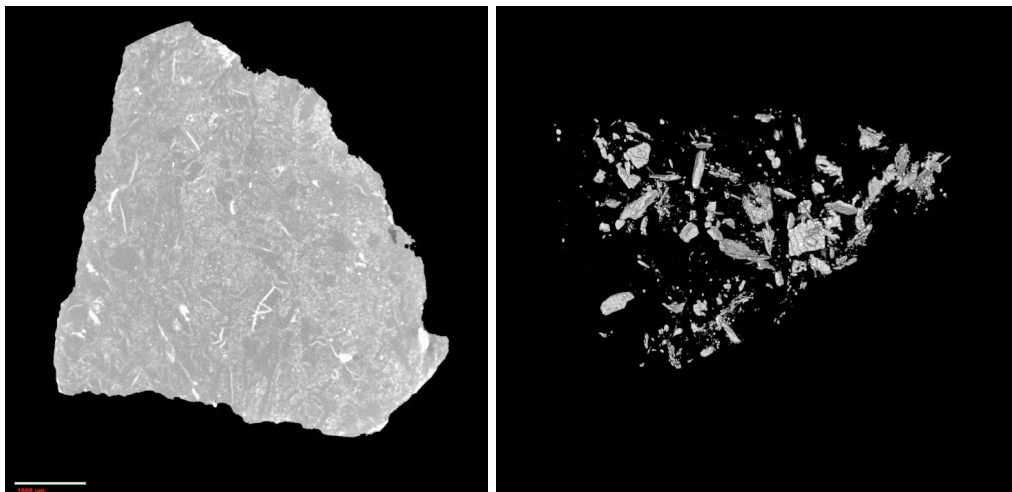


Figure 73: 2D reconstructed slice from CXT data-set for a chip of U4 shale following mercury porosimetry (left, scale bar at $1000\mu\text{m}$), it is possible to see where mercury has intruded along the edges of the sample, and an example of a 3D reconstruction (right) of CXT images of chip of U4 shale following mercury porosimetry.

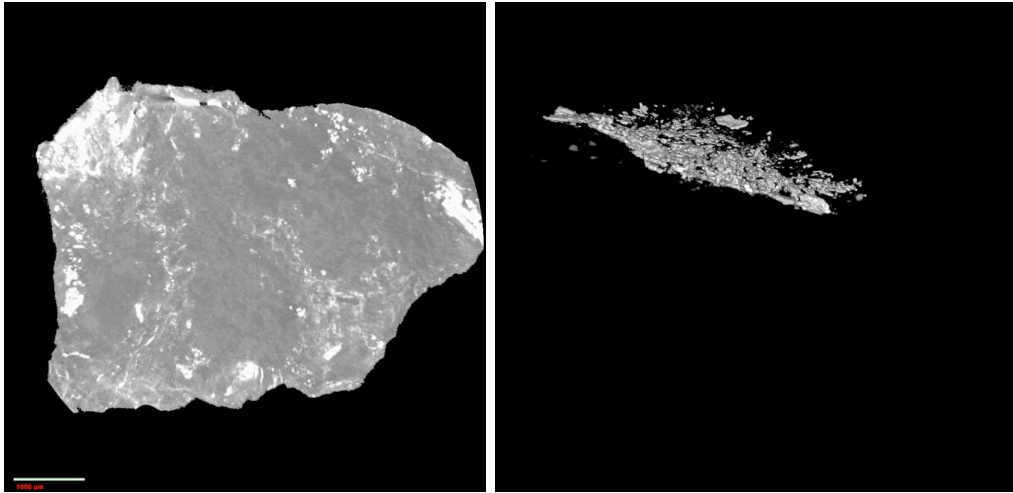
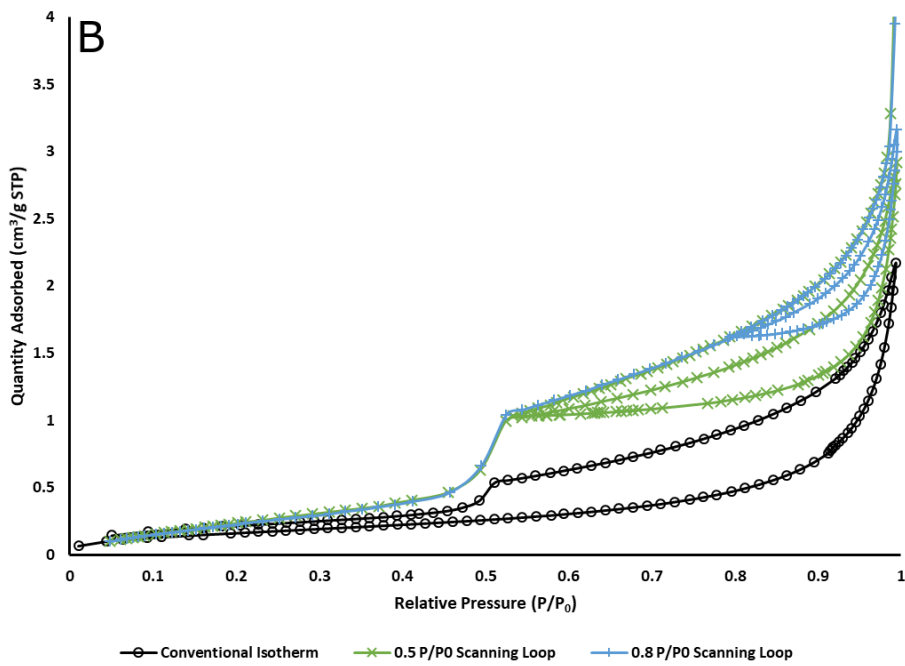
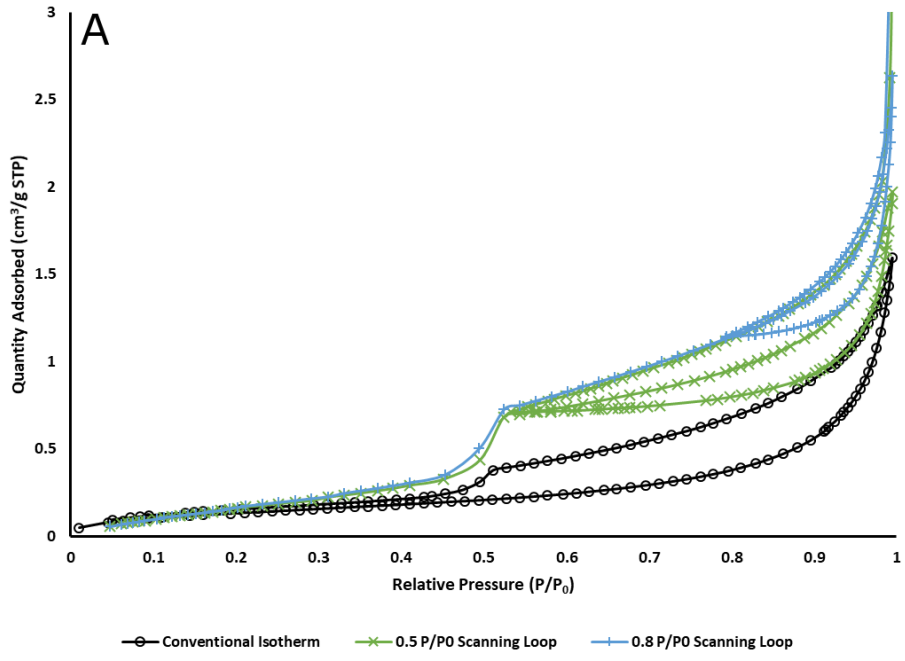


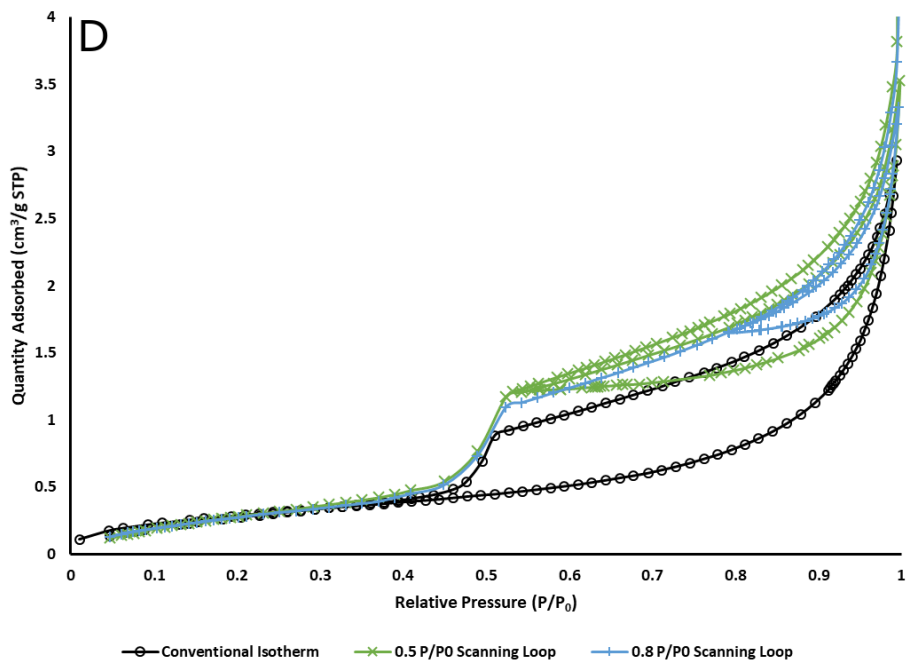
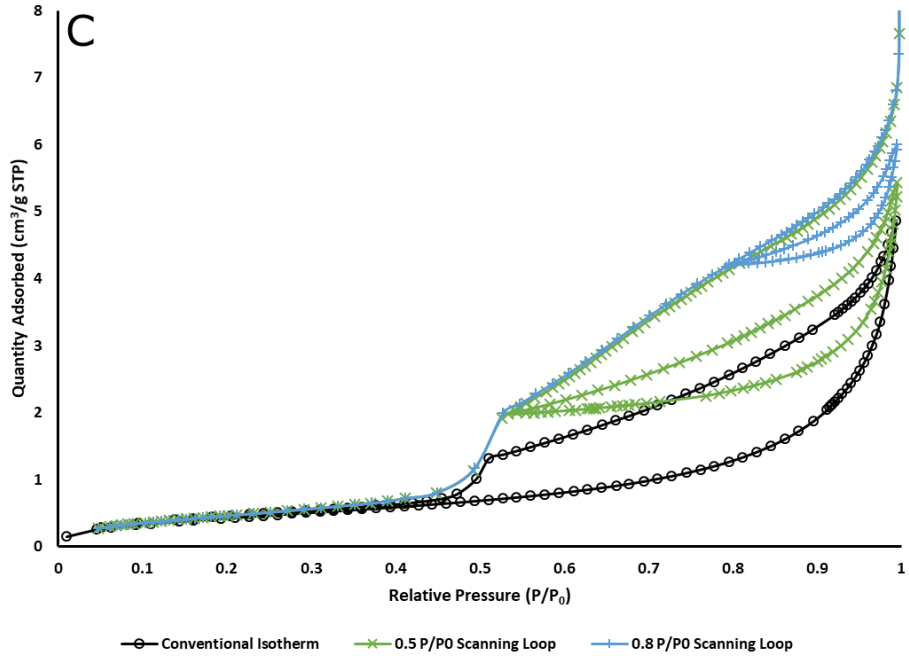
Figure 74: 2D reconstructed slice from CXT data-set for a chip of U5 shale following mercury porosimetry (left, scale bar at 1000 μ m), it is possible to see where mercury has intruded along the edges of the sample, and an example of 3D reconstruction (right) of CXT images of chip of U5 shale following mercury porosimetry.

6.3.4. Gas Sorption

Figure 75 shows the conventional nitrogen sorption isotherms, overcondensation boundary desorption isotherms, and scanning curves for the Utica shale samples.. A scanning curve is formed when on the desorption branch following overcondensation the pressure is increased at a point (i.e. $0.8 \frac{p}{p_0}$) to the highest relative pressure possible in a conventional isotherm. Following this the pressure is further reduced to 0, or to another point at which a scanning loop will be completed. The benefit of this is to observe where particular phases of pore sizes are responsible for the increased adsorption resulting from overcondensation. Consequently it is possible to further breakdown and investigate the various limiting cases for each analysed sample.

From a comparison of Figure 75A-E it can be seen that sample U3 has the highest ultimate gas uptake in both the conventional and overcondensation experiments. U3 also has the largest amount adsorbed at the marked step at a relative pressure of approximately 0.5 in the overcondensation desorption isotherm.





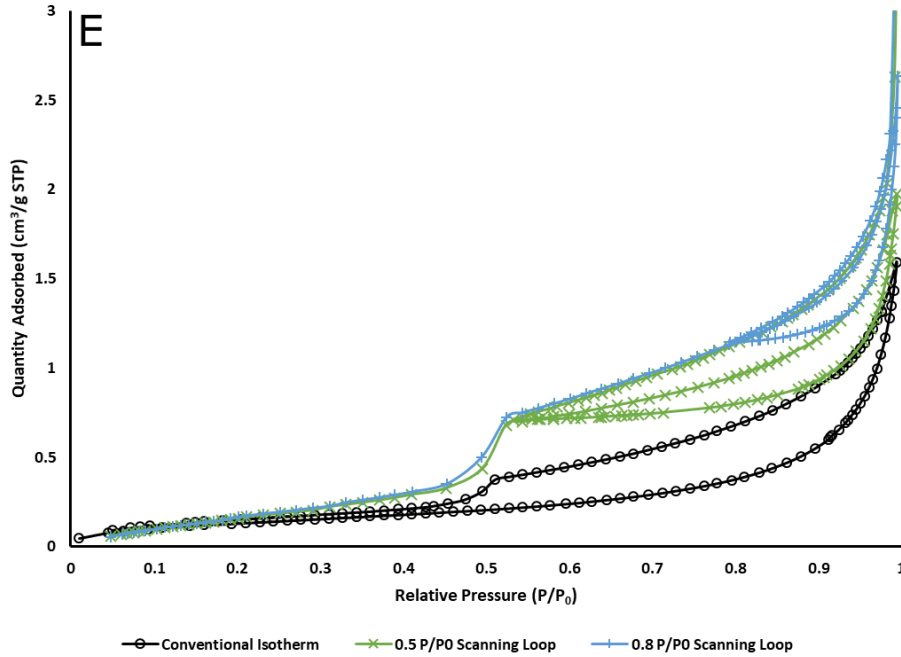


Figure 75: Conventional nitrogen sorption isotherms (empty ●), overcondensation boundary desorption isotherms, a $0.5 \frac{P}{P_0}$ scanning loop (X), and a $0.8 \frac{P}{P_0}$ scanning loop (X) for chip samples of Utica shales (A) U1, (B) U2, (C) U3, (D) U4 and (E) U5.

The overall forms of the boundary adsorption and desorption isotherms for samples U1 to U5 in Figure 75 are generally very similar. Following the BET region, the adsorption isotherms rise almost linearly until a relative pressure of 0.6-0.7 where they begin to curve upwards, at first gently, and then more sharply beyond relative pressures of 0.9. The ultimate amount adsorbed achieved for the conventional isotherms is lower than the top of the overcondensation desorption isotherm. In all cases, the overcondensation boundary desorption isotherm, broadly, consists of three regions. Following the vertical fall in amount adsorbed at relative pressure 0.995, that represents the evaporation of bulk condensate, the first section of the intra-particle desorption is typically a concave hyperbolic curve down until a relative pressure of approximately 0.5 where there is a steep, near vertical, step down to the lower hysteresis closure point. Thereafter, the desorption isotherm overlays the adsorption isotherm, as expected for reversible multi-layer adsorption. However, sample U3 is an exception to this otherwise general pattern, since the upper part of the boundary desorption isotherm is convex, with a marked knee at a relative pressure of 0.75-0.8. Further, from Figure 75C, it can be seen that the relative size of the step in the conventional desorption isotherm at relative pressure approximately 0.5 grows, as a fraction of the corresponding step in the overcondensation boundary desorption isotherm, for the series U1-U4. U5 has a relatively very small step at a relative pressure of approximately 0.5.

Given the presence of two knees in the overcondensation boundary desorption isotherm for U3, it was decided to probe the hysteresis for all samples with ascending scanning loops springing from the relative pressures in the regions of the U3 isotherm where the knees occur. Hence, in all cases, the ascending branches of two scanning loops were initiated at relative pressures of 0.5 (henceforth denoted scanning loop 1, SL1) and 0.8 (SL2), respectively, on the overcondensation boundary desorption isotherm, and the descending branches of both loops were initiated at a relative pressure of 0.995. The corresponding pore radii from the Broekhoff de Boer method for hemispherical menisci are 2.6 (SL1), 6.4 (SL2), and 300 nm, respectively. From Figure 75, it can be seen that, for all samples, both the scanning loops have an overall crescent shape. The ascending branches of the scanning loops cross the majority of the hysteresis gap with very little additional adsorption, and

then rise sharply as they approach the region of the boundary adsorption isotherm. Desorption commences immediately on the descending branch of the loops and, in some cases, U2 and U3 particularly, hysteresis remains relatively narrow compared to the width of the hysteresis between the boundary curves. However, the relative juxtaposition of the loops changes between samples. While, for samples U1 and U5, the ultimate amount adsorbed at the top of the adsorption branch increases markedly over the series consisting of the conventional isotherm, SL1, and SL2, the corresponding amounts adsorbed are very similar for sample U4. Samples U2 and U3 show behaviour intermediate between the two. It is also noted, that for sample U1, the conventional desorption isotherm, SL1 and SL2 do not cross each other. Although, it is the case that the ascending branch of SL1 overlays the conventional desorption isotherm for relative pressures 0.91-0.97, while the descending branch overlays the ascending branch of SL2 over the relative pressure range 0.95-0.98. In contrast, for sample U2, the ascending branch of SL2 unambiguously crossed the descending branch of SL1. Further, for samples U3 and U5, the ascending branch of SL1 crossed the conventional desorption isotherm. For sample U4, the ascending branches of both SL1 and SL2 cross the conventional desorption isotherm. In addition, it is noted that the descending branches of both SL1 and SL2 for sample U4 more or less overlay the overcondensation boundary desorption isotherm, whereas for samples U1 and U5 it is only the desorption branch of SL2 that overlays the boundary desorption isotherm. This suggests that the ranges of pore body and neck sizes involved in the scanning loops are different in each sample. The forms of the scanning loops will be interpreted further in the discussion.

Figure 76 shows the variation across the shale series U1 to U5 of the kerogen mass fraction from the fits to the aforementioned homotattic patch models with either fractal BET or finite multilayer BET equations. Also shown in Figure 76 is the variation across the Utica shale series U1-5 of the total organic carbon. From Figure 76, it can be seen that the TOC% and the kerogen isotherm contribution fractions all show a rising and falling trend with a peak for sample U3. This shows how the parameter optimisation for the homotattic patch model fitting procedure is able to distinguish samples which have the greatest contribution from their organic content component.

Despite the variation in the absolute values of the kerogen fractions for the respective fits to the homotattic patch models involving fractal BET or finite multilayer BET equations, both produce the same distribution of values which allow for consistent comparisons across a dataset for either model to assess the impact that the organic component of the sample has. It is also noted that the TOC% data includes a contribution from the overcondensation that is inaccessible to the exterior. However, overall, the isotherm homotattic model fitting suggested that the higher accessible surface area present in U3 shale is organic material, due to the higher TOC%.

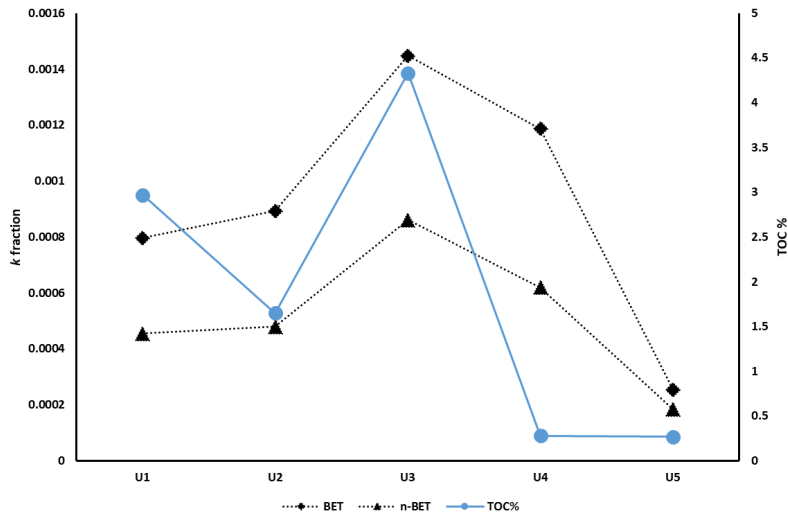


Figure 76: Variation across the shale series U1-5 of the k -value (●) from the fits to the homotactic patch models with either fractal BET (◆) (eq.6) or finite multilayer BET (▲) (eq.7). Also shown is the variation across the Utica shale series U1-5 of the total organic carbon (TOC%). Parameters used to calculate these values are shown in Table 10.

| | fBET | | | | nBET | | | |
|-----------|---------------------------|--------------------------------|---------------------------|---------------------------|---------------------------|--------------------------------|-----|----------------------------|
| | C | V_m (cm ³ /g STP) | D | k - value | C | V_m (cm ³ /g STP) | N | k - value |
| U1 | 47.36406 ± 2.848009 | 0.385275 ± 0.003896 | 2.241188 ± 0.014634 | 0.000797 ± 0.000008 | 49.39205 ± 1.928238 | 0.383252 ± 3.23E-06 | 7 | 0.000455 ± 1.804E-09 |
| U2 | 48.92447 ± 2.930557 | 0.373289 ± 0.002328 | 2.243202 ± 0.006847 | 0.000879 ± 0.000005 | 55.76718 ± 1.386536 | 0.431395 ± 0.002098 | 7 | 0.000549 ± 4.15E-09 |
| U3 | 32.20889 ± 1.700259 | 0.680334 ± 0.007694 | 2.229568 ± 0.013330 | 0.001448 ± 0.000108 | 36.09552 ± 1.182177 | 0.674172 ± 0.00202 | 8 | 0.000861 ± 2.56E-08 |
| U4 | 66.04899 ± 2.960567 | 0.430387 ± 0.00173 | 2.333958 ± 0.009353 | 0.001186 ± 0.000007 | 69.60184 ± 0.816255 | 0.431387 ± 0.001816 | 6 | 0.000619 ± 2.51E-09 |
| U5 | 43.0456 ± 2.458375 | 0.116331 ± 0.001835 | 2.289126 ± 0.014604 | 0.000253 ± 0.000003 | 44.7796 ± 1.960964 | 0.114864 ± 0.001117 | 6 | 0.000183 ± 6.63E-10 |

Table 10: parameters used to model the values in Figure 76.

Figure 77 compares the conventional sorption isotherms and overcondensation desorption isotherms for samples of shale U3 in chip (approximately mm particle size) and powder form. It can be seen that the ultimate amount adsorbed increased for the powder sample in both conventional and overcondensation experiments. It is also noted that the sharpness of the higher knee in the overcondensation boundary desorption isotherm is slightly reduced for the powder sample. It can also be seen that neither of the conventional desorption isotherms for chip or powder samples have any sign of convexity.

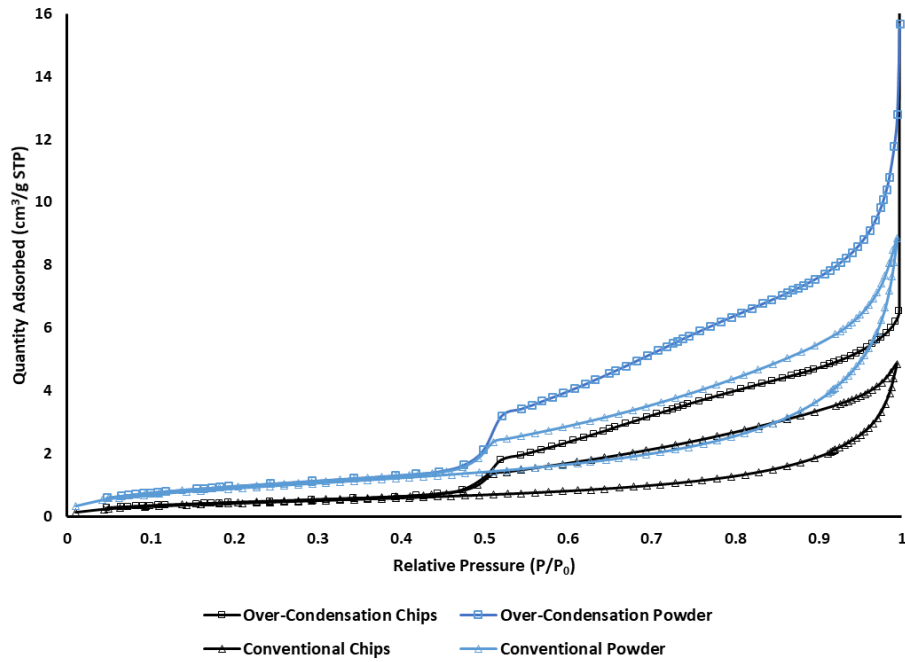


Figure 77: compares the conventional sorption isotherms (empty ▲) and overcondensation desorption isotherm (empty ■) for samples of shale U3 in chip (approximately mm particle size, represented by black symbols) and powder form (represented by blue symbols). It can be seen that the ultimate amount adsorbed increased for the powder sample in both conventional and overcondensation experiments. It is also noted that the sharpness of the higher knee in the overcondensation boundary desorption isotherm is slightly reduced for the powder sample. It can also be seen that neither of the conventional desorption isotherms for chip or powder samples have any sign of convexity.

6.4. Discussion

6.4.1. Sedimentology

From the SEM images (Figure 57, Figure 59, Figure 61, Figure 63 and Figure 65), it was possible to identify that through the series U1-5, there is a transition from a shallow carbonate platform into a cyclic series of authigenic and bioclastic calcite grains likely deposited as a result of the area being storm-dominated. Samples U4 and U5 were deposited during a period of closure within an epicontinental sea with little sediment input as there are low quantities of clay in these samples. In sample U3 there are still significant volumes of carbonate, but there is also clay input and a high quantity of organic matter. By geological descriptions of the area U3 can be placed at the base of the Utica Formation which is organic and carbonate rich. It is hypothesised that U3 has been sampled from a period where there has been some opening (or it has just opened) to the epicontinental sea which has allowed sediment input increasing the mineral heterogeneity of the sample. As a result of the previously enclosed sea and formation of carbonate cements the environment is more anoxic allowing for greater preservation of organic matter. Samples U1 to U2 are sampled from later in the Utica Formation (younger and shallower) where it has transitioned from carbonate to clay rich. At this point the epicontinental sea had spent a longer period of time open allowing sediment transport which resulted in the dominant mineral composition transitioning from carbonate to calcite. As the sea had been open it would have been re-oxidised making organic matter less easily preserved.

6.4.2. Typical Pore Structure of Shales (a model)

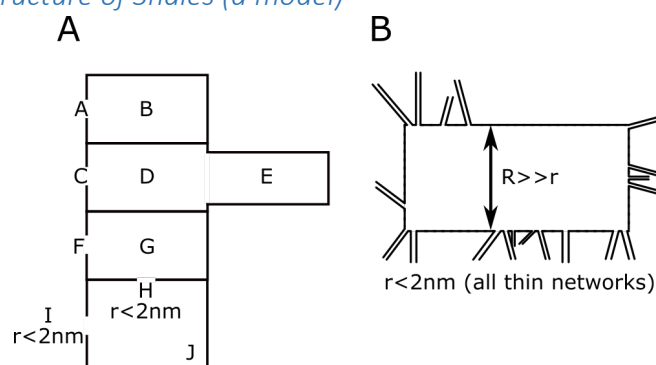


Figure 78: schematic depictions of the model pore spatial arrangements probed by scanning loops in samples (a) U1, U2 and U5, and (B) U3 described in the main text. The model in part (A) is a “jam-jar” type arrangement with inter-connections, with the bottom very largest pore shielded by very narrow necks. The model in part (B) has a large macro-pore surrounded by a disordered “sea” of smaller pores.

A transition across the series U1 to U5 is evident in the pore structure as manifested in the gas sorption data. The crossing ascending scanning curves obtained here for Utica shales are similar in type to those obtained for Rempstone shale by Rigby *et al.*, (2020) and for Middle Eastern shales by Barsotti *et al.*, (2020), probably because the underlying pore geometries of Utica and Rempstone shales probed by scanning data have some similarities. The overall form of the conventional adsorption isotherm, overcondensation boundary desorption isotherm, and scanning loops suggests a void space consisting of large pore bodies shielded by narrow pore windows with a relatively much wider range of sizes than for the bodies, as shown in Figure 78A. The pores thus have a typical shape similar to a jam-jar (preserve jar). The relatively flat (almost horizontal for U5) form of the conventional adsorption isotherm, and the ascending branches of SL1 and SL2, for relative pressures in the range approximately 0.50 to 0.85 (corresponding to pore sizes of approx. 4-12 nm), followed by a steep rise at high relative pressures, suggests capillary condensation in pore bodies of just relatively larger sizes, as seen in Figure 79. In contrast, the overcondensation boundary desorption isotherms show steady declines in amount adsorbed over the whole relative pressure range from 0.995 to 0.5 (corresponding to pore sizes of approximately 500-5 nm), apart from the hiatus for sample U3 at a relative pressure of approx. 0.75-0.8. This suggests a much wider range of shielding pore window sizes than pore body sizes, which means pore bodies steadily empty in order of shielding necks down the overcondensation isotherm as seen in Figure 79.

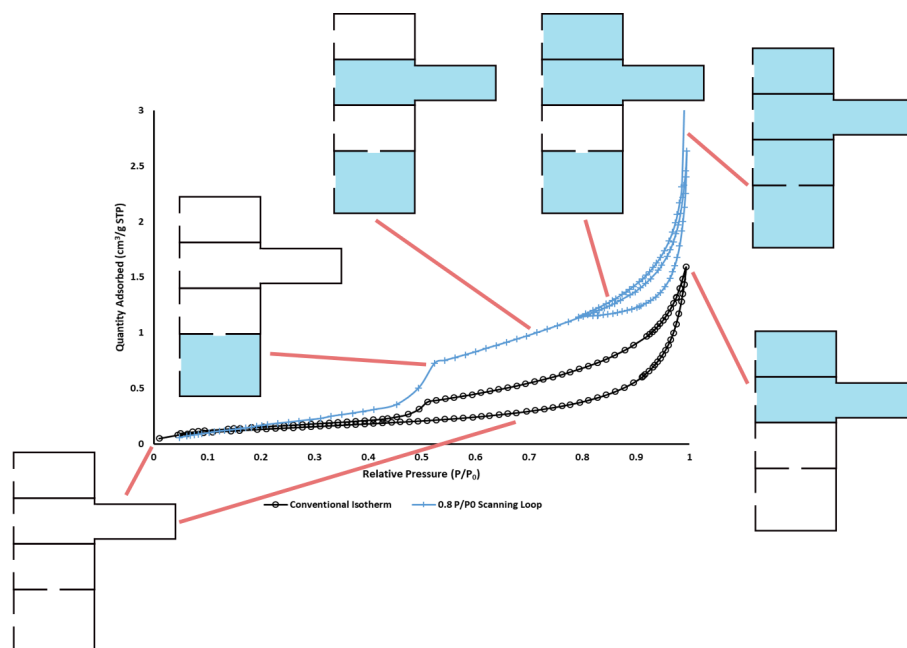


Figure 79: Schematic diagram of the state of pore-filling with condensate (blue shading) of the model pore system shown in Figure 78A at various positions (indicated by red arrows) around the conventional and overcondensation isotherms of the form found in this work. Regions left white represent vapour-filled pores. It is noted that the multilayer film build-up is omitted for simplicity.

The very wide range of relative pressures over which amount adsorbed declines on the boundary desorption isotherm suggests that even larger windows have direct external access and the corresponding model for the pore structure would be like an array of similar “jam-jar”- like pores with a range of mouth sizes, as seen in Figure 78. These pore mouths may also empty directly into the type of large macro-pores evident in the CXT images of samples U1 and U2 after mercury entrapment in Figure 70 and Figure 71, as these would empty at the very top of the desorption isotherm. The ‘penumbra’ of entrapped mercury bordering the mercury-filled macroporosity in the CXT images of U2 may represent entrapment within this jam-jar porosity along their length.

6.4.3. Pore-Pore Co-Operative Effects in Gas Sorption Data

However, there is also evidence for pore-pore co-operative effects in sorption, and, thus, also more network complexity. The aforementioned hiatus in the overcondensation boundary desorption isotherm at relative pressures approximately 0.75-0.8 (corresponding to pore sizes approx. 10-17 nm) for sample U3 is a percolation knee. The pause in the decline in amount adsorbed is caused by shielding of pore body and neck sizes larger than the knee by the smaller neck sizes at the knee, as shown schematically in Figure 80. This enhanced shielding arises when the spatial juxtaposition of pore necks (and bodies) is more jumbled. The presence of greater shielding is also consistent with the reduction in the sharpness of the percolation knee with the decline in particle size from chip to powder evident in Figure 77, since a reduction in lattice size of a random pore network leads to a smearing out of the percolation transition due to less shielding arising in smaller lattices (Seaton, 1991).

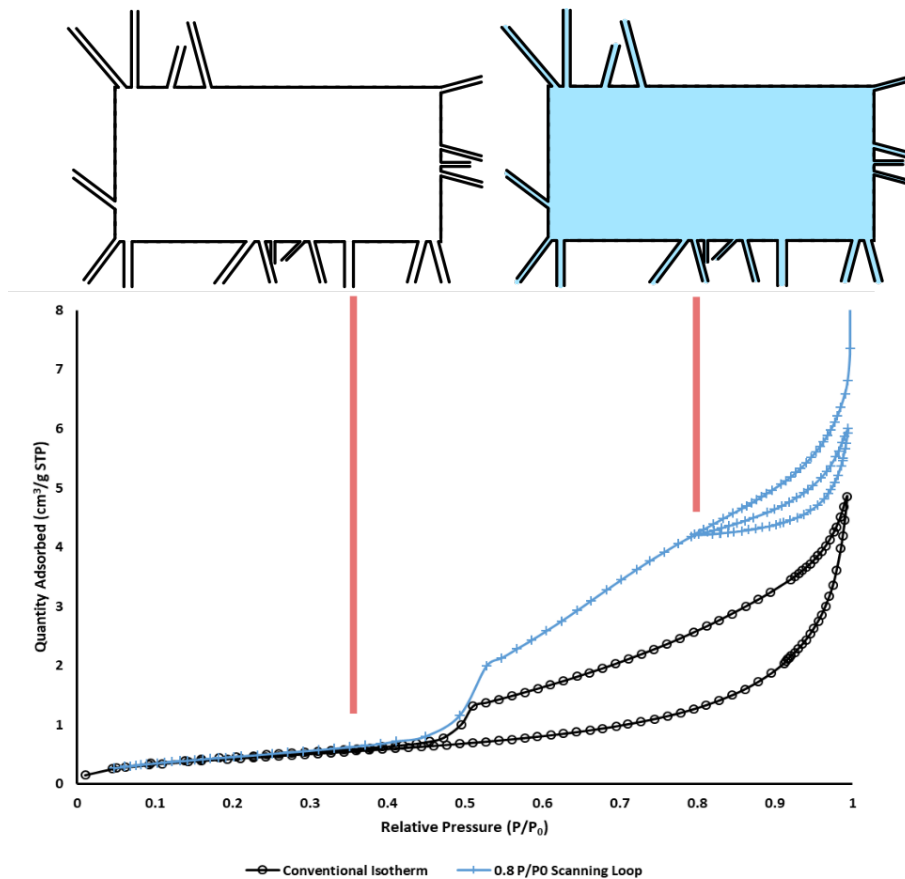


Figure 80: schematic diagram of the state of pore-filling with condensate at two positions along the overcondensation desorption isotherm for the pore structural model, given in Figure 78B, for shale sample U3. The blue shading represents pores filled with condensate, while white represent an empty pore.

It is noted that the sign of greater complexity in the desorption data (the percolation knee) occurs for the same sample, U3, for which the mineralogy data in Figure 54 also suggests has a more complex mixture of components, and the SEM data (Figure 57, Figure 59, Figure 61, Figure 63 and Figure 65) suggests has a more jumbled spatial arrangement of component mineral grains and inter-granular cements. The overall crossover from high illite content to high calcite content, and spike in TOC%, around the depth of sample U3, together with the morphological data indicating increased disorder in this sample, suggests that some sort of high energy transition from a primarily marine to a primarily terrestrial source of sediments occurred, that also caused a transient increase in influx and/or lay-down of organic material in the sediments. The existence of this evidence for the high disorder in the complex sediments in U3 suggests it was rapidly fixed by relatively swift subsequent burial and inter-granular cementation processes following initial lay-down, since otherwise it would have been removed by longer timescale processes.

Besides the pore-pore co-operative effect (pore-blocking) in the desorption data there is also evidence for network-related co-operative effects in the adsorption data too. The ultimate amount adsorbed at the top (highest pressure) of the conventional adsorption isotherm (CAI) and the ascending branches of SL1 and SL2 increases in that order for samples U1 and U5. Further, the ultimate amount adsorbed for SL1 and SL2 for sample U2 is much higher than the ultimate amount adsorbed on the conventional adsorption isotherm. The difference in step heights, at relative pressure of approximately 0.5 (corresponding to a pore size approximately 4-5 nm), between the conventional and overcondensation desorption isotherms suggests that some of the very largest pores filled only by overcondensation remain filled with condensate even down to a relative pressure of approx. 0.5, as shown in Figure 79. This is because (as shown schematically in Figure

78A) the very largest pores (pore J, in Figure 78A) are shielded by very narrow pore necks of sizes (diameters) smaller than approximately 4 nm (necks H & I in Figure 78A), and the aforementioned step in desorption is due to the cavitation effect (Gregg and Sing, 1982). For SL1, these very largest pores, shielded by very narrow necks, remain filled at the start of the loop, in addition to those that would be filled by the conventional adsorption isotherm. Hence, this head-start in condensate amount means that the ultimate adsorption volume for SL1 will necessarily be higher than that for the conventional isotherm. However, it is noted that, for SL1, for samples U1, U2 and particularly U5, the additional ultimate amount adsorbed, compared to the conventional isotherm, is actually larger than that anticipated simply from the difference in step height, at relative pressure of approx. 0.5, between the overcondensation and conventional desorption isotherms. This means some additional adsorption is occurring on the ascending branch of SL1, for samples U1, U2 and U5, than occurred on the corresponding conventional adsorption isotherm. This is because the presence of residual condensate in some larger pore bodies (pore J in Figure 78A) may mean that adjoining empty pore bodies connected via narrower windows (like pore G in Figure 78A) may, themselves, fill with condensate at a lower relative pressure, via a hemispherical meniscus rather than via a cylindrical-sleeve meniscus in a co-operative adsorption effect (Rigby, 2018, 2020). This is shown schematically in Figure 81. This means that the ultimate pressure at the top of the scanning loop adsorption branches exceeds the filling pressure of more pores than is the case for the conventional adsorption isotherm starting with no already filled pores. Hence, the pores that fill via hemispherical menisci at the pressures towards the upper end of SL1 for samples U1, U2 and U5 are specifically the large pores that adjoin, and inter-connect with, the very largest pores blocked by narrow necks of sizes below approx. 4 nm (see Figure 78A and Figure 81). While pore-blocking can only arise from pores located between a given pore and the path(s) to the exterior, co-operative condensation can arise from neighbouring pores in any direction, including laterally (as in Figure 81), or stowards the interior. This feature of the two effects allows them to be utilised independently in interpreting gas sorption data. The presence of co-operative condensation thereby suggests that rather than being largely disconnected “jam-jar” pores, the pore bodies do form an inter-connected network via adjoining necks.

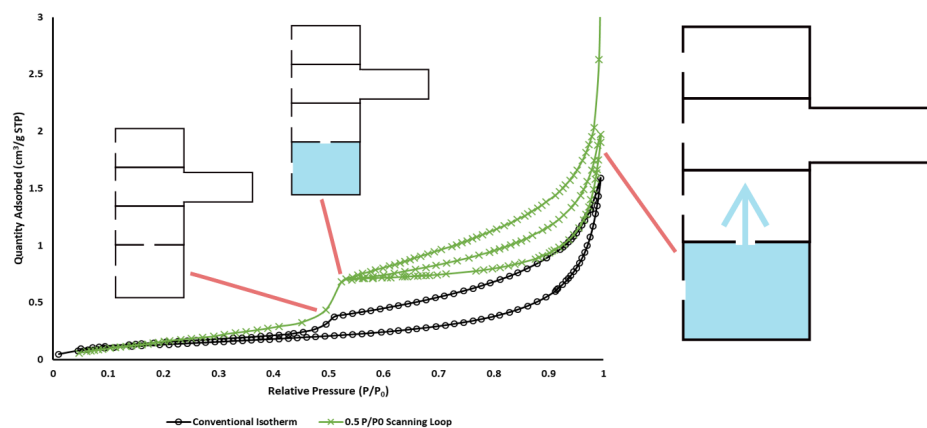


Figure 81: schematic diagram of pore filling via a co-operative pore-pore mechanism, as described in main text. The blue shading indicates the presence of condensate and the arrow indicates the direction of the co-operative pore-filling process originating from the still-filled pore body. The diagram also shows the difference in pore-filling at the springing off point for SL1, compared with the boundary adsorption isotherm at the same pressure.

For sample U5 the ultimate amount adsorbed for SL2 exceeds that for SL1, and the desorption branch for SL2 follows, more or less, the overcondensation boundary desorption isotherm, suggesting there are no even larger pores left unfilled at the top of SL2. The additional ultimate amount adsorbed for SL2, over and above its initial head-start on SL1 (the vertical distance between the springing off point for SL2 and the adsorption branch of SL1 at the same pressure), must result from co-operative adsorption initiated from pores still left filled at the springing off point of SL2, but

unfilled at the inception of SL1 and the conventional adsorption isotherm. The SL2 head-start pores thus must be shielded by pore necks that empty on the boundary desorption isotherm below the springing-off point of SL2 but before the step at relative pressure of approx. 0.5. Hence, the spatial juxtaposition of the particular pores surrounding those that fill additionally for SL2 in U5 can be deduced from the overcondensation and SC data.

The similarity in ultimate adsorbed amounts for SL1 and SL2, and also their closeness to the ultimate amount adsorbed for the conventional isotherm too, for sample U4, compared to U1, suggests that there are fewer very large pore bodies in the distribution for U4 than that for U1. This is consistent with the much lower intra-particle intruded volume in the mercury porosimetry data for U4 compared to U1 and U3. In addition, this suggestion is also reflected in the fact that the step at a relative pressure of approx. 0.5 in the conventional desorption isotherm is a larger fraction of the height of the corresponding step in the overcondensation desorption isotherm, meaning relatively more pore bodies shielded by very narrow pore necks (approximately <4 nm) are filled in the conventional experiment.

6.4.4. Hysteresis Width in Gas Sorption Data

The width of the hysteresis between the adsorption and desorption branches of the scanning loops varies amongst the various examples in the data in Figure 75. However, there are key trends in this variation. It is noted that the thinnest hysteresis occurs for those cases when the ultimate amount adsorbed for that loop, compared to those of the other loop or the conventional adsorption isotherm, suggests that many more of the largest pore bodies are left unfilled with condensate (i.e. there is a big gap between the top of the loop and the overcondensation isotherm). Conversely, the widest hysteresis (when desorption is nearest the path of the boundary desorption isotherm), such as that for both loops for sample U4, occurs when there is relatively less difference between the complete pore filling at the top of the overcondensation boundary curve and the top of the loop itself. When large pore bodies (say like pore A in Figure 82) are left unfilled at the top of adsorption branches they provide alternative locations, in addition to the exterior of the sample, into which condensate (such as in neighbouring pore B in Figure 82) can evaporate via free menisci, thereby making desorption easier (i.e. earlier), in the sense that pore-blocking is reduced. This process is known as seeded percolation (Parlar and Yortsos, 1988). In Figure 82, pore A acts as the seed site for the penetration of the vapour phase into pore B. For this to happen in the shale there must be connections or windows between the largest pore bodies left unfilled with condensate, and the pores that fill on the adsorption branches of the loops or boundary adsorption isotherm.

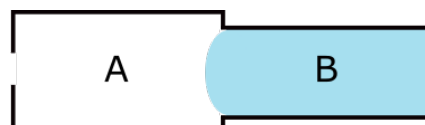


Figure 82: schematic diagram of the seeded percolation process. The blue shading represents the presence of liquid condensate, while regions left white represent vapour-filled pores. The arrow signifies the presence of a free meniscus from which desorption can occur in the direction shown.

It is noted that, for the series of SL2s for samples from U1 to U3, the ultimate adsorbed amount at the top of the loop (i.e. the loop height) decreased relative to the corresponding adsorbed amount on the overcondensation isotherm, and the hysteresis width of the loop decreased from the maximum possible. Therefore, the gap between the top of the SL2 and the overcondensation isotherm, and the gap between the desorption branch and the boundary desorption, increased, across the series. However, for the next sample in the series, U4, the height and width of the SL2 had returned to the maximum possible, as for sample U1. It is also noted that the amount (shown by intra-particle intruded volume) of the largest, accessible pores, detected by mercury intrusion porosimetry, also increases in the series U1 to U3 and then drops back down markedly for sample U4. This correlation between the trends in gas sorption SLs and mercury porosimetry data suggests

the trend in the SL2s occurs because of the increasing prevalence of very large pore bodies that can act as percolation seeds (as suggested by greater spatial dispersion of entrapped mercury in CXT images of U3), which then disappear again for U4 (where CXT pixel intensity is reduced relative to U3). Hence, the width of the hysteresis of the scanning loops indicates when there is a close juxtaposition and good interconnections between the pore sizes that fill in the loop and the very largest pores in the material. The very largest pores in U3 must be shielded by smaller pores that have critical pressures such that they empty on the overcondensation boundary desorption isotherm towards the springing off point of SL2, since, otherwise, this boundary curve would have taken a path more similar to that of the desorption branch of SL2.

Experiments in glass micro-models by (Wardlaw and McKellar, 1981) have shown that the shielding of larger pore bodies by narrow necks, or a surrounding sea of smaller pores, leads to high mercury entrapment. Hence, the proposed juxtaposition of pore sizes above for U3 is consistent with the high mercury entrapment observed in the porosimetry data for sample U3. The more pervasive and jumbled locations of entrapped mercury, observed in the CXT images of sample U3 after porosimetry, suggest a more disordered structure than U1 and U2. Figure 78 shows schematic diagrams of the pore size spatial arrangements for samples before (U1) and at (U3) the palaeodepositional transition. The thinning of the hysteresis of SL2 tracks the development and loss of the largest pores, and the thinnest hysteresis corresponds to the crux of the paleodepositional transition occurring at the depth of sample U3. However, the development of the percolation knee on the overcondensation boundary desorption isotherm for U3 below SL2 means that, at this transition, the next set of pores down are surrounded by a more complex network structure containing the smaller pore (-neck)s (of sizes approx. 10-17 nm) that provide the pore shielding that the knee represents (see Figure 78B).

6.5. Conclusions

The mineralogical, SEM and multilayer adsorption data have revealed the presence of a palaeodepositional transition in the Utica shale series U1 to U5, associated with a change-over in the predominant inorganic phase and a peak in the organic phase. The overcondensation desorption isotherm data has demonstrated the presence of very large pore bodies not detected in conventional sorption experiments, and the scanning curves have revealed their structural relationship to smaller pores below the limits of many imaging modalities. Hence, overcondensation allows the bridging between very diverse length-scales in the pore structure. Further, uniquely in the depth series considered, the overcondensation desorption isotherm for sample U3 exhibits a percolation knee, consistent with the presence of a more complex, disordered pore structure at this depth, not evident in the conventional sorption data. The disorder in the pore structure, represented by the percolation knee, is consistent with the more complex mixture of mineralogical phases present in U3. Complementary integrated mercury porosimetry and CXT data has also shown an evolution in the macroscopic spatial distribution of the accessible nanoporosity across the depositional transition. This is associated with the changes in amount and spatial disposition of the carbonate minerals.

6.6. Additional Work

Differential scanning calorimetry (DSC) was used in conjunction with mercury intrusion porosimetry to try and reveal pores that were shielded during the mercury intrusion experiments. When a fluid is within a pore body (black blobs in previous slide) its melting temperature decreases as a function of the pore size it is in. The methodology for this experimental procedure is detailed in 4.3. Differential Scanning Calorimetry (DSC), and the results from this are shown below (samples analysed were U1, U2, U3 and U5). Conclusions of the experiment were unsuccessful due to the pores in which mercury was trapped being too large to differentiate from the bulk mercury peak in the DSC results (Figure 83). In samples U1, U2 and U3 mercury trapped in pores melted enough before the bulk melting

peak to skew the symmetry of this. An example of a sample which has suppressed the melting point below that of bulk mercury and produced a separate melting peak is included (Figure 18).

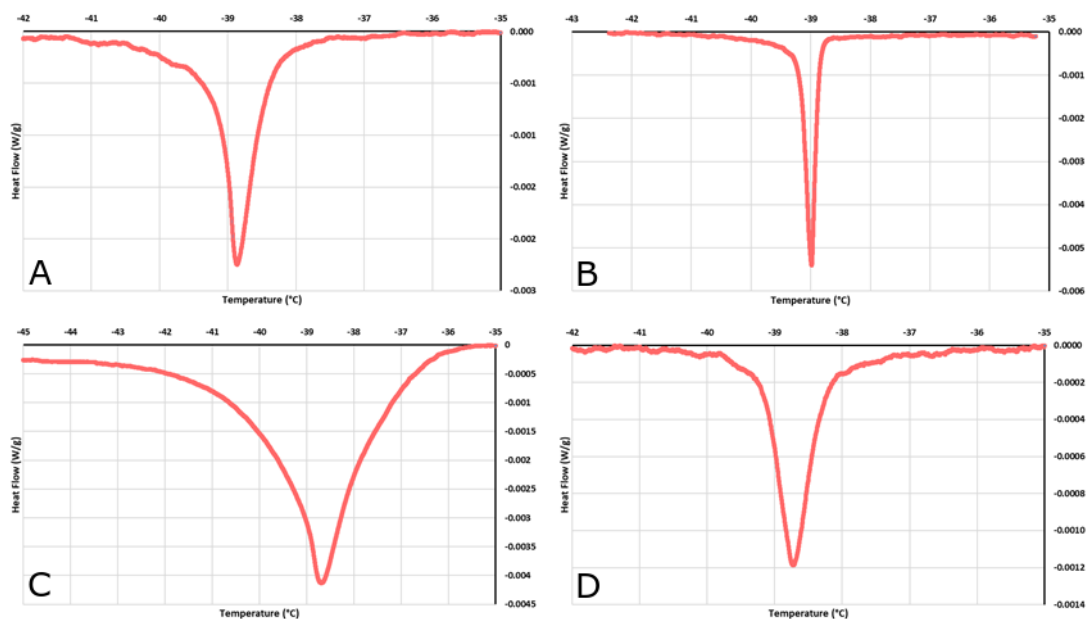


Figure 83: (A) DSC for U1 where there is some depression of the bulk mercury peak skewing the symmetry of it, however the lack of separate peak means that the determining pore size distributions accurately from this data is not possible, (B) DSC for U2 where there is some depression of the bulk mercury peak skewing the symmetry similar to U1, (C) DSC for U3 where the bulk peak appears significantly more skewed than for U1 and U2, however no separate peak is formed making accurate determination of the pore size distribution not possible and (D) DSC for U5 where there is no skewed symmetry of the bulk peak in comparison to U1, U2 and U3.

The maximum heat flow achieved by each sample is correlated to the volume of trapped mercury. From Figure 67 it can be seen that U2 and U3 have a similar quantity of trapped mercury and both have a maximum heat flow of approximately -0.004 W/g (Figure 83B) to approximately -0.005 W/g (Figure 83C), U1 has the next largest volume of trapped mercury (Figure 67) and has a maximum heat flow of approximately -0.002 W/g (Figure 83D) and finally U4 the smallest volume of trapped mercury for these samples (Figure 67) and a maximum heat flow of approximately -0.001 W/g (Figure 82D).

By comparing the DSC results of U2 (Figure 83B) and U3 (Figure 83C) it can be seen that the relative depression to the bulk melting peak is significantly greater for U3 than for U2. This can specifically be seen by comparing the “wavelength” of the peak where U2 spans 2°C and U3 7°C and begins melting at -43°C compared to U2 at -41°C. From this it is possible to say that in U3 trapped mercury is trapped in pores of a smaller size than they are for U2.

Although the desired results were not achieved, analysis of the bulk peaks can still be used to identify potential complexity of the pore networks and where mercury is trapped in smaller or larger pores. Further, these results are in line with the other results of the Utica samples showing that although separate melting peaks were not derived the measured results were consistent with the findings of other experiments.

7. The Bowland Shale

7.1. Materials

The three samples studied in this work were obtained from the British Geological Survey, Keyworth, UK. They were originally taken from the Preese Hall Well 1 in north-western England, as shown in Table 11.

| Sample | Reference | Source | Depth (m) |
|--------------------|-----------|---------------|-----------|
| Above Marine Band | BLD3 | Preese Hall-1 | 2500.92 |
| Within Marine Band | BLD2 | Preese Hall-1 | 2501.17 |
| Below Marine Band | BLD1 | Preese Hall-1 | 2501.37 |

Table 11: details of shale samples studied in this work.

The Bowland Shale was deposited during the Carboniferous (Visean to Bashkirian) time period, and makes up a part of the Craven Group; it overlies the Pendeseide Formation and is overlain by the Millstone Grit. Data on the Bowland Shale is known from a combination of outcrop data and subsurface borehole data across the north of England, Isle of Man, parts of North Wales and the Midlands.

During the depositional period for the Bowland Shale sea level fluctuations led to the sedimentary successions developing in a cyclical fashion with non-marine and marine shales. Marine shales make up the minor bands in the sequence and are associated with maximum flooding surfaces and the maximum rate of sea level rise (Hough *et al.*, 2014; Gross *et al.*, 2015). There is significant interest in this cyclicity and the consequential variations in total organic carbon throughout the cycle because of where certain areas may be of a greater or lesser prospect for oil or gas production. As has been seen in the 6. The Utica Shale there is a lot of variation across these boundaries which greatly affects the resultant pore surface area, pore volume and total organic carbon content of the sample. Specifically seen in the increased complexity of the mineral assemblage resulting (for U3) in a highly heterogeneous pore network.

7.2. Methodology

7.2.1. Gas Sorption

A Micromeritics 3Flex was used for conventional sorption experiments, using nitrogen (at 77K) and carbon dioxide (at 273.15K) as adsorbates, over the relative pressure range $0-0.995 \frac{p}{p_0}$, and $0-0.035 \frac{p}{p_0}$, respectively, for shale chip samples of characteristic sizes of 3-5mm. This technique is used to measure pore sizes in the range of 2-50nm, although the analysis can provide data for larger pore sizes, it is not possible to be confident that complete filling of these pores has occurred. Hence, nitrogen overcondensation experiments were also performed on a Micromeritics ASAP 2020 physisorption analyser to probe the larger pore sizes and upper end of the hysteresis. In the overcondensation experiment, the pressure is increased above the standard vapour pressure of nitrogen which should facilitate condensation such that even the largest pores are filled with liquid nitrogen at the start of the desorption isotherm. With the overcondensation adaptation to the standard gas adsorption technique, it is possible to analyse pores which are greater in size than 50nm. Further, the overcondensation experiment also incorporated scanning loops. The ascending branches of two scanning loops were initiated at relative pressures of 0.5 (henceforth denoted scanning loop 1, SL1) and 0.8 (SL2), respectively, on the overcondensation boundary desorption isotherm, and the descending branches of both loops were initiated at a relative pressure of 0.995. The pore radii corresponding to these relative pressures from the Broekhoff and de Boer (1967, 1968), method for hemispherical menisci are 2.6 (SL1), 6.4 (SL2), and 300 nm, respectively.

Secondary analysis was carried out on an Autosorb iQ – Chemisorption (& Physisorption) Gas Sorption Analyser (iQ-C/MP/Kr/MS) from Quantachrome Instruments coupled to an in-situ mass spectrometry and calorimetry system (Setaram SenSys EVO 3D TG-DSC) with carbon dioxide at 283.15K over the relative pressure range of 0-0.027 (lower pressure reached due to increased temperature). The coupling of these systems provides the data to analyse the system kinetics and heat of adsorption at each pressure step.

As part of the analysis conditions, the degas and equilibration times were varied to investigate the effect of sample pre-treatment on the results. Experiments were conducted where the intensity of the thermal pre-treatment was varied in terms of temperature and time, and the equilibration time during the gas sorption experiment itself was also varied. In this way the impact of any degassing on the pore structure and its subsequent accessibility can be assessed. The primary aim is to investigate the pore properties and characterisation of the samples, as opposed to measuring the impact of mineral swelling on potential production and storage uses.

Shale samples were pre-treated in a range of different ways before adsorption experiments. Samples were given either no thermal pre-treatment at all (just evacuation to vacuum), or were degassed at 110°C for 16 hours overnight, or degassed at 140°C for 3 hours, or degassed at 140°C for 16 hours, and then degassed at 140°C for a further 3 hours after initial degassing and a nitrogen sorption experiment. Nitrogen sorption experiments were conducted with equilibration times of either 20 s or 60 s.

7.2.1.1. Gas Sorption Theory

Fractals provide a mathematical model that can quantitatively describe some of the pore structural heterogeneity found in shales, and thus fractals have been used extensively in characterisation studies of shale rocks (Ojha *et al.*, 2017; Wang *et al.*, 2019). One way in which the particular geometry of fractals is made manifest is through its effects on gas sorption data. Fractal surfaces are rough, with the surface fractal dimension providing an index of that roughness, with a value of 2 meaning the surface is flat, and a value of 3 implies the surface is very contorted such that the surface is space-filling. The impact of fractal geometry on multi-layer build-up in gas has been incorporated into physical models of this process. Two examples of this include the fractal version of the BET equation (Mahnke and Mögel, 2003):

$$\log(V) = \log(V_m) + \log\left[\frac{Cx}{1-x+Cx}\right] - (3-D)\log(1-x) \quad (15.1)$$

where V is the amount adsorbed, x is the relative pressure, V_m is the monolayer capacity, C is the BET constant, and D is the fractal dimension. The Frankel-Halsey-Hill (FHH) model for adsorbed films has also been adapted for fractal surfaces, such that (Rigby, 2020):

$$\frac{V}{V_m} = B \left[\ln\left(\frac{1}{x}\right) \right]^s \quad (15.2)$$

where B is a constant and s is an exponent that depends upon the mechanism of adsorption. At lower pressures, during the early stages of multilayer build-up, the film/gas interface is controlled by attractive van der Waals forces which tends to make the said interface replicate the surface roughness. In this case, the value of the constant s is given by $\frac{(D-3)}{3}$. However, at higher coverages, the position of the interface is determined by the liquid/gas surface tension which makes the interface move further away from the surface so as to reduce the surface area. In this second case, s is given by $(D-3)$. Hence, the FHH model can incorporate the influence of surface tension, and thus fitting can be extended into regions of the isotherm where capillary condensation might be

occurring, whereas the BET model only takes account of van der Waals interactions, and thus applicability is strictly limited to multilayer build-up regions.

The Toth isotherm model is often used to describe adsorption on heterogeneous surfaces (Tóth, 1995). The Toth isotherm is given by (Kumar *et al.*, 2011):

$$q = \frac{q_m p}{(b + p^T)^{1/T}} \quad (15. 3)$$

where q is amount adsorbed and p is pressure, and the three characteristic Toth parameters are q_m , which is the maximum adsorption capacity, b , which is a constant related to the binding affinity and specific to particular adsorbate–adsorbent combinations and T is an exponent related to surface heterogeneity, which typically has a value less than or equal to unity.

Composite materials, like shales, have further types of heterogeneity besides surface roughness, and these can be accounted for in other ways. The homotattic patch model was introduced in order to account for the effects of chemical heterogeneity of surfaces on adsorption (Walker and Zettlemoyer, 1948). This model considers the surface of the adsorbent to consist of a patchwork of different types of site each with their own characteristic adsorption behaviour. The model assumes that each of these patches is large, such that edge effects, where they neighbour other patches, are negligible. The resulting overall adsorption is thus a composite of the behaviour of the set of patches, such that:

$$V = V_m(f_1 I_1 + f_2 I_2 + \dots + f_i I_i + \dots) \quad (15. 4)$$

where I_i is the isotherm equation describing adsorption on the i th patch, and f_i is the fraction of the surface occupied by patches of type I_i , such that the various f_i -values obey:

$$f_1 + f_2 + \dots + f_i + \dots = 1 \quad (15. 5)$$

The homotattic patch is based on the understanding that different materials will have different sorption behaviours based on their surface chemistry. Shales have a very heterogeneous surface formed of organic and inorganic minerals. In this work, the homotattic patch theory will be used to separate the contributions to adsorption from each of the organic and inorganic matter phases in the shale. The homotattic patch models used represented adsorption on the inorganic phase using the fractal BET equation, or the FHH isotherm, while the organic phase was represented by an empirical fit to an experimental isotherm for a pure kerogen sample extracted by acid-dissolution of the inorganic matrix.

7.2.1.2. Mass Transport

Gas phase mass transfer rates for coupled diffusion with adsorption processes within the shale were probed by two independent methods, namely mass uptake and adsorption (micro) calorimetry (Auroux, 2013). In adsorption calorimetry the raw data consists of the heat-flow produced from the sample in the course of a given pressure step in the adsorption isotherm. The longer-time trailing edge of this heat-flow data is typically fitted to an exponential decay function to obtain the characteristic time constant, denoted t . The time constant, t , is defined by the exponential decay function:

$$D(t) = D_m e^{-\frac{t}{\tau}} \quad (15. 6)$$

where $D(t)$ is the deviation of heatflow at a given time, D_m is the maximum deviation of the heatflow, and t is time.

The alternate method also used in this work was the measurement of the kinetic mass uptake with time. The raw data from this experiment typically takes the mathematical form of an exponential growth, and is often fitted to the so-called Linear Driving Force (LDF) model (Glueckauf, 1955; Sircar and Hufton, 2000). The characteristic parameter of this process is the mass transfer coefficient, denoted k . The LDF k -value is defined by the function (Rigby, 2020):

$$M = M_0(1 - e^{-kt}) \quad (15.7)$$

where M the amount of carbon dioxide adsorbed at time t , M_0 is the ultimate total adsorbed amount of carbon dioxide for the adsorption pressure point, and k is the mass transfer coefficient. The apparent mass transfer coefficient, obtained from a fit to raw uptake data, must be corrected for the effect of concurrent adsorption using the slope of the isotherm at the relevant adsorption pressure point. In this way the actual mass transfer coefficient is obtained. The mass transfer coefficient can be converted to an equivalent time constant by taking the reciprocal.

The thermokinetic parameter is thought to characterise the accessibility of adsorption sites, since it is obtained from the heat evolved when molecules reach their adsorption sites (Auroux *et al.*, 2009). The LDF model is thought to particularly characterise the limitations arising from surface barriers.

7.2.2. Mercury Intrusion Porosimetry (MIP)

A Micromeritics AutoPore IV 9500 was used for low- and high-pressure mercury intrusion porosimetry at ambient temperature and constant volume. The low- and high- analysis ports take the sample from atmospheric pressure, to under vacuum, and then to 207MPa (low-pressure) and 414MPa (high-pressure). Mercury intrusion porosimetry enables the analysis of macro-pores, but only measures the throat size of the pore and not the body size (which gas adsorption does). The mercury is also only able to access pores which have throat sizes >4nm which can lead to very low intruded volumes in samples which are dominated by micro-pores or fine meso-pores.

7.2.3. Scanning Electron Microscopy with Mineral Liberation Analysis (SEM MLA)

SEM MLA was carried out on an FEI Quanta 600 (operated at 20kV, working distance of 13mm and spot size 7) equipped with mineral liberation analysis software. This enables the quantification of sample mineralogy by taking several energy dispersive X-ray (EDX) points which are associated with a specific dispersive X-ray spectra and can be matched to known minerals from a mineral database. The necessity of comprehensive mineralogical understanding is such that the adsorptive properties of the samples can be thoroughly understood and analysed.

7.3. Results

7.3.1. Sample Petrology

As can be seen from Figure 84, the Bowland Shale samples analysed in this work are clay dominated with the presence of some silicates (predominantly quartz) and a variable quantity of carbonates (limestone). Considering the aforementioned depositional environment of the samples, the mineralogy supports the locations from which they were taken. Below the marine band is a period of shallowing sea levels where the quantity of carbonates is increasing as the carbonate platform begins to form, although deposition is still dominated by the transport of mud sized particles. The marine band is a period of the lowest sea level where there was a greater carbonate platform and less input from mud sized particles in hemipelagic flows. The sea level then fluctuates again and increases moving towards a maximum flooding surface in the above marine band sample, during this

time there is a much greater input of sediment and results in a clay dominated sample with very little carbonate content.

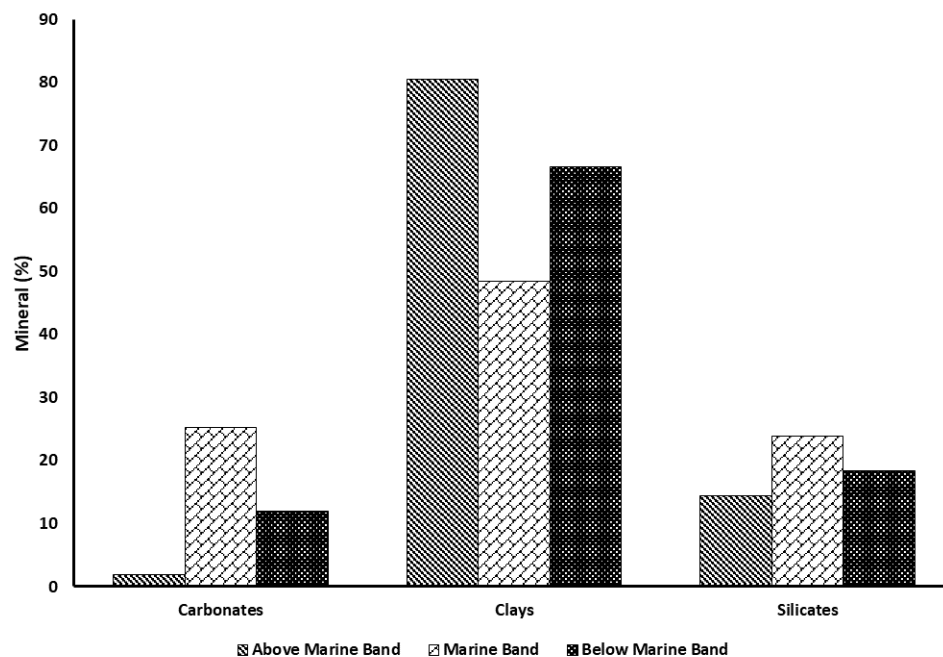


Figure 84: mineral composition of the above marine band (grey textured), marine band (diagonal empty bricks) and below marine band (textured black) shale samples studied in this work.

Figure 85, Figure 86 and Figure 87 show typical scanning electron microscopy (SEM) images of the three Bowland samples. It can be seen that the texture is dominated by clay-particles, but also with coarser quartz and calcite grains throughout the samples. With decreasing depth of origin of the shale, the coarseness of the quartz and calcite grains decreases, and they are more aligned with a particular direction. While visual inspection of the images suggests a similar incidence of total organic carbon (TOC%) in the below marine and marine band samples, there is a much greater quantity of (visible) TOC% in the above marine band sample. The above and below marine band samples exhibit some suggestion of an ordering in the TOC% distribution, where the long axis of particles is aligned in the same direction, but this is not seen in the marine band sample, where the distribution and direction of TOC% is non-uniform. Additionally, with decreasing depth there is an increase in the quantity of pyrite within the samples which indicates an excess quantity of iron and sulphides within an anoxic environment, as, in the presence of oxygen, iron oxides such as hematite would have preferentially formed.

At the resolution of these SEM images it is not clear whether there are any biogenic carbonate inputs from fossils or tracks, and it also appears that all carbonate inputs are as a result of sedimentary deposition and not precipitation. Consequently, it is likely that, in this particular area, a shallow marine environment may have not formed, or have had time to form, and lead to the preservation of any fossil evidence.

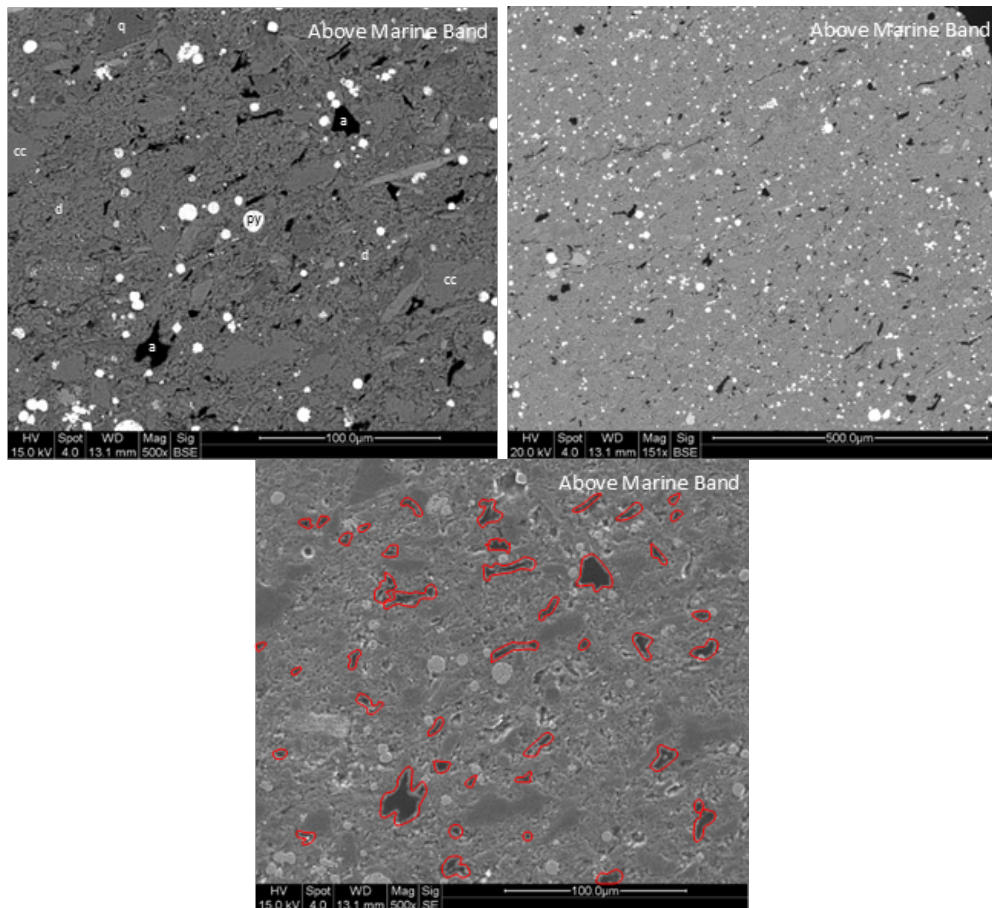


Figure 85: BSE SEM image (top), and corresponding SE (bottom) SEM image, from the above marine band showing a clay sized particle matrix [denoted d] dominated by illite with courser quartz [denoted q] and carbonate [denoted cc] grains interspersed throughout. These are aligned bottom left to top right across the image, and the total organic carbon [denoted a] is similarly aligned, the presence of pyrite [denoted py] is indicative of an anoxic environment. In the SE image (bottom) the organic carbon particles have been highlighted with a red border. In the second BSE SEM image (top right) the mineral and organic matter alignment can be seen more clearly.

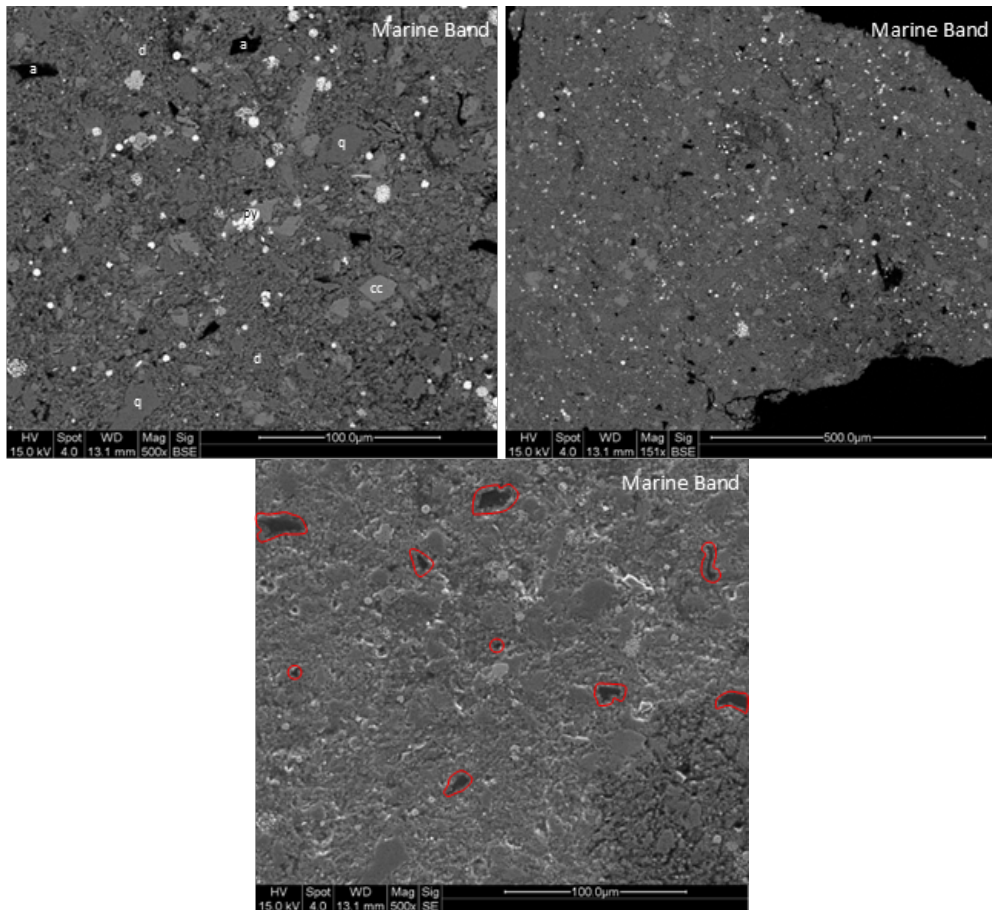


Figure 86: BSE SEM image (top), and corresponding SE (bottom) SEM image, from the marine band showing a clay sized particle matrix [d] dominated by illite. There are coarser grains of carbonate [cc] and quartz [q] which are not preferentially aligned. In the SE image (bottom) the organic carbon particles have been highlighted with a red border. The second BSE SEM image (top right) samples a different field of view.

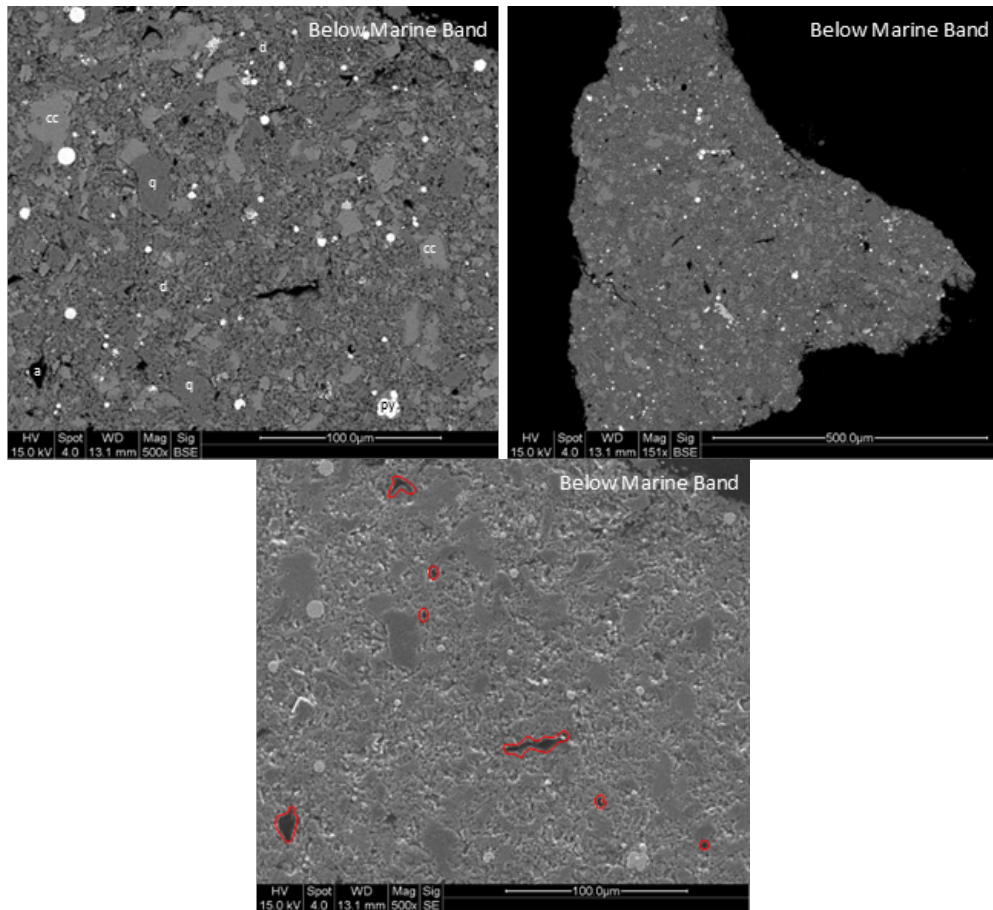


Figure 87: BSE SEM image (top), and corresponding SE (bottom) SEM image, for the below marine band shale. The images show a clay sized particle matrix [d] dominated by illite, with coarser quartz [q] and carbonate [cc] grains interspersed and showing no preferential alignment. The decrease in total organic carbon [a] and pyrite [py], relative to Figure 85 and Figure 86, potentially indicates a less anoxic environment.

7.3.2. Conventional Nitrogen Sorption and Overcondensation

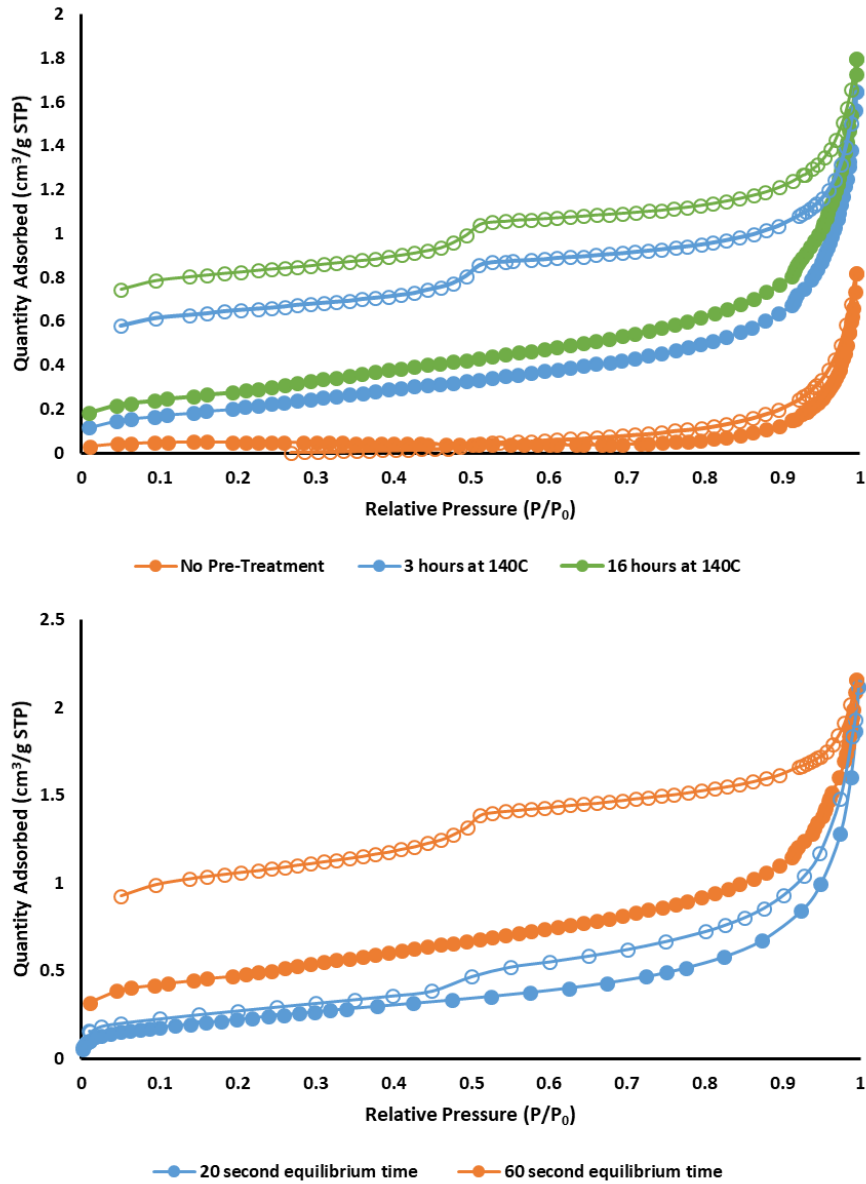


Figure 88: nitrogen adsorption (solid symbols) and desorption (open symbols) isotherms for the marine band shale obtained under a variety of pre-treatment and experimental conditions, namely either no thermal pre-treatment (●) at all (just evacuation to vacuum) and equilibration time (ET) of 20 s, or degassed at 140°C for 3 hours and ET=20 s (●), or degassed at 140°C for 16 hours and ET=20 s (●). The sample was then degassed at 140°C for a further 3 hours after initial degassing and nitrogen sorption experiment before conducting a further nitrogen sorption experiment with ET=60 s (●) in the second figure.

Nitrogen sorption isotherms were obtained at 77K for samples of the marine band shale, that had previously been exposed to the atmosphere for 8 days, utilising a variety of pre-treatment and experimental conditions, namely either no thermal pre-treatment at all (just evacuation to vacuum) and equilibration time (ET) of 20s (condition #1), or degassed at 140°C for 3 hours and ET=20s (#2), or degassed at 140°C for 16 hours and ET=20s (#3), and then degassed at 140°C for a further 3 hours after initial degassing and nitrogen sorption experiment before conducting a further nitrogen sorption experiment with ET=60s (#4). From Figure 88, it can be seen that as the harshness of the thermal pre-treatment conditions increases through conditions sets 1-3, the degree of low pressure hysteresis increased. However, for conditions set 4, the low pressure hysteresis is lower. It is noted that the times for equilibration of the first data-point in each of the isotherms 1-4 in Figure 88, were 54, 119, 214 and 835 minutes, respectively. The micro-pore volumes from these initial data points

were 0.046, 0.180, 0.282, and 0.497ml/g, for isotherms 1-4, respectively. These findings suggest there is some phase which if given minimal pre-treatment (#1) or gentle pre-treatment probably keeps much of pre-adsorbed atmospheric moisture, which freezes at 77K and thus the phase is inaccessible to N_2 , and the isotherm is reversible. If a progressively harsher (longer time at higher temperature) pre-treatment is applied then more water is released from this phase, and nitrogen can enter slowly, and not leave over experimental timescales, so there is increasing low pressure hysteresis. However, this water loss or other process can be overcome with even longer outgassing and longer equilibration times (#4) but these are getting very long to be practicable for routine analysis. The narrowing of hysteresis between experimental conditions sets #3 and #4 suggests some stabilisation of structure and equilibrating of isotherm can occur but these are very slow processes. Hence, in subsequent data discussed in this section a gentler pre-treatment data will be used which means the gas sorption characterisation is thus restricted to characterising other non-swelling phases only. It is noted that the marine band shale sample was the least stable against varying thermal pre-treatment conditions, while the above marine band (data not shown) was much more stable.

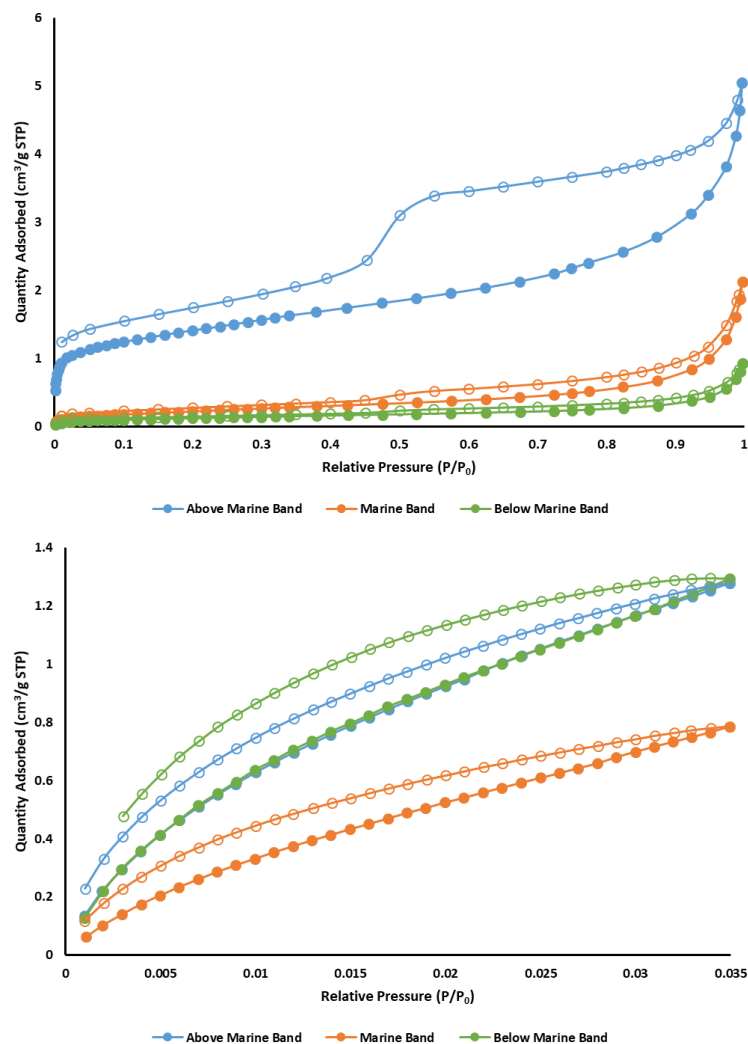
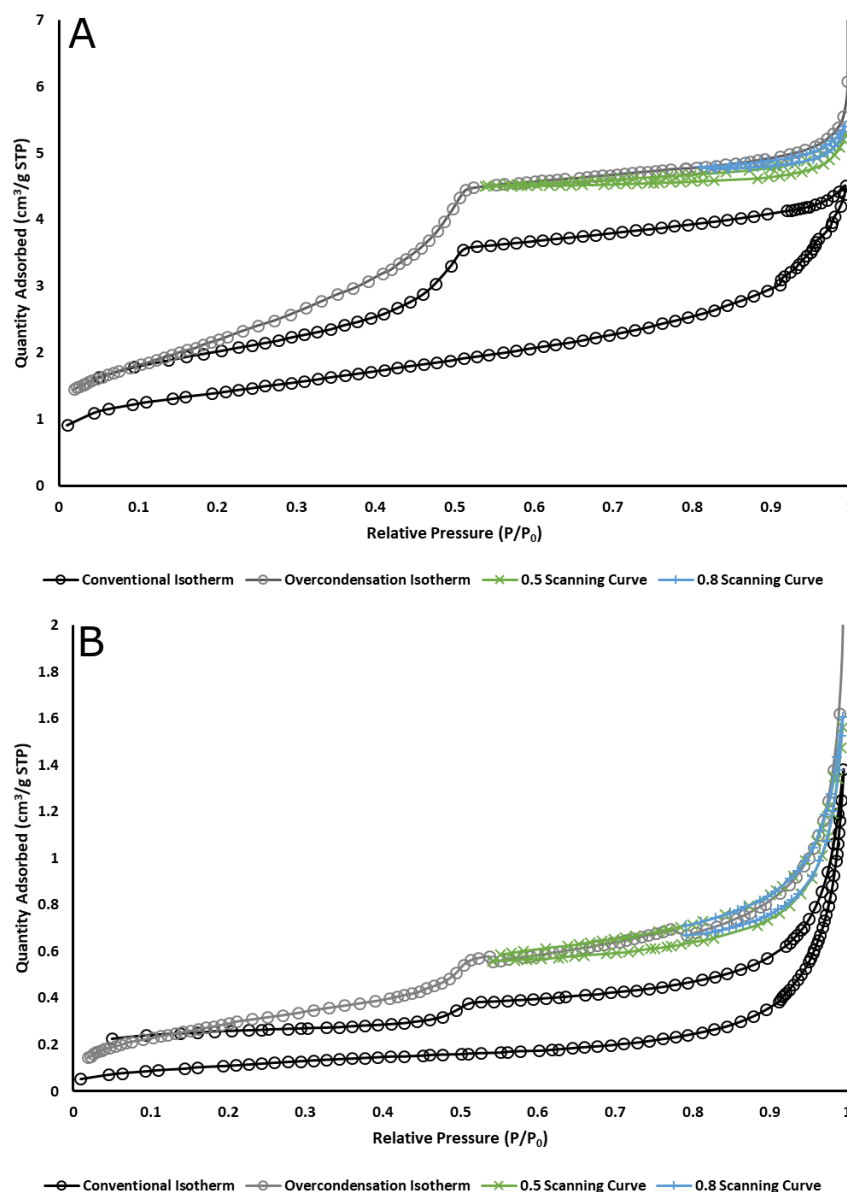


Figure 89: conventional nitrogen (top) and carbon dioxide (bottom) adsorption (solid symbols) and desorption (open symbols) isotherms obtained for samples of the above marine band (●), marine band (●), and below marine band shales (●) with equilibration times of 30 s for the micro-pore region, and 20 s for the meso-pore and above region, following degassing at 110°C for 16 hours.

Figure 89 shows the conventional nitrogen sorption isotherms obtained for the three different shale samples, following degassing at 110°C for 16 hours, and using equilibration times of 30 s for the

micro-pore region and 20 s for the meso-pore and above region. It is noted that this set of conditions results in little low pressure hysteresis, especially compared with harsher outgassing conditions, as seen in Figure 88. It can be seen that each isotherm still has a steep step at low relative pressure associated with the filling of some microporosity, with the above marine band having a larger step than the other two samples. Thereafter the adsorption isotherms increase slowly in a linear fashion. However, at higher relative pressures above 0.8, there is a significant rise in amount adsorbed. The top of all the conventional adsorption isotherms has a hyperbolic form suggesting that complete pore-filling has not been achieved at the ultimate pressure obtained in the conventional experiment. In all three cases, desorption commences immediately upon the reverse of the change in pressure and the top of the isotherms are reversible. However, all three isotherms show a widening of the hysteresis with decreasing pressure on the desorption branch. While the width of hysteresis remains narrow for the marine band and below marine band shales, it widens into a large rhomboid-shape for the above marine band sample. All three shale samples also have a sharp knee in the desorption branch at relative pressure of 0.45-0.5, it is much steeper for the above marine band shale.



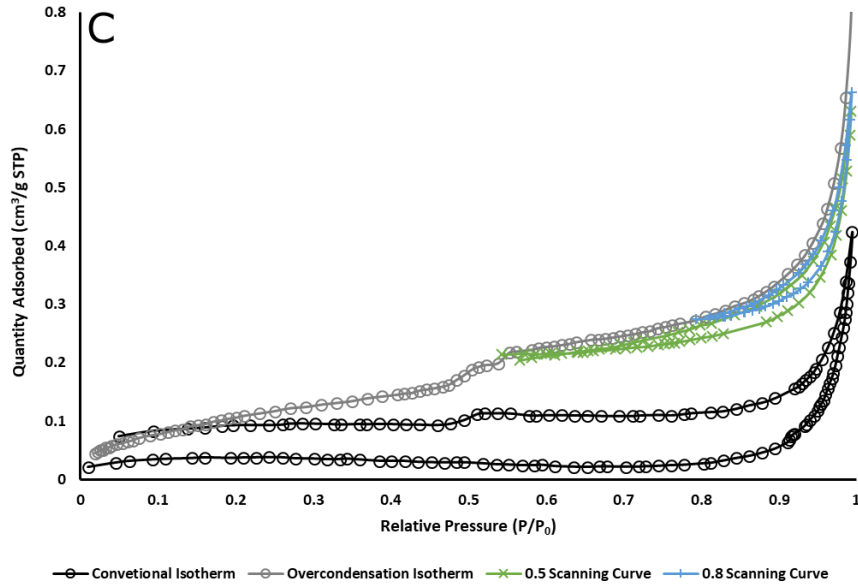


Figure 90: a comparison of the conventional isotherm (empty ●) with the overcondensation boundary desorption isotherm (empty ●) with scanning loops SL1 ($0.5 \frac{P}{P_0}$ scanning loop X) and SL2 ($0.8 \frac{P}{P_0}$ scanning loop X) for samples of the (A) above marine band, (B) marine band and (C) below marine band shales. The equilibration time for the isotherm points was 20 s.

Figure 90 shows a comparison of the nitrogen overcondensation desorption isotherm with the conventional sorption isotherms, all obtained with an equilibration time of 20s, for all three shale samples. From Figure 90, it can be seen that while SL2 crosses SL1 for the below marine band shale, it does not for the above marine band shale, where the ascending branch for the former merely touches the descending branch of the latter. From Figure 90, it can be seen that the height of the step at a relative pressure of 0.45-0.5 is increased in the overcondensation desorption isotherm, when compared to the conventional desorption isotherm, for the above marine band shale.

7.3.3. Conventional Carbon Dioxide Sorption

Figure 91 shows carbon dioxide isotherms obtained at 273.15K obtained for the three different shale samples, following degassing at 110°C for 16 hours. It can be seen that uptake is highest for the above and below marine band samples over the pressure range obtained.

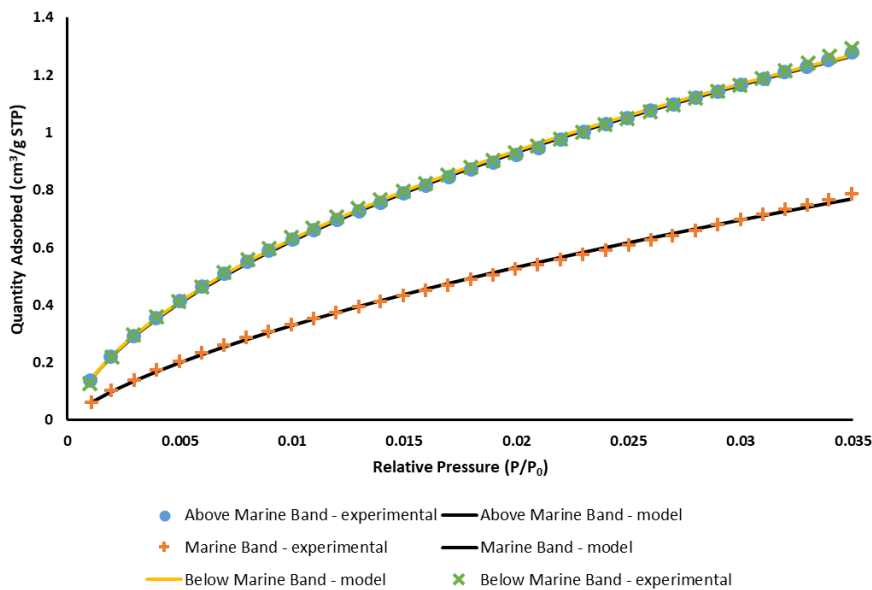


Figure 91: carbon dioxide adsorption isotherms obtained at 273.16 K for the above marine band (●), marine band (+), and below marine band (x) shale samples. Also shown (solid lines) are fits of the adsorption data to the Toth isotherm equation. The resultant fitted parameters are given in Table 14.

7.3.4. Mercury Intrusion Porosimetry (MIP)

Figure 92 shows the raw mercury porosimetry data for the three shale samples. The initial steep rise in the intrusion curves for the marine band and below marine band samples represents inter-particle intrusion. For all three samples the intra-particle intrusion at higher pressures (>1000 psi) is very small indeed. Hence, mercury intrusion seems unable to access the interior of the samples, thereby suggesting that pore openings on the exterior are all below approximately 3.5nm, which is the lower limit for the mercury porosimeter used in this work.

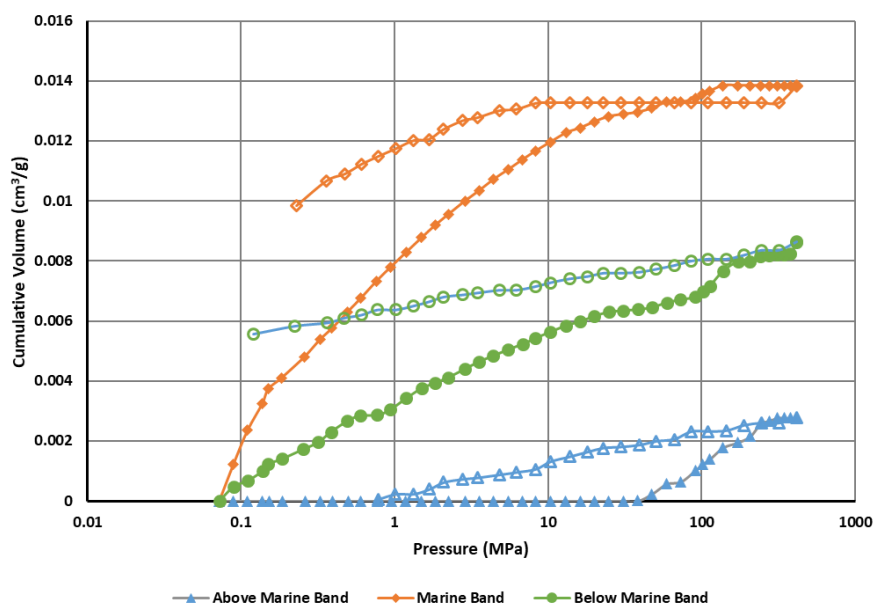


Figure 92: mercury intrusion (solid symbols) and extrusion (open symbols) porosimetry data for the above marine band (▲), marine band (●), and below marine band (◆) shale samples.

7.3.5. Mass Transfer

Figure 93 shows typical examples of raw data-sets obtained from the carbon dioxide adsorption kinetics experiments to study mass transport in the shales. From Figure 93A, it can be seen that the heat-flow for a typical adsorption step, obtained by microcalorimetry, exhibits the ‘shark-fin’ like asymmetric peak form, as observed in previous studies of carbon monoxide adsorption on carbon materials (Aurox *et al.*, 2009). There is an initial relatively steep rise in heat released, followed by a slower decrease. It can be seen, from the good fit of (15. 6) obtained to the trailing edge of the shark’s fin, that it follows an exponential decay. The region fitted was well beyond the peak but stopped at the marked change in slope. In addition, from Figure 93B, it can be seen that the mass uptake response with time for the same typical adsorption step follows an exponential growth akin to the form of ((15. 7).

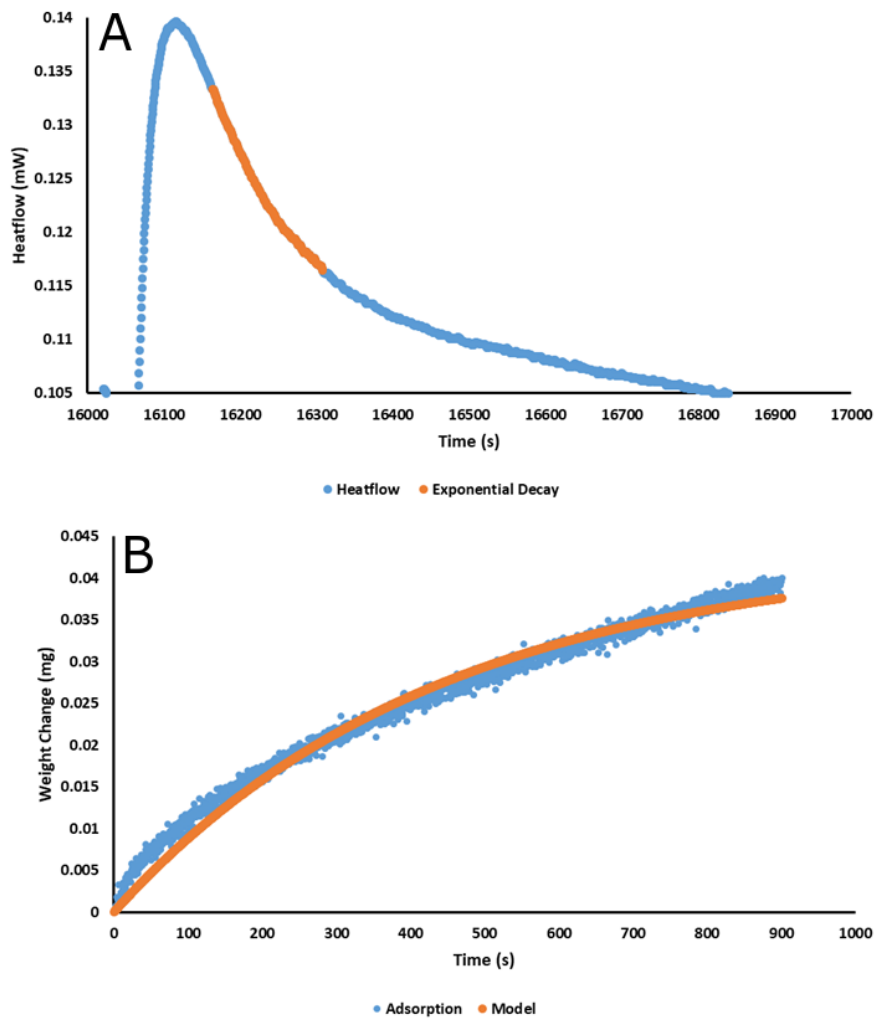


Figure 93: typical raw data-sets for the eighth adsorption point from an adsorption calorimetry experiment on a sample of above marine band shale, (A) showing heat-flow and (B) mass uptake. Also shown (solid orange lines) are fits of the experimental data to equations 6 (a) and 7 (b).

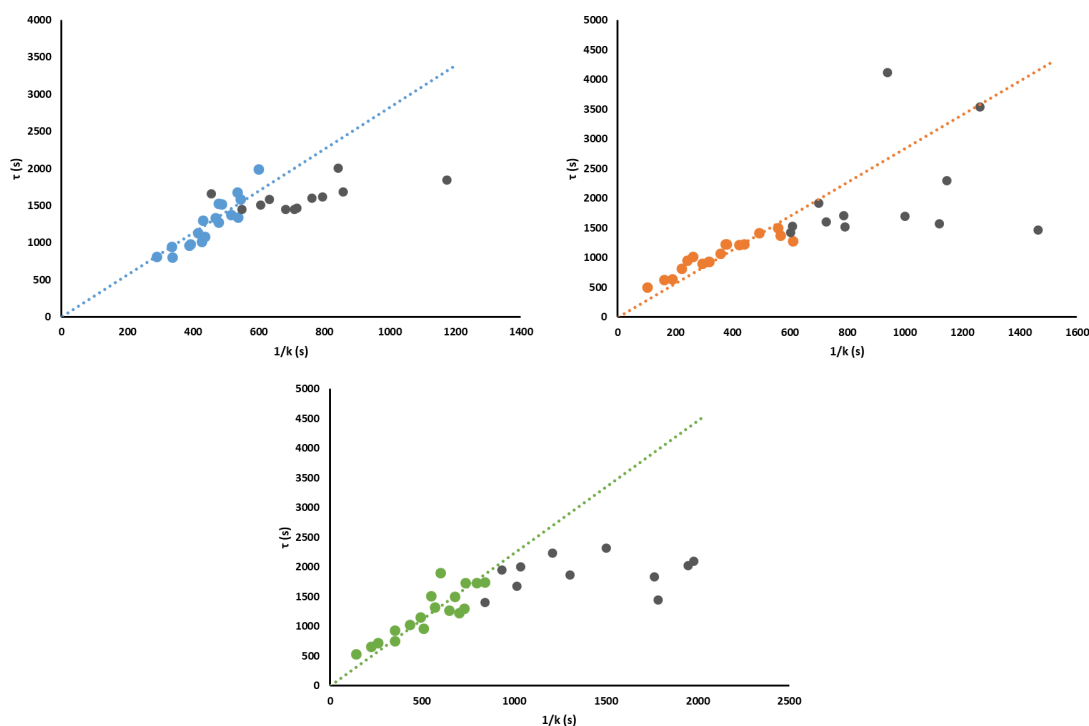


Figure 94: comparisons of the mass transfer parameters obtained from the adsorption calorimetry and adsorption-corrected mass uptake methods at different carbon dioxide saturations for adsorption isotherms on the above marine band (●), marine band (●) and below marine band (●) shales. The dashed lines shown are fits of the data to straight line functions through the origin including data points from 0-730 mbar. Where the straight line fit has not been modelled is indicated with a ●

Figure 94 shows correlations of the characteristic mass transfer parameters obtained from the adsorption microcalorimetry (t in equation (15. 6)) and mass uptake (k in equation (15. 7)) methods for the same adsorption step for a range of saturation levels of carbon dioxide during adsorption experiments on the three shale samples. The observed mass transfer coefficients k , as obtained from plots like Figure 93B, have been corrected for adsorption before plotting in Figure 94, but the correction factors were very close to unity due to low saturations in shales. It can be seen that over the pressure range 0-730 mbar, which is associated to the lowest and medium-sized values of time constant, t , there is a good fit to a straight line correlation with the reciprocal of the mass transfer coefficient. This relationship suggests that both methods are probing the same mass transfer processes and could thus be interchangeable as a kinetics measurement at the lower pressure region. When the fits deviate from the straight line at pressures greater than 730 mbar (larger time constants) there is a tendency for the fits to form a plateau where the reciprocal of k , increases at a greater rate than τ . In further work the fit of another trendline could be analysed which is in the form of a Langmuir, where a derived constant from this method is indicative of the amount of “shuffling” occurring within a sample and thus the overall sample internal complexity.

Figure 95 shows the variation in mass transport coefficient parameter k with carbon dioxide saturation. From Figure 95 it can be seen that the rate of mass transfer declines steeply with increasing carbon dioxide saturation for all three shale samples.

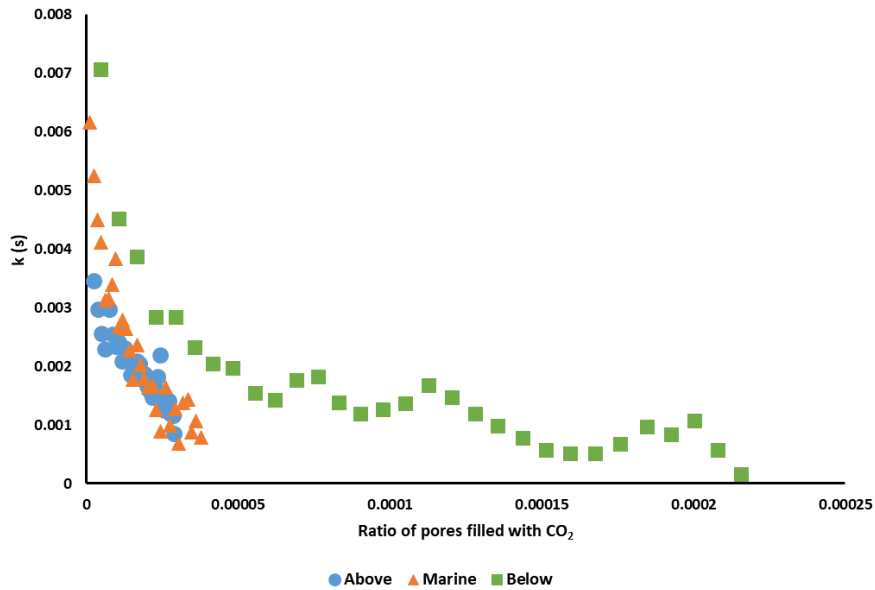


Figure 95: variation of mass transfer coefficient k with fractional carbon dioxide saturation for the above marine band (●), marine band (▲), and below marine band (■) shale samples.

It should be noted that in the calculation of carbon dioxide saturation used in this work, the determination of the Gurvitsch volume (specific pore volume from quantity of liquid adsorbate required to completely fill the void space) used nitrogen as the adsorbate. The result is that the pore volume probed could be different from that by carbon dioxide, and, when a sample has an especially low volume of pores larger than micro-pore sizes, then the Gurvitsch volume method will potentially underestimate the specific pore volume resulting in the ratio of quantity adsorbed between nitrogen and carbon dioxide to be skewed. Consequently the trend of the data for the samples is more significant than the exact values which are derived from the analysis.

7.3.6. Numerical Modelling

The nitrogen adsorption isotherms shown in Figure 89 were each fitted to separate fractal versions of the BET (12. 2) or FHH (12. 4) model isotherms over relative pressure ranges of 0.2-0.5 and 0.5-0.995 in order to obtain the surface fractal dimensions that applied over these two ranges, denoted D_1 and D_2 , respectively. The cut-offs for these relative pressure ranges were selected as follows. The FHH model is only valid above monolayer coverage, where the surface film is complete, and so a lower relative pressure cut-off well above the initial knee (known as Point B Gregg and Sing, (1982)) was selected. The cut-off relative pressure of 0.5 corresponds to the upper bound for cavitation effects for nitrogen (Rouquerol *et al.*, 2014). Cavitation is associated with desorption from pore bodies shielded by very narrow necks (<4nm diameter). The fits to the fractal BET and FHH models gave very similar results so only those for the FHH model are explicitly reported here.

Figure 96 shows the variation of surface fractal dimension D_1 , and the clay content, for the three shale samples. It can be seen that there is a correlation between D_1 and the clay content. This might be anticipated because the fitting range for D_1 corresponds to the small mesopore sizes expected in clay materials.

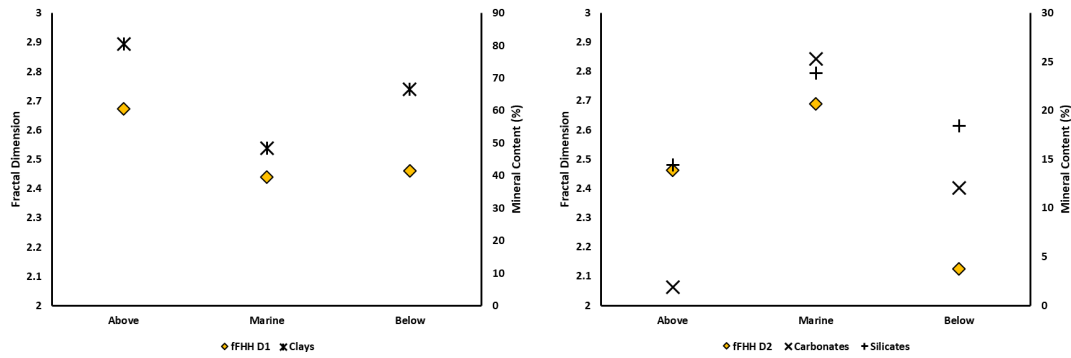


Figure 96: variation of surface fractal dimension D_1 (♦) from a fit of the fractal FHH model to nitrogen adsorption isotherms over relative pressure ranges of 0.2-0.5 (left), and the clay content (*), for the three shale samples and comparison of the variation of D_2 (♦), and the carbonate (X) and silicate (+) mineral composition (right), for the three shales. Parameters used are listed in Table 12.

| | V_{m1} (cm ³ /g STP) | D_1 | V_{m2} (cm ³ /g STP) | D_2 |
|---------------|-----------------------------------|------------|-----------------------------------|------------|
| Above | 1.194125 | 2.673499 | 1.143949 | 2.461631 |
| | ± | ± | ± | ± |
| | 0.0702553 | 0.00272335 | 0.06941411 | 0.0018165 |
| Marine | 0.202592 | 2.440007 | 0.204128 | 2.688219 |
| | ± | ± | ± | ± |
| | 0.01057948 | 0.00373475 | 0.0107589 | 0.00110031 |
| Below | 0.105632 | 2.461348 | 0.100682 | 2.125772 |
| | ± | ± | ± | ± |
| | 0.00601543 | 0.00336458 | 0.00644917 | 0.00212069 |

Table 12: parameters used for the modelled values presented in Figure 96.

It was found that there was no correlation between the values of D_1 and D_2 for each shale, suggesting that the structures over larger length-scales are different to those for shorter length-scales, which might be expected if the origins of the porosity over these length-scales was different. Figure 96 shows that D_2 correlated well with the carbonate and silicate content in the shale samples.

The BJH PSDs were obtained from the conventional nitrogen adsorption isotherms in Figure 89, and are shown in Figure 97. It was assumed that the multi-layer build-up was described by the Harkins-Jura t -layer equation and capillary condensation occurred via a hemispherical meniscus. The range of pore sizes in the BJH PSD for the cumulative surface area and pore volume parameters discussed below was 0.7-320nm. It can be seen that the above marine band shale had substantially more mesoporosity than the other two shale samples, particularly at the lower end of the range. The amounts of microporosity were more similar in the range probed.

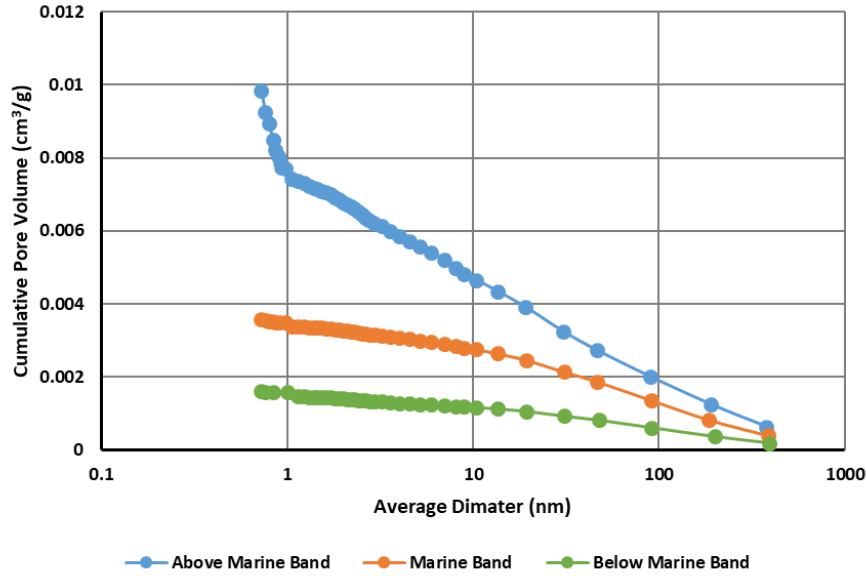


Figure 97: BJH pore size distributions for the above marine band (●), marine band (●), and below marine band shales (●).

Figure 98 compares the variation of the fraction of the accessible void space surface occupied by organic carbon (kerogen), according to the homotattic patch model (8. 6), across the three different shale samples with the variation in the standard BET specific surface area, and the BJH cumulative surface area and pore volume for pores with diameters in the range 0.7-320nm. It can be seen that the accessible kerogen surface fraction shows the same trend across the three shale samples as the total surface area and pore volume parameters.

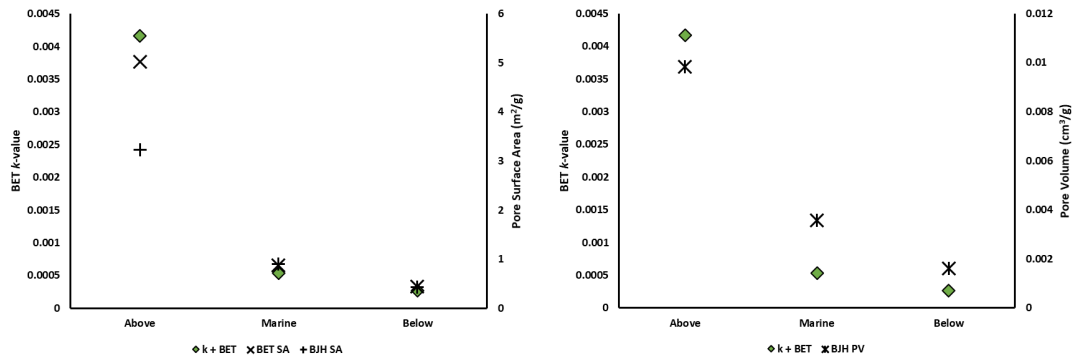


Figure 98: variation of homotattic patch fraction for kerogen (◆), standard BET surface area (X), BJH cumulative surface area (+) (left), and BJH cumulative pore volume (*) (right), for the three shale samples. Parameters used are listed in Table 13.

| | C | V_m (cm ³ /g STP) | D | $k - value$ |
|---------------|------------|--------------------------------|------------|-------------|
| Above | 144.7331 | 0.9964751 | 2.60097 | 0.0041649 |
| | ± | ± | ± | ± |
| | 1.97078392 | 0.01352281 | 0.03223904 | 0.0003414 |
| Marine | 32.469475 | 0.18461085 | 2.4209555 | 0.0005328 |
| | ± | ± | ± | ± |
| | 1.60347824 | 0.00579659 | 0.0367809 | 7.27E-05 |
| Below | 41.57727 | 0.09563398 | 2.453311 | 0.0002667 |
| | ± | ± | ± | ± |
| | 2.35616744 | 0.00193564 | 0.0364394 | 3.06E-05 |

Table 13: parameters used for modelled values presented in Figure 98.

The experimental carbon dioxide sorption data shown in Figure 91 was fitted to the Toth isotherm equation, and the resultant fitted isotherm parameters are shown in Table 14. From Table 14, it can be seen that the adsorption capacity parameter is highest for the marine band shale, followed by the above marine and then below marine shales. This is different to the trend in the corresponding nitrogen sorption data which suggested the above marine band had the highest capacity. It is noted that the exponent T increases from above marine band, through marine, to below marine band. Since a T value of unity is what is expected for a homogeneous surface, this suggests the degree of surface heterogeneity, as perceived by carbon dioxide, increases from below to above the marine band. The surface affinity parameter b peaks for the marine band, with the overall pattern of variation amongst the shale samples similar to that seen for the silicates in Figure 96.

| Sample | Capacity parameter (cm ³ /g) | Affinity parameter (b) | Toth exponent |
|---------------------------|---|------------------------|---------------|
| Above Marine Band | 66.3 | 0.603 | 0.194 |
| Within Marine Band | 116 | 0.920 | 0.209 |
| Below Marine Band | 43.7 | 0.548 | 0.212 |

Table 14: parameters from fits of Toth isotherm (15. 3) to carbon dioxide adsorption isotherms for shale samples.

7.4. Discussion

It has been seen that Bowland shale samples present several issues for the standard methods and data analysis techniques used for common pore structure characterisation techniques, such as conventional gas sorption and mercury porosimetry. However, while very little mercury can intrude in from the surface of the shale samples, it is possible to probe the macroporosity, and other elements of the void space, of the shale samples using nitrogen overcondensation. Hence, this work demonstrates that overcondensation can probe very tight shale rocks that are impossible for mercury porosimetry. Overcondensation also has the advantage that high pressures are not needed to conduct the experiment, as in mercury intrusion, which risk crushing the sample.

However, careful sample preparation is necessary for gas sorption studies. The increase in the width of the low pressure hysteresis with increasing equilibration time in the nitrogen sorption data is opposite to the direction of change expected if mass transport limitations were causing the hysteresis. The low temperature of the nitrogen experiments means that the nitrogen mass transport is slow. This low temperature often means that the nitrogen diffusivity is small and, thence, the allowed equilibration time can be too short to enable all of the desorbed nitrogen to leave the sample in the time permitted. The low pressure hysteresis observed here for Bowland shale samples is in marked contrast to the lack, or very little, low pressure hysteresis observed for Utica, Norland and Rempstone shales studied in previous work (Rigby *et al.*, 2020).

The sharp step down at a relative pressure of 0.4-0.5 in desorption isotherms is generally considered to be due to cavitation associated with the evaporation of unstable condensate in larger pore bodies shielded by pore necks of small sizes <4nm (Rouquerol *et al.*, 2014). It is likely that it is these small necks that prevent access of mercury to the interior of the shale samples, as they are too narrow for mercury to intrude even at the highest pressures. For the marine band and below marine band shales the size of the cavitation step remains shallow even in the overcondensation boundary desorption isotherms suggesting only a small fraction of the larger pore bodies are shielded by very small necks. The predominantly narrow hysteresis at the upper part of the isotherms for these two shales suggests relatively small differences between pore bodies and pore necks for the largest pore sizes in these shales.

The overall form of the nitrogen sorption isotherms for the above marine band sample is very different to the form of the other two shale samples. The very wide rhomboid hysteresis loop of the above marine band shale data suggests a much greater fraction of the large pore bodies in this shale

are shielded by narrow necks <4 nm in size, compared to the other shales. The higher overcondensation data suggests that the conventional adsorption experiment misses some very large pore bodies that are shielded by necks smaller than 4 nm.

It is noted that, for the above marine band shale, the conventional desorption isotherm between relative pressures of approximately 0.9 and 0.55 is tilted down at a similar angle to the overcondensation boundary desorption isotherm, while the ascending branch of SL1 is much flatter (horizontal). These findings suggest that a large fraction of the pores that empty on the overcondensation curve between these relative pressures are the large pore bodies that can fill in the conventional adsorption experiment and are shielded by necks that have radii over a wide range from 2.5 to 13 nm. Hence, a large fraction of the pores that are only filled by overcondensation, and are thus very large (radius >100 nm), are probably ultimately shielded by very narrow necks of sizes <4 nm.

The gaps between the descending (desorption) branches of SL1, or SL2, and the overcondensation boundary desorption isotherm for the above marine band shale suggest that seeded percolation of vapour phase penetration is occurring for the desorption on the scanning curves (Parlar and Yortsos, 1988). This means that the very largest pores left unfilled with condensate at the top of SL1 and SL2, but are filled by overcondensation, are sufficiently well dispersed and pervasive to act as efficient seed sites for desorption to commence at higher pressures than on the overcondensation desorption boundary curve. In contrast, the adsorption and desorption branches of SL1 and SL2 for the marine band converge with the overcondensation desorption isotherm at the top of each, suggesting less residual vapour pockets exist then. The narrowness of the equivalent gaps for the below marine band sample also suggests few residual vapour pockets.

The ultimate amounts adsorbed at the tops of SL1 and SL2, at a relative pressure of 0.995, for the above marine band shale both greatly exceed that at the top of the conventional adsorption boundary isotherm at a relative pressure of 0.995. This suggests that some of the additional very large pores filled by overcondensation still remained filled at the springing-off point of SL1, due to the very small necks shielding them. The relative flatness of the adsorption branch of SL1 between relative pressures of 0.55 and 0.9 suggests that the additional adsorption is not due to a swelling phase. It is also noted that, for the above marine band shale, the difference in amount adsorbed, at a relative pressure of 0.8, between the adsorption branch of SL1 and the springing off point for SL2 on the overcondensation desorption boundary curve is larger than the difference in ultimate amount adsorbed at the tops of SL1 and SL2 at a relative pressure of 0.994. Hence, this ultimate relative pressure is insufficient to refill some pores that were empty at the springing-off point of SL1 (relative pressure of 0.55) but were still filled at the springing-off point for SL2 (relative pressure of 0.8). This suggests that the gap between the tops of SL1 and SL2 is due to very large pores that emptied between relative pressures of 0.8 and 0.55 on the overcondensation desorption boundary curve that can only be re-filled by overcondensation. Further, this means that this small volume of very large pores (0.2 ml/g) is shielded by necks in the range 2.9 to 6.4 nm.

As has been seen, the characteristic time constants from adsorption calorimetry and mass uptake measurements of mass transfer rates in the shales are very well correlated up to the (relatively) longer time-scales associated with ingress at high existing carbon dioxide saturations. Thereafter the pattern of variation of the mass transport parameters diverges, with the calorimetry time constant t showing signs of plateauing out at a more or less constant value. This suggests that at higher saturations the mass transfer processes probed by the two different experimental techniques are different. The foregoing pore structural characterisation suggests that the void space of the shales consists, to an extent, of larger pore bodies shielded by very much narrower pore necks, in an 'hour-glass' type configuration. Dynamic mean-field density function theory simulations of the kinetics of

adsorption into carbon pore networks, consisting of pore bodies surrounded and interspersed by pore necks, suggests that the early stages of adsorption are characterised by filling of the pore necks with plugs of adsorbate (Woo and Monson, 2003; Desouza and Monson, 2021). Thereafter, there is a slower filling process for the progressively more deeply buried pore bodies. Therefore, it is suggested, for the Bowland shale, that adsorption proceeds as follows. The initial rapid adsorption at low saturation fills adsorption sites at narrow pore necks. However, as most of these necks become filled, access to the larger pore bodies becomes more restricted. The mechanism of adsorption then consists of the adsorbate initially adsorbing near a neck site, thereby releasing most of the heat of adsorption. However, this adsorption is metastable because a lower energy configuration of adsorbate involving more deeply buried adsorption sites is possible. There, thus, then follows a slower re-configuration of the adsorbed phase to a more stable arrangement. This process releases much less heat of adsorption over a longer period than the initial adsorption, and so is harder to detect with calorimetry, but can be detected by mass uptake methods, as the re-arrangement of adsorbed phase makes more room for further uptake. If this model is correct then the saturation levels where the calorimetry time constant plateaus out for a given shale characterises the accessibility of the pore network in the shale, and the degree of shielding provided by the aforementioned pore necks. The earlier plateauing of the time constant comparison plot in Figure 95, and the more rapid decline in k -values with saturation, for the above marine band shale suggest that the pore necks most severely restrict the accessibility of the interior void spaces in this shale, compared to the others. This is consistent with the higher cavitation step in the nitrogen desorption isotherm for the above marine band shale. This also has implications for gas flow through this shale, and, thus, expected relative producibility.

7.5. Conclusions

It has been seen that gas overcondensation can be used to study macroporosity within shale samples impenetrable by mercury intrusion. There is a general decline in macroporosity and its accessibility from above to below the marine band in the Bowland shale samples studied here. In the above marine band, in particular, some very large macro-pores are shielded by very narrow pore necks which significantly restrict mass transport.

8. Shale Treatment

8.1. Rationale

An important, and more recent area of research is the impact of acidisation on the shale matrix during the different stages of production. There are several points and ways in which acidisation could occur; this is to remove drilling and completion damage (Morsy *et al.*, 2013) where fines may have blocked the natural permeability of the formation and these can be removed with weak acids, hydraulic fracturing where fracturing fluid is often at the strength of a very weak acid (Morsy *et al.*, 2013), and the potential acidisation of pore water due to CO₂ injection (Hall *et al.*, 2016). In matrix acidisation the objective is to dissolve calcite in natural fractures in order to improve the conductivity in the reservoir (Morsy *et al.*, 2013), and for acid fracturing the aim is to dissolve sediments which will result in improved permeability (Morsy *et al.*, 2013).

Work carried out by Morsy *et al.*, (2013) concluded that low HCl acid concentrations (0.8-3% active HCl) could improve porosity and recovery factors without affecting rock stability by opening natural micro-fractures via calcite dissolution. However, matrix acidising can have no significant impact if the rock mineralogy is unsuitable. Morsy *et al.*, (2013) also observed improved oil recovery rates in the Eagle Ford shale when low concentrations of HCl were introduced into the rock. Morsy *et al.*, (2013) additionally noted mineral changes in some samples, as well as other physical properties alterations, which may suggest not all rocks will remain stable under matrix acidisation. In their study four different shales underwent matrix acidisation; these shales were Barnett (quartz-dominant mudstone shale), Eagle Ford (carbonate rich shale), Marcellus, and Mancos (quartz-rich phyllosilicate-bearing shales). The Eagle Ford shale was the only sample with any significant

improvement in oil recovery. This was likely due to the reactive nature of carbonates with HCl. Hall *et al.*, (2016) specifically identified mass loss and increased secondary porosity to be as a result of dissolution of interparticle cements and k-feldspar grains as well as some loss of clay, carbonate and mudstone clasts.

8.2. Methodology

Nitrogen (N₂) and carbon dioxide (CO₂) gas adsorption was carried out using a Micromeritics 3Flex (volumetric gas adsorption). Nitrogen gas adsorption was carried out over the relative pressure range of 0-0.995 $\frac{p}{p_o}$ at 77K; and carbon dioxide was carried out over the relative pressure range 0-0.035 $\frac{p}{p_o}$ at 273.15K. Following this Hiden Isochema XEMIS and Autosorb iQ – Chemisorption (& Physisorption) Gas Sorption Analyser (iQ-C/MP/Kr/MS) from Quantachrome Instruments which is coupled to an in-situ mass spectrometry and calorimetry system (Setaram SenSys EVO 3D TG-DSC), experiments were carried out in the order given described. XEMIS and Autosorb iQ were used to investigate samples in more detail since the results from Micromeritics 3Flex. Hiden Isochema XEMIS is a gravimetric sorption analyser which is designed for use with a range of gases up to vapour pressures of 200 bar (XEMIS is limited to 60 bar as the transducers are not installed to reach 200 bar), isotherms were carried out at 20°C up to 0.87 $\frac{p}{p_o}$ (XEMIS). Autosorb iQ – Chemisorption (& Physisorption) Gas Sorption Analyser (iQ-C/MP/Kr/MS) from Quantachrome Instruments was used at 10°C up to 0.27 $\frac{p}{p_o}$. Following the completion of these analysis SEM MLA was carried out on an FEI Quanta 600 (operated at 20kV, working distance of 13mm and spot size 7) equipped with mineral liberation analysis software by JKTech/FEI to visualise and quantify the mineral changes by taking several energy dispersive X-ray (EDX) points. For completeness fractal analysis was carried out using the 2-part FHH as described in 4.7.1. Fractal Dimensions.

8.2.1. Acidisation Sample Preparation

The acid treatment carried out was based on the methods used by Harrison *et al.*, (2017) and Jew *et al.*, (2017). Grains (106-150µm) of Marcellus and Utica samples were acidised in conditions used to recreate those of hydraulic fracturing fluid in the formation. This was established based on patents (Dawson and Le, 2005) and in-line with sample treatment carried out by others for similar experimental work. Shale samples were placed in a closed batch reactor and stirred for 3 hours at 60°C with a rock/fluid ratio of 1/100 and HCl of 0.12 weight%.

8.3. Results

8.3.1. Clay-Rich Sample (Marcellus)

Results for the clay-rich sample show a consistent decrease in quantity adsorbed and uptake with the acid treated sample across nitrogen and carbon dioxide over a range of relative pressures up to 0.995 $\frac{p}{p_o}$ (Figure 99), 0.035 $\frac{p}{p_o}$ (Figure 100), 0.027 $\frac{p}{p_o}$ (Figure 101) and 0.87 $\frac{p}{p_o}$ (Figure 102).

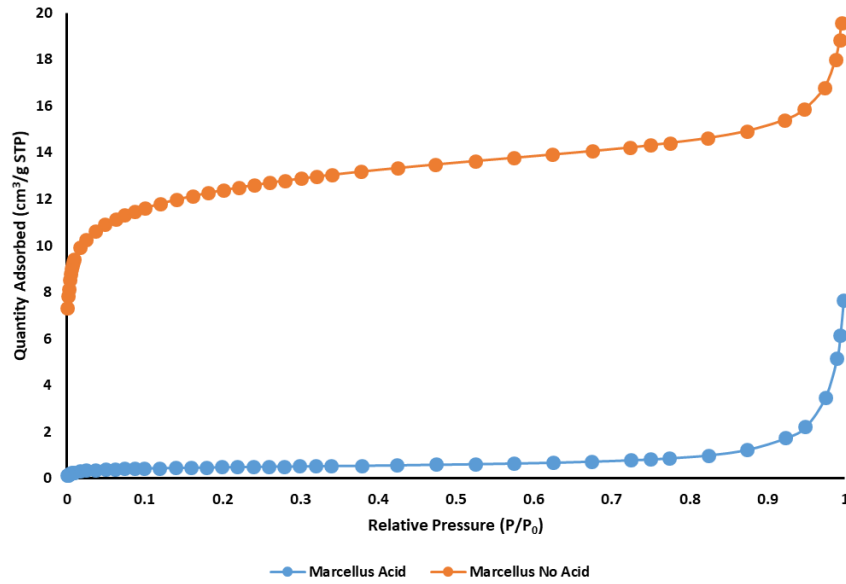


Figure 99: N_2 isotherm at 77K from Micromeritics 3Flex for the clay rich sample before (●) and after acid treatment (●).

Figure 99 shows that acid treatment resulted in a large reduction in the quantity of nitrogen adsorbed compared with the untreated sample, both isotherms were close to reversible and so the desorption branch has been excluded so the adsorption branches are clearer.

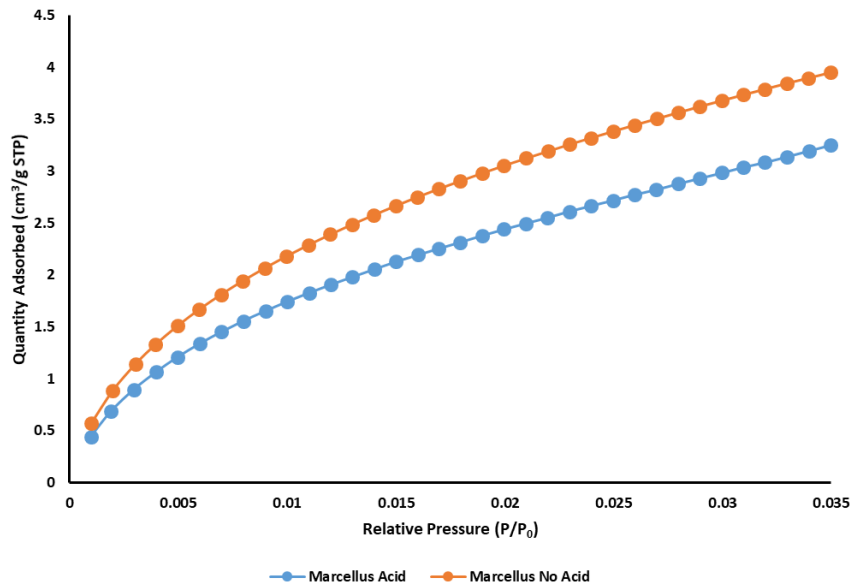


Figure 100: CO_2 isotherm at 273.15K from Micromeritics 3Flex for the clay-rich sample before (●) and after acid treatment (●).

Figure 100, Figure 101 and Figure 102 show that the impact of acid treatment (●) was a reduction in the quantity of carbon dioxide adsorbed compared to the untreated sample (●). The difference compared to Figure 99 is much less indicating that the impact of acidisation on the micro- and fine meso-pores is less significant than on the much larger pores.

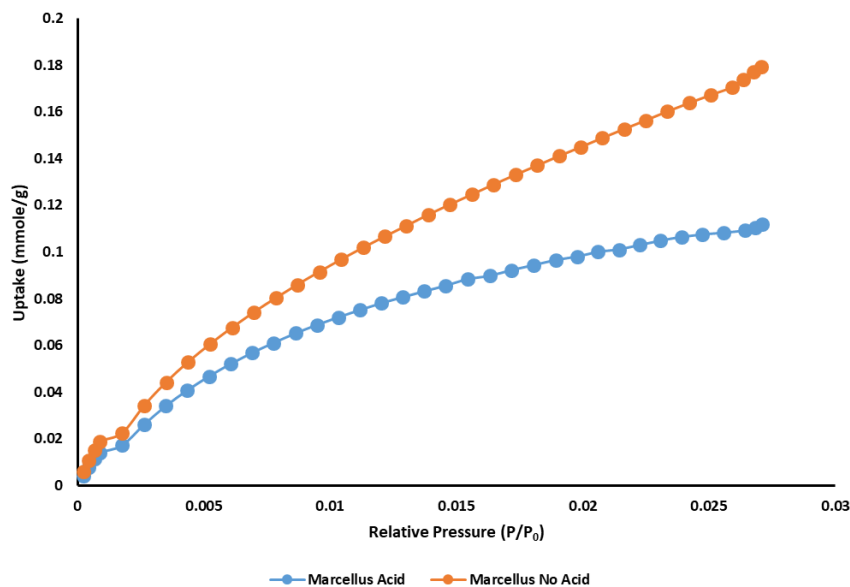


Figure 101: CO₂ isotherm at 283.15K from Autosorb iQ for the clay-rich sample showing before (●) and after (●) acid treatment.

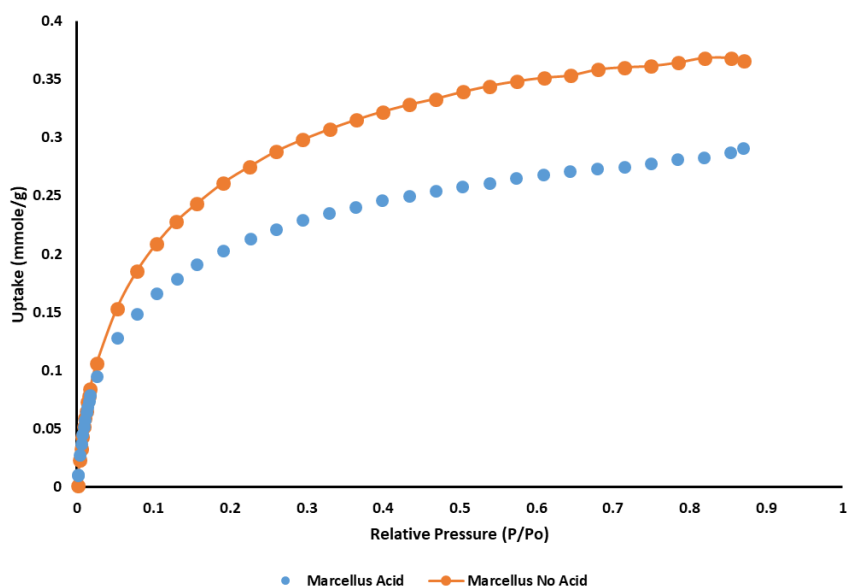


Figure 102: CO₂ isotherm at 293.15K from XEMIS for the clay-rich sample showing before (●) and after (●) acid treatment.

The greatest difference between samples is seen for N₂ sorption (Figure 99) where the uptake for the acid treated Marcellus is near 0 cm³/g until 0.8 $\frac{p}{p_0}$, for all CO₂ sorption isotherms (Figure 100, Figure 101 and Figure 102) the same trend is seen where the acid and not acid treated samples diverge with increasing relative pressure. Autosorb iQ provides the opportunity to analyse the mass transfer kinetics by a linear driving force model proposed by Glueckauf (1955) and used recently by Sircar and Hufton (2000). From the results of Figure 103 it can be seen that the mass transfer kinetics after acidisation are significantly slower than those of the sample not treated with acid. By considering the results of SEM MLA (Figure 105 and Figure 106) it is possible to see that a significant portion of the matrix has been broken down making the length of the diffusion path significantly longer in comparison to the untreated sample, resultantly making k smaller.

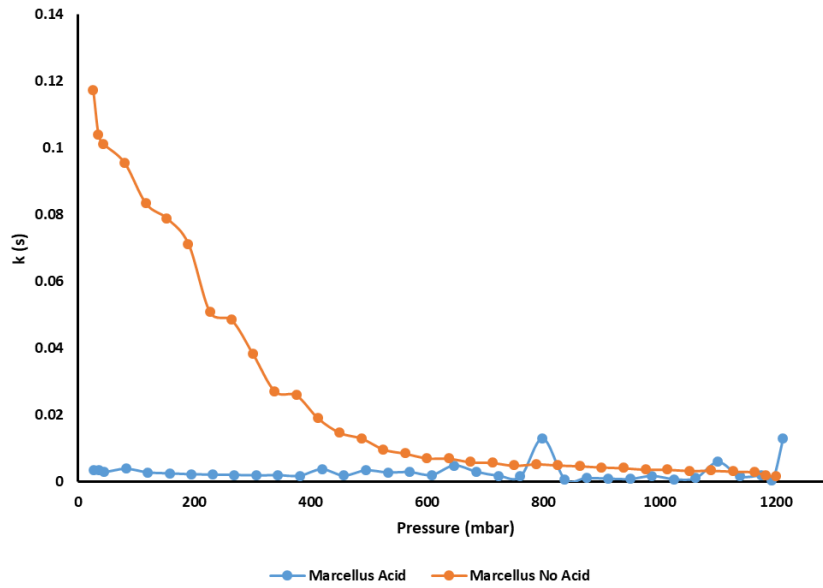


Figure 103: mass transfer kinetics from Autosorb iQ showing the acid treated sample (●) to have an incredibly slow rate of mass transfer when compared to the untreated sample (●).

Figure 105 and Figure 106 for the SEM MLA results shows that there has been a relative increase in the quantity of clays and a decrease in the carbonate quantity. SEM MLA produces percent values based on what is imaged which can sometimes lead to misleading results, i.e. a reduction in carbonates as a result of dissolution from the acid will lead to a relative increase in clay content although the quantity may still be the same.

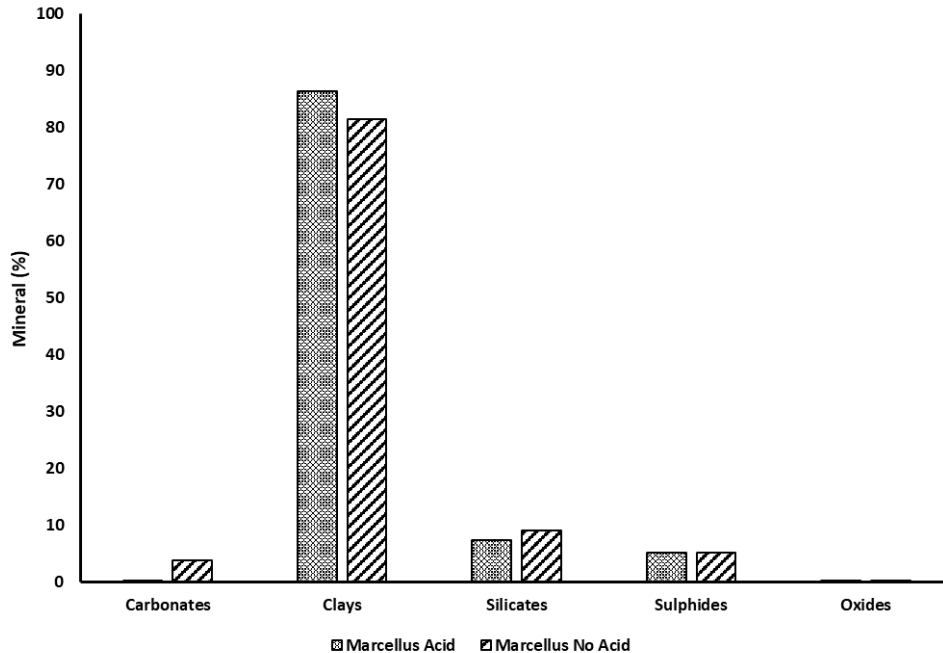


Figure 104: SEM MLA for the clay-rich samples showing the mineral quantities before (textured grey) and after acid (diagonal stripes) treatment.

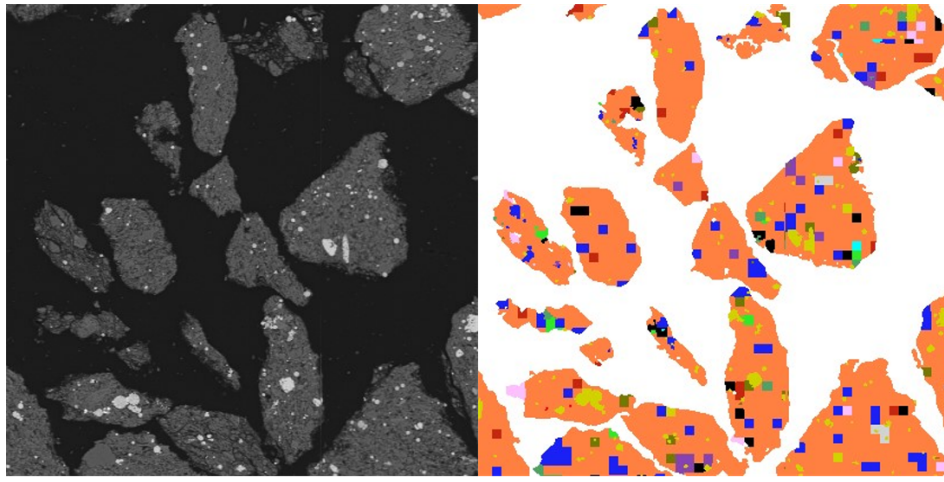


Figure 105: BSE and mineral maps for the untreated Marcellus sample showing a fine grained illite (orange) matrix with some fine grained quartz (blue) and other material interspersed throughout (with a 0.5mm scale bar).

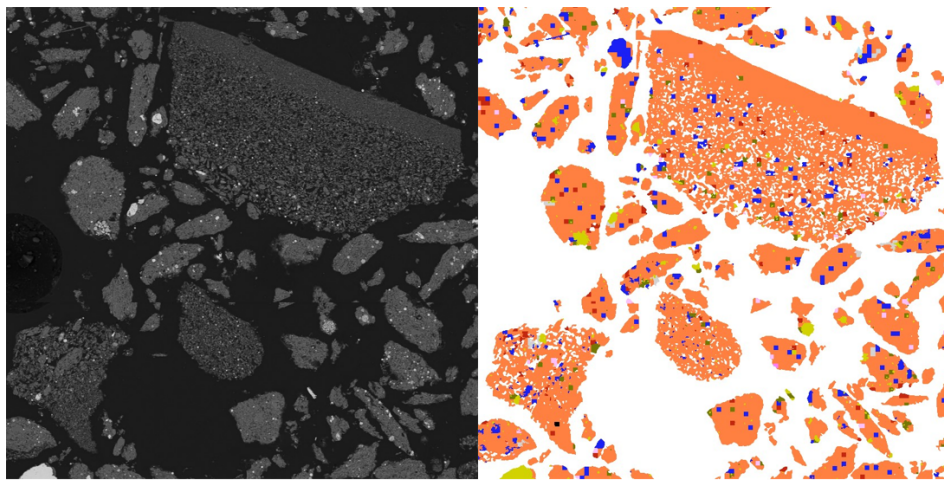


Figure 106: BSE and mineral maps for the acid treated Marcellus sample showing that there have been significant changes to the illite (orange) matrix (with a 0.5mm scale bar).

The relative quantity of clays (Figure 104) is greater for the acid treated sample than it is for the untreated sample. There has also been a large change in the quantity of carbonates and some changes to the silicate quantity. By also considering the results of Figure 105 and Figure 106 it can be seen that significant changes have been made to the illite matrix (Figure 106) which has now got many additional “holes” within it lengthening the diffusion paths to the centre of the particle. It is likely that where these holes now exist is where the carbonates (turquoise) were present within the illite matrix, and they have now been almost completely dissolved. The quartz (blue) grains appear unaffected and are still interspersed throughout the sample.

8.3.2. Carbonate-Rich Sample (Utica)

Results for the carbonate-rich sample show an inconsistency with the quantity adsorbed and uptake between the acid and untreated sample. For nitrogen sorption up to $0.995 \frac{p}{p_0}$ (Figure 107) there is a relative low quantity adsorbed for both samples which demonstrate a hyperbolic shape at maximum relative pressure. This indicates that there may be a presence of macro-pores which have remain unfilled due to the nitrogen not condensing as a result of the rig design to avoid bulk condensation in conventional sorption. Carbon dioxide sorption up to $0.027 \frac{p}{p_0}$ (Figure 109) shows the untreated sample to have a greater uptake, however at this point there is a hyperbolic increase in the acid

treated sample where the uptake increases at a greater rate than for the untreated sample. CO₂ gas sorption was carried out at 273.15K using Micromeritics 3Flex to investigate up to 0.035 $\frac{p}{p_o}$ (Figure 108) it can be seen that at 0.027 $\frac{p}{p_o}$ the acid treated sample crosses over the untreated sample and then continues to adsorb a greater quantity of CO₂. Following this CO₂ gas sorption was carried out at 293.15K using XEMIS up to 0.87 $\frac{p}{p_o}$ (Figure 110) where it is possible to see that following the acid treated sample crossing the untreated sample the acid treated sample continues to uptake a greater quantity of CO₂.

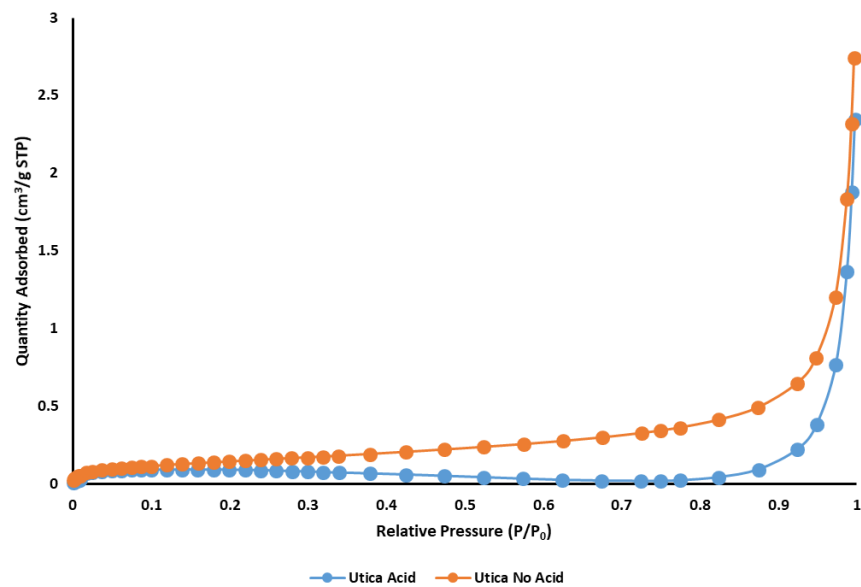


Figure 107: N₂ isotherm at 77K from Micromeritics 3Flex for the carbonate-rich sample, showing the before (●) and after (●) acid treated samples.

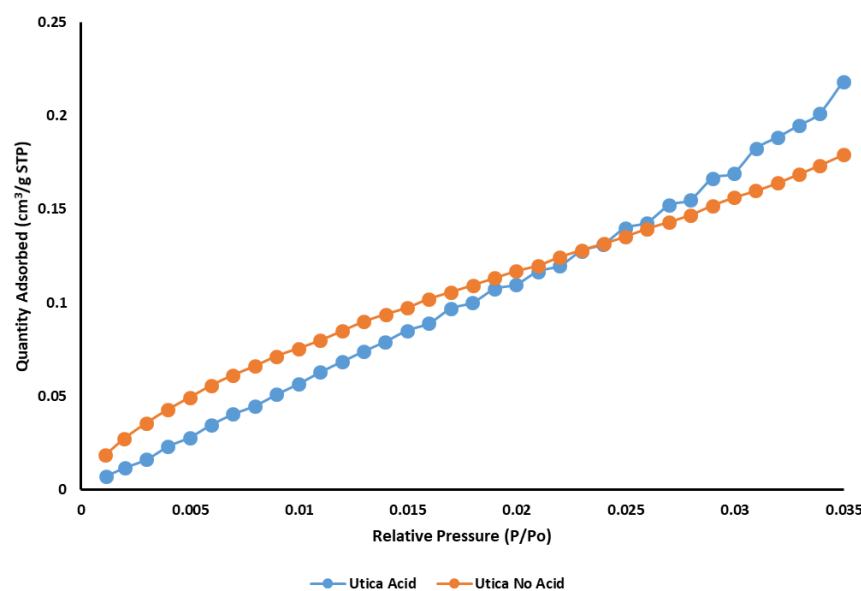


Figure 108: CO₂ isotherm at 273.15K from Micromeritics 3Flex for the carbonate-rich sample, showing the before (●) and after (●) acid treated samples.

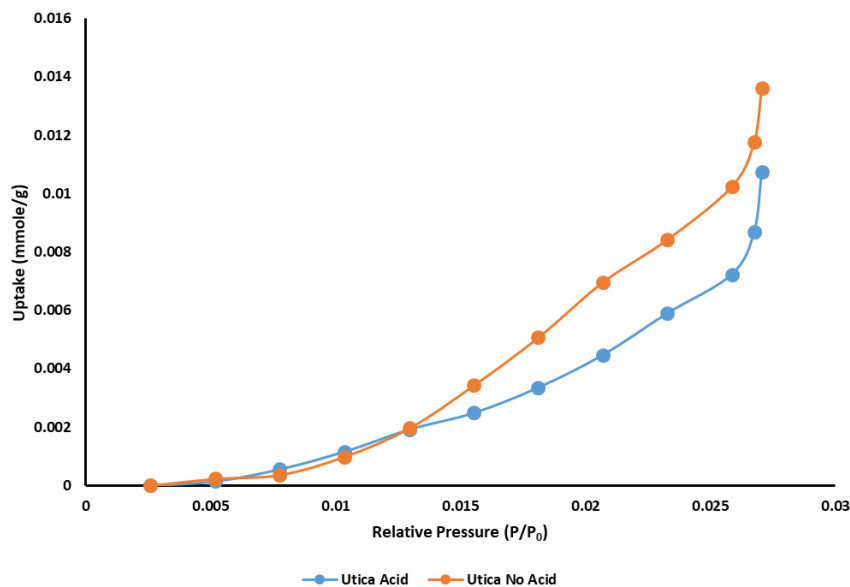


Figure 109: CO₂ isotherm at 283.15K from Autosorb iQ for the carbonate-rich sample, showing the before (●) and after (●) acid treated samples.

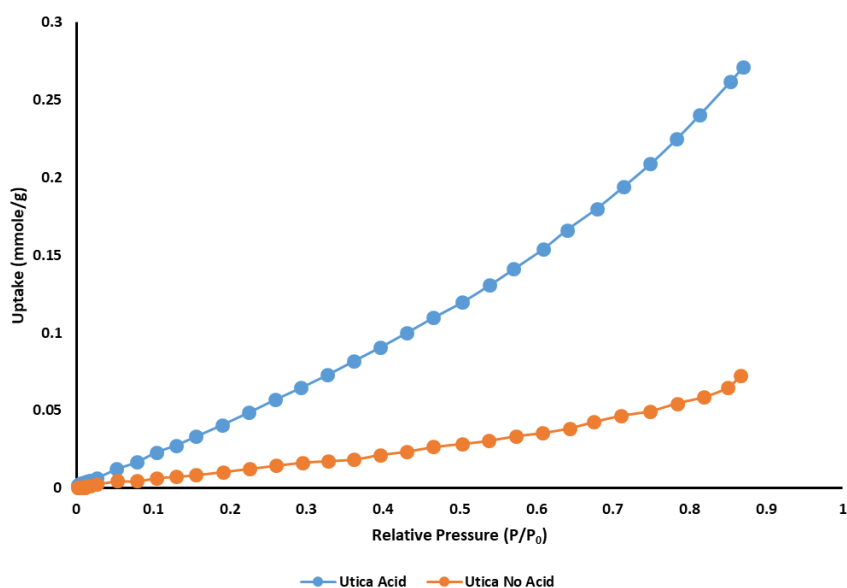


Figure 110: CO₂ isotherm at 293.15K from XEMIS for the carbonate-rich showing the before (●) and after (●) acid treated samples.

The results (Figure 107) show a decrease in quantity adsorbed after acid treatment compared to the untreated sample, however the variation observed is not significant and only diverges at $0.2 \frac{p}{p_o}$ then converge at $0.95 \frac{p}{p_o}$. It may be that only pores in the meso-pore region have been affected by the process of acidisation and micro- and macro-pores have been unaffected. For the CO₂ results (Figure 108) there is an initial decrease in quantity adsorbed before acid treatment, but at $0.025 \frac{p}{p_o}$ the isotherms cross over and the acid treated sample adsorbs a greater quantity. Overall the difference is minimal however and by looking at the low pressure region of the N₂ isotherms (Figure 107) they overlap and are indistinct from each other. The same trend is seen in the Autosorb iQ results (Figure 109) as for 3Flex (Figure 108) where there is a decrease in uptake for the acid treated sample, however at $0.025 \frac{p}{p_o}$ there is an increase in the acid treated isotherm where it looks as though it may cross over with the untreated sample. These are the same results as seen in the CO₂ isotherm from

3Flex. XEMIS (Figure 110) allows for analysis beyond $0.025 \frac{p}{p_o}$ and $0.035 \frac{p}{p_o}$ up to $0.87 \frac{p}{p_o}$ where the trend of the acid treated sample increasing above the untreated sample continue.

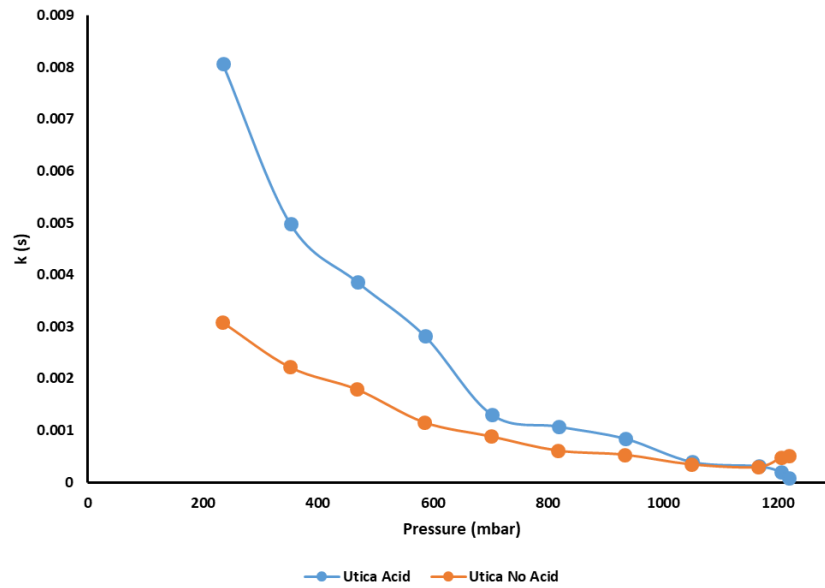


Figure 111: mass transfer kinetics form Autosorb iQ before (●) and after (●) acid treatment.

Using Autosorb iQ again the mass transfer kinetics can be analysed by the linear driving force model (Glueckauf, 1955; Sircar and Hufton, 2000), showing that after acid treatment the mass transfer is faster than it was for the untreated sample (Figure 111). This may be that the length of diffusion paths may have decreased as a result of the acid treatment where the relative quantity of silicates is much greater (Figure 112).

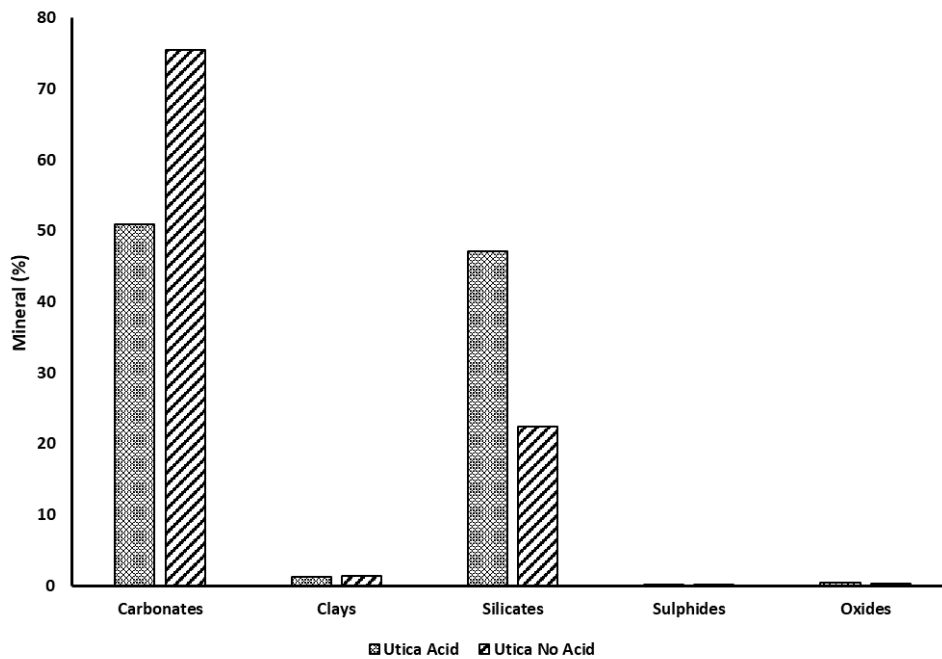


Figure 112: SEM MLA for the carbonate-rich samples showing that after acid treatment (textured grey) the relative quantity of carbonate is much lower than before acid treatment (diagonal stripes).

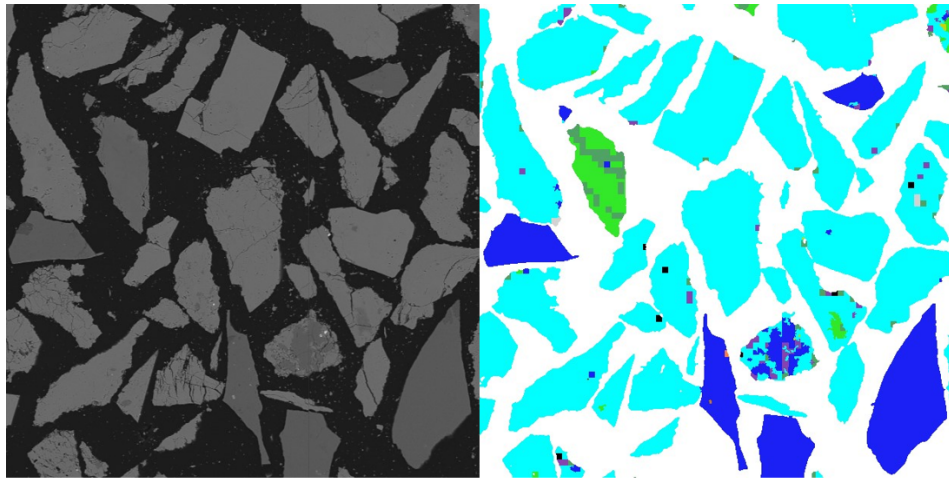


Figure 113: BSE and mineral map images for the untreated Utica sample showing predominantly carbonate (turquoise) grains, with some quartz (blue) grains and a dolomite (green) grain. There are some finer quartz (blue) grains within the carbonate (turquoise) grains, however overall the individual grains have a much simpler mineralogy than the corresponding Marcellus sample (with a 0.5mm scale bar).

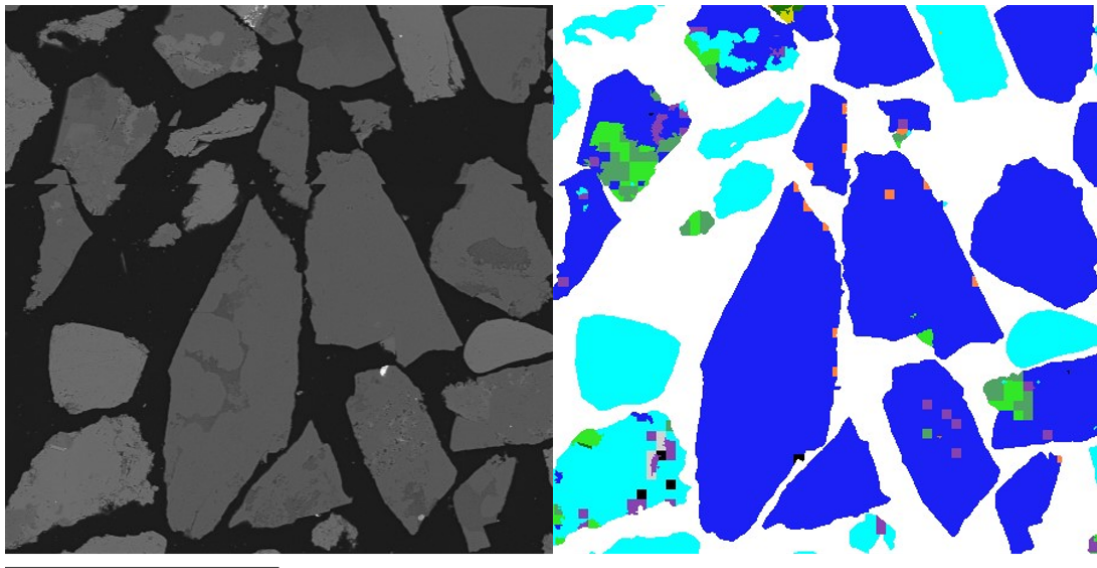


Figure 114: BSE and mineral map for the acid treated Utica shale where there is a considerable increase in the number of quartz (blue) grains and a decrease in the number of carbonate (turquoise) grains in comparison to the untreated sample (with a 0.5mm scale bar).

Figure 112 for the quantity of minerals shows there's been a large change in the quantity of carbonates and silicates, although it is likely that the increase in silicate content is a relative increase reflecting the decrease in carbonate content (silicates are inert minerals which do not react to weak acid). The results from SEM MLA (Figure 113 and Figure 114) show there to be no intra-particle alterations where diffusion paths are created into the centre of the particle as observed for the clay-rich sample, however there is a much more significant change to the overall sample mineralogy (Figure 112). Most notably there is a large decrease in the carbonate content which leads to a relative perceived increase in the silicate content. Since the overall change due to acid treatment (in the context of individual grains and not as a reservoir) is to the overall composition, instead of intra-particle structures, the sorption results therefore vary in-line with what could be expected of samples of a slightly different composition (i.e. U4 and U5 from 6. The Utica Shale) which have not undergone any chemical alteration.

8.3.3. Fractal Analysis

Nitrogen adsorption results were used to obtain the fractal dimensions for the acid and none acid treated samples to identify where particular changes have occurred as defined by (Wang *et al.*, 2015). Here D_1 is a measure of surface roughness and D_2 a measure of network complexity.

| Sample | V_{m1} (cm ³ /g STP) | D_1 | V_{m2} (cm ³ /g STP) | D_2 |
|-------------------|-----------------------------------|---------------|-----------------------------------|---------------|
| Utica No Acid | 0.125963 ± | 2.407622 ± | 0.122771 ± | 2.549896 ± |
| | 0.0079398 | 0.0037426 | 0.0042458 | 0.0019922 |
| Utica Acid | 9.989156 ± | 2.665422 ± | 9.598778 ± | 2.91157 ± |
| | 0.3961581 | 0.0026854 | 0.6228177 | 0.0010565 |
| Marcellus No Acid | 10.70661 ± | 2.610574 ± | 10.91071 ± | 2.784031 ± |
| | 0.5749593 | 0.0071145 | 0.6792774 | 0.0019307 |
| Marcellus Acid | 0.125963 ± | 2.407622 ± | 0.387821 ± | 2.582339 ± |
| | 0.0079398 | 0.0037426 | 0.0241014 | 0.0013335 |

Table 15: fractal dimensions for the acid and none acid treated samples using a two part FHH model to derive a fractal dimension for the surface roughness and network complexity.

D_2 for the network complexity verifies the results in Figure 103 and Figure 111 where mass transfer was slowest for Utica Acid and Marcellus No Acid. D_1 (surface fractal) decreases for the acid treated Marcellus sample, and increases for the acid treated Utica sample which correlates to previous conclusions where a more rough surface has a greater adsorption capacity. In (Figure 99 and Figure 107) it can be seen that the acid treated Utica sample adsorbs a greater quantity than the untreated Utica sample (Figure 107), and the acid treated Marcellus sample adsorbs a smaller quantity compared to the untreated Marcellus sample (Figure 99). The results of the fractal analysis strongly support the experimental findings since the trend was consistent with the experimental results where the acid treatment of the clay- and carbonate-rich samples affected the samples differently.

8.4. Discussion

While, fine-grained matrix samples with carbonates within the sample matrix showed less difference in mineralogy however they were the most affected in sorption experiments due to intra-particle alterations impacting the pore network of the sample. When samples were made up of coarser carbonate grains the overall impact on the sorption result was minimal. This is likely due to fewer intra-particle alterations where structures were affected as was the case for the Marcellus. Importantly, although there were more significant changes to the Utica mineralogy than the Marcellus mineralogy, the expected sorption results were not seen due to the lack of internal particle alteration and instead due to whole carbonate grains being dissolved.

The implications of these results when scaled to a reservoir however are uncertain since the behaviour of the carbonate-rich sample has not been accurately assessed with the use of powdered shale. To obtain a better understanding this experimental work would need to be carried out on a core sample to assess. The clay-rich sample on the other hand seems to have effectively created more diffusion paths to the centre of the particle enabling more easy movement of gas into and out of the sample. Although the intra-particle alterations have been witnessed for the Marcellus it is uncertain how extensive these impacts would be at reservoir scale and so repeating this experimental work on a core sample would be extremely beneficial to the other understanding of the impact on acid treatment.

8.5. Conclusion

The effect of acid on fine-grained matrix samples is much more significant on this scale (106-150 μm) than it is for coarse grained samples. Observed changes for the fine-grained sample are within the individual grain and thus influence the overall sorption of the sample. For the coarse grained sample whole grains of carbonate are dissolved creating a more quartz dominant sample where the pore networks of the grains are not significantly changed in comparison.

9. Discussion

The first aim of the project was to characterise all shale samples by the standard methods used in literature, the rationale behind this was so there was a starting point of characterisation obtained via standard methodology which novel characterisation could then build on. The shale properties which are universally reported; surface area and pore volume (gas sorption and mercury intrusion porosimetry), mineralogy (XRD and SEM MLA), the organic content (RockEval). By doing this it has enabled specific identification where the novel techniques have gone above the limitations of standard methodology in characterisation, and also to identify the heterogeneity within samples from one formation. By using gas sorption, pore size distributions have been established over the range 0.4-2nm (CO₂) and 2-50nm (N₂). Mercury intrusion porosimetry then allows the measurement of the distribution of pores in the range of 3.2nm to 1000µm. Although the combination of these three techniques allows measurement of (most) micro-pores through to macro-pores and some micro-fractures, because they are conducted independently the continuity of measurement across the pore ranges is poor. Consequently, assessment of the connectivity of the pore network in a wider context is not effectively characterised and important network properties are overlooked.

The grain size of the samples was varied to assess how significant the differences in results were and to highlight that there are properties and pores missed when just one grain size is used. For the Marcellus 7795'-7798' sample, varying grain size meant larger pores were opened as shown by the isotherm data for the two finest grain sizes (Figure 27). 106-150µm and 150-212µm overlay each other until $0.9 \frac{p}{p_0}$ when they diverged and 106-150µm increases at a greater rate than 150-212µm, this relative pressure (by the Broekhoff de Boer method) is associated to pores >11nm. The coarsest grains (212-425µm and 425-600µm) overlay each other until $0.75 \frac{p}{p_0}$ when they diverge and 212-425µm increases at a greater rate than 150-212µm, the pore sizes associated to this relative pressure are >5nm. These two pairs of grain sizes, 106-150µm and 150-212µm, pair one and 212-425µm and 425-600µm, pair 2 overlay each other until $0.6 \frac{p}{p_0}$ where they diverge and pair 1 increases at a greater rate than pair 2 ($0.6 \frac{p}{p_0}$ is associated to pores >3nm). By looking at the Gurvitsch volume (complete pore filling) it is possible to determine the overall increase in accessible pore network for the sample, from the grain size study of the Marcellus 7795'-7798' it is possible to see that for a grain size four times larger the respective decrease in quantity adsorbed was only by a factor of 0.78.

Gas adsorption analysis was repeated for some samples to demonstrate the repeatability of the method. Figure 115, shows two N₂ and two CO₂ sorption isotherms with two repetitions each.

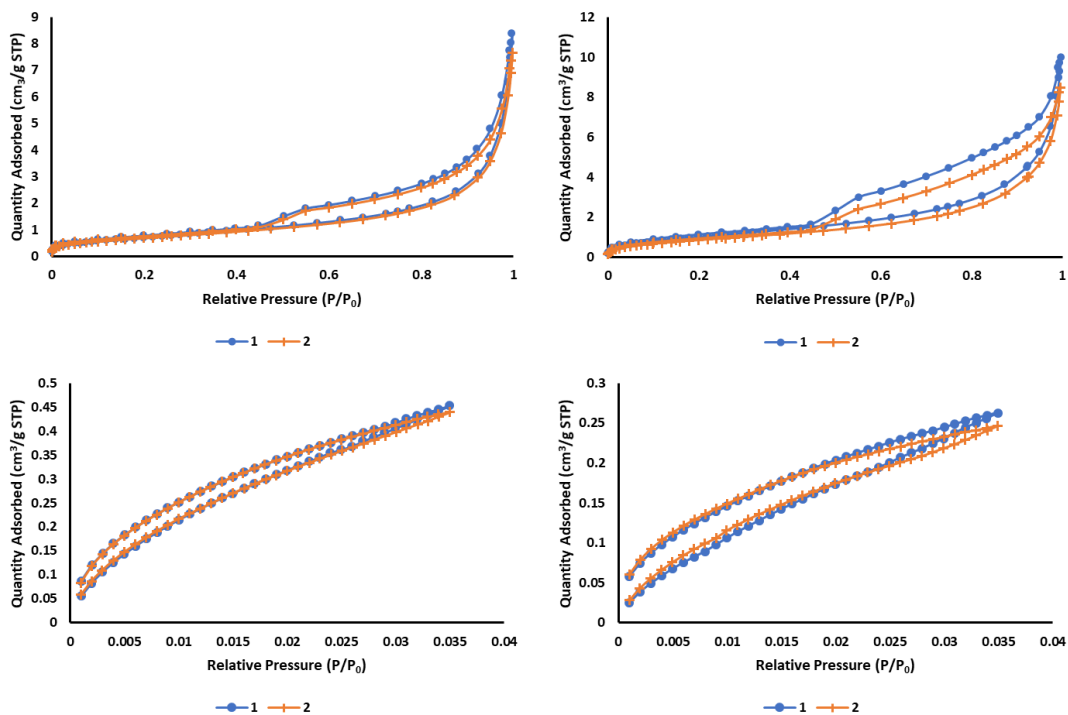


Figure 115: N_2 and CO_2 sorption isotherms with two repetitions to show repeatability of the procedure.

From these results it is clear that although there is a small amount of variability in the repeated analysis the results derived are the same and the method is repeatability. Where there is a slightly larger degree of variation present, this coincides with a greater degree of hysteresis and perhaps shows that from the first to second treatment there is some residual adsorbate which is not successfully removed. For the same sample with repeated analysis these results demonstrate the repeatability of the experimental technique, however the similarity in results was also assessed for different sub-sections of one sample (Figure 116).

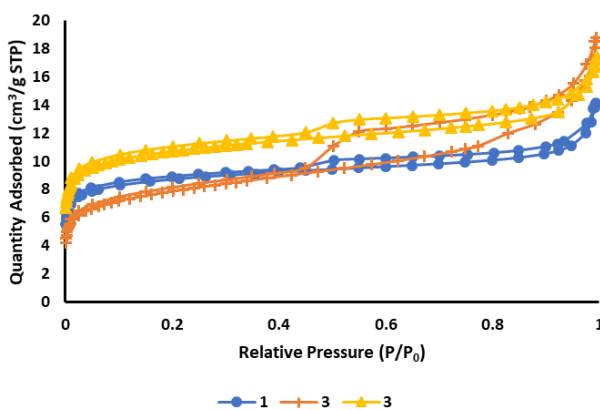


Figure 116: three Marcellus 7864'-7867' N_2 sorption analysis from different sub-sections.

For different sub-sections of the same sample there is a degree of variability in the sorption isotherm across the Gurvitsch volume, hysteresis and the flattening through the meso-pore region. It was because of this that the decision was made, to as much as possible, focus on ensuring there was a mix of sample across the section as well as maintaining consistency with the analysis material (i.e. performing all gas sorption analysis prior to a destructive experimental technique).

By performing grain size analysis over a larger range of grains sizes and on other samples it may be possible to build a large enough set of data which can enable the forecasting of the quantity adsorbed for larger grain sizes through to chips and core plugs. Due to the unavailability of equipment it was only possible to analyse samples up to approximately 5mm in size due to the limiting neck size of the sample tube used for Micromeritics 3Flex (Figure 14). The neck size of the sample tube used for Autosorb iQ limits analysis of samples up to approximately 2mm, and the mass balance of XEMIS is in the order of micrograms and thus not capable of holding a much larger sample.

Depth analysis was carried out for different samples of the Marcellus (three), Utica (fifteen) and Bowland (three) shales, using gas sorption (N_2 and CO_2) and SEM MLA to compare the surface area, pore volume and mineralogy. The Gurvitsch volume for the Marcellus shale was correlated to depth where the deepest sample (7864'-7867') had the smallest Gurvitsch volume. However, when the surface area and pore volumes for the Marcellus shale are analysed the correlation to depth breaks down and the middle sample (7834'-7837') has the lowest surface area and pore volume suggesting that the relationship governing these properties is more complex. The Bowland shale demonstrates the same Gurvitsch correlation to depth as the Marcellus, and also maintains this correlation for the pore surface area and pore volume which are correlated to depth. Both the Marcellus and Bowland shales are comprised of three samples and span 70 feet and 1 foot respectively. The Utica however is comprised of fifteen samples spanning 300' and provides a much better set of samples to assess the depth dependence of sorption data. From the Utica shale results it is clear that there is no correlation to depth with the gas sorption technique. It was previously hypothesised in 5. The Marcellus Shale that these properties are more strongly correlated to sedimentary environment and the resultant mineralogy of the sample.

Having hypothesised that the mineralogy, sedimentary environment and diagenetic processes were likely the primary control on sample properties (surface area, pore volume, surface roughness, pore network connectivity etc.) and not depth, these need to be accurately quantified. Evidence of diagenesis and the sedimentary environment can be seen in the sample mineralogy and so this needed to be quantitatively determined. X-ray diffraction (XRD) was initially used but did not provide the quantitative detail needed for thorough analysis, and so scanning electron microscopy mineral liberation analysis (SEM MLA) was used to quantitatively view and measure the mineral content of the exposed sample surfaces. The values obtained are area values of the exposed surface, and it is not overlooked that these values represent only a small part of the core section. In order to overcome these limitations several chips have been used from across the core section and embedded in different orientations to the bedding plane to try and capture all possible heterogeneities of the sample and not produce a dataset with any bias. Additionally, since shales have a high degree of complexity in the clay sized particle matrix caution must be taken in the deconvolution of these mineral phases since the accuracy of SEM MLA is only to the precision that EDX points can be measured. For the very fine grained clay matrices it is difficult to resolve the mineral boundaries with the resolution available to us, consequently the given value is more of an average over the area, i.e. if there is a $1\mu m^2$ area which is actually comprised of 85% clay and 15% carbonates the SEM MLA result will likely measure the whole $1\mu m^2$ area as 100% illite.

All samples are predominantly comprised of carbonates, silicates and clays; specifically calcite or limestone, quartz and illite. By simplifying the mineralogy into these components correlations between surface area and pore volume were made, however no strong correlations were present besides a generally positive correlation of the surface area to illite. Once RockEval was completed it was clear that the strong correlation was between TOC% and the surface area of the samples; the mineralogy will be discussed further when combined with the numerical analysis models.

Taking into consideration the shortcomings of conventional gas sorption, namely the inability to condense in larger pores, then nitrogen overcondensation was used to extend the pore size range by ensuring complete condensation of N₂ in the larger pores. By comparing the differences in the conventional isotherms and the overcondensation isotherm it is possible to identify the points at which more pores have been filled, and whether secondary levels of hysteresis are present within samples. Taking U3 as a particular example the additional hysteresis at approximately $0.75 \frac{p}{p_0}$ (pore sizes >10 nm) demonstrates where there is shielding of pores by narrower necks which are wider than the small neck sizes (>4 nm) attributed to hysteresis at $0.5 \frac{p}{p_0}$. Across all other samples there was an increase in the size of the hysteresis loop at $0.5 \frac{p}{p_0}$ as a result of leading neck sizes <4nm, however this second hysteresis step at $0.75 \frac{p}{p_0}$ is only seen in one sample (U3) and showing that it is not an artefact of the overcondensation method and it is a measure of the network present in the sample.

The secondary hysteresis in U3 for the overcondensation has not been correlated to a particular mineralogy, however it has been correlated to a transition in sedimentary environments where a greater degree of chaos is present leading to more disorder within the sample. Further detail can be gained from the overcondensation technique by performing scanning loops where particular increases in the isotherm can be identified and attributed to certain pore sizes based on the deviation from the conventional isotherm. Where scanning loops deviate from the conventional isotherm it is possible to conclude that additional pores have been filled by overcondensation which were not filled by the conventional isotherm.

Although weaknesses of mercury intrusion porosimetry have been discussed previously it has been utilised in the development of a two stage method to analyse the intrusion network based on imaging trapped mercury. Mercury is able to access much larger pores than gas sorption (conventional and overcondensation), but it is handicapped by the minimum pore size it can intrude. Therefore, large micro- and fine meso-pore phases are overlooked by this technique, and where samples are highly complex they will also stop the flow of mercury into larger pores which are connected to the network via smaller (inaccessible to mercury) pores. Further, mercury measures the neck size of a pore and not the pore body which consequently makes the comparison to gas adsorption results difficult since the pore dimension measured is different (gas adsorption measures the pore body). It is mathematically possible to relate the different properties, however it is not easy to do since there is a lack of knowledge regarding the specific pore geometry (e.g. slit, spherical, cylindrical). The pore geometry needs to be known since this geometry is used to transform the data for mercury into a dataset comparable to gas sorption. Mercury intrusion however offers an invaluable experimental insight due to the high contrast imaging potential that it has to visualise mercury trapped in the sample. When mercury intrudes pore networks of a highly complex geometry and the difference in the pore neck and body varies such that during extrusion the mercury column in the pore body becomes disconnected from the column in the pore neck which empties at a higher pressure than the pore body. However, this technique is only useful when the mercury is able to access the pore network. Work in NMR failed due to the inability of an intrusion fluid to sufficiently saturate the sample.

Imaging shales is often problematic due to the resolution needed to identify pore networks or micro-fracture networks. Trapped mercury offers the option to image where it is trapped and to assign likely intrusion mechanisms based on the resultant 3D reconstructions. Resultantly it provides additional value to the results where intrusion can be assigned to a particular mechanism and more information gained about the sample. This also aids the broader understanding of a sample alongside other experimental results, where a sample may have an unusually high intruded volume in comparison to sorption results (which will not show micro-fractures) meaning can be given to this

and a more detailed understanding of the pore network gained. Additional image analysis can take place so that the quantity of mercury trapped in the sample still can be calculated based on the number of white voxels when the mercury is isolated.

Alongside the development of novel experimental techniques, more robust, and novel, numerical analysis was developed to analyse the datasets acquired through standard methods. Current analysis is often carried out using trend line fits in excel, or with the use of Solver, also in excel, by using R. a more rigorous analysis methodology can be developed where objective constraints can be placed on the data to remove any subjective data range selections.

Across the different models there was a propensity for values to be high or low as a set (a set is defined by the model, i.e. one set is the fBET and another set would be the fFHH), with a variation across the models of <0.3 i.e. across the BET, one part FHH and two part FHH the fractal dimension for one sample may range from 2.3-2.6. However, the distribution of samples for one dataset (e.g. the Marcellus) were consistent across all four models (Figure 46).

Values for the fractal FHH (one part) and D_1 of the two part FHH directly overlay each other, and values for the fractal BET and D_2 for the two part FHH overlay each other (Figure 46). The likely reason for this overlapping in values is because of the analysis code including a greater or fewer number of pressure points. Thus, the analysis code has analysed roughly the same range of pressure values for the FHH (one part) and D_1 of the two part FHH, and vice versa for the fractal BET and D_2 of the two part FHH. Going forward it may only be necessary to perform the two part FHH (one code script to fit two separate pressure ranges of the isotherm) to describe the fractal dimension for the surface roughness, and fractal dimensions for the network complexity; this would result in a decreased computing time. The fractal dimension models also allow for the constants V_m (all models) and C (BET) to be optimised within a set of boundaries chosen by the researcher to allow flexibility around the software calculated constants. In time it would be good to create a model where the only input needed is the isotherm and the constants can be defined by the constraints, $V_m \geq 0$ and $C \geq 1$ and the resultant model fits match those produced by the analysis software.

To give an uncertainty of the numerical modelling results the standard deviation was taken of the ten repetitions and this was used to produce a value and plus or minus that standard deviation. The decision was taken to measure uncertainty in this way since the degree of flexibility written into the code for each parameter was 10% of the value given at the beginning (this value was given by Micromeritics 3Flex). The quantity of the standard deviation between the reported runs however was far smaller than this 10% variation permitted, consequently the uncertainty has been reported as the standard deviation in results of repeated numerical modelling runs.

The numerical modelling in R. was further developed to create a novel characterisation technique which includes more of the experimental data acquired previously. The homotattic patch was set up with an isotherm model (one of the fractal BET, fractal FHH or the nBET) and the experimental isotherm for a mineral constituent which was primarily the TOC%, but later extensions to the model also included illite. The homotattic patch has been used to successfully model the mineral components of the isotherms for shales based on the sorption results of pure mineral phases (TOC% and illite). It was found that the resultant ratio of the values for TOC% and illite from the model matched the ratio of the mineral BET surface area multiplied by the mineral % derived by SEM MLA and RockEval. For cases where ratios are not equal it is hypothesised that this is an indicator of the accessibility of this mineral phase to the adsorbate used, or to the SEM MLA measurements. Depending on how the ratio swings will determine by which process the mineral phase has been impacted.

When the ratio of R. derived values (*mod*, as described in 5.3.4. Numerical Modelling) and ratio of experimentally derived values (*exp*, as described in 5.3.4. Numerical Modelling) are equal it tells us that there the TOC% and illite are equally accessed by the isotherm used for numerical modelling and the SEM MLA. In the situation where $exp > mod$ it can be inferred that the quantity of TOC% measured is not recognised by the isotherm fit from the model indicating that the TOC% phases are not easily accessed. For the case that $exp < mod$ the same can be said for the illite phase being less accessible to gas sorption analysis. The isotherm hysteresis loop size should provide an indication to adsorbate accessibility, but this is based on pore neck sizes and access to the sample in general. The addition of the homotactic patch can highlight, in particular, where certain mineral phases have/have not been accessed. It is possible that this can help identify where a sample is particularly heterogeneous on a larger scale such that these heterogeneities are not captured within 1-2g of sample, in these cases variation across all experimental techniques is likely to occur and so must be mindful of talking too specifically about any single result and instead consider the results in a wider context.

The previously discussed methods and results were developed using the Marcellus and Utica samples, they were then repeated on the Bowland shale where the most appropriate methods were selected. An additional analysis methodology was introduced for the Bowland shale samples using two different methods to calculate the kinetics of the adsorption within the sample, whereby one method used mass uptake against time (with characteristic parameter for mass transport from LDF k -value) and the other used heatflow against time (τ) as described by (Auroux, 2013) for each adsorption point. The values of k and τ should be linearly correlated to the graph of one against the inverse of the other. This correlation held well with LDF MTC k -value from mass uptake curves, as would be expected if τ probes mass transfer as (Auroux, 2013) claims. However, the correlation only held for low adsorbate saturation levels. Once the amount adsorbed reached a certain level (that differed between samples) τ plateaued out, but k still changed. It is theorised that at low saturation incoming CO₂ can readily diffuse within the sample and easily access the highest energy adsorption sites. However, as saturation is increased the pore network is blocked by the already adsorbed phase and molecules end up initially sitting at a non-optimal adsorption site. In order for the system to reach equilibrium, the configuration of the adsorbed phase needs to restructure to reach the lowest energy state. This involves the molecules shuffling around to make room for incoming adsorbate, and find the lowest energy arrangement. It is believed that this occurs for samples with very slow adsorption related to lower porosities and hence a reduced ability for the adsorbate to move through the sample, therefore this provides another measure for determining the complexity of the samples pore network. The point at which the distribution of values (if at all) strays from the linear relationship indicates at how low, or high pressure the uptake is affected such that molecules cannot easily access adsorption sites.

Additional investigations were made on these results by using differing equilibrium times in N₂ gas sorption experiments (Figure 88) to observe what differences are seen in the isotherms, and whether these support the hypothesis that at the higher relative pressure points more time is needed for the adsorbate to achieve the optimal arrangement. There was an increase in the width of the low pressure hysteresis with increasing equilibration time in the nitrogen sorption data which is the opposite to the direction of change expected if mass transport limitations were causing the hysteresis. Given the N₂ sorption takes place at low temperature it means mass transport is slow. This low temperature often means that the nitrogen diffusivity is small and, thence, the allowed equilibration time can be too short to enable all of the desorbed nitrogen to leave the sample in the time permitted. However, in the case of the samples studied here the hysteresis width increased with equilibration time suggesting that more N₂ has been able to enter highly confined spaces, which are also difficult for the nitrogen to leave. This is in marked contrast to the lack, or very little, low pressure hysteresis observed for Utica, Norland and Rempstone shales studied in previous work

(Rigby *et al.*, 2020). These late adaptations to current standard analysis techniques have demonstrated how pore characterisation can be enhanced with not only the novel development of techniques, but with the novel use of current techniques.

10. Conclusion

10.1. Introduction

In this chapter the aim is to demonstrate how the conclusions of each chapter, Marcellus, Utica, and Bowland feed into, and build on the findings of each other. Additional work on Acid Treated samples aims to show the relevance of the work directly to the industrial world. Finally, future work will be laid out and steps provided as to work that can be carried out to further the development of this research.

The main objective of this study was to develop novel characterisation methods to overcome the existing drawbacks in the characterisation of pore systems in seal rocks which are used for downhole gas production (CH_4) and storage (CO_2), in the context of this study shale rocks have been used as the analysis seal rock. To achieve this the project was broken down into several objectives laid out to meet the aims of the project; the first to characterise samples with a set of basic characterisation techniques, secondly introduce more rigorous numerical analysis techniques and finally to develop novel techniques capable of measuring pore sizes over several orders of magnitude (i.e. micro-pores through to macro-pores) in one technique (further explanation of these aims is in 3. Aims and Objectives). Whilst working to achieve the first aim it was quickly determined that characterisation using conventional gas sorption, mercury intrusion porosimetry and microscopy could not be used as a standalone analysis techniques. Although all techniques have their merits they ultimately result in “data gaps” across pore size measurements, and in an insufficient quantity of information regarding the network complexity and ability for a fluid to move through the sample. This led to the investigation of data analysis where fractal dimensions were used to characterise the surface roughness (D_1) and network complexity (D_2) (Tang *et al.*, 2003; Wang *et al.*, 2015; S. Zhang *et al.*, 2018), and develop a more rigorous modelling approach that was able to fit models to the data instead of “best-fit” lines. The main questions which were sought to be answered with the transition into the second aim were; can model fitting with the use of coding (R.) be used to elevate current data analysis techniques by removing any subjective bias in “best-fit” lines? And can more rigorous data analysis techniques provide additional information regarding the intra-particle properties without additional experimental techniques? Finally the development of novel experimental techniques sought to demonstrate that it is possible to characterise pore systems with fewer analysis techniques, and to simplify the dependencies of surface area and pore volume in shale samples.

10.2. Empirical Findings

Results of 5. The Marcellus Shale, 6. The Utica Shale and 7. The Bowland Shale have shown that by using standard characterisation techniques you can gain a very good suite of important information, e.g. surface area, pore volume and pore size distributions. However, the broader translation of these values across orders of magnitude is unclear and leaves uncertainty regarding the pore size ranges overlooked by each experimental method, e.g. from nitrogen gas sorption to mercury intrusion porosimetry. It can also be seen with 5. The Marcellus Shale, 6. The Utica Shale and 7. The Bowland Shale that the characterisation successes of these techniques varies with the sample; the Marcellus was characterised well with the combination of nitrogen gas sorption where it demonstrated relatively narrow hysteresis closure loops, whereas samples of the Utica and Bowland were not as well characterised by nitrogen gas sorption with some samples having large hysteresis closure loops. This demonstrates the presence of a significant number of small pores (<4nm) controlling the movement of the adsorbate into and out of the sample. This due to the variation in intra-particle complexity and the openness of the pore networks reflecting the adsorbate ability to move throughout the sample.

Gas sorption results for Marcellus 7795'-7798' using variable grain sizes have shown that by doing this you can infer network complexity however the ability of this technique to give a quantitative measurement of the complexity was limited. It was determined that the process of crushing creates more pore volume, but has a negligible effect on the pore surface area. There is potential in this technique for forecasting to much larger samples which would address an industry problem where scaling laboratory findings to reservoir engineering recommendations is often poor.

Mineralogy was quantified using SEM MLA, and TOC% was quantified using RockEval. Following this correlations could be made with the surface area and pore volume to mineralogy and TOC% for all the Marcellus and Utica samples. In 5. The Marcellus Shale it was seen that TOC% and clay content had the strongest correlation to surface area and pore volume for all samples, where carbonates and quartz had negative correlations to these properties. For 6. The Utica Shale the correlations between mineralogy, and the surface area and pore volume, were not as strong, where correlations to TOC% were the dominant correlation and the correlation to clays was tenuous. After this fractal dimensions were calculated for all samples and were correlated to the mineralogy and TOC%. It was seen that the TOC% correlated to the fractal dimensions for all samples as seen in 5. The Marcellus Shale, 6. The Utica Shale and 7. The Bowland Shale. By using the fractal dimension correlation to minerals it has enabled specific sample characteristics, e.g. surface roughness and pore connectivity, to be attributed to certain minerals thus indicating which minerals are responsible. In a similar vein to Wang *et al.*, (2015), by making correlations between the mineralogy and D_1 it shows which minerals make surfaces rougher and provide the most adsorption sites.

By developing the rigorous model fitting procedure for isotherm data, it has been possible to produce a homotactic patch model which can deconvolute some of the surface-accessible constituents of the sample, identified to be significant from the previous work (clays and TOC%). Results from the Marcellus and Utica shale produced a strong correlation of the derived TOC% from the homotactic patch to the values established from RockEval. While RockEval data was not acquired for the Bowland shale, by using an isotherm for experimentally extracted kerogen and illite (Clay Minerals Society), TOC% and illite quantities were modelled. The quantities of kerogen (k -value) and illite (i -value) derived from the homotactic patch model produced the expected correlation to surface area, pore volume and fractal dimensions based on results from the Marcellus and Utica shale.

Having achieved the aim of producing a more rigorous numerical analysis technique which has successfully provided information beyond the limits of standard analysis, the focus moved onto the use of novel characterisation techniques. With the aim of overcoming the existing drawbacks of shale characterisation overcondensation gas sorption was used as the primary novel characterisation technique. Gas overcondensation has been shown to be successful at bridging the gaps across very diverse length-scales in the pore structure, by demonstrating the presence of very large pore bodies in the Utica shale which were undetected by conventional gas sorption. With the addition of scanning curves the structural relationship to smaller pores was able to be further understood beyond the use of desorption hysteresis in conventional isotherms. This was first used in 6. The Utica Shale, and was used again for Bowland characterisation where macroporosity was identified that was impenetrable by mercury intrusion porosimetry as a result of the narrow leading necks which mercury could not enter thus restricting mass transport in the sample.

Additional work was carried out with the overcondensation gas sorption results where the transition in mineralogy was probed to identify if additional complexities are introduced into pore systems of shales with a change in mineral regime. In 6. The Utica Shale there is an identified change-over in the predominant inorganic phase, which is also associated to a peak in the organic phase. The sample at

which this particular transition occurs is observed to have the most complex, disordered pore structure as evidenced by a percolation knee not seen in the conventional gas sorption data. This observation was confirmed with the use of Hg-CXT which showed mercury to be trapped in this sample by a significantly different mechanism than the other samples at different levels in the succession. In 7. The Bowland Shale, overcondensation samples were taken before during and after the presence of a marine band. By studying the samples across this boundary it was identified that the shale deposited immediately above the marine band possessed the greatest pore surface area, pore volume and likely also organic matter (as indicated by the homotactic patch model). This discovery is also in-line with the findings of 6. The Utica Shale where U5 demonstrated these properties in relation to the other Utica samples.

The shale characterisation in 7. The Bowland Shale, in addition to the overcondensation method, used mass transfer and thermokinetic parameters to identify and establish the complexity of pore networks, accessibility of the adsorbate to the sample and the length of the diffusion paths. This work on kinetics was then applied to industry based work by assessing the effect of acid on fine-grained matrix samples. It was observed that for samples with fine grained carbonate grains throughout the impact on the intra-particle properties was significantly more than for samples with coarse grains of carbonates. Where fine-grains of carbonates were present the overall impact was on lengthening diffusion paths to the centre of the particle however this also had the effect of making mass transfer significantly slower.

10.3. Future Work

Four main areas where future work can be done have been identified. The first of these areas involves a more in-depth investigation of the grain size analysis and the ability for the Gurvitsch volume to be scaled up. Additional scaling should be done on the acid treatment study in 8. Shale Treatment to understand how samples behave when in a core plug compared to what was seen with the use of powdered samples. Continued use of gas overcondensation with complimentary mass transfer and thermokinetic parameters to understand the spatial juxtaposition of pores and the adsorbate movement throughout the sample. Finally, the use of a wider set of samples with more variation in their mineralogy but critically in their organic matter (e.g. thermal maturity and type).

The proposed future work for the grain size analysis would be to test much larger samples (core plug) with nitrogen gas sorption and use the measured Gurvitsch volume to examine the trend in the maximum filling values with varying particle size (mid-point of the grain size). It may be possible to infer the spatial distribution of pores within the samples, and by forecasting to larger samples scale up the results. Figure 117 shows how this process would be carried out, although the grain sizes available do not allow for any reliable scaling of results. Scaling up the acid treatment work is also of interest since the work outlined in this study used powdered samples which may act differently to core plug samples. For the carbonate-rich samples whole grains of carbonate were dissolved resulting in an overall mineralogy change but minimal change to the pore structures. The dissolution of these grains within a core plug may have a more noticeable impact on the gas sorption results following acid treatment.

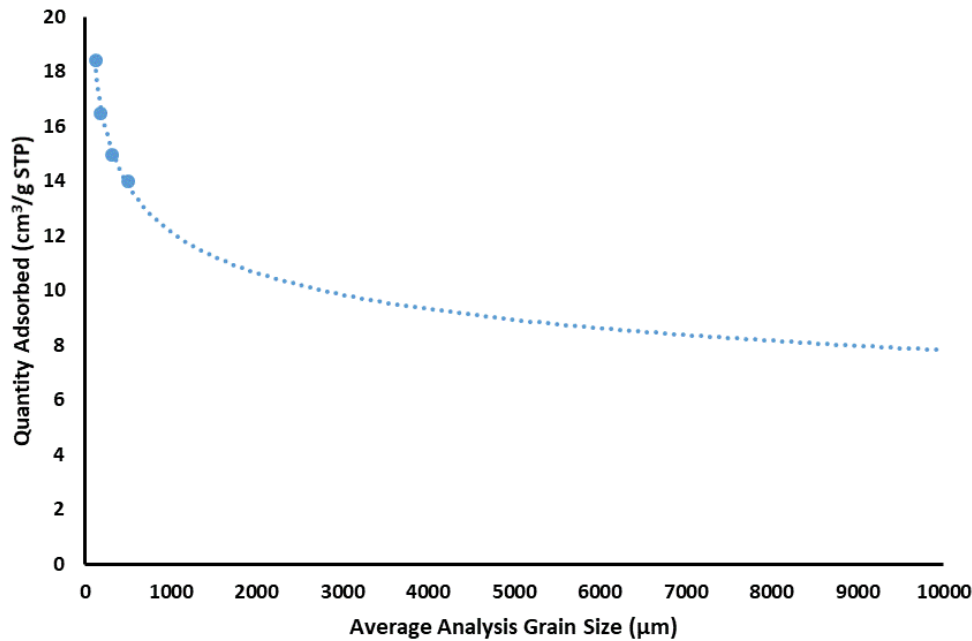


Figure 117: using the Gurvitsch volume against grain size and using trend line forecasting to predict what the maximum quantity adsorbed may be for larger samples.

Further work could be carried out on the use of gas overcondensation, mass transfer kinetics and the thermokinetic parameters. Work in 7. The Bowland Shale outlined results where the combined use of these methodologies was able to identify where some very large macropores existed (by using overcondensation), however these were shielded by pores with very narrow necks resulting in restricted mass transport (kinetics).

The final area of future work is focused on broadening the mineralogy and organic matter by introducing samples which vary more greatly to the population of samples used in this study. By doing this it will test the applicability of the methods to other samples, and determine how universally the homotattic patch model can be used. The main focus of this additional work will be on acquiring samples with more varied organic matter properties, such as the thermal maturity and organic matter type. Both these organic matter properties have been identified as key controlling factors on sample surface area and pore volume and will provide a true test of the homotattic patch model. To achieve this a database of other pure mineral types, organic matter of different thermal maturities and types will need to be formed such that samples of a more varied mineral composition can be analysed.

10.4. Summary

It has been shown that standalone characterisation methods are insufficient in characterisation the pore surface area, pore volume and pore network of shale samples where several key observations are overlooked which could be influential to industry. By developing a more rigorous numerical analysis system it has been possible to extend the knowledge gained from standard characterisation techniques, and in some cases reduce the quantity of specific experimental work needed (i.e. homotattic patch work). Further the development of experimental techniques, such as overcondensation gas sorption and the coupled mass transfer and thermokinetic parameters have enabled more information about the pore networks and fluid movement through the samples to be gained. Both the numerical analysis and novel characterisation techniques have been proven to exceed the results of standard characterisation techniques.

Appendix 1

Data from Ross and Bustin (2009), showing the wide variety in shale properties within a geological time period and also across several geological time periods

| Sample ID | TOC* (wt%) | Pore structure/surface area data | | | | Moisture (wt%) | Sorbed gas capacity | | Maturity data** (Vro %) | Inorganic composition data** | | | |
|----------------|------------|----------------------------------|---|--|---|----------------|------------------------------|---------------------|-------------------------|------------------------------|------------------------------------|-----------|---------|
| | | Hg porosity* (%) | N ₂ BET surface area (m ² /g) | CO ₂ micropore volume (cc/100g) | CO ₂ equivalent surface area (m ² /g) | | Moisture EQ. at 6 Mpa (cc/g) | Dry (cc/g at 6 Mpa) | | SiO ₂ (%) | Al ₂ O ₃ (%) | Si/Al (%) | CaO (%) |
| MU1416-1 | 2.1 | 4.4 | 19.5 | 0.8 | 28.9 | 3.2 | 0.9 | 2.1 | 1.6 | 64.1 | 17.5 | 3.7 | 0.8 |
| MU1416-4 | 1.7 | 2.2 | 10.1 | 0.6 | 23.7 | 3.5 | 0.7 | - | 1.6 | 65.8 | 14.7 | 4.5 | 0.7 |
| MU1416-7 | 2.1 | 2.2 | 9.1 | 0.8 | 29.2 | 3.5 | 1.2 | 2.2 | 1.6 | 68.6 | 12.7 | 5.4 | 0.6 |
| MU1416-9 | 0.4 | 1.4 | 3.4 | 0.3 | 11.1 | 2.5 | 0.2 | 0.6 | 1.6 | 5.5 | 1.7 | 3.3 | 44.6 |
| MU714-3 | 1.6 | 1 | 10.5 | 0.5 | 18.8 | 1.9 | 0.7 | 1.7 | 1.7 | 36.6 | 7.2 | 5.1 | 16.4 |
| MU414-1 | 3.7 | 3.7 | 10.7 | 1 | 36.7 | 3.1 | 0.8 | - | n/a | 73.5 | 9.9 | 7.4 | 0.6 |
| UBS-C15-1331-1 | 1.4 | 5.4 | 16.8 | 0.5 | 19.1 | 2.4 | 0.3 | 1.6 | 2.5 | 78.3 | 9.9 | 7.9 | 1.2 |
| UBS-C15-1331-5 | 4 | 6 | 44.5 | 1.3 | 47.2 | 4.1 | 1.6 | 3.2 | 2.5 | 60.7 | 16.9 | 3.6 | 0.6 |
| UBS1331-4 | 4 | 7.2 | 29.3 | 0.9 | 32.9 | 4.9 | 1.2 | 3 | 2.5 | 47.3 | 23 | 2.1 | 1.2 |
| UBS1331-5 | 4.9 | 5.1 | 20 | 1 | 38.3 | 4.4 | 1.3 | 3.5 | 2.5 | 50.9 | 24.1 | 2.1 | 0.6 |
| UBS1331-6 | 4.7 | 5.2 | 31 | 1.2 | 44.7 | 4.1 | 1.6 | 4 | 2.5 | 45.1 | 22.3 | 2 | 1.2 |
| UBS1331-11 | 3.8 | 4.6 | 22.3 | 0.8 | 29.8 | 5.2 | 0.8 | 3 | 2.5 | 48 | 22.9 | 2.1 | 0.8 |
| LBM325-1 | 2 | 1.2 | 10.3 | 0.5 | 17.6 | 1.6 | 0.6 | - | n/a | 82.4 | 5.7 | 14.5 | 0.8 |
| LBM325-5 | 2.1 | 1.3 | 12.8 | 0.5 | 18.2 | 1.8 | 0.7 | 1.6 | n/a | 78.9 | 9.6 | 8.2 | 0.3 |
| LBM325-7 | 0.9 | 0.4 | 5.5 | 0.3 | 9.5 | 1.5 | 0.3 | - | n/a | 30 | 3 | 10 | 19.4 |

| | | | | | | | | | | | | | |
|--------------------|------------|------------|-------------|----------|-------------|------------|------------|-----|------------|-------------|------------|-------------|------------|
| LBM2563-1 | 4.8 | 1.6 | 16.3 | 1 | 37.6 | 1.4 | 1.6 | - | n/a | 80.7 | 5.9 | 13.7 | 1.2 |
| LBM2563-3 | 4.4 | 2.1 | 12.4 | 0.8 | 29.7 | 1.8 | 1.2 | 2.6 | n/a | 80.2 | 6.3 | 12.8 | 1.2 |
| LBM2563-5 | 2.8 | 0.8 | 13.9 | 0.6 | 21.9 | 2.3 | 0.8 | - | n/a | 82.4 | 6.6 | 12.5 | 0.5 |
| LBM2563-7 | 2.5 | 1.1 | 12.3 | 0.7 | 25.6 | 1.9 | 0.9 | 1.8 | n/a | 79.4 | 7.9 | 10.1 | 0.8 |
| PSS 1416-1 | 0.3 | 2.6 | 13.6 | 0.5 | 18 | 4.8 | 0.2 | 1.4 | 1.6 | 56.6 | 19.5 | 2.9 | 1.7 |
| PSS 1416-5 | 0.2 | 3 | 15 | 0.5 | 18.6 | 3.3 | 0.1 | 1.4 | 1.6 | 55.5 | 19.2 | 2.9 | 1.8 |
| PSS 5245-1 | 0.3 | 4.3 | 20.5 | 0.6 | 22.3 | 3.1 | 0.1 | 0.6 | n/a | 61 | 19.2 | 3.2 | 0.4 |
| PSS 12140-6 | 0.3 | 3.9 | 24.7 | 0.8 | 29.5 | 2.8 | 0.4 | 1.7 | n/a | 59.1 | 19.8 | 3 | 0.5 |
| PSS 1238-1 | 0.3 | 2.5 | 10.4 | 0.4 | 15.9 | 2.5 | 0.1 | 1.1 | n/a | 56.6 | 20.6 | 2.7 | 10 |
| PSS 947-3 | 0.2 | 1.9 | 11.3 | 0.4 | 14.9 | 2.4 | 0.3 | 1.2 | n/a | 40.4 | 12.9 | 3.1 | 17 |

Table A1. 1: Composition, surface areas, thermal maturity and sorption capacities of Devonian – Mississippian shales.

| | | | | | | | | | | | | | |
|-----------------|------|-----|-----|-----|------|-----|-----|-----|-----|------|------|------|------|
| N5378-11 | 1.6 | - | 9.3 | 0.6 | 21.9 | - | - | - | - | - | - | - | - |
| N8354-11 | 26.2 | - | 0 | 0.5 | 19.4 | - | - | - | - | - | - | - | - |
| N8354-4 | 37.8 | - | 1.6 | 0.6 | 23.7 | - | - | - | 0.9 | 24.8 | 5.4 | 4.6 | 26.8 |
| N376-1 | 1.4 | 0.5 | 0.6 | 0.2 | 6.2 | 0.7 | 0.1 | 0.4 | 1.8 | 18.8 | 3.2 | 5.9 | 24.5 |
| N2557-2 | 3.1 | 2.6 | 1.8 | 0.2 | 8.4 | 2.3 | 0.1 | - | 0.7 | 65 | 0.4 | 16.2 | 6.7 |
| N6080-1 | 4.3 | 2.8 | 2.8 | 0.5 | 18.5 | 8.5 | 0.3 | 0.4 | 1.3 | 54.9 | 15.2 | 3.6 | 1.2 |
| N3773-2 | 5 | 0.5 | 6.3 | 0.8 | 28.8 | 1.8 | 1.2 | 2.1 | 2.5 | 63.9 | 5.8 | 11.1 | 8.6 |
| N89-1 | 5.2 | 0.8 | 2.8 | 0.3 | 12.7 | 1.6 | 0.5 | 1.2 | 1.1 | 16.8 | 5.5 | 3.1 | 35 |
| N230-1 | 7.1 | 2.2 | 1.5 | 0.3 | 11.4 | 2.5 | 0.6 | 1.3 | 0.9 | 42.7 | 11.3 | 3.8 | 14.3 |
| N3793-1 | 9 | - | 1.7 | 1.1 | 40.3 | 2.8 | 2 | 3.6 | 2.5 | 47.3 | 8.5 | 5.5 | 13.8 |
| N49-2 | 10 | 1.5 | 2.8 | 0.6 | 23.4 | 2.3 | 1.5 | 2 | 1.2 | 38 | 7.6 | 5 | 18.2 |
| N91-1 | 10.2 | 4.2 | 2.3 | 0.4 | 15.3 | 0.6 | 1 | 1.3 | 1.3 | 62.9 | 1 | 62.9 | 11.5 |
| N174-1 | 11.8 | - | 1.2 | 0.4 | 16.1 | 1.7 | 1.6 | 1.6 | 1.1 | 61 | 1.3 | 45.8 | 11.7 |

Table A1. 2: Composition, surface areas, thermal maturity and sorption capacities of Jurassic shales.

The table below is data from (Y. Chen *et al.*, 2015) to demonstrate further variety in shale properties.

| Sample | Ro (%) | TOC (wt%) | Total porosity | Quartz | Dolomite | Calcite | Ankerite | All carbonates | Illite /smectite | Kaolinite | Chlorite | All clays | Albite | Sanidine | All feldspars | Pyrite |
|--------------|--------|-----------|----------------|--------|----------|---------|----------|----------------|------------------|-----------|----------|-------------|--------|----------|---------------|--------|
| 472-1 | 0.35 | 2.37 | 9.1 | 14.5 | 15.5 | 22 | 9.4 | 46.9 | 21.9 | 0.4 | 1.7 | 24.1 | 2.1 | 8.2 | 10.3 | 1.8 |
| 634-1 | 0.5 | 21.54 | 2.3 | 22.9 | 0 | 0.6 | 0 | 0.6 | 38.3 | 1.4 | 0.4 | 40.1 | 11 | 2.1 | 13.1 | 1.7 |
| MIM4 | 0.55 | 13 | 4.1 | 33.8 | 0.3 | 0.7 | 0 | 1 | 32.9 | 1.9 | 0.4 | 35.2 | 4.2 | 11.4 | 15.6 | 1.5 |
| 554-2 | 0.61 | 6.53 | 1 | 26.3 | 1 | 0.7 | 6.9 | 8.6 | 42.4 | 0.7 | 0 | 43.1 | 10 | 3.5 | 13.5 | 2 |
| NA2 | 0.65 | 5.3 | 5.1 | 37.5 | 1.4 | 0.9 | 2.8 | 5.1 | 26.5 | 2.5 | 0.5 | 29.5 | 6.3 | 12.9 | 19.2 | 3.4 |
| IL6 | 0.7 | 6.01 | n.d. | 35.4 | 0.4 | 1.1 | 0 | 1.5 | 36.1 | 1.8 | 0.2 | 38.1 | 5.5 | 12.8 | 18.3 | 0.8 |
| IL4 | 0.83 | 6.2 | 1.1 | 24.8 | 3.5 | 1.2 | 0 | 4.7 | 39.3 | 2.1 | 0.1 | 41.6 | 5 | 16.3 | 21.3 | 1.4 |
| IL5 | 1.15 | 4.29 | 1.5 | 27.8 | 18.1 | 10.5 | 0 | 28.6 | 23.4 | 0 | 0 | 23.5 | 5.3 | 8.6 | 13.9 | 2 |
| IL3 | 1.27 | 5.5 | 2.5 | 35.7 | 0.1 | 1.6 | 0 | 1.7 | 36.5 | 0.1 | 2.4 | 39 | 3.9 | 13.3 | 17.2 | 0.9 |
| IL2 | 1.3 | 3.3 | 3.5 | 22.3 | 4.9 | 0 | 0 | 4.9 | 0 | 0.5 | 1.1 | 1.5 | 33.9 | 32.7 | 66.6 | 1.4 |
| IL1 | 1.41 | 6.29 | 3.5 | 19.9 | 11.7 | 0 | 0 | 11.7 | 1.2 | 0.7 | 0.7 | 2.7 | 25.2 | 27 | 52.2 | 7.3 |

Table A1. 3: total porosity (vol.%) and mineralogical compositions (wt.%) of shale samples.

Appendix 2

$$\frac{\text{Initial Mass} - \text{Moisture Mass}}{\text{Initial Mass}} \times 100$$

A2. 1: moisture %

$$\frac{\text{Moisture Mass} - \text{Volatile Mass}}{\text{Initial Mass}} \times 100$$

A2. 2: volatiles %

$$\frac{\text{Ash Mass}}{\text{Initial Mass}} \times 100$$

A2. 3: ash %

$$100 - (\text{Moisture} + \text{Volatile} + \text{Ash})$$

A2. 4: fixed carbon %

$$\frac{100}{100 - \text{Moisture}} \times \text{Volatile}$$

A2. 5: volatile dry %

$$\frac{100}{100 - \text{Moisture}} \times \text{Ash}$$

A2. 6: ash dry %

$$100 - (\text{Volatile Dry} + \text{Ash Dry})$$

A2. 7: fixed carbon dry %

The above equations were used to calculate the contributions to each sample (Corporation, 2010) where moisture mass was taken at 110°C, volatile mass taken at 920°C and ash mass taken at 600°C (after the gas change).

Appendix 3

Appendix 3.1

Appendix 3.1.1

Below is the code used for the BET fractal analysis in R. with annotations explaining what each function does. The code can be altered for K number of generated numbers - where a greater K value will result in a higher degree of accuracy i.e. the smallest value of the summed residuals.

```
# Read the data
data = read.csv("filepath.csv")

# Assign observational data (x,y) to DF
DF <- data[, 1:2]

# Cut data at relative pressure greater than 0.8
df <- DF[which(DF$x <= 0.8),]

# Assign initial parameters from the file read to data in the form (C,Vm,D)
init_parameters <- data.frame("C" = data[1, 3],
                              "Vm" = data[1, 4],
                              "D" = 2.5)

# Simulate K number of uniformly distributed random numbers for each of the
# parameters where prop is the proportion above and below the initial
# parameters to generate
generateRandomParameters <-
  function(K, initial_parameters, prop = 0.1) {
    initial_parameters <- as.numeric(initial_parameters)
    C <- initial_parameters[1]
    Vm <- initial_parameters[2]
    D <- initial_parameters[3]

    parameters <-
      data.frame(
        "C" = runif(K, min = C * (1 - prop), max = C * (1 + prop)),
        "Vm" = runif(K, min = Vm * (1 - prop), max = Vm *
                     (1 + prop)),
        "D" = runif(K, min = 2, max = 3)
      )
    return(parameters)
  }

# Use the BET equation and return v and the residual sum of squares
BET_Eq <- function(obs_data, parameters) {
  parameters <- as.numeric(parameters)
  x <- obs_data$x
  y <- obs_data$y
  C <- parameters[1]
  Vm <- parameters[2]
  D <- parameters[3]

  v <- Vm * ((C * x) / (1 + x * (C - 1))) * (1 - x) ^ (-(3 - D))

# Discard combinations of parameters where the modelled isotherm is greater
# than the experimental
  if(sum(y) >= sum(v)) {
    RSS <- sum((y - v) ^ 2)
  } else {
    RSS <- NA
  }
  RSS <- sum((y - v) ^ 2)
}
```

```

output <- list("v" = v,
             "RSS" = RSS)
return(output)
}

# Return the RSS given the observed data at the given parameter values
using the function BET_Eq
returnRSS <- function(obs_data, parameters) {
  BET <- BET_Eq(obs_data, parameters)
  RSS <- BET$RSS
  return(RSS)
}

# Minimize the residual sum of squares by cycling through K random
parameters and returning the row which best fits the data
minimizeRSS <-
function(K, obs_data, initial_parameters, prop = 0.1) {
  # Simulate K random parameters using the function defined above
  parameters <-
    generateRandomParameters(K, initial_parameters, prop)

  # Calculate the RSS by evaluating the function at every row of the
  parameters
  matrix, i.e. each combination of the simulated parameter values
  RSS <- apply(parameters, 1, returnRSS, obs_data = obs_data)
  minimizedLocation <- which.min(RSS)
  optimisedParameters <- as.numeric(parameters[minimizedLocation, ])
  output <- data.frame(
    "C" = optimisedParameters[1],
    "Vm" = optimisedParameters[2],
    "D" = optimisedParameters[3],
    "RSS" = RSS[minimizedLocation]
  )
  return(output)
}

# Optimise the parameters by minimising the residuals with K simulated
numbers for the data points 1 to i, for i = 1,2,...,N where N is the number
of observations
incrementMinimize <-
function(K, obs_data, initial_parameters, prop = 0.1) {
  N <- nrow(obs_data)
  outputMatrix <- matrix(rep(NA, N * 4), nrow = N)
  cur_output <-
    minimizeRSS(K, obs_data, initial_parameters, prop)
  outputMatrix <- as.numeric(cur_output)
  return(outputMatrix)
}

# Return the optimised parameters by incrementing
minimised_data <- incrementMinimize(K, df, init_parameters)

print(minimised_data)

```

The output of the code will look like the below example, where values are "C", "Vm", "D" and "RSS" respectively.

```
[1] 49.97430287  0.44629110  2.27408888  0.04065305
```

Iterations of the code can be increased by telling the whole function to run against for n number of times and K number of generated parameters.

```
# Repeat the incrementMinimize function
Reps = t(replicate(n, incrementMinimize(K, df, init_parameters)))

# Write reps to a csv file
write.csv(reps, "filepath.csv")
```

The output of the additional code will write to a .csv document with each value taking up a single cell such that data is easily analysed after. By having the additional repetitions of the function it is possible to see how reproducible the code is and see how the summed residuals are affected by the variations in K .

Appendix 3.1.2

The code below is the **one part FHH** fractal analysis which consists of less complex code to establish the pressure range for analysis. The pressure range was established with the use of a moving window where the mid-point of the data is established and a window of increasing size is applied over the data e.g. 2 data points, 4 data points, 6 data points etc. This is achieved by having $n-1$ and $n+1$ where n is the mid-point and repeating this process to include a greater and greater portion of the data. Several conditions were then put in place such that the r-squared value must be greater than 0.88, and at least two-thirds the whole dataset was included i.e. if the data set had 60 points there must be at least 40. Once these conditions were met the dataset which had the smallest r-squared value was used as the data for the FHH fractal analysis.

```
# Read the data
Imp = read.csv("filepath.csv")

# Pressure_Op is a function to optimise the pressure range over which to
conduct the fractal analysis
Pressure_Op <-
  function(obs_data) {
    x <- obs_data$x
    y <- obs_data$y

    # One part FHH occupies the middle part of the pressure data. An
    increasing window
    size of data points from mid-point of data is analysed for the best fit
    linear line
    FHH_Pressure <-
      function(a, b, obs_data) {
        # Call R-Squared package from the library
        library(rsq)

        # Define the parameters needed for the linear model from the imported
        dataset
        x <- obs_data$x
        y <- obs_data$y
        Vm = rep(obs_data$Vm[1], length(y))

        # Make the x- and y- axis for the straight line graph and create a
        new
        dataframe
        xt <- log(log((1 / (x[a:b])), exp(1)), exp(1))
        yt <- log(y[a:b] / Vm[a:b], exp(1))
        dft <- data.frame(xt, yt)

        # Conduct linear analysis to find the gradient of the straight line
        graph
```

```

l1 <- lm(yt~xt)
r2 <- rsq(l1)

# Set that the R-squared value must be greater than 0.88
R <- ifelse(r2 >= 0.88, r2, NA)

# n is the length of the data set - difference between a and b which
decrease and increase respectively to form the moving window
n <- (b-a)

# Set that N the length of the analysis dataset must be at least two-
thirds the
length of the total dataset
N <- ifelse( n >= 2 / 3 * length(x), n, NA)

# Report the R-squared, gradient, intercept, low and high pressure points
and
the length of the dataset. Where a column contains an NA the whole row is
omitted such that only values are reported which fit the analysis
conditions
laid out
values = na.omit(data.frame("R2" = R, "Gradient" =
l1$coefficients[2],
"Intercept" = l1$coefficients[1], "P1" = x[a], "P2" = x[b],
"Length" = N))

return(values)

}

# Define the mid-point as halfway through the data set
mid = as.integer((1 / 2) * length(imp$x))

# Call the moving window function
FHH = data.frame(t(apply(1:(mid-1), function(i){FHH_Pressure(abs(mid-
i), (mid+i),
imp))}))

# Return the row which contains the maximum R-squared value
FHH_P <- FHH[which.max(FHH$R2),]

# Call the data over which the relevant pressure range applies
DF <- data.frame(X=(x[which(x >= FHH_P$P1 &
x <= FHH_P$P2)]),Y = (y[which(y >= y[which(x == FHH_P$P1)] & y <=
y[which(x == FHH_P$P2)])]))

# Sigma is determined for Van der Waals or Capillary Condensation as
this will
change how the fractal dimension is calculated from the gradient
sig = 3 * (1 + as.numeric(FHH_P$Gradient)) - 2
sigma = rep(sig, length(DF[,1]))

return(cbind(DF, sigma))
}

Pressure_range=Pressure_Op(imp)

# Assign observational data (x,y) to df
df <- Pressure_range

# Assign initial parameters from the file read to data in the form (C,Vm,D)

```

```

init_parameters <- data.frame("C" = 6,
                             "Vm" = imp$Vm[1],
                             "D" = 2.5)

# Simulate K number of uniformly distributed random numbers for each of the
# parameters where prop is the proportion above and below the initial
# parameters to generate
generateRandomParameters <-
  function(K, initial_parameters, prop = 0.1) {
    initial_parameters <- as.numeric(initial_parameters)
    C <- initial_parameters[1]
    Vm <- initial_parameters[2]
    D <- initial_parameters[3]

    parameters <-
      data.frame(
        "C" = runif(K, min = -10, max = 10),
        "Vm" = runif(K, min = Vm * (1 - prop), max = Vm *
                      (1 + prop)),
        "D" = runif(K, min = 2, max = 3)
      )
    return(parameters)
  }

# Use the FHH equation and return v and the residual sum of squares
FHH_Eq <- function(obs_data, parameters) {

  parameters <- as.numeric(parameters)
  x <- obs_data$X
  y <- obs_data$Y

  C <- parameters[1]
  Vm <- parameters[2]
  D <- parameters[3]

  # Select the correct fractal equation based on the sigma value
  if(obs_data$sigma[1] >= 0){
    M <- ((D - 3) / 3)
  }else{
    M <- D - 3
  }

  # Modelled isotherm
  v <- Vm * exp(C) * (log((1 / x), exp(1))) ^ (M)

  # Ensure that the modelled isotherm doesn't exceed the experimental
  if(sum(y) >= sum(v)){
    RSS <- sum((y - v) ^ 2)
  } else {
    RSS <- NA
  }

  RSS <- sum((y - v) ^ 2)
  output <- list("v" = v,
                "RSS" = RSS)

  return(output)
}

# Return the RSS given the observed data at the given parameter values
# using the function FHH_Eq
returnRSS <- function(obs_data, parameters) {

```

```

FHH <- FHH_Eq(obs_data, parameters)
RSS <- FHH$RSS
return(RSS)
}

# Minimise the residual sum of squares by cycling through K random
parameters and returning the row which best fits the data
minimizeRSS <-
function(K, obs_data, initial_parameters, prop = 0.1) {
  # Simulate K random parameters using the function defined above
  parameters <-
    generateRandomParameters(K, initial_parameters, prop)

  # Calculate the RSS by evaluating the function at every row of the
parameters
matrix, i.e. each combination of the simulated parameter values
RSS <- apply(parameters, 1, returnRSS, obs_data = obs_data)
minimizedLocation <- which.min(RSS)
optimisedParameters <- as.numeric(parameters[minimizedLocation, ])
output <- data.frame(
  "C" = optimisedParameters[1],
  "Vm" = optimisedParameters[2],
  "D" = optimisedParameters[3],
  "RSS" = RSS[minimizedLocation]
)
return(output)
}

# Optimise the parameters by minimising the residuals with K simulated
numbers for the data points 1 to i, for i = 1,2,...,N where N is the number
of observations
incrementMinimize <-
function(K, obs_data, initial_parameters, prop = 0.1) {
  N <- nrow(obs_data)
  outputMatrix <- matrix(rep(NA, N * 4), nrow = N)
  cur_output <-
    minimizeRSS(K, obs_data, initial_parameters, prop)
  outputMatrix <- as.numeric(cur_output)
  return(outputMatrix)
}

# Return the optimised parameters
minimised_data <- incrementMinimize(K, df, init_parameters)

print(minimised_data)

```

The output of the code will look the same as the fractal BET code with values in the order "C", "Vm", "D" and "RSS" respectively. Iterations of the code can be increased by telling the whole function to run against for n number of times and K number of generated parameters, this add-on is also the same as in the fractal BET.

Appendix 3.1.3

The following code outlines the process taken for the **two part FHH** fractal analysis where establishing the separate pressure ranges was a more complex task. The data was modelled to the linear form of the FHH, a linear fit was applied to this and the residuals derived. The data was separated at the point that the residuals were greatest, this is identified to be the point at which the linear trend will change from the first to the second fractal dimension. This data is the transformed back into the form of the experimental data (relative pressure and quantity adsorbed). For the first

fractal dimension it does not apply over relative pressure ranges less than 0.25, we have chosen to cut the data off at 0.2 to allow the code some flexibility in fitting. This data separation is carried out in functions `Fractal_Data_1` and `Fractal_Data_2` whose output is the data frame needed for the fractal analysis including `Vm` and `sigma`. This data is then analysed with functions `Fractal_Dimension_1` and `Fractal_Dimension_2`, the output of these functions is the same as the output from the fractal BET and one part FHH (these functions are the same as in the one part FHH).

The final line of code:

```
result <- unique(rbind(Fractal1, rep(0, 4), Fractal2)),
```

combines the two sets of results for D_1 and D_2 with a line of zeroes between two ensure data separation when exported to a .csv.

```
# Import data for
Imp = read.csv("filepath.csv")

# Import the r-squared package from the library()
library(rsq)

# Separating the first set of data for D1 fractal dimension, describing the
surface properties of the sample
Fractal_Data_1 <- function(data) {
  # Linear form of the FHH
  x1 = log(log((1 / data$x), exp(1)), exp(1))
  Vm = data$Vm[1]
  y1 = log((data$y / replicate(length(data$y), Vm)), exp(1))

  # Line of best fit and residuals of the fit
  Linear = lm(y1~x1)
  res = linear$residuals

  # Cutting off the data at the point that the residuals are greatest
  df = data.frame(res, x1)
  end = df[which.max(df$res)]
  x = na.omit(ifelse(x1 >= end$x1, x1, NA))
  y = na.omit(ifelse(x1 >= end$x1, y1, NA))

  # Returning values to experimental form, relative pressure and quantity
adsorbed
  XX = 1 / exp(exp(x))
  YY = exp(y) * replicate(length(y), Vm)
  X = na.omit(ifelse(XX >= 0.2, XX, NA))
  Y = na.omit(ifelse(XX >= 0.2, YY, NA))

  # Calculating sigma for the data so that the correct form of D is applied
  Lin = lm(y~x)
  Grad = lin$coefficients[2]
  sig = 3 * (1 + Grad)-2
  sigma = replicate(length(Y), sig)

  # Forming the dataset for fractal analysis with Vm and sigma
  Vm = replicate(length(Y), Vm)
  df1 = data.frame(X, Y, Vm, sigma)
  return(df1)
}

df1 <- Fractal_Data_1(imp)

Fractal_Dimension_1 <- function(data){
```

```

# Assign initial parameters from the file read to data in the form
(C,Vm,D)
init_parameters <- data.frame("C" = 6,
                              "Vm" = data$Vm[1],
                              "D" = 2.5)

# Simulate K number of uniformly distributed random numbers for each of the
parameters where prop is the proportion above and below the initial
parameters to generate
generateRandomParameters <-
  function(K, initial_parameters, prop = 0.1) {
    initial_parameters <- as.numeric(initial_parameters)
    C <- initial_parameters[1]
    Vm <- initial_parameters[2]
    D <- initial_parameters[3]

    parameters <-
      data.frame(
        "C" = runif(K, min = -10, max = 10),
        "Vm" = runif(K, min = Vm * (1 - prop), max = Vm *
                     (1 + prop)),
        "D" = runif(K, min = 2, max = 3)
      )
    return(parameters)
  }

# Use the FHH equation and return V and the residual sum of squares
FHH_Eq <- function(data, parameters) {
  parameters <- as.numeric(parameters)
  x <- data$X
  y <- data$Y

  C <- parameters[1]
  Vm <- parameters[2]
  D <- parameters[3]

  # Select the correct fractal equation based on the sigma value
  if(data$sigma[1] >= 0){
    M <- ((D - 3) / 3)
  }else{
    M <- D - 3
  }

  # Modelled isotherm
  V <- Vm * exp(C) * (log((1/x), exp(1)))^M

  # Ensuring that modelled isotherm doesn't exceed the experimental
  if(sum(y) >= sum(V)){
    RSS <- sum((y - V) ^ 2)
  } else {
    RSS <- NA
  }

  RSS <- sum((y - V) ^ 2)
  output <- list("V" = V,
                "RSS" = RSS)
  return(output)
}

```

```

# Return the RSS given the observed data at the given parameter values
using the function FHH_Eq
returnRSS <- function(data, parameters) {
  FHH <- FHH_Eq(data, parameters)
  RSS <- FHH$RSS
  return(RSS)
}

# Minimise the residual sum of squares by cycling through K random
parameters and returning the row which best fits the data
minimizeRSS <-
function(K, data, initial_parameters, prop = 0.1) {
  # Simulate K random parameters using the function defined above
  parameters <-
  generateRandomParameters(K, initial_parameters, prop)

  # Calculate the RSS by evaluating the function at every row of the
parameters
matrix, i.e. each combination of the simulated parameter values
RSS <- apply(parameters, 1, returnRSS, data = data)
minimizedLocation <- which.min(RSS)
optimisedParameters <- as.numeric(parameters[minimizedLocation, ])
output <- data.frame(
  "C" = optimisedParameters[1],
  "Vm" = optimisedParameters[2],
  "D" = optimisedParameters[3],
  "RSS" = RSS[minimizedLocation]
)

# Return the optimised parameters by incrementing minimised_data <-
minimizeRSS(1000, df, init_parameters)
return(output)
}

# Optimise the parameters by minimising the residuals with K simulated
numbers for the data points 1 to i, for i = 1,2,...,N where N is the
number of observations
incrementMinimize <-
function(K, data, initial_parameters, prop = 0.1) {
  N <- nrow(data)
  outputMatrix <- matrix(rep(NA, N * 6), nrow = N)
  cur_output <-
  minimizeRSS(K, data, initial_parameters, prop)
  outputMatrix <- as.numeric(cur_output)
  return(outputMatrix)
}

# Repeat the incrementMinimize function
reps = t(replicate(n, incrementMinimize(K, df, init_parameters)))
return(reps)
}

# Call the function for fractal dimension D1 and call Fractal1
Fractal1 <- Fractal_Dimension_1(df1)

# Fractal dimension 2 for the pore network properties using FHH model
Fractal_Data_2 <- function(data) {
  #Linear form of the FHH

```

```

x2 = log(log((1 / data$x), exp(1)), exp(1))
Vm = data$Vm[1]
y2 = log((data$y / replicate(length(data$y), Vm)), exp(1))

# Line of best fit and residuals of the fit
Linear = lm(y2~x2)
res = linear$residuals

# Cutting off the data at the point that the residuals are greatest
df = data.frame(res, x2)
end = df[which.max(df$res),]
x = na.omit(ifelse(x2 <= end$x2, x2, NA))
y = na.omit(ifelse(x2 <= end$x2, y2, NA))

# Returning values to experimental form, relative pressure and quantity
adsorbed
X = 1 / exp(exp(x))
Y = exp(y) * replicate(length(y), Vm)

# Calculating sigma for the data so that the correct form of D is applied
Lin = lm(y~x)
Grad = lin$coefficients[2]
sig = 3 * (1 + Grad) - 2
sigma=replicate(length(Y), sig)

# Forming the dataset for fractal analysis with Vm and sigma
Vm = replicate(length(Y), Vm)
df2 = data.frame(X, Y, Vm, sigma)
return(df2)
}

df2 <- Fractal_Data_2(imp)

Fractal_Dimension_2 <- function(data){

# Assign initial parameters from the file read to data in the form
(C,Vm,D)
init_parameters <- data.frame("C" = 6,
                              "Vm" = data$Vm[1],
                              "D" = 2.5)

# Simulate K number of uniformly distributed random numbers for each of the
parameters where prop is the proportion above and below the initial
parameters to generate
generateRandomParameters <-
function(K, initial_parameters, prop = 0.1) {
  initial_parameters <- as.numeric(initial_parameters)
  C <- initial_parameters[1]
  Vm <- initial_parameters[2]
  D <- initial_parameters[3]

  parameters <-
  data.frame(
    "C" = runif(K, min = -10, max = 10),
    "Vm" = runif(K, min = Vm * (1 - prop), max = Vm *
                  (1 + prop)),
    "D" = runif(K, min = 2, max = 3)
  )
  return(parameters)
}

```

```

# Use the FHH equation and return V and the residual sum of squares
FHH_Eq <- function(data, parameters) {
  parameters <- as.numeric(parameters)
  x <- data$X
  y <- data$Y

  C <- parameters[1]
  Vm <- parameters[2]
  D <- parameters[3]

  # Select the correct fractal equation based on the sigma value
  if(data$sigma[1] >= 0){
    M <- ((D - 3) / 3)
  }else{
    M <- D - 3
  }

  # Modelled isotherm
  V <- Vm * exp(C) * (log((1 / x), exp(1))) ^ (M)

  # Ensuring that modelled isotherm doesn't exceed the experimental
  if(sum(y) >= sum(V)){
    RSS <- sum((y - V) ^ 2)
  } else {
    RSS <- NA
  }

  RSS <- sum((y - V) ^ 2)
  output <- list("V" = V,
                "RSS" = RSS)
  return(output)
}

# Return the RSS given the observed data at the given parameter values
using the function FHH_Eq
returnRSS <- function(data, parameters) {
  FHH <- FHH_Eq(data, parameters)
  RSS <- FHH$RSS
  return(RSS)
}

# Minimise the residual sum of squares by cycling through K random
parameters and returning the row which best fits the data
minimizeRSS <-
function(K, data, initial_parameters, prop = 0.1) {
  # Simulate K random parameters using the function defined above
  parameters <-
  generateRandomParameters(K, initial_parameters, prop)

  # Calculate the RSS by evaluating the function at every row of the
parameters
matrix, i.e. each combination of the simulated parameter values
RSS <- apply(parameters, 1, returnRSS, data = data)
minimizedLocation <- which.min(RSS)
optimisedParameters <- as.numeric(parameters[minimizedLocation, ])
output <- data.frame(
  "C" = optimisedParameters[1],
  "Vm" = optimisedParameters[2],

```

```

        "D" = optimisedParameters[3],
        "RSS" = RSS[minimizedLocation]
    )

# Return the optimised parameters by incrementing minimised_data <-
minimizeRSS(1000, df, init_parameters)
    return(output)
}

# Optimise the parameters by minimising the residuals with K simulated
numbers for the data points 1 to i, for i = 1,2,...,N where N is the
number of observations
incrementMinimize <-
    function(K, data, initial_parameters, prop = 0.1) {
        N <- nrow(data)
        outputMatrix <- matrix(rep(NA, N * 6), nrow = N)
        cur_output <-
            minimizeRSS(K, data, initial_parameters, prop)
        outputMatrix <- as.numeric(cur_output)
        return(outputMatrix)
    }

# Repeat the incrementMinimize function
reps=t(replicate(n = N, incrementMinimize(K, df, init_parameters)))
return(reps)
}

Fractal2 <- Fractal_Dimension_2(df2)

result <- unique(rbind(Fractal1, rep(0, 4), Fractal2))

# Write result to a csv file
write.csv(result,"filepath.csv")

```

The output of these different fractal dimension analysis can then be compared to each other for continuity and also to physical parameters of the shales established through experimental analysis. It is expected, that although the values won't be exactly the same, the trend between the BET, FHH and FHH D_1 should be the same and correlate to the same properties as one another. FHH D_2 on the other hand is the only one of these fractal analysis to describe the pore network properties of the shale and is expected to be different to the other fractal dimensions and correlate to different physical properties.

Appendix 3.2

Appendix 3.2.1

The homotattic patch for the BET and n-BET models are dealt with in the exact some way with the change of variable from D to N and the model equation from the BET to the n-BET. The areas of code which are changed for one another in the model are highlighted in grey.

```

# Read the data
imp = read.csv("filepath.csv")

# Organise data into a dataframe containing x, y, kerogen, C and Vm
parameters
Data <-
    function(data) {
        # Omit values where the relative pressure range is greater than 0.8
        x = na.omit(ifelse(data[,1] <= 0.8, data[,1], NA))
        y = na.omit(ifelse(data[,1] <= 0.8, data[,2], NA))
    }

```

```

# Create the kerogen isotherm over the relative pressure range defined
above
x1 = na.omit(ifelse(x > 0 & x <= 0.025, x, NA))
x2 = na.omit(ifelse(x > 0.025 & x <= 0.7, x, NA))
x3 = na.omit(ifelse(x > 0.7 & x <= 0.925, x, NA))
x4 = na.omit(ifelse(x > 0.925 & x <= 1, x, NA))
y1 = 6.8705 * log(x1, base = exp(1)) + 92.807
y2 = -34.08 * (x2 ^ 2) + 110.81 * x2 + 76.7
y3 = 56.209 * exp(1.2458 * x3)
y4 = (67470 * x4 ^ 2) - 128284 * x4 + 61174

k = append(append(y1, y2), append(y3, y4))

# Create the illite isotherm over the relative pressure range defined
above
x11 = na.omit(ifelse(x > 0 & x <= 0.00125, x, NA))
x22 = na.omit(ifelse(x > 0.00125 & x <= 0.01, x, NA))
x33 = na.omit(ifelse(x > 0.01 & x <= 0.915, x, NA))
x44 = na.omit(ifelse(x > 0.915 & x <= 0.975, x, NA))

y11 = 15.795 * x11 ^ 0.2645
y22 = 10.37 * x22 ^ 0.2047
y33 = (23.882 * x33 ^ 3) + (-28.421 * x33 ^ 2) + (15.257 * x33) + 4.085
y44 = (1824.5 * x44 ^ 2) - 3348 * x44 + 1549.6

i = append(append(y1, y2), append(y3, y4))

C = data$C[1]
Vm = data$Vm[1]

# Make a dataframe of the relative pressure, quantity adsorbed, kerogen
isotherm,
illite isotherm and experimentally derived values of C and Vm
DF = data.frame(x, y, k, i, C, Vm)

return(DF)
}

df=Data(imp)

# Define the model parameters
initial_parameters <- data.frame("C" = df$C[1],
                                "Vm" = df$Vm[1],
                                "D" = 2.5,
                                "N" = 1,
                                "p" = 0.5,
                                "q" = 0.5,
                                "r" = 0.5)

# Simulate K number of uniformly distributed random numbers for each of the
parameters here prop is the proportion above and below the initial
parameters to generate
generateRandomParameters <-
function(K, initial_parameters, prop = 0.1) {
  initial_parameters <- as.numeric(initial_parameters)
  C <- initial_parameters[1]
  Vm <- initial_parameters[2]
  D <- initial_parameters[3]
  N <- initial_parameters[3]
  p <- initial_parameters[4]

```

```

q <- initial_parameters[5]
r <- initial_parameters[6]

parameters2 <-
  data.frame(
    "C" = runif(K, min = C * (1 - prop), max = C * (1 + prop)),
    "Vm" = runif(K, min = Vm * (1 - prop), max = Vm *
      (1 + prop)),
    "D" = runif(K, min = 2, max = 3),
    "N" = as.integer(runif(K, min = 1, max = 10)),
    "p" = runif(K, min = 0, max = 1),
    "q" = runif(K, min = 0, max = 1),
    "r" = runif(K, min = 0, max = 0)
  )

for (i in 1:K){
  parameters2$r[i] <- 1 - (parameters2$p[i] + parameters2$q[i])
  if (parameters2$r[i] >= 0){
    parameters2$r[i] = parameters2$r[i]
  } else {
    parameters2$r[i] = NA
  }
  parameters <- na.omit(parameters2)
}

return(parameters)
}

# Use the BET or n-BET equation and return v1 and the residual sum of
squares
BET_Eq <- function(obs_data, parameters) {
  parameters <- as.numeric(parameters)

  x <- obs_data$x
  y <- obs_data$y
  k <- obs_data$k
  i <- obs_data$i

  C <- parameters[1]
  Vm <- parameters[2]
  D <- parameters[3]
  N <- parameters[3]

  p <- parameters[4]
  q <- parameters[5]
  r <- parameters[6]

  # BET for data
  v1 <- Vm * ((C * x) / (1 + x * (C - 1))) * (1 - x) ^ (-(3 - D))

  # n-BET for data
  v1 = Vm * ( C / (( 1 / x ) - 1 ) ) * (( 1 - ( N + 1 ) * x ^ N + N * x ^ (
N + 1 ) ) / (
1 + ( C - 1 ) * x - C * x ^ ( N + 1 ) ) )

  # Homotattic patch data
  V <- (v1 * p) + (k * q) + (i * r)

  # Remove values where the modelled isotherm is greater than the
experimental

```

```

if(sum(y) >= sum(V)){
  RSS <- sum((y - V) ^ 2)
} else {
  RSS <- NA
}
RSS <- sum((y - V) ^ 2)
output <- list("V" = V,
              "RSS" = RSS
            )
return(output)
}

# Return the RSS given the observed data at the given parameter values
using the function BET_Eq
returnRSS <- function(obs_data, parameters) {
  BET <- BET_Eq(obs_data, parameters)
  RSS <- BET$RSS
  return(RSS)
}

# Minimize the residual sum of squares by cycling through K random
parameters and returning the the row which best fits the data
minimizeRSS <-
function(K, obs_data, initial_parameters, prop = 0.1) {
  # Simulate K random parameters using the function defined above
  parameters <-
    generateRandomParameters(K, initial_parameters, prop = 0.1)

  # Calculate the RSS by evaluating the function at every row of the
parameters
matrix, i.e. each combination of the simulated parameter values
RSS <- apply(parameters, 1, returnRSS, obs_data = obs_data)
minimizedLocation <- which.min(RSS)
optimisedParameters <- as.numeric(parameters[minimizedLocation, ])
output <- data.frame(
  "C" = optimisedParameters[1],
  "Vm" = optimisedParameters[2],
  "D" = optimisedParameters[3],
  "N" = optimisedParameters[3],
  "p" = optimisedParameters[4],
  "q" = optimisedParameters[5],
  "r" = optimisedParameters[6],
  "RSS" = RSS[minimizedLocation]
)
return(output)
}

# Optimise the parameters by minimising the residuals with K simulated
numbers for the data points 1 to i, for i = 1,2,...,N where N is the number
of observations
incrementMinimize <-
function(K, obs_data, initial_parameters, prop = 0.1) {
  N <- nrow(obs_data)
  outputMatrix <- matrix(rep(NA, N * 6), nrow = N)
  cur_output <-
    minimizeRSS(K, obs_data, initial_parameters, prop)
  outputMatrix <- as.numeric(cur_output)
  return(outputMatrix)
}

# Return the optimised parameters by incrementing

```

```

minimised_data <- incrementMinimize(K, df, init_parameters)

# Repeat the incrementMinimize function
reps = t(replicate(n, incrementMinimize(K, df, initial_parameters)))

# Write reps to a csv file
write.csv(reps, "filepath.csv")

```

Appendix 3.2.2

The homotatic patch model for the FHH is based on the one part fractal dimension code and also includes the kerogen and illite isotherms.

```

# Read the data
imp = read.csv("filepath.csv")

# Pressure_Op is a function to optimise the pressure range over which to
conduct the fractal analysis
Pressure_Op <-
  function(obs_data) {
    x <- obs_data$x
    y <- obs_data$y

    # One part FHH occupies the middle part of the pressure data. An
    increasing window
    size of data points from mid-point of data is analysed for the best fit
    linear line
    FHH_Pressure <-
      function(a, b, obs_data) {
        # Call R-Squared package from the library
        library(rsq)

        # Define the parameters needed for the linear model from the
        imported dataset
        x <- obs_data$x
        y <- obs_data$y
        Vm = rep(obs_data$Vm[1], length(y))

        # Make the x- and y- axis for the straight line graph and create a new
        dataframe
        xt <- log(log((1 / (x[a:b])), exp(1)), exp(1))
        yt <- log(y[a:b] / Vm[a:b], exp(1))
        dft <- data.frame(xt, yt)

        # Conduct linear analysis to find the gradient of the straight line graph
        l1 <- lm(yt~xt)
        r2 <- rsq(l1)

        # Set that the R-squared value must be greater than 0.88
        R <- ifelse(r2 >= 0.88, r2, NA)

        # n is the length of the data set - difference between a and b
        which decrease and increase respectively to form the moving window
        n <- (b - a)

        # Set that N the length of the analysis dataset must be at least two-
        thirds the
        length of the total dataset
        N <- ifelse(n >= 2 / 3 * length(x), n, NA)

```

```

# Report the R-squared, gradient, intercept, low and high pressure points
and
the length of the dataset. Where a column contains an NA the whole row is
omitted such that only values are reported which fit the analysis
conditions
laid out
values = na.omit(data.frame("R2" = R, "Gradient" =
l1$coefficients[2],
"Intercept" = l1$coefficients[1], "P1" = x[a], "P2" = x[b],
"Length" = N))

return(values)

}

# Define the mid-point as halfway through the data set
mid = as.integer((1 / 2) * length(imp$x))

# Call the moving window function
FHH = data.frame(t(sapply(1:(mid - 1), function(i){FHH_Pressure(abs(mid
- i), (mid + i), imp)})))

# Return the row which contains the maximum R-squared value
FHH_P <- FHH[which.max(FHH$R2),]

# Call the data over which the relevant pressure range applies
DF <- data.frame(X = (x[which(x >= FHH_P$P1 &
x <= FHH_P$P2)]), Y = (y[which(y >= y[which(x == FHH_P$P1)] & y <=
y[which(x == FHH_P$P2)])]))

# Kerogen isotherm data given the selected pressure range
onex = na.omit(ifelse(DF[,1] > 0 & DF[,1] <= 0.025, DF[,1], NA))
twox = na.omit(ifelse(DF[,1] > 0.025 & DF[,1] <= 0.7, DF[,1], NA))
threex = na.omit(ifelse(DF[,1] > 0.7 & DF[,1] <= 0.925, DF[,1], NA))
fourx = na.omit(ifelse(DF[,1] > 0.925 & DF[,1] <= 1, DF[,1], NA))
oney = 6.8705 * log(onex, base = exp(1)) + 92.807
twoy = -34.08 * (twox ^ 2) + 110.81 * twox + 76.7
threey = 56.209 * exp(1.2458 * threex)
fourey = (67470 * fourx ^ 2) - 128284 * fourx + 61174

k <- append(append(oney, twoy), append(threey, fourey))

# Illite isotherm data given the selected pressure range
onexx = na.omit(ifelse(DF[,1] > 0 & DF[,1] <= 0.0125, DF[,1], NA))
twoxx = na.omit(ifelse(DF[,1] > 0.0125 & DF[,1] <= 0.01, DF[,1], NA))
threexx = na.omit(ifelse(DF[,1] > 0.01 & DF[,1] <= 0.915, DF[,1], NA))
fourxx = na.omit(ifelse(DF[,1] > 0.915 & DF[,1] <= 0.975, DF[,1], NA))
oneyy = 15.795 * onexx ^ 0.2645
twoyy = 10.37 * twoxx ^ 0.2047
threeyy = (23.882 * threexx ^ 3) + (-28.421 * threexx ^ 2) + (15.257 *
threexx) + 4.085
fouryy = (1824.5 * fourxx ^ 2) - 3348 * fourxx + 1549.6

i <- append(append(oney, twoy), append(threey, fourey))

# Sigma is determined for Van der Waals or Capillary Condensation as
this will
change how the fractal dimension is calculated from the gradient
sig = 3 * (1 + as.numeric(FHH_P$Gradient)) - 2
sigma = rep(sig, length(DF[,1]))

```

```

Vm <- rep(obs_data$Vm[1], length(k))

return(cbind(Df, k, i, sigma, Vm))
}

Pressure_range=Pressure_Op(imp)

# Assign observational data (x,y) to df
df <- Pressure_range

# Assign initial parameters from the file read to data in the form (C,Vm,D)
initial_parameters <- data.frame("C" = 6,
                                "Vm" = df$Vm[1],
                                "D" = 2.5,
                                "p" = 0.5,
                                "q" = 0.5,
                                "r" = 0.5)

# Simulate K number of uniformly distributed random numbers for each of the
parameters where prop is the proportion above and below the initial
parameters to generate
generateRandomParameters <-
function(K, initial_parameters, prop = 0.1) {
  initial_parameters <- as.numeric(initial_parameters)
  C <- initial_parameters[1]
  Vm <- initial_parameters[2]
  D <- initial_parameters[3]
  p <- initial_parameters[4]
  q <- initial_parameters[5]
  r <- initial_parameters[6]

  parameters2 <-
  data.frame(
    "C" = runif(K, min = -10, max = 10),
    "Vm" = runif(K, min = Vm * (1 - prop), max = Vm *
                  (1 + prop)),
    "D" = runif(K, min = 2, max = 3),
    "p" = runif(K, min = 0, max = 1),
    "q" = runif(K, min = 0, max = 1),
    "r" = runif(K, min = 0, max = 0)
  )

  for (i in 1:K){
    parameters2$r[i] <- 1 - (parameters2$p[i] + parameters2$q[i])
    if (parameters2$r[i] >= 0){
      parameters2$r[i] = parameters2$r[i]
    } else {
      parameters2$r[i] = NA
    }
  }
  parameters <- na.omit(parameters2)
}

return(parameters)
}

# Use the FHH equation and return v1 and the residual sum of squares
FHH_Eq <- function(obs_data, parameters) {

  parameters <- as.numeric(parameters)

```

```

x <- obs_data$X
y <- obs_data$Y
k <- obs_data$k
i <- obs_data$i

C <- parameters[1]
Vm <- parameters[2]
D <- parameters[3]

p <- parameters[4]
q <- parameters[5]
r <- parameters[6]

# Select the correct fractal equation based on the sigma value
if(obs_data$sigma[1] >= 0){
  M <- ((D - 3) / 3)
}else{
  M <- D - 3
}

# Modelled isotherm
v1 <- Vm * exp(C) * (log((1 / x), exp(1))) ^ (M)

# Homotattic patch isotherm
V <- (v1 * p) + (k * q) + (i * r)

# Ensure that modelled isotherm doesn't exceed the experimental
if(sum(y) >= sum(V)){
  RSS <- sum((y - V) ^ 2)
} else {
  RSS <- NA
}

RSS <- sum((y - V) ^ 2)
output <- list("V" = V,
              "RSS" = RSS)
return(output)
}

# Return the RSS given the observed data at the given parameter values
using the function FHH_Eq
returnRSS <- function(obs_data, parameters) {
  FHH <- FHH_Eq(obs_data, parameters)
  RSS <- FHH$RSS
  return(RSS)
}

# Minimize the residual sum of squares by cycling through K random
parameters and returning the row which best fits the data
minimizeRSS <-
function(K, obs_data, initial_parameters, prop = 0.1) {
  # Simulate K random parameters using the function defined above
  parameters <-
  generateRandomParameters(K, initial_parameters, prop)

  # Calculate the RSS by evaluating the function at every row of the
parameters
matrix, i.e. each combination of the simulated parameter values
RSS <- apply(parameters, 1, returnRSS, obs_data = obs_data)
minimizedLocation <- which.min(RSS)

```

```

optimisedParameters <- as.numeric(parameters[minimizedLocation, 1])
output <- data.frame(
  "C" = optimisedParameters[1],
  "Vm" = optimisedParameters[2],
  "D" = optimisedParameters[3],
  "p" = optimisedParameters[4],
  "q" = optimisedParameters[5],
  "r" = optimisedParameters[6],
  "RSS" = RSS[minimizedLocation]
)
return(output)
}

# Optimise the parameters by minimising the residuals with K simulated
numbers
# for the data points 1 to i, for i = 1,2,...,N where N is the number of
observations
incrementMinimize <-
function(K, obs_data, initial_parameters, prop = 0.1) {
  N <- nrow(obs_data)
  outputMatrix <- matrix(rep(NA, N * 6), nrow = N)
  cur_output <-
  minimizeRSS(K, obs_data, initial_parameters, prop)
  outputMatrix <- as.numeric(cur_output)
  return(outputMatrix)
}

# Return the optimised parameters by incrementing
minimised_data <- incrementMinimize(K, df, init_parameters)

# Repeat the incrementMinimize function
reps = t(replicate(n, incrementMinimize(K, df, initial_parameters)))

# Write reps to a csv file
write.csv(reps, "filepath.csv")

```

The output of this data within .R is as below where the values are "C", "Vm", "D" ("N"), "p", "q", "r" and "RSS" respectively. When the replicate() function is used the .csv output is n rows of the output where each values occupies one cell.

```
[1] 714.5896 7.0821 2.8491 8.9763e-01 3.8994e-02 6.3373e-02 2.8593
```

Appendix 4

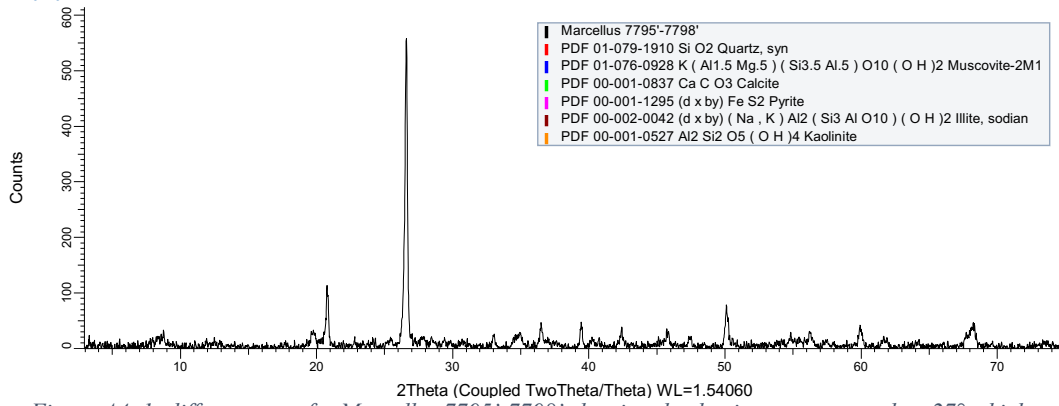


Figure A4. 1: diffractogram for Marcellus 7795'-7798' showing the dominant quartz peak at 27° which causes all other signals to be part of the noise.

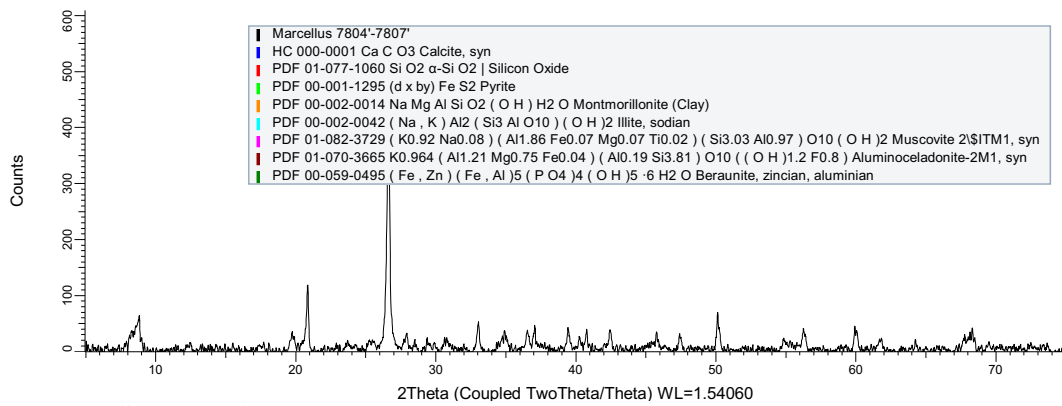


Figure A4. 2: diffractogram for Marcellus 7804'-7807' showing the dominant quartz peak at 27° which causes all other signals to be part of the noise.

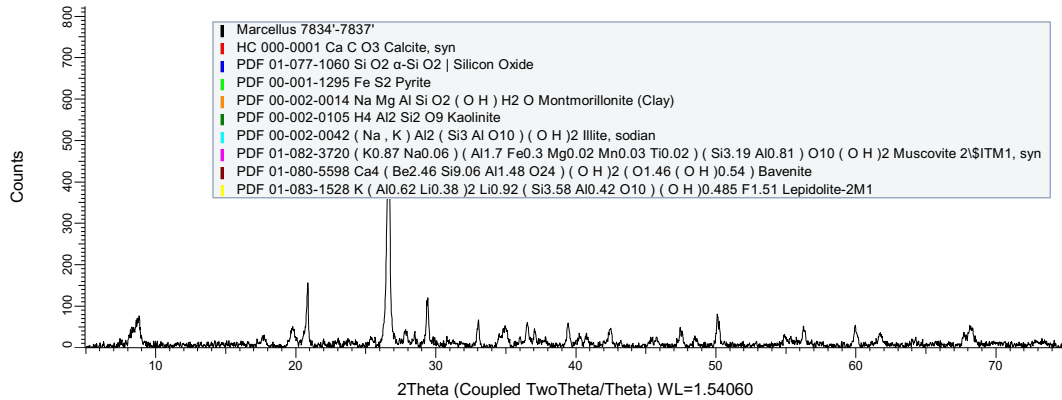


Figure A4. 3: diffractogram for Marcellus 7834'-7837' showing the dominant quartz peak at 27° which causes all other signals to be part of the noise.

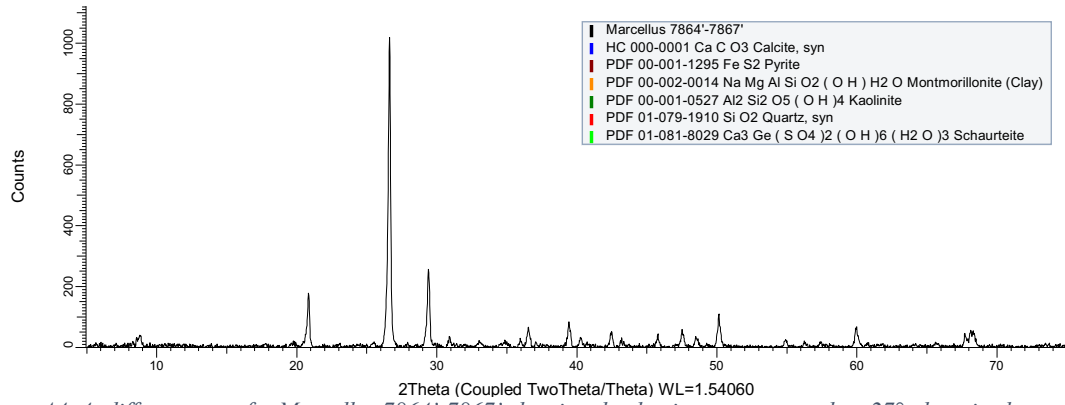


Figure A4. 4: diffractogram for Marcellus 7864'-7867' showing the dominant quartz peak at 27°, there is also a clear carbonate based peak at 29°. Both these dominant signals cause all other signals to be part of the noise.

Appendix 5

Appendix 5.1

| Sample ID | Mineral % by area | | | | | | | | | | | TOC% |
|----------------------------|-------------------|----------|--------|------------------------|--------|-----------|--------|--------|--------|----------|--|----------|
| | Calcite | Dolomite | Illite | Kaolinite and Geothite | Quartz | Muscovite | Albite | Pyrite | Oxides | Unknowns | | |
| Marcellus 7795'-7798' | 3.015 | 0.61 | 73.455 | 0.06 | 9.27 | 7.61 | 1.95 | 1.11 | 0.02 | 2.9 | | 6.876667 |
| Marcellus 7804'-7807' | 2.63 | 1.4 | 77.925 | 0.02 | 7.265 | 1.48 | 1.35 | 4.98 | 0.08 | 2.87 | | 7.22 |
| Marcellus 7834'-7837' | 5.13 | 0.27 | 76.93 | 0.03 | 8.54 | 1.455 | 1.29 | 3.57 | 0.055 | 2.73 | | 4.39 |
| Marcellus 7864'-7867' | 10.81 | 0.94 | 40.785 | 0.02 | 42.015 | 0.85 | 0.61 | 1.97 | 0.16 | 1.84 | | 6.11 |
| Utica 5800'-5803' (U1) | 21.45 | 3.45 | 49.94 | 0.06 | 9.11 | 8.825 | 1.18 | 0.81 | 0.985 | 4.19 | | 2.97 |
| Utica 5860'-5863' | 22.925 | 2.19 | 58.955 | 0.03 | 7.7 | 2.785 | 1.54 | 1.02 | 0.295 | 2.56 | | 2.33 |
| Utica 5869'-5872' | 28.055 | 1.89 | 49.925 | 0.03 | 11.23 | 3.275 | 2.52 | 1.34 | 0.375 | 1.36 | | 1.36 |
| Utica 5872'-5875' (1) (U2) | 14.095 | 1.47 | 58.885 | 0.04 | 6.9 | 11.345 | 1.14 | 1.22 | 0.245 | 4.66 | | 1.79 |
| Utica 5872'-5875' (2) | 19.745 | 2.52 | 55.275 | 0.05 | 11.46 | 3.795 | 2.73 | 0.96 | 0.525 | 2.94 | | 1.65 |
| Utica 5875'-5878' | 36.325 | 4.96 | 33.65 | 0.03 | 15.015 | 2.265 | 3.65 | 0.71 | 1.005 | 2.39 | | 1.27 |
| Utica 5899'-5902' (1) | 29.765 | 3.25 | 44.715 | 0.04 | 8.06 | 7.285 | 1.04 | 0.89 | 0.375 | 4.58 | | 1.2 |
| Utica 5899'-5902' (2) | 26.49 | 4.31 | 44.805 | 0.05 | 8.915 | 7.475 | 1.33 | 0.68 | 0.455 | 5.49 | | 1.38 |
| Utica 5899'-5902' (3) | 24.67 | 3.78 | 49.735 | 0.03 | 8.325 | 7.295 | 1.12 | 0.71 | 0.405 | 3.93 | | 1.46 |
| Utica 5998-6001' (1) | 51.09 | 2.87 | 28 | 0.02 | 14.16 | 0.335 | 0.77 | 0.94 | 0.405 | 1.41 | | 2.67 |
| Utica 5998-6001' (2) (U3) | 52.255 | 3.61 | 25.365 | 0.01 | 12.8 | 0.56 | 0.6 | 0.84 | 0.61 | 3.35 | | 4.33 |
| Utica 6102'-6103' (U4) | 69.64 | 9.92 | 10.015 | 0 | 4.615 | 0.755 | 0.04 | 0.39 | 1.415 | 3.21 | | 0.28 |
| Utica 6103'-6106' (U5) | 60.49 | 1.86 | 0.565 | 0 | 32.885 | 0.025 | 0 | 0.02 | 0.195 | 3.96 | | 0.27 |
| Utica 6102'-6106' (1) | 73.77 | 4.98 | 9.4 | 0.01 | 6.86 | 0.915 | 0.41 | 0.46 | 0.865 | 2.33 | | 0.39 |
| Utica 6102'-6106' (2) | 81.21 | 5.08 | 4.26 | 0.02 | 5.5 | 0.39 | 0.78 | 0.2 | 1.02 | 1.54 | | 0.18 |

| | | | | | | | | | | | |
|-----------------------------------|--------------|-------------|---------------|-------------|------------|--------------|------------|-------------|--------------|-------------|---|
| Bowland Above Marine Band | 1.605 | 0.26 | 75.365 | 5.17 | 5.6 | 7.325 | 1.5 | 2.55 | 0.045 | 0.58 | - |
| Bowland Marine Band | 24.965 | 0.33 | 48.43 | 0.06 | 23.055 | 0.205 | 0.56 | 1.85 | 0.075 | 0.47 | - |
| Bowland Below Marine Band | 11.845 | 0.19 | 66.495 | 0.13 | 17.13 | 0.385 | 0.89 | 2.51 | 0.065 | 0.36 | - |
| Marcellus Not Acid Treated | 2.475 | 1.23 | 81.42 | 0.01 | 6.555 | 1.46 | 1.03 | 5.14 | 0.09 | 0.59 | - |
| Marcellus Acid Treated | 0.15 | 0 | 86.325 | 0.12 | 4.925 | 1.58 | 0.77 | 5.17 | 0.03 | 0.93 | - |
| Utica Not Acid Treated | 71.33 | 4.14 | 1.355 | 0 | 22.365 | 0.06 | 0.03 | 0.18 | 0.3 | 0.24 | - |
| Utica Acid Treated | 47 | 3.85 | 1.22 | 0 | 47.05 | 0.055 | 0.03 | 0.1 | 0.475 | 0.22 | - |

Table A5.1. 1: all SEM MLA data for the samples analysed in this thesis

Appendix 5.2

Mineral BET

Quartz (SiO₂) is formed when there is silica present in excess, i.e. it has not been consumed by other silicate minerals. The Earth's crust becomes enriched in silica by magmatic differentiation of silica-rich igneous rocks, and continued accumulation when it is formed into quartz. Carbonates are defined by containing the compound CO₃ which reacts with carbonic acids to form carbonates. There are many different carbonates depending on what other elements they contain. They are formed by precipitation from aqueous solutions which forms the significant difference between clastic sediments (deposited) and carbonate sediments (precipitated). Clays are generally defined as hydrous phyllosilicates and are major components of many rocks. They are hugely varying in their composition depending on available elements at the time of formation. As well as this one type of clay, for example montmorillonite will have different end members such as calcium or sodium, aluminium or magnesium causing its composition to cover a range. There will be other minerals present more closely related to the depositional environment, or as derivatives of another mineral altered due to burial, uplift, weathering etc.

| | | |
|------------------------|---|---|
| Quartz | SiO ₂ | 0.041±0.002 m²/g (Meloni <i>et al.</i>, 2012) 2.26 m²/g (Pennell, 2016) |
| Muscovite | KAl ₂ (AlSi ₃ O ₁₀)(OH) ₂ | 2.3 m ² /g (Kini <i>et al.</i> , 2005) 2.36 ± 0.05 m ² /g (Lammers <i>et al.</i> , 2017) |
| Calcite | CaCO ₃ | 29.4-34.0 m ² /g (Ahsan, 1992) |
| Pyrite | FeS ₂ | 17.4 m ² /g (Chiang <i>et al.</i> , 1988) |
| Illite | K _{0.65} Al _{2.0} [Al _{0.65} Si _{3.35} O ₁₀](OH) ₂ | 67-100 m ² /g (Diamond and Kinter, 1956) 46 m ² /g (Macht <i>et al.</i> , 2010) |
| Kaolinte | Al ₂ (Si ₂ O ₅)(OH) ₄ | 7-30 m ² /g (Diamond and Kinter, 1956) 10.05 m ² /g (Pennell, 2016) |
| Montmorillonite | (Na,Ca) _{0.33} (Al,Mg) ₂ (Si ₄ O ₁₀)(OH) ₂ · nH ₂ O | 72 m ² /g (Macht <i>et al.</i> , 2010) 31.82-97.42 m ² /g (Pennell, 2016) |

Table A5.2. 1: BET surface area of various minerals which make up the majority of shales.

Appendix 6
Appendix 6.1



Figure A6.1. 1: U1 core sample of clay sized grain shale with planar lamination and no evidence of bioturbation at core scale. Cracks in the core are presumed to be as a result of drilling from depth, and transportation from the United States

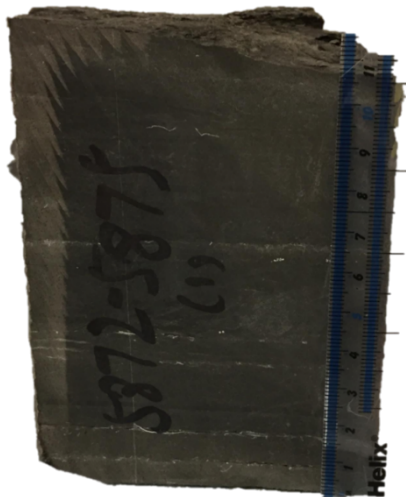


Figure A6.1. 2: U2 core sample of clay sized grain shale with predominantly planar lamination, there is some potential evidence of additional mineralogical input between laminations although cannot be confident that this has not been imbibed during the drilling process.



Figure A6.1. 3: U3 core sample of clay sized grain shale with a mix of planar and wavy laminations. There are visible pore network openings on the surface of the core and a mineralogical transition at 5.5 cm (on the ruler) from a darker to lighter mineral phase. Cracks in the core are presumed to be as a result of drilling from depth, and transportation from the United States.



Figure A6.1. 4: U4 core sample of clay sized grains which are in three phases from 2-3cm, 5-6cm and 10-11cm. These sections have wavy laminations and there is some additional mineral input in 5-6cm and 10-11cm from the underlying parts. From 3-5cm and 6-10cm there is a coarser grained section with some pore openings to the core surface, as well as some vein like mineral phases in wavy laminated layers.



Figure A6.1. 5: U5 core sample of very fine grained sample with no visible laminations, there's some isolated areas of darker sediment, juxtaposed by some more vein like mineral phase. From 3-6cm vertically, half-way across horizontally there is a separation in the lighter grey sediment with a column of darker sediment due to a mud injectite where it's been overpressured and flamed through the overlying section. The areas of lighter colour which are more round in nature are only on the surface and believed to be an artefact of the drilling process.

Appendix 6.2

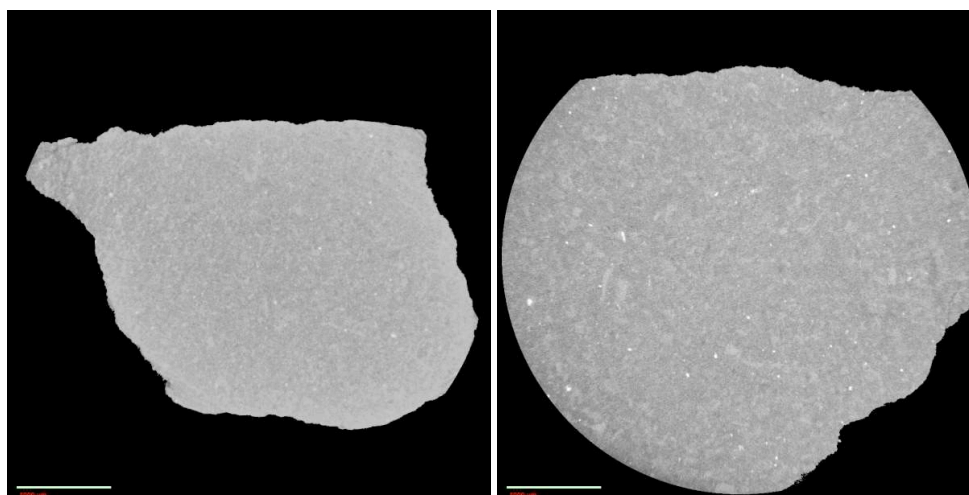


Figure A6.2. 1: reconstructed 2D slice CVT images of fresh samples of U1 (left) and U3 (right), with a 1000 μm scale bar.

Bibliography

Abell, A. B., Willis, K. L. and Lange, D. A. (1999) 'Mercury Intrusion Porosimetry and Image Analysis of Cement-Based Materials', *Journal of Colloid and Interface Science*, 211(1), pp. 39–44. doi: 10.1006/jcis.1998.5986.

Afsharpoor, A. and Javadpour, F. (2018) 'Pore Connectivity Between Organic and Inorganic Matter in Shale: Network Modeling of Mercury Capillary Pressure', *Transport in Porous Media*, 125(3), pp. 503–519. doi: 10.1007/s11242-018-1132-0.

Alemu, B. L., Agaard, P., Munz, I. A. and Skurtveit, E. (2011) 'Caprock interaction with CO₂: A laboratory study of reactivity of shale with supercritical CO₂ and brine', *Applied Geochemistry*. Elsevier Ltd, 26(12), pp. 1975–1989. doi: 10.1016/j.apgeochem.2011.06.028.

ALothman, Z. (2012) 'A Review: Fundamental Aspects of Silicate Mesoporous Materials', *Materials*, 5(12), pp. 2874–2902. doi: 10.3390/ma5122874.

Ambegaokar, V., Halperin, B. I. and Langer, J. S. (1971) 'Hopping Conductivity in Disordered Systems', *Physical Review B*, 4(8), pp. 2612–2620. doi: 10.1103/PhysRevB.4.2612.

Andrews, I. J. (2013) 'The Carboniferous Bowland Shale gas study: geology and resource estimation. British Geological Survey for Department of Energy and Climate Change, London, UK.', *British Geological Survey for Department of Energy and Climate Change, London, UK*. doi: 10.1080/10962247.2014.897270.

Anovitz, L. M. and Cole, D. R. (2015) 'Characterization and Analysis of Porosity and Pore Structures', *Reviews in Mineralogy and Geochemistry*, 80(1), pp. 61–164. doi: 10.2138/rmg.2015.80.04.

Appels, W. M., Wall, S. N., Barbour, S. L., Hendry, M. J., Nichol, C. F. and Chowdhury, S. R. (2017) 'Pyrite weathering in reclaimed shale overburden at an oil sands mine near Fort McMurray, Canada', *Mine Water and the Environment*. Springer Berlin Heidelberg, 36(4), pp. 479–494. doi: 10.1007/s10230-017-0454-4.

Arthur, M. (1994) 'Marine Shales: Depositional Mechanisms and Environments of Ancient Deposits', *Annual Review of Earth and Planetary Sciences*, 22(1), pp. 499–551. doi: 10.1146/annurev.earth.22.1.499.

Aukett, P. N. and Jessop, C. A. (1996) 'Assessment of Connectivity in Mixed Meso/Macroporous Solids Using Nitrogen Sorption', in, pp. 59–66. doi: 10.1007/978-1-4613-1375-5_6.

Auroux, A. (2013) *Calorimetry and Thermal Methods in Catalysis*. Edited by A. Auroux. Berlin, Heidelberg: Springer Berlin Heidelberg (Springer Series in Materials Science). doi: 10.1007/978-3-642-11954-5.

Avnir, D., Farin, D. and Pfeifer, P. (1983) 'Chemistry in noninteger dimensions between two and three. II. Fractal surfaces of adsorbents', *The Journal of Chemical Physics*, 79(7), pp. 3566–3571. doi: 10.1063/1.446211.

Avnir, D. and Jaroniec, M. (1989) 'An Isotherm Equation for Adsorption on Fractal Surfaces of Heterogeneous Porous Materials', *Langmuir*, 5(6), pp. 1431–1433. doi: 10.1021/la00090a032.

Balbuena, P. B. and Gubbins, K. E. (1992) 'Classification of adsorption behavior: simple fluids in pores

of slit-shaped geometry', *Fluid Phase Equilibria*, 76, pp. 21–35. doi: 10.1016/0378-3812(92)85075-J.

Balbuena, P. B. and Gubbins, K. E. (1993) 'Theoretical interpretation of adsorption behavior of simple fluids in slit pores', *Langmuir*, 9(7), pp. 1801–1814. doi: 10.1021/la00031a031.

Barsotti, E. *et al.* (2016) 'A review on capillary condensation in nanoporous media: Implications for hydrocarbon recovery from tight reservoirs', *Fuel*, 184, pp. 344–361. doi: 10.1016/j.fuel.2016.06.123.

Barsotti, E., Tan, S. P., Piri, M. and Chen, J. H. (2020) 'Capillary-condensation hysteresis in naturally-occurring nanoporous media', *Fuel*, 263, p. 116441. doi: 10.1016/j.fuel.2019.116441.

Bažant, Z. P. *et al.* (2014) 'Why Fracking Works', *Journal of Applied Mechanics*, 81(10). doi: 10.1115/1.4028192.

Beebe, R. A. and Young, D. M. (1954) 'Heats of Adsorption of Argon', *The Journal of Physical Chemistry*, 58(1), pp. 93–96. doi: 10.1021/j150511a023.

Behar, F., Beaumont, V. and De B. Pentead, H. L. (2001) 'Rock-Eval 6 Technology: Performances and Developments', *Oil & Gas Science and Technology*, 56(2), pp. 111–134. doi: 10.2516/ogst:2001013.

Betts, J. N. and Holland, H. D. (1991) 'The oxygen content of ocean bottom waters, the burial efficiency of organic carbon, and the regulation of atmospheric oxygen', *Palaeogeography, Palaeoclimatology, Palaeoecology*, 97(1–2), pp. 5–18. doi: 10.1016/0031-0182(91)90178-T.

Bielicki, J. M., Langenfeld, J. K., Tao, Z., Middleton, R. S., Menefee, A. H. and Clarens, A. F. (2018) 'The geospatial and economic viability of CO₂ storage in hydrocarbon depleted fractured shale formations', *International Journal of Greenhouse Gas Control*, 75(May), pp. 8–23. doi: 10.1016/j.ijggc.2018.05.015.

Blunt, M. (2010) 'Carbon dioxide storage', *Grantham Institute for climate change*, (4), pp. 1–12.

Brandani, S., Mangano, E. and Sarkisov, L. (2016) 'Net, excess and absolute adsorption and adsorption of helium', *Adsorption*, 22(2), pp. 261–276. doi: 10.1007/s10450-016-9766-0.

Brendow, K. (2003) 'Global oil shale issues and perspectives: Synthesis of the symposium on oil shale held in Tallinn (Estonia) on 18 and 19 November 2002', *Oil Shale*, 20(1), pp. 81–92.

Brinkley, S. A. (2016) 'Petroleum Geology of the Utica/Point Pleasant Play in Washington County, Ohio', *East Carolina University*.

van den Broek, M., Ramírez, A., Groenenberg, H., Neele, F., Viebahn, P., Turkenburg, W. and Faaij, A. (2010) 'Feasibility of storing CO₂ in the Utsira formation as part of a long term Dutch CCS strategy. An evaluation based on a GIS/MARKAL toolbox', *International Journal of Greenhouse Gas Control*, 4(2), pp. 351–366. doi: 10.1016/j.ijggc.2009.09.002.

Broekhoff, J. (1967) 'Studies on pore systems in catalysts X. Calculations of pore distributions from the adsorption branch of nitrogen sorption isotherms in the case of open cylindrical pores B. Applications', *Journal of Catalysis*, 9(1), pp. 15–27. doi: 10.1016/0021-9517(67)90175-3.

Broekhoff, J. (1968) 'Studies on pore systems in catalysts XIII. Pore distributions from the desorption branch of a nitrogen sorption isotherm in the case of cylindrical pores B. Applications', *Journal of Catalysis*, 10(4), pp. 377–390. doi: 10.1016/0021-9517(68)90153-X.

- Brunauer, S. and Emmett, P. H. (1935) 'The use of van der waals adsorption isotherms in determining the surface area of iron synthetic ammonia catalysts', *Journal of the American Chemical Society*, 57(9), pp. 1754–1755. doi: 10.1021/ja01312a503.
- Brunauer, S., Emmett, P. H. and Teller, E. (1938) 'Adsorption of Gases in Multimolecular Layers', *Journal of the American Chemical Society*, 60(2), pp. 309–319. doi: 10.1021/ja01269a023.
- Brunauer, S., Skalny, J. and Bodor, E. (1969) 'Adsorption on nonporous solids', *Journal of Colloid and Interface Science*, 30(4), pp. 546–552. doi: 10.1016/0021-9797(69)90423-8.
- Burnett, J. W. (2013) 'Hydraulic fracturing and U.S. water policy abstract', *AGH Drilling, Oil, Gas*, 30(1), p. 311. doi: 10.7494/drill.2013.30.1.311.
- Busch, A., Alles, S., Gensterblum, Y., Prinz, D., Dewhurst, D. N., Raven, M. D., Stanjek, H. and Krooss, B. M. (2008) 'Carbon dioxide storage potential of shales', *International Journal of Greenhouse Gas Control*, 2(3), pp. 297–308. doi: 10.1016/j.ijggc.2008.03.003.
- Cao, T., Song, Z., Wang, S. and Xia, J. (2015) 'A comparative study of the specific surface area and pore structure of different shales and their kerogens', *Science China Earth Sciences*, 58(4), pp. 510–522. doi: 10.1007/s11430-014-5021-2.
- Chalmers, G. R. L. and Bustin, R. M. (2015) 'Porosity and pore size distribution of deeply-buried fine-grained rocks: Influence of diagenetic and metamorphic processes on shale reservoir quality and exploration', *Journal of Unconventional Oil and Gas Resources*, 12, pp. 134–142. doi: 10.1016/j.juogr.2015.09.005.
- Charmas, B. and Skubiszewska-Zięba, J. (2017) 'Application of differential scanning calorimetry to study porous structure of hydrothermally modified silicas', *Journal of Thermal Analysis and Calorimetry*, 129(1), pp. 23–32. doi: 10.1007/s10973-017-6126-6.
- Chen, L., Lu, Y., Jiang, S., Li, J., Guo, T. and Luo, C. (2015) 'Heterogeneity of the lower silurian longmaxi marine shale in the southeast sichuan basin of China', *Marine and Petroleum Geology*. Elsevier Ltd, 65, pp. 232–246. doi: 10.1016/j.marpetgeo.2015.04.003.
- Chen, S., Zhu, Y., Wang, H., Liu, H., Wei, W. and Fang, J. (2011) 'Shale gas reservoir characterisation: A typical case in the southern Sichuan Basin of China', *Energy*. Elsevier Ltd, 36(11), pp. 6609–6616. doi: 10.1016/j.energy.2011.09.001.
- Chen, Y., Wei, L., Mastalerz, M. and Schimmelmann, A. (2015) 'The effect of analytical particle size on gas adsorption porosimetry of shale', *International Journal of Coal Geology*, 138, pp. 103–112. doi: 10.1016/j.coal.2014.12.012.
- Chen, Y., Jiang, C., Yin, G., Zhang, D., Xing, H. and Wei, A. (2019) 'Permeability evolution under true triaxial stress conditions of Longmaxi shale in the Sichuan Basin, Southwest China', *Powder Technology*, 354, pp. 601–614. doi: 10.1016/j.powtec.2019.06.044.
- Chen, Z., Lavoie, D. and Malo, M. (2014) *Geological characteristics and petroleum resource assessment of Utica Shale, Quebec, Canada, Geological Survey of Canada, Open File*. doi: 10.4095/293793.

Colton, G. W. (1961) 'Geologic Summary of the Appalachian Basin, With Reference To the Subsurface Disposal of Radioactive Waste Solutions', (June).

Comisky, J. T., Santiago, M., McCollom, B., Buddhala, A. and Newsham, K. E. (2011) 'Sample Size Effects on the Application of Mercury Injection Capillary Pressure for Determining the Storage Capacity of Tight Gas and Oil Shales', in *All Days*. SPE. doi: 10.2118/149432-MS.

Corporation, L. (2010) 'Moisture, Volatile Matter, Ash, and Fixed Carbon Determination-Solid Fuel Characterization Measurements in Coke', *Organic Application Note, Form 203-821-381, LECO Corporation, St. Joseph, Mich, USA*.

Cracknell, R. F., Gubbins, K. E., Maddox, M. and Nicholson, D. (1995) 'Modeling Fluid Behavior in Well-Characterized Porous Materials', *Accounts of Chemical Research*, 28(7), pp. 281–288. doi: 10.1021/ar00055a001.

Curtis, C. D. (1980) 'Diagenetic alteration in black shales.', *Journal of the Geological Society*, 137(2), pp. 189–194. doi: 10.1144/gsjgs.137.2.0189.

Curtis, M. E. (2010) 'Structural Characterization of Gas Shales on the Micro- and Nano-Scales', in *All Days*. SPE. doi: 10.2118/137693-MS.

Curtis, M. E., Cardott, B. J., Sondergeld, C. H. and Rai, C. S. (2012) 'Development of organic porosity in the Woodford Shale with increasing thermal maturity', *International Journal of Coal Geology*, 103, pp. 26–31. doi: 10.1016/j.coal.2012.08.004.

Dalhoff, F. *et al.* (2011) 'CCS demo Denmark: The vedsted case', *Energy Procedia*. Elsevier, 4, pp. 4704–4710. doi: 10.1016/j.egypro.2011.02.432.

Dang, S. (2017) 'A New Approach to Measure Organic Density', 17(4), pp. 341–359.

Dawson, J. C. and Le, H. Van (2005) 'Fracturing Fluids And Methods of Making And Using Same', *United States Patent*, 2(12).

Desouza, A. and Monson, P. A. (2021) 'Modeling fluids confined in three-dimensionally ordered mesoporous carbons', *Adsorption*, 27(2), pp. 253–264. doi: 10.1007/s10450-020-00285-6.

Diamond, S. and Earl B. Kinter (1956) 'Surface Areas of Clay Minerals as Derived from Measurements of Glycerol Retention', *Clays and Clay Minerals*, 5(1), pp. 334–347. doi: 10.1346/CCMN.1956.0050128.

Dooley, J. J., Dahowski, R. T. and Davidson, C. L. (2009) 'The potential for increased atmospheric CO₂ emissions and accelerated consumption of deep geologic CO₂ storage resources resulting from the large-scale deployment of a CCS-enabled unconventional fossil fuels industry in the U.S.', *International Journal of Greenhouse Gas Control*, 3(6), pp. 720–730. doi: 10.1016/j.ijggc.2009.08.004.

Dræge, A., Jakobsen, M. and Johansen, T. A. (2006) 'Rock physics modelling of shale diagenesis', *Petroleum Geoscience*, 12(1), pp. 49–57. doi: 10.1144/1354-079305-665.

Dusseault, M. B. (2004) 'Coupled Thermo-Mechano-Chemical Processes in Shales: The Petroleum Borehole', in pp. 573–580. doi: 10.1016/S1571-9960(04)80101-0.

Dutta, N. C. (1985) 'SHALE COMPACTION, BURIAL DIAGENESIS. In Thermal Modeling in Sedimentary Basins', *1st IFP Exploration Research Conference*, Vol. 44, p. 149.

Edlmann, K., Haszeldine, S. and McDermott, C. I. (2013) 'Experimental investigation into the sealing capability of naturally fractured shale caprocks to supercritical carbon dioxide flow', *Environmental Earth Sciences*, 70(7), pp. 3393–3409. doi: 10.1007/s12665-013-2407-y.

EL-Sayed, S. A. and Mostafa, M. E. (2014) 'Analysis of Grain Size Statistic and Particle Size Distribution of Biomass Powders', *Waste and Biomass Valorization*, 5(6), pp. 1005–1018. doi: 10.1007/s12649-014-9308-5.

Emmett, P. H. and Brunauer, S. (1937) 'The Use of Low Temperature van der Waals Adsorption Isotherms in Determining the Surface Area of Iron Synthetic Ammonia Catalysts', *Journal of the American Chemical Society*, 59(8), pp. 1553–1564. doi: 10.1021/ja01287a041.

Engelder, T. and Lash, G. G. (2008) 'Marcellus Shale play's vast resource potential creating stir in Appalachia', *American Oil and Gas Reporter*, 51(May), pp. 76–87.

Esparza, J. M., Ojeda, M. L., Campero, A., Dominguez, A., Kornhauser, I., Rojas, F., Vidales, A. M., Lopez, R. H. and Zgrablich, G. (2004) 'N₂ sorption scanning behavior of SBA-15 porous substrates', *Colloids and Surfaces A: Physicochemical and Engineering Aspects*, 241(1–3), pp. 35–45. doi: 10.1016/j.colsurfa.2004.04.010.

Farber, L. (2019) 'Microstructure and Mechanical Properties of Granules Formed in High Shear Wet Granulation', in *Handbook of Pharmaceutical Wet Granulation*. Elsevier, pp. 37–88. doi: 10.1016/B978-0-12-810460-6.00003-8.

Fathi, E. and Akkutlu, I. Y. (2009) 'Matrix heterogeneity effects on gas transport and adsorption in coalbed and shale gas reservoirs', *Transport in Porous Media*, 80(2), pp. 281–304. doi: 10.1007/s11242-009-9359-4.

Fleury, M. and Romero-Sarmiento, M. (2016) 'Characterization of shales using T1-T2 NMR maps', *Journal of Petroleum Science and Engineering*. Elsevier, 137, pp. 55–62. doi: 10.1016/j.petrol.2015.11.006.

Fox, J.P., Jackson, D.E., Sakaji, R.H., Daughton, C.G. and Selleck, R. E. (1980) 'Spent Shale as a Control Technology for Oil Shale Retort Waterle', *Energy and Environment Division 1979 Annual Report*.

Franco, N., Kalkreuth, W. and Do Carmo Ruaro Peralba, M. (2010) 'Geochemical characterization of solid residues, bitumen and expelled oil based on steam pyrolysis experiments from Irati oil shale, Brazil: A preliminary study', *Fuel*. Elsevier Ltd, 89(8), pp. 1863–1871. doi: 10.1016/j.fuel.2009.11.018.

Gabbott, P. (2008) *Principles and Applications of Thermal Analysis*. Edited by P. Gabbott. Oxford, UK: Blackwell Publishing Ltd. doi: 10.1002/9780470697702.

Giesche, H. (2006) 'Mercury porosimetry: A general (practical) overview', *Particle and Particle Systems Characterization*, 23(1), pp. 9–19. doi: 10.1002/ppsc.200601009.

Glueckauf, E. (1955) 'Theory of chromatography.', *Transactions of the Faraday Society*.

Godec, M., Koperna, G., Petrusak, R. and Oudinot, A. (2013) 'Potential for enhanced gas recovery

and CO₂ storage in the Marcellus Shale in the Eastern United States', *International Journal of Coal Geology*. Elsevier B.V., 118, pp. 95–104. doi: 10.1016/j.coal.2013.05.007.

Godec, M., Koperna, G., Petrusak, R. and Oudinot, A. (2014) 'Enhanced gas recovery and CO₂ storage in gas shales: A summary review of its status and potential', *Energy Procedia*. Elsevier B.V., 63, pp. 5849–5857. doi: 10.1016/j.egypro.2014.11.618.

Gómez-Gualdrón, D. A., Moghadam, P. Z., Hupp, J. T., Farha, O. K. and Snurr, R. Q. (2016) 'Application of Consistency Criteria To Calculate BET Areas of Micro- And Mesoporous Metal–Organic Frameworks', *Journal of the American Chemical Society*, 138(1), pp. 215–224. doi: 10.1021/jacs.5b10266.

Good, R. J. and Mikhail, R. S. (1981) 'The contact angle in mercury intrusion porosimetry', *Powder Technology*, 29(1), pp. 53–62. doi: 10.1016/0032-5910(81)85004-8.

Gor, G. Y., Thommes, M., Cychosz, K. A. and Neimark, A. V. (2012) 'Quenched solid density functional theory method for characterization of mesoporous carbons by nitrogen adsorption', *Carbon*, 50(4), pp. 1583–1590. doi: 10.1016/j.carbon.2011.11.037.

Gosden, E. and Clancy, R. (2013) *Shale gas in northern England could meet Britain's gas needs for 40 years*, *The Telegraph*. Available at: <https://www.telegraph.co.uk/finance/newsbysector/energy/10145414/Shale-gas-in-northern-England-could-meet-Britains-gas-needs-for-40-years.html>.

Gregg, S. J. and Sing, K. S. W. (1982) 'Adsorption, Surface Area and Porosity', *Academic Press, London*. doi: 10.1002/bbpc.19820861019.

Grillet, Y., Rouquerol, F. and Rouquerol, J. (1979) 'Two-dimensional freezing of nitrogen or argon on differently graphitized carbons', *Journal of Colloid and Interface Science*, 70(2), pp. 239–244. doi: 10.1016/0021-9797(79)90029-8.

Grim, R. E. (1951) 'The depositional environment of red and green shales', 21(4), pp. 226–232.

Gross, D., Sachsenhofer, R. F., Bechtel, A., Pytlak, L., Rupprecht, B. and Wegner, E. (2015) 'Organic geochemistry of Mississippian shales (Bowland Shale Formation) in central Britain: Implications for depositional environment, source rock and gas shale potential', *Marine and Petroleum Geology*, 59, pp. 1–21. doi: 10.1016/j.marpetgeo.2014.07.022.

Hall, M. R., Rigby, S. P., Dim, P., Bateman, K., Mackintosh, S. J. and Rochelle, C. A. (2016) 'Post-CO₂ injection alteration of the pore network and intrinsic permeability tensor for a Permo-Triassic sandstone', *Geofluids*, 16(2), pp. 249–263. doi: 10.1111/gfl.12146.

Harding, F. C., James, A. T. and Robertson, H. E. (2018) 'The engineering challenges of CO₂ storage', *Proceedings of the Institution of Mechanical Engineers, Part A: Journal of Power and Energy*, 232(1), pp. 17–26. doi: 10.1177/0957650918756542.

Harper, J. A. (1999) 'Geology of Pennsylvania', *Scientific American*, 7(13), pp. 99–99. doi: 10.1038/scientificamerican12131851-99c.

Harrison, A. L., Jew, A. D., Dustin, M. K., Thomas, D. L., Joe-Wong, C. M., Bargar, J. R., Johnson, N., Brown Jr, G. E. and Maher, K. (2017) 'Element release and reaction-induced porosity alteration

during shale-hydraulic fracturing fluid interactions', *Applied Geochemistry*. Elsevier Ltd, 82, pp. 47–62. doi: 10.1016/j.apgeochem.2017.05.001.

Hemes, S., Desbois, G., Urai, J. L., Schröppel, B. and Schwarz, J. O. (2015) 'Multi-scale characterization of porosity in Boom Clay (HADES-level, Mol, Belgium) using a combination of X-ray μ -CT, 2D BIB-SEM and FIB-SEM tomography', *Microporous and Mesoporous Materials*, 208, pp. 1–20. doi: 10.1016/j.micromeso.2015.01.022.

Herzog, H. and Golomb, D. (2004) 'Carbon Capture and Storage from Fossil Fuel Use', *Encyclopedia of Energy*, 1, pp. 277–287. doi: 10.1016/b0-12-176480-x/00422-8.

Hickman, John; Eble, Cortland; Riley, Ronald A.; Erenpreiss, Matthew; Carter, Kristin M.; Harper, John A.; Dunst, Brian; Smith, Langhorne "Taury"; Cooney, Michele L.; Soeder, Daniel; Metzger, Garrecht; Moore, Jessica; Hohn, Michael E.; Pool, Susan; Saucer, D. G. (2015) 'A Geologic Play Book for Utica Shale Appalachian Basin Exploration', *Appalachian Oil and Natural Gas Research Consortium*. 2. Available at: <https://researchrepository.wvu.edu/aongrc/2>.

HM Government (2013) 'UK Oil and Gas: Business and Government Action', (March), pp. 1–53. Available at:

https://www.gov.uk/government/uploads/system/uploads/attachment_data/file/175480/bis-13-748-uk-oil-and-gas-industrial-strategy.pdf.

Hoffman, A., Olsson, G. and Lindström, A. (2014) *Shale Gas and Hydraulic Fracturing Framing the Water Issue*. Available at: www.siwi.org.

Holmes, R., Rupp, E. C., Vishal, V. and Wilcox, J. (2017) 'Selection of Shale Preparation Protocol and Outgas Procedures for Applications in Low-Pressure Analysis', *Energy & Fuels*, 31(9), pp. 9043–9051. doi: 10.1021/acs.energyfuels.7b01297.

Horsrud, P., Sønsteb \emptyset , E. F. and Bøe, R. (1998) 'Mechanical and petrophysical properties of North Sea shales', *International Journal of Rock Mechanics and Mining Sciences*, 35(8), pp. 1009–1020. doi: 10.1016/S0148-9062(98)00162-4.

Hossain, M. E. and Islam, M. R. (2018) 'Directional and Horizontal Drilling Problems', *Drilling Engineering Problems and Solutions*, pp. 497–547. doi: 10.1002/9781118998632.ch10.

Hough, E., Vane, C. H., Smith, N. J. and Moss-Hayes, V. L. (2014) 'The Bowland Shale in the Roosecote Borehole of the Lancaster Fells sub-Basin, Craven Basin, UK: a Potential UK Shale gas Play?', in *Day 1 Tue, February 25, 2014*. SPE. doi: 10.2118/167696-MS.

Ishikiryama, K. and Todoki, M. (1995) 'Pore Size Distribution Measurements of Silica Gels by Means of Differential Scanning Calorimetry', *Journal of Colloid and Interface Science*, 171(1), pp. 103–111. doi: 10.1006/jcis.1995.1155.

Isirikyan, A. A. and Kiselev, A. V. (1961) 'The absolute adsorption isotherms of vapors of nitrogen, benzene and n-hexane, and the heats of adsorption of benzene and n-hexane on graphitized carbon blacks. I. Graphitized thermal blacks', *The Journal of Physical Chemistry*, 65(4), pp. 601–607. doi: 10.1021/j100822a004.

Jew, A. D., Dustin, M. K., Harrison, A. L., Joe-Wong, C. M., Thomas, D. L., Maher, K., Brown Jr, G. E. and Barger, J. R. (2017) 'Impact of Organics and Carbonates on the Oxidation and Precipitation of Iron during Hydraulic Fracturing of Shale', *Energy and Fuels*, 31(4), pp. 3643–3658. doi:

10.1021/acs.energyfuels.6b03220.

Ji, L., Zhang, T., Milliken, K. L., Qu, J. and Zhang, X. (2012) 'Experimental investigation of main controls to methane adsorption in clay-rich rocks', *Applied Geochemistry*, 27(12), pp. 2533–2545. doi: 10.1016/j.apgeochem.2012.08.027.

Ji, W., Song, Y., Jiang, Z., Meng, M., Liu, Q., Chen, L., Wang, P., Gao, F. and Huang, H. (2016) 'Fractal characteristics of nano-pores in the Lower Silurian Longmaxi shales from the Upper Yangtze Platform, south China', *Marine and Petroleum Geology*, 78, pp. 88–98. doi: 10.1016/j.marpetgeo.2016.08.023.

Ji, W., Hao, F., Schulz, H. M., Song, Y. and Tian, J. (2019) 'The architecture of organic matter and its pores in highly mature gas shales of the lower Silurian Longmaxi Formation in the upper Yangtze platform, south China', *AAPG Bulletin*, 103(12), pp. 2909–2942. doi: 10.1306/04101917386.

Jiang, Y. and Bhattacharyya, D. (2016) 'Process modeling of direct coal-biomass to liquids (CBTL) plants with shale gas utilization and CO₂ capture and storage (CCS)', *Applied Energy*. Elsevier Ltd, 183, pp. 1616–1632. doi: 10.1016/j.apenergy.2016.09.098.

Josh, M., Esteban, L., Delle Piane, C., Sarout, J., Dewhurst, D. N. and Clennell, M. B. (2012) 'Laboratory characterisation of shale properties', *Journal of Petroleum Science and Engineering*. Elsevier B.V., 88–89, pp. 107–124. doi: 10.1016/j.petrol.2012.01.023.

Kang, S. M., Fathi, E., Ambrose, R. J., Akkutli, I. Y. and Sigal, R. F. (2011) 'Carbon Dioxide Storage Capacity of Organic-Rich Shales', *SPE Journal*, 16(04), pp. 842–855. doi: 10.2118/134583-PA.

Kargbo, D. M., Wilhelm, R. G. and Campbell, D. J. (2010) 'Natural gas plays in the marcellus shale: Challenges and potential opportunities', *Environmental Science and Technology*, 44(15), pp. 5679–5684. doi: 10.1021/es903811p.

Katsube, T. J. and Williamson, M. A. (1994) 'Effects of diagenesis on shale nano-pore structure and implications for sealing capacity', *Clay Minerals*, 29(4), pp. 451–461. doi: 10.1180/claymin.1994.029.4.05.

Kaufman, G. M. (1993) 'Statistical Issues in the Assessment of Undiscovered Oil and Gas Resources', *The Energy Journal*, 14(1). doi: 10.5547/issn0195-6574-ej-vol14-no1-8.

Keating, G. N., Middleton, R. S., Viswanathan, H. S., Stauffer, P. H. and Pawar, R. J. (2011) 'How storage uncertainty will drive CCS infrastructure', *Energy Procedia*. Elsevier, 4(2010), pp. 2393–2400. doi: 10.1016/j.egypro.2011.02.132.

Keil R. G., Tsamakis, E., Fuh, C. B., Giddings, J. C. and Hedges, J. I. (1994) 'Mineralogic controls on the organic composition of coastal marine sediments: Hydrodynamic separation using SPLITT-fractionation', *Geochimica et Cosmochimica Acta*, 58(2), pp. 879-893.

Keller, L. M., Schuetzm P., Erni, R., Rossell, M. D., Lucas, F., Gasser, P. and Holzer, L. (2013) 'Characterization of multi-scale microstructural features in Opalinus Clay', *Microporous and Mesoporous Materials*, 170, pp. 83–94. doi: 10.1016/j.micromeso.2012.11.029.

Kenomore, M., Hassan, M., Dhakal, H. and Shah, A. (2017) 'Total organic carbon evaluation of the Bowland Shale Formation in the Upper Bowland of the Widmerpool Gulf', *Journal of Petroleum*

Science and Engineering, 150, pp. 137–145. doi: 10.1016/j.petrol.2016.11.040.

Kenomore, M. (2020) *Shale Gas Characterization and Production Forecasting: A Case Study on UK Bowland Shale and the US Barnett Shale*. University of Portsmouth.

Ketcham, R. A. and Carlson, W. D. (2001) 'Acquisition, optimization and interpretation of X-ray computed tomographic imagery: applications to the geosciences', *Computers & Geosciences*, 27(4), pp. 381–400. doi: 10.1016/S0098-3004(00)00116-3.

Khan, C., Amin, R. and Madden, G. (2013) 'Carbon dioxide injection for enhanced gas recovery and storage (reservoir simulation)', *Egyptian Journal of Petroleum*. Egyptian Petroleum Research Institute, 22(2), pp. 225–240. doi: 10.1016/j.ejpe.2013.06.002.

Kim, T. H., Cho, J. and Lee, K. S. (2017) 'Evaluation of CO₂ injection in shale gas reservoirs with multi-component transport and geomechanical effects', *Applied Energy*, 190, pp. 1195–1206. doi: 10.1016/j.apenergy.2017.01.047.

King, G. E. (2010) 'Thirty Years of Gas Shale Fracturing: What Have We Learned?', in *All Days*. SPE. doi: 10.2118/133456-MS.

Kini, K. A., Manser, R. M. and Joy, A. S. (2005) 'Surface area of silicate minerals by the B.E.T. method using the adsorption of xenon at -78.deg.', *The Journal of Physical Chemistry*, 72(6), pp. 2127–2129. doi: 10.1021/j100852a042.

Kissinger, A., Helmig, R., Ebigbo, A., Class, H., Lange, T., Sauter, M., Heitfeld, M., Klünker, J. and Jahnke, W. (2013) 'Hydraulic fracturing in unconventional gas reservoirs: Risks in the geological system, part 2: Modelling the transport of fracturing fluids, brine and methane', *Environmental Earth Sciences*, 70(8), pp. 3855–3873. doi: 10.1007/s12665-013-2578-6.

Kumar, K. V. *et al.* (2011) 'A site energy distribution function from Toth isotherm for adsorption of gases on heterogeneous surfaces', *Physical Chemistry Chemical Physics*, 13(13), p. 5753. doi: 10.1039/c0cp00902d.

Kuuskräa; S. H. Stevens; D.Moodhe, A. (2013) 'Technically recoverable shale oil and shale gas resources: An assessment of 137 shale formations in 41 countries outside the United States: Washington, DC', *US Energy Information Administration*, (June), p. 76.

Lafargue, E., Marquis, F. and Pillot, D. (1998) 'Rock-Eval 6 applications in hydrocarbon exploration, production, and soil contamination studies', *Revue de l'Institut Français du Pétrole*, 53(4), pp. 421–437. doi: 10.2516/ogst:1998036.

Lammers, K., Smith, M. M. and Carroll, S. A. (2017) 'Muscovite dissolution kinetics as a function of pH at elevated temperature', *Chemical Geology*. Elsevier, 466(January), pp. 149–158. doi: 10.1016/j.chemgeo.2017.06.003.

Landers, J., Gor, G. Y. and Neimark, A. V. (2013) 'Density functional theory methods for characterization of porous materials', *Colloids and Surfaces A: Physicochemical and Engineering Aspects*, 437, pp. 3–32. doi: 10.1016/j.colsurfa.2013.01.007.

Landry, M. R. (2005) 'Thermoporometry by differential scanning calorimetry: Experimental considerations and applications', *Thermochimica Acta*, 433(1–2), pp. 27–50. doi:

10.1016/j.tca.2005.02.015.

Lange, T., Sauter, M., Heitfeld, M., Schetelig, K., Brosig, K., Jahnke, W., Kissinger, A., Helmig, R., Ebigbo, A. and Class, H. (2013) 'Hydraulic fracturing in unconventional gas reservoirs: Risks in the geological system part 1', *Environmental Earth Sciences*, 70(8), pp. 3839–3853. doi: 10.1007/s12665-013-2803-3.

Langmuir, I. (1918) 'The Evaporation of Small Spheres', *Physical Review*, 12(5), pp. 368–370. doi: 10.1103/PhysRev.12.368.

Langmuir, I. (1916) 'The Evaporation, Condensation and Reflection of Molecules and the Mechanism of Adsorption', *Physical Review*, 8(2), pp. 149–176. doi: 10.1103/PhysRev.8.149.

Lastoskie, C., Gubbins, K. E. and Quirke, N. (1993) 'Pore size distribution analysis of microporous carbons: a density functional theory approach', *The Journal of Physical Chemistry*, 97(18), pp. 4786–4796. doi: 10.1021/j100120a035.

Latham, M. A. (2011) 'The BP Deepwater Horizon: A Cautionary Tale for CCS, Hydrofracking, Geoengineering and Other Emerging Technologies with Environmental and Human Health Risks.', *Wm. & Mary Env'tl. L. & Pol'y*, 36, p. 31.

Laughrey, C. D., Billman, D. A. and Canich, M. R. (2004) 'Petroleum geology and geochemistry of the Council Run gas field, north central Pennsylvania', *AAPG Bulletin*, 88(2), pp. 213–239. doi: 10.1306/10060301104.

Lavoie, D., Rivard, C., Lefebvre, R., Séjourné, S., Thériault, R., Duchesne, M. J., Ahad, J. M., Wang, B., Benoît, N. and Lamontagne, C. (2014) 'The Utica Shale and gas play in southern Quebec: Geological and hydrogeological syntheses and methodological approaches to groundwater risk evaluation', *International Journal of Coal Geology*. Elsevier B.V., 126, pp. 77–91. doi: 10.1016/j.coal.2013.10.011.

Lehr, J. H., Keeley, J. and Kingery, T. B. (eds) (2016) *Alternative Energy and Shale Gas Encyclopedia*. Hoboken, NJ, USA: John Wiley & Sons, Inc. doi: 10.1002/9781119066354.

Levitt, M. H. (2002) 'Spin dynamics: basics of nuclear magnetic resonance.', *John Wiley & Sons*, 40(12), pp. 800–800. doi: 10.1002/mrc.1092.

Li, T., Tian, H., Chen, J. and Cheng, L. (2016) 'Application of low pressure gas adsorption to the characterization of pore size distribution of shales: An example from Southeastern Chongqing area, China', *Journal of Natural Gas Geoscience*, 1(3), pp. 221–230. doi: 10.1016/j.jnggs.2016.07.001.

Liu, F., Ellett, K., Xiao, Y. and Rupp, J. A. (2013) 'Assessing the feasibility of CO₂ storage in the New Albany Shale (Devonian-Mississippian) with potential enhanced gas recovery using reservoir simulation', *International Journal of Greenhouse Gas Control*. Elsevier Ltd, 17, pp. 111–126. doi: 10.1016/j.ijggc.2013.04.018.

Liu, J., Xie, L., Elsworth, D. and Gan, Q. (2019) 'CO₂/CH₄ Competitive Adsorption in Shale: Implications for Enhancement in Gas Production and Reduction in Carbon Emissions', *Environmental Science & Technology*, 53(15), pp. 9328–9336. doi: 10.1021/acs.est.9b02432.

Liu, J., Xie, L., Yao, Y., Gan, Q., Zhao, P. and Du, L. (2019) 'Preliminary Study of Influence Factors and Estimation Model of the Enhanced Gas Recovery Stimulated by Carbon Dioxide Utilization in Shale',

ACS Sustainable Chemistry & Engineering, 7(24), pp. 20114–20125. doi: 10.1021/acssuschemeng.9b06005.

Lowell, S. (1980) 'Continuous scan mercury porosimetry and the pore potential as a factor in porosimetry hysteresis', *Powder Technology*, 25(1), pp. 37–43. doi: 10.1016/0032-5910(80)87006-9.

Lowell, S. and Shields, Joan E. (1981) 'Hysteresis, entrapment, and wetting angle in mercury porosimetry', *Journal of Colloid And Interface Science*, 83(1), pp. 273–278. doi: 10.1016/0021-9797(81)90032-1.

Lowell, S. and Shields, J. E. (1981) 'Influence of contact angle on hysteresis in mercury porosimetry', *Journal of Colloid And Interface Science*, 80(1), pp. 192–196. doi: 10.1016/0021-9797(81)90175-2.

Luft, S. J. (1971) *Geologic map of part of the Covington quadrangle, northern Kentucky*. doi: 10.3133/gq955.

Lynch, F. L. (1997) 'Frio Shale Mineralogy and the Stoichiometry of the Smectite-to-Illite Reaction: The Most Important Reaction in Clastic Sedimentary Diagenesis', *Clays and Clay Minerals*, 45(5), pp. 618–631. doi: 10.1346/CCMN.1997.0450502.

Ma, L., Fauchille, A. L., Dowey, P. J., Pilz, F. F., Courtois, L., Taylor, K. G. and Lee, P. D. (2017) 'Correlative multi-scale imaging of shales: a review and future perspectives', *Geological Society, London, Special Publications*, 454(1), pp. 175–199. doi: 10.1144/SP454.11.

Ma, L., Taylor, K. G., Dowey, P. J., Courtois, L., Gholinia, A. and Lee, P. D. (2017) 'Multi-scale 3D characterisation of porosity and organic matter in shales with variable TOC content and thermal maturity: Examples from the Lublin and Baltic Basins, Poland and Lithuania', *International Journal of Coal Geology*, 180, pp. 100–112. doi: 10.1016/j.coal.2017.08.002.

Ma, L., Dowey, P. J., Rutter, E., Taylor, K. G. and Lee, P. D. (2019) 'A novel upscaling procedure for characterising heterogeneous shale porosity from nanometer-to millimetre-scale in 3D', *Energy*, 181, pp. 1285–1297. doi: 10.1016/j.energy.2019.06.011.

Macht, F., Totsche, K. U., Eusterhues, K., Pronk, G. and Gilkes, R. (2010) 'Topography and surface properties of clay minerals analyzed by atomic force microscopy', (August), pp. 206–209.

Maddox, M. W. and Gubbins, K. E. (1995) 'Molecular Simulation of Fluid Adsorption in Buckytubes', *Langmuir*, 11(10), pp. 3988–3996. doi: 10.1021/la00010a059.

Mahnke, M. and Mögel, H. J. (2003) 'Fractal analysis of physical adsorption on material surfaces', *Colloids and Surfaces A: Physicochemical and Engineering Aspects*, 216(1–3), pp. 215–228. doi: 10.1016/S0927-7757(02)00577-0.

Mandelbrot, B. B. (1982) 'The Fractal Geometry of Nature', *American Journal of Physics*, pp. 286–287. doi: 10.1119/1.13295.

Mason, G. (1982) 'The effect of pore space connectivity on the hysteresis of capillary condensation in adsorption—desorption isotherms', *Journal of Colloid and Interface Science*, 88(1), pp. 36–46. doi: 10.1016/0021-9797(82)90153-9.

McDowell, R. C. (1986) 'The Geology of Kentucky: A Text to Accompany the Geologic Map of

Kentucky; a Description of the Stratigraphic Units Shown on the State Geologic Map, with Discussions of the Structural Geology, Economic Geology, and Physiography of the State.', *US Government Printing Office*.

McMillan, W. G. and Teller, E. (1951) 'The Assumptions of the B.E.T. Theory.', *The Journal of Physical Chemistry*, 55(1), pp. 17–20. doi: 10.1021/j150484a003.

Meloni, P., Carcangiu, G. and Delogu, F. (2012) 'Specific surface area and chemical reactivity of quartz powders during mechanical processing', *Materials Research Bulletin*. Elsevier Ltd, 47(1), pp. 146–151. doi: 10.1016/j.materresbull.2011.09.014.

Milliken, K. L., Rudnicki, M. and Awwiller, D. (2013) 'Organic matter-hosted pore system, Marcellus Formation (Devonian), Pennsylvania', *AAPG Bulletin*, 97(2), pp. 177–200. doi: 10.1306/07231212048.

Moghadasi, R., Rostami, A. and Hemmati-Sarapardeh, A. (2018) *Enhanced Oil Recovery Using CO₂, Fundamentals of Enhanced Oil and Gas Recovery from Conventional and Unconventional Reservoirs*. Elsevier Inc. doi: 10.1016/B978-0-12-813027-8.00003-5.

Montgomery, S. L., Jarvie, D. M., Bowker, K. A. and Pollastro, R. M. (2005) 'Mississippian Barnett Shale, Fort Worth basin, north-central Texas: Gas-shale play with multi-trillion cubic foot potential', *AAPG Bulletin*, 89(2), pp. 155–175. doi: 10.1306/09170404042.

Moro, F. and Böhni, H. (2002) 'Ink-bottle effect in mercury intrusion porosimetry of cement-based materials', *Journal of Colloid and Interface Science*, 246(1), pp. 135–149. doi: 10.1006/jcis.2001.7962.

Morsy, S., Sheng, J. J., Hetherington, C. J., Soliman, M. Y. and Ezewu, R. O. (2013) 'Impact of Matrix Acidizing on Shale Formations', (August). doi: 10.2118/167568-ms.

Murray, K. L., Seaton, N. A. and Day, M. A. (1999) 'An Adsorption-Based Method for the Characterization of Pore Networks Containing Both Mesopores and Macropores', *Langmuir*, 15(20), pp. 6728–6737. doi: 10.1021/la990159t.

Nagy, E. (2012) *Basic Equations of the Mass Transport through a Membrane Layer*. Elsevier. doi: 10.1016/C2011-0-04271-0.

Nair, H. A., Singh Rajawat, G. and Nagarsenker, M. S. (2018) 'Stimuli-responsive micelles', in *Drug Targeting and Stimuli Sensitive Drug Delivery Systems*. Elsevier, pp. 303–342. doi: 10.1016/B978-0-12-813689-8.00008-2.

Neimark, A. V. (1990) 'Calculating Surface Fractal Dimensions of Adsorbents', *Adsorption Science & Technology*, 7(4), pp. 210–219. doi: 10.1177/026361749000700402.

Neimark, A. V., Lin, Y., Ravikovitch, P. I. and Thommes, M. (2009) 'Quenched solid density functional theory and pore size analysis of micro-mesoporous carbons', *Carbon*, 47(7), pp. 1617–1628. doi: 10.1016/j.carbon.2009.01.050.

Neimark, A. V., Ravikovitch, P. I. and Vishnyakov, A. (2003) 'Bridging scales from molecular simulations to classical thermodynamics: density functional theory of capillary condensation in nanopores', *Journal of Physics: Condensed Matter*, 15(3), pp. 347–365. doi: 10.1088/0953-8984/15/3/303.

Nepryahin, A., Holt, E. M., Fletcher, R. S. and Rigby, S. P. (2016) 'Structure-transport relationships in disordered solids using integrated rate of gas sorption and mercury porosimetry', *Chemical Engineering Science*, 152, pp. 663–673. doi: 10.1016/j.ces.2016.06.057.

Nepryahin, A., Fletcher, R. S., Holt, E. M. and Rigby, S. P. (2016) 'Techniques for direct experimental evaluation of structure–transport relationships in disordered porous solids', *Adsorption*, 22(7), pp. 993–1000. doi: 10.1007/s10450-016-9806-9.

Nia, S. F., Dasani, D., Tsotsis, T. T. and Jessen, K. (2016) 'An Integrated Approach for the Characterization of Shales and Other Unconventional Resource Materials', *Industrial & Engineering Chemistry Research*, 55(12), pp. 3718–3728. doi: 10.1021/acs.iecr.5b04761.

Nichols, C. and Victor, N. (2015) 'Examining the relationship between shale gas production and carbon capture and storage under CO₂ taxes based on the social cost of carbon', *Energy Strategy Reviews*. Elsevier Ltd, 7, pp. 39–54. doi: 10.1016/j.esr.2015.03.005.

Nicholson, P., Nicholson, D., Nicholson, W. and Parsonage, N. G. (1982) *Computer simulation and the statistical mechanics of adsorption*.

Ojha, S. P., Misra, S., Tinni, A., Sondergeld, C. and Rai, C. (2017) 'Pore connectivity and pore size distribution estimates for Wolfcamp and Eagle Ford shale samples from oil, gas and condensate windows using adsorption-desorption measurements', *Journal of Petroleum Science and Engineering*, 158, pp. 454–468. doi: 10.1016/j.petrol.2017.08.070.

Orr, F. M. (2009) 'CO₂ capture and storage: Are we ready?', *Energy and Environmental Science*, 2(5), pp. 449–458. doi: 10.1039/b822107n.

Ougier-Simonin, A., Renard, F., Boehm, C. and Vidal-Gilbert, S. (2016) 'Microfracturing and microporosity in shales', *Earth-Science Reviews*. Elsevier B.V., 162, pp. 198–226. doi: 10.1016/j.earscirev.2016.09.006.

Palchik, V. (2003) 'Formation of fractured zones in overburden due to longwall mining', *Environmental Geology*, 44(1), pp. 28–38. doi: 10.1007/s00254-002-0732-7.

Parlar, M. and Yortsos, Y. (1988) 'Percolation theory of vapor adsorption—desorption processes in porous materials', *Journal of Colloid and Interface Science*, 124(1), pp. 162–176. doi: 10.1016/0021-9797(88)90337-2.

Patchen, D. G. and Carter, K. (2015) 'A geologic play book for Utica Shale Appalachian Basin exploration. West Virginia University Appalachian Oil & Gas Consortium.'

Pavlovskaya, G., Six, J., Meersman, T., Gopinathan, N. and Rigby, S. P.. (2015) 'NMR imaging of low pressure, gas-phase transport in packed beds using hyperpolarized xenon-129', *AIChE Journal*, 61(11), pp. 4013–4019. doi: 10.1002/aic.14929.

Pennell, K. D. (2016) *Specific Surface Area, Powder Technology*. Elsevier Inc. doi: 10.1201/9781420044119.ch3.8.

Pettijohn, F. J. (1957) 'Sedimentary Rocks', *Geological Magazine*, 94(6), pp. 516–516. doi: 10.1017/s0016756800070254.

- Pfeifer, P., Wu, Y. J., Cole, M. W. and Krim, J. (1989) 'Multilayer adsorption on a fractally rough surface', *Physical Review Letters*, 62(17), pp. 1997–2000. doi: 10.1103/PhysRevLett.62.1997.
- Pfeifer, P. and Liu, K.-Y. (1997) 'Chapter 12. Multilayer adsorption as a tool to investigate the fractal nature of porous adsorbents', in, pp. 625–677. doi: 10.1016/S0167-2991(97)80075-4.
- Pomonis, P. J. and Tsaousi, E. T. (2009) 'Frenkel-Halsey-Hill equation, dimensionality of adsorption, and pore anisotropy', *Langmuir*, 25(17), pp. 9986–9994. doi: 10.1021/la901121c.
- Popova, O. (2017) 'Utica Shale Play. Geology review', *US: EIA*, (April), pp. 1–21. Available at: https://www.eia.gov/maps/pdf/UticaShalePlayReport_April2017.pdf.
- Postole, G., Bennici, S. and Auroux, A. (2009) 'Calorimetric study of the reversibility of CO pollutant adsorption on high loaded Pt/carbon catalysts used in PEM fuel cells', *Applied Catalysis B: Environmental*, 92(3–4), pp. 307–317. doi: 10.1016/j.apcatb.2009.08.009.
- Ravikovitch, P. I., O'Domhnaill, S. C., Neimark, A. V., Schiith, F. and Unger, K. K. (1995) 'Capillary Hysteresis in Nanopores: Theoretical and Experimental Studies of Nitrogen Adsorption on MCM-41', *Langmuir*, 11(12), pp. 4765–4772. doi: 10.1021/la00012a030.
- Ravikovitch, P. I. and Neimark, A. V. (2001) 'Characterization of nanoporous materials from adsorption and desorption isotherms', *Colloids and Surfaces A: Physicochemical and Engineering Aspects*, 187–188, pp. 11–21. doi: 10.1016/S0927-7757(01)00614-8.
- Raza, A., Gholami, R., Rezaee, R., Bing, C. H., Nagarajan, R. and Hamid, M. A. (2018) 'CO₂ storage in depleted gas reservoirs: A study on the effect of residual gas saturation', *Petroleum*. Elsevier Ltd, 4(1), pp. 95–107. doi: 10.1016/j.petlm.2017.05.005.
- Rigby, S. P., Barwick, D., Fletcher, R. S. and Riley, S. N. (2003) 'Interpreting mercury porosimetry data for catalyst supports using semi-empirical alternatives to the Washburn equation', *Applied Catalysis A: General*, 238(2), pp. 303–318. doi: 10.1016/S0926-860X(02)00348-4.
- Rigby, S. P., Chigada, P. I., Perkins, E. L., Watt-Smith, M. J., Lower, J. P. and Edler, K. J. (2008) 'Fundamental studies of gas sorption within mesopores situated amidst an inter-connected, irregular network', *Adsorption*, 14(2–3), pp. 289–307. doi: 10.1007/s10450-007-9091-8.
- Rigby, S. P. (2018) 'Recent Developments in the Structural Characterisation of Disordered, Mesoporous Solids', *Johnson Matthey Technology Review*, 62(3), pp. 296–312. doi: 10.1595/205651318X696710.
- Rigby, S. P., Jahan, H., Stevens, L., Uguna, C., Snape, C., Macnaughton, B., Large, D. J. and Fletcher, R. S. (2020) 'Pore structural evolution of shale following thermochemical treatment', *Marine and Petroleum Geology*, 112, p. 104058. doi: 10.1016/j.marpetgeo.2019.104058.
- Rigby, S. P. (2020) *Structural Characterisation of Natural and Industrial Porous Materials: A Manual*. Cham: Springer International Publishing. doi: 10.1007/978-3-030-47418-8.
- Rigby, S. P. and Edler, K. J. (2002) 'The influence of mercury contact angle, surface tension, and retraction mechanism on the interpretation of mercury porosimetry data', *Journal of Colloid and Interface Science*, 250(1), pp. 175–190. doi: 10.1006/jcis.2002.8286.

- Ross, D. J. K. and Marc Bustin, R. (2009) 'The importance of shale composition and pore structure upon gas storage potential of shale gas reservoirs', *Marine and Petroleum Geology*. Elsevier Ltd, 26(6), pp. 916–927. doi: 10.1016/j.marpetgeo.2008.06.004.
- Rouquerol, J., Rouquerol, F., Llewellyn, P., Maurin, G. and Sing, K. (2014) *Adsorption by Powders and Porous Solids*. Elsevier. doi: 10.1016/C2010-0-66232-8.
- Rouquerol, J. *et al.* (1994) 'Recommendations for the characterization of porous solids (Technical Report)', *Pure and Applied Chemistry*, 66(8), pp. 1739–1758. doi: 10.1351/pac199466081739.
- Saif, T., Lin, Q., Bijeljic, B. and Blunt, M. J. (2017) 'Microstructural imaging and characterization of oil shale before and after pyrolysis', *Fuel*, 197, pp. 562–574. doi: 10.1016/j.fuel.2017.02.030.
- Schön, J. H. (2015) 'Rocks—Their Classification and General Properties', in, pp. 1–19. doi: 10.1016/B978-0-08-100404-3.00001-9.
- Seaton, N. A. (1991) 'Determination of the connectivity of porous solids from nitrogen sorption measurements', *Chemical Engineering Science*, 46(8), pp. 1895–1909. doi: 10.1016/0009-2509(91)80151-N.
- Seaton, N. A., Friedman, S. P., MacElroy, J. M. D. and Murphy, B. J. (1997) 'The Molecular Sieving Mechanism in Carbon Molecular Sieves: A Molecular Dynamics and Critical Path Analysis', *Langmuir*, 13(5), pp. 1199–1204. doi: 10.1021/la9510644.
- Seaton, N. A., Walton, J. P. R. B. and Quirke, N. (1989) 'A new analysis method for the determination of the pore size distribution of porous carbons from nitrogen adsorption measurements', *Carbon*, 27(6), pp. 853–861. doi: 10.1016/0008-6223(89)90035-3.
- Seemann, T., Bertier, P., Kroos, B. M. and Stanjek, H. (2017) 'Water vapour sorption on mudrocks', *Geological Society, London, Special Publications*, 454(1), pp. 201–233. doi: 10.1144/SP454.8.
- Seri-Levy, A. and Avnir, D. (1993) 'Effects of heterogeneous surface geometry on adsorption', *Langmuir*, 9(11), pp. 3067–3076. doi: 10.1021/la00035a054.
- Shiko, E., Edler, K. J., Lowe, J. P. and Rigby, S. P. (2013) 'Probing hysteresis during sorption of cyclohexane within mesoporous silica using NMR cryoporometry and relaxometry', *Journal of Colloid and Interface Science*. Elsevier Ltd, 398(4), pp. 168–175. doi: 10.1016/j.jcis.2013.02.002.
- Sing, K. S. (1998) 'Adsorption methods for the characterization of porous materials', *Advances in Colloid and Interface Science*, 76–77, pp. 3–11. doi: 10.1016/S0001-8686(98)00038-4.
- Singh, V. K. and Anil Kumar, E. (2016) 'Measurement and analysis of adsorption isotherms of CO₂ on activated carbon', *Applied Thermal Engineering*, 97, pp. 77–86. doi: 10.1016/j.applthermaleng.2015.10.052.
- Sircar, S., Hufton, J. (2000) 'Why Does the Linear Driving Force Model for Adsorption Kinetics Work?', *Adsorption*, 6, pp. 137–147. doi: <https://doi.org/10.1023/A:1008965317983>.
- Slowakiewicz, M. *et al.* (2015) 'Shale-Gas potential of the mid-carboniferous bowland-hodder unit in the Cleveland basin (Yorkshire), Central Britain', *Journal of Petroleum Geology*, 38(1), pp. 59–75. doi: 10.1111/jpg.12598.

- Smith, J. E. (1971) 'The dynamics of shale compaction and evolution of pore-fluid pressures', *Journal of the International Association for Mathematical Geology*, 3(3), pp. 239–263. doi: 10.1007/BF02045794.
- Smith, J. W. and Young, N. B. (1967) 'Organic composition of Kentucky's New Albany Shale: Determination and uses', *Chemical Geology*, 2(C), pp. 157–170. doi: 10.1016/0009-2541(67)90014-9.
- Smith, L. B. (2013) 'Shallow Transgressive Onlap Model for Ordovician and Devonian Organic-Rich Shales, New York State', in *Unconventional Resources Technology Conference, Denver, Colorado, 12-14 August 2013*. Society of Exploration Geophysicists, American Association of Petroleum Geologists, Society of Petroleum Engineers, pp. 524–533. doi: 10.1190/urtec2013-055.
- Sondergeld, C. H., Newsham, K., Comisky, J., Rice, M. and Rai, C. (2010) 'Petrophysical Considerations in Evaluating and Producing Shale Gas Resources', in *All Days*. SPE. doi: 10.2118/131768-MS.
- Song, H., Min, L., Jun, X., Lushi, S., Peishang, L., Sheng, S. and Xuexin, S. (2004) 'Fractal characteristic of three Chinese coals', *Fuel*, 83(10), pp. 1307–1313. doi: 10.1016/j.fuel.2003.12.011.
- Song, J. and Zhang, D. (2013) 'Comprehensive Review of Caprock-Sealing Mechanisms for Geologic Carbon Sequestration', *Environmental Science & Technology*, 47(1), pp. 9–22. doi: 10.1021/es301610p.
- Sonibare, O. O., Ehinola, O. A. and Egashira, R. (2005) 'Thermal and geochemical characterization of Lokpanta oil shales, Nigeria', *Energy Conversion and Management*, 46(15–16), pp. 2335–2344. doi: 10.1016/j.enconman.2005.01.001.
- Spanakos, D. and Rigby, S. P. (2020) 'Predicting Surface Diffusivities of Gas Molecules in Shale', *Energy & Fuels*, 34(10), pp. 12417–12428. doi: 10.1021/acs.energyfuels.0c02441.
- Speight, J. G. (2015) *Drilling Technology and Well Completion, Subsea and Deepwater Oil and Gas Science and Technology*. Elsevier Inc. doi: 10.1016/b978-1-85617-558-6.00005-2.
- Stanjek, H. H. W. (2004) '3-Basics of X-Ray Diffraction', pp. 107–119.
- Stocker, T.F., Qin, D., Plattner, G.K., Tignor, M.M., Allen, S.K., Boschung, J., Nauels, A., Xia, Y., Bex, V. and Midgley, P. M. (2014) *Climate Change 2013 - The Physical Science Basis*. Edited by Intergovernmental Panel on Climate Change. Cambridge: Cambridge University Press. doi: 10.1017/CBO9781107415324.
- Stow, D. A. V, Huc, A. and Bertrand, P. (2001) 'Black_shales.pdf', 18, pp. 491–498.
- Ver Straeten, C. A., Griffing, D. H. and Brett, C. E. (1994) 'The lower part of the Middle Devonian Marcellus "Shale," central to western New York State; stratigraphy and depositional history; Field trip guidebook; New York State Geological Association; 66th annual meeting', *Guidebook - New York State Geological Association, Meeting*, 66(January), pp. 271–323.
- Swapp, S. (2017) 'Scanning Electron Microscopy (SEM)', *University of Wyoming*.
- Sweda, E. (2019) 'A Geological Analysis of the Appalachian Basin and How It Affects the Oil & Gas Industry', (April).

- Sylvester, P. J. (2012) 'Use of the mineral liberation analyzer (MLA) for mineralogical studies of sediments and sedimentary rocks', (May), pp. 1–16.
- Szabó, Z., Hellevang, H., Király, C., Sendula, E., Kónya, P., Falus, G., Török, S. and Szabó, C. (2016) 'Experimental-modelling geochemical study of potential CCS caprocks in brine and CO₂-saturated brine', *International Journal of Greenhouse Gas Control*. Elsevier Ltd, 44, pp. 262–275. doi: 10.1016/j.ijggc.2015.11.027.
- Szekely, J., Neumann, A. W. and Chuang, Y. K. (1971) 'The rate of capillary penetration and the applicability of the washburn equation', *Journal of Colloid And Interface Science*, 35(2), pp. 273–278. doi: 10.1016/0021-9797(71)90120-2.
- Tan, Y., Pan, Z., Feng, X., Zhang, D., Connell, D. and Li, S. (2019) 'Laboratory characterisation of fracture compressibility for coal and shale gas reservoir rocks: A review', *International Journal of Coal Geology*. Elsevier, 204(January), pp. 1–17. doi: 10.1016/j.coal.2019.01.010.
- Tang, P., Chew, N. Y. K., Chan, H and Raper, J. A.. (2003) 'Limitation of Determination of Surface Fractal Dimension Using N₂ Adsorption Isotherms and Modified Frenkel–Halsey–Hill Theory', *Langmuir*, 19(7), pp. 2632–2638. doi: 10.1021/la0263716.
- Taylor, D. G., Nenadic, C. M. and Crable, J. V. (1970) 'Infrared Spectra for Mineral Identification', *American Industrial Hygiene Association Journal*, 31(1), pp. 100–108. doi: 10.1080/0002889708506215.
- Thommes, M., Smarsly, B., Groenewolt, M., Ravikovitch, P. I. and Neimark, A. V. (2006) 'Adsorption Hysteresis of Nitrogen and Argon in Pore Networks and Characterization of Novel Micro- and Mesoporous Silicas', *Langmuir*, 22(2), pp. 756–764. doi: 10.1021/la051686h.
- Thompson, A. H., Katz, A. J. and Krohn, C. E. (1987) 'The microgeometry and transport properties of sedimentary rock', *Advances in Physics*, 36(5), pp. 625–694. doi: 10.1080/00018738700101062.
- Toga, A. W. (2002) 'Book Review: Imaging Databases and Neuroscience', *The Neuroscientist*, 8(5), pp. 423–436. doi: 10.1177/107385802236971.
- Tompsett, G. A., Krogh, L., Griffin, D. W. and Conner, W. C.. (2005) 'Hysteresis and Scanning Behavior of Mesoporous Molecular Sieves', *Langmuir*, 21(18), pp. 8214–8225. doi: 10.1021/la050068y.
- Tóth, J. (1995) 'Uniform interpretation of gas/solid adsorption', *Advances in Colloid and Interface Science*, 55, pp. 1–239. doi: 10.1016/0001-8686(94)00226-3.
- Tourtelot, H. (1960) 'Origin and use of the word "shale"', *American Journal of Science*, pp. 335–343.
- Vajda, P. and Felinger, A. (2014) 'Multilayer adsorption on fractal surfaces', *Journal of Chromatography A*, 1324, pp. 121–127. doi: 10.1016/j.chroma.2013.11.028.
- Walker, W. C. and Zettlemyer, A. C. (1948) 'A Dual-Surface B.E.T. Adsorption Theory', *The Journal of Physical and Colloid Chemistry*, 52(1), pp. 47–58. doi: 10.1021/j150457a006.
- Wang *et al.* (2019) 'Full-Scale Pore Structure and Fractal Dimension of the Longmaxi Shale from the Southern Sichuan Basin: Investigations Using FE-SEM, Gas Adsorption and Mercury Intrusion Porosimetry', *Minerals*, 9(9), p. 543. doi: 10.3390/min9090543.

Wang, J., Ryan, D. and Anthony, E. J. (2011) 'Reducing the greenhouse gas footprint of shale gas', *Energy Policy*, Elsevier, 39(12), pp. 8196–8199. doi: 10.1016/j.enpol.2011.10.013.

Wang, M., Xue, H., Tian, S., Wilkins, R. W. T. and Wang, Z. (2015) 'Fractal characteristics of Upper Cretaceous lacustrine shale from the Songliao Basin, NE China', *Marine and Petroleum Geology*, 67, pp. 144–153. doi: 10.1016/j.marpetgeo.2015.05.011.

Wang, P., Jiang, Z., Ji, W., Zhang, C., Yaun, Y., Chen, L. and Yin, L. (2016) 'Heterogeneity of intergranular, intraparticle and organic pores in Longmaxi shale in Sichuan Basin, South China: Evidence from SEM digital images and fractal and multifractal geometries', *Marine and Petroleum Geology*. Elsevier Ltd, 72, pp. 122–138. doi: 10.1016/j.marpetgeo.2016.01.020.

Wang, Q. Chen, X., Jha, A. N. and Rogers, H. (2014) 'Natural gas from shale formation – The evolution, evidences and challenges of shale gas revolution in United States', *Renewable and Sustainable Energy Reviews*, 30, pp. 1–28. doi: 10.1016/j.rser.2013.08.065.

Wardlaw, N. C. and McKellar, M. (1981) 'Mercury porosimetry and the interpretation of pore geometry in sedimentary rocks and artificial models', *Powder Technology*, 29(1), pp. 127–143. doi: 10.1016/0032-5910(81)85011-5.

Washburn, E. W. (1921) 'Note on a Method of Determining the Distribution of Pore Sizes in a Porous Material', *Proceedings of the National Academy of Sciences*, 7(4), pp. 115–116. doi: 10.1073/pnas.7.4.115.

Watt-Smith, M. J., Edler, K. J. and Rigby, S. P. (2005) 'An experimental study of gas adsorption on fractal surfaces', *Langmuir*, 21(6), pp. 2281–2292. doi: 10.1021/la048186t.

White, C. M., Smith, D. H., Jones, K. L., Goodman, A. L., Jikich, S. A., LaCount, R. B., DuBose, S. B., Ozdemir, E., Morsi, B. I. and Schroeder, K. T. (2005) 'Sequestration of Carbon Dioxide in Coal with Enhanced Coalbed Methane Recovery A Review †', *Energy & Fuels*, 19(3), pp. 659–724. doi: 10.1021/ef040047w.

Whittig, L. D. (2015) 'X-Ray Diffraction Techniques for Mineral Identification and Mineralogical Composition', in, pp. 671–698. doi: 10.2134/agronmonogr9.1.c49.

Wickstrom, L. H. (2013) 'Geology and activity of the Utica-Point Pleasant of Ohio', *Search and Discovery*, 10490, p. 49pp.

Woo, H.-J. and Monson, P. A. (2003) 'Phase behavior and dynamics of fluids in mesoporous glasses', *Physical Review E*, 67(4), p. 041207. doi: 10.1103/PhysRevE.67.041207.

Wood, A. (2017) 'Invited Review Article Characterization of Organic Shales for Petroleum Exploration & Exploitation: A Review Part 1: Bulk Properties, Multiple Geometry and Gas Adsorption', 28(5), pp. 739–757.

Wood, D. A. and Hazra, B. (2017) 'Characterization of organic-rich shales for petroleum exploration & exploitation: A review-Part 2: Geochemistry, thermal maturity, isotopes and biomarkers', *Journal of Earth Science*, 28(5), pp. 758–778. doi: 10.1007/s12583-017-0733-9.

Yang, F., Ning, Z. and Liu, H. (2014) 'Fractal characteristics of shales from a shale gas reservoir in the

- Sichuan Basin, China', *Fuel*, 115, pp. 378–384. doi: 10.1016/j.fuel.2013.07.040.
- Yu, W., Sepehrnoori, K. and Patzek, T. W. (2016) 'Modeling Gas Adsorption in Marcellus Shale With Langmuir and BET Isotherms', *SPE Journal*, 21(02), pp. 589–600. doi: 10.2118/170801-pa.
- Zdravkov, B. *et al.* (2007) 'Pore classification in the characterization of porous materials: A perspective', *Open Chemistry*, 5(2), pp. 385–395. doi: 10.2478/s11532-007-0017-9.
- Zhang, P., Lu, S., Li, J., Chen, C., Xue, H. and Zhang, J. (2018) 'Petrophysical characterization of oil-bearing shales by low-field nuclear magnetic resonance (NMR)', *Marine and Petroleum Geology*. Elsevier, 89(November 2017), pp. 775–785. doi: 10.1016/j.marpetgeo.2017.11.015.
- Zhang, S., Xian, X., Zhou, J., Liu, G., Guo, Y., Zhao, Y. and Lu, Z. (2018) 'Experimental Study of the Pore Structure Characterization in Shale With Different Particle Size', *Journal of Energy Resources Technology*, 140(5). doi: 10.1115/1.4039022.
- Zhang, T., Ellis, G.S., Ruppel, S.C., Milliken, K. and Yang, R. (2012) 'Effect of organic-matter type and thermal maturity on methane adsorption in shale-gas systems', *Organic Geochemistry*, 47, pp. 120–131. doi: 10.1016/j.orggeochem.2012.03.012.
- Zhang, Z. and Huisingh, D. (2017) 'Carbon dioxide storage schemes: Technology, assessment and deployment', *Journal of Cleaner Production*. Elsevier Ltd, 142, pp. 1055–1064. doi: 10.1016/j.jclepro.2016.06.199.
- Zhong, J., Chen, G., Lv, C., Yang, W., Xu, Y., Yang, S. and Xue, L. (2016) 'Experimental study of the impact on methane adsorption capacity of continental shales with thermal evolution', *Journal of Natural Gas Geoscience*, 1(2), pp. 165–172. doi: 10.1016/j.jnggs.2015.12.001.
- Zoback, M., Kitasei, S. and Copithorne, B. (2010) 'Addressing the Environmental Risks from Shale Gas Development Natural Gas and Sustainable Energy Initiative Addressing the Environmental Risks from Shale Gas Development', (July).